Geomorphology and Geochemistry of Back Arc Basins in the Havre Trough, Southwest Pacific

by

Vanisha Theresa Pullan

A thesis submitted to Victoria University of Wellington in fulfilment of the requirements for the degree of Masters of Science in Geology

School of Geography, Environment and Earth Sciences

Victoria University of Wellington, New Zealand

May 2018

Abstract

The Havre Trough back arc system located behind the Kermadec Arc, in the southwest Pacific, is a classic example of an intra-oceanic back arc system. Subduction driven magmatism is focused at the arc front, and melting in the back arc is accompanied by back arc rifting. This study examines the deep back arc basins of the southern Havre Trough. Compared to the well-studied Kermadec Arc front volcanoes, the back arc basins remain poorly explored, yet are important features in understanding key structural and geochemical dynamics of the subduction system.

The back arc is characterised by areas of deeper basins and constructional cross-arc volcanic edifices, which had previously been attributed to 'rift regime' and 'arc regime', respectively. In this study, recently acquired multibeam data was used to produce digital terrain maps that show individual basins within the Havre Trough that host a range of different morphological features, such as elongated ridges, nearly-flat basin floors, and small volcanic cones. Lavas dredged from the 10 basins were analysed, eight of which sample the rift regime and two sample the arc regime.

The back arc basin lavas are basalts to basaltic-andesites and show fractionation of olivine + pyroxene ± plagioclase mineral assemblages. Olivine phenocrysts were tested for chemical equilibrium and predominantly show that crystallisation occurred in equilibrium with host melts. However, petrographic features such as dissolution and zoning within plagioclase show evidence of multistage magmatic evolution.

Whole rock trace element geochemistry reveals trace element characteristics typical of volcanic arc lavas, such as enrichments in large ion lithophile elements (LILE) and Pb relative to high field strength elements (HFSE). From west to east, the back arc basin lavas show a decrease in Nb_N/Yb_N, consistent with trench perpendicular flow and progressive melt extraction towards the volcanic front. There is also a broad correlation between Nb_N/Yb_N and distance along the strike

of the subduction zone. This may suggest a component of trench parallel flow of the mantle wedge, with increasing depletion northwards, although further evidence is needed to rule out pre-existing mantle heterogeneity.

Ba/Th values, which trace the addition of slab-derived aqueous fluids, decrease with distance from the arc front. This indicates that the aqueous fluid component becomes less prominent with increasing distance from the arc front. Conversely, the basin lavas exhibit broadly increasing La_N/Sm_N values with distance from the arc front. As La_N/Sm_N can be used to trace the deep subduction component, i.e. sediment melt contribution, greater La_N/Sm_N suggests increasing contribution of a sediment signature away from the arc front. The parameters that measure recycled component flux are comparable between rift and arc regimes, so it is unlikely that increased volatile fluxing leads to the larger concentrations of magmatic activity displayed in arc regimes. Gill volcano (arc regime) has similar to higher Nb_N/Yb_N than lavas from adjacent basins, suggesting increased magmatic activity may in part relate to pockets of more fertile mantle. This study shows that back arcs and associated volcanism can be complicated, further research is integral in determining mechanisms for voluminous magmatic activity spread throughout the back arc.

Acknowledgments

I would like to first and foremost thank my supervisors, Monica Handler, Richard Wysoczanski, and Christian Timm for taking me on board in the first place and for all your educational support, guidance and critique during this research.
Monica, thank you for always finding the time to answer even the smallest of questions and making sense of all the trace element data. Richard, thank you for helping me make sense of all the major element and mineral data. Thank you for organising the opportunity to spend the first half of my thesis at NIWA and to attend the Geosciences Conference. Christian, thank you for always finding the time to provide critical insight and unique feedback for my research even when in transit and battling jetlag.

Thank you to NIWA and GNS for providing financial support allowing this thesis to go ahead.

A heartfelt thanks to my family for always providing me with moral and financial support whilst I continued to be a stereotypical student. To Manaia, thank you for your everlasting patient, encouragement and in particular, technical support whilst I battled the evils of Microsoft Word. Thank you for sticking through all the late nights especially over the last few weeks.

To my VUW friends I have met along the way, thank you for making my time on and off campus more enjoyable than a regular arts degree. In particular to Olya and Anya for encouraging me to continue on to post-grad and always finding the time to read through any work I had. To all my friends outside of VUW thank you for always believing in me.

Table of Contents

Table of Figures

List of Tables

Chapter 1:

Introduction

1.1 Thesis context

Magmatism at subduction zones represents one of the principal forms of volcanic activity on Earth, where significant mass and chemical transfer occurs amongst the crust, mantle, hydrosphere, and atmosphere (e.g. Stern, 2002; Tatsumi, 2003). Arc magmatism is generated through volatile flux melting in the mantle wedge, triggered through dehydration reactions in subducting oceanic crust, and typically results in arcuate chains of volcanoes (e.g., Gill, 1981; Wysoczanski et al., 2006) (Figure 1.1).

Back arc basins are located behind the magmatic arc on the overriding plate (Figure 1.1), and may display a wide range of tectonic and magmatic styles depending on varying strain rates, which are strongly controlled by the convergence rate, and the age and dip of the subducting slab (Jarrard, 1986; Stern, 2002, Tatsumi, 2003; Wallace et al., 2005). In situations where the strain rate is low, active extension, rifting, and sea floor spreading characterise the back arc region. In immature settings rifting is initiated when the extensional regime propagates along the strike of the arc system. As the system matures over time back arc rifting may evolve to oceanic spreading, where volcanism is primarily focused at the spreading centre rather than along rifts, faults, and/or weaknesses in the crust. In contrast, high strain rates are associated with back arc thrusting and folding, and may lead to the development of foreland basins behind the magmatic arc. For example, the Andean arc in western North America has developed fold and thrust belts in response to the subduction of buoyant young crust and crustal shortening and compression (e.g., Jarrard, 1986; Stern, 2002).

Back arc magmas form in response to passive upwelling in extensional zones. Mantle that is entering the subduction zone is melted first beneath the back arc or spreading centre before reaching the arc front. Thus, back arc basin basalts

(BABB) derived from mantle entering the subduction zone provide insights into this component of the subduction system (e.g., Tatsumi et al., 2005).

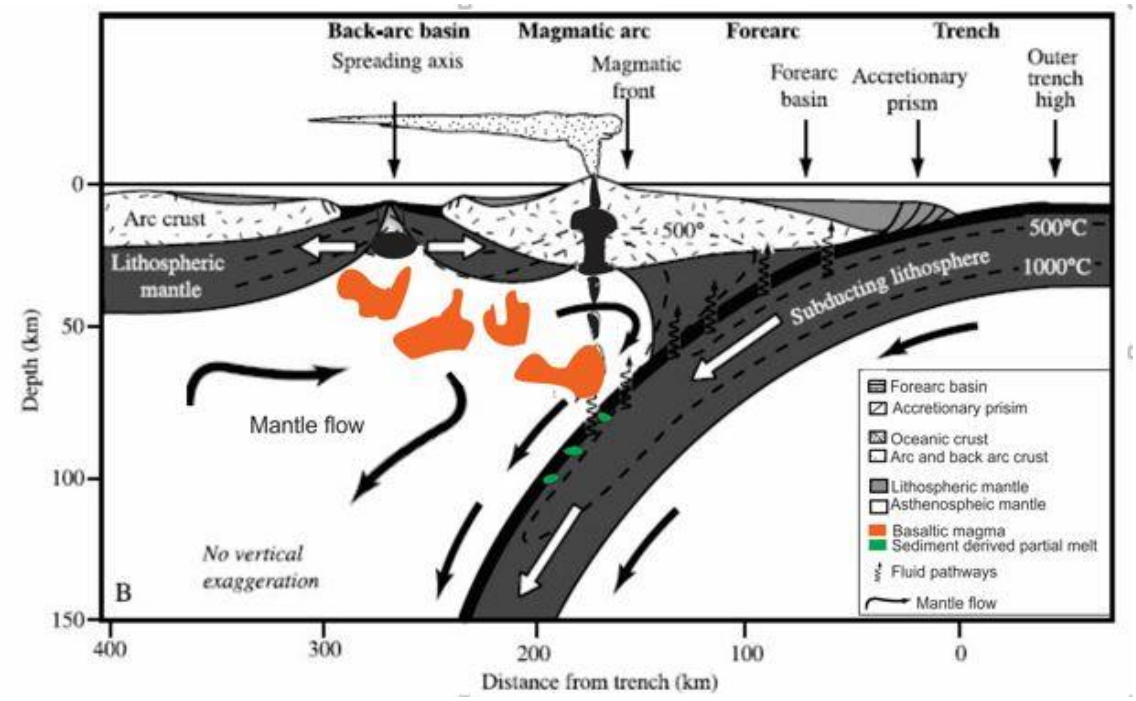

Figure 1.1: Model cross section of an oceanic subduction zone showing process that lead to the generation of subduction zone magmatism in the arc front and back arc. Modified from Stern, (2002).

The Kermadec Arc-Havre Trough subduction zone (KAHT; Figure 1.2), located in the southwest Pacific Ocean, is a young, intra-oceanic, active arc - back arc system. The primary focus of research in this region has been on the Kermadec volcanic front, with most studies focusing on identifying key structural, geophysical, and geochemical characteristics of the arc front since the 1960s (e.g., Gamble et al., 1990; 1991; 1993; 1995; 1996; Gamble and Wright, 1995; Smith and Price, 2006; Wright et al., 2006; Graham et al., 2008; Haase et al., 2002) and more recently the back arc (e.g., Gamble et al., 1994; Todd et al., 2010; 2011; Timm et al., 2011; 2012; 2013; 2014; Wysoczanski et al., 2006; 2010; 2012) and back-arc stratovolcanoes (e.g Wright, 2006; Todd et al., 2010; 2011; Zohrab, 2016). In contrast, deeper back arc basins, remain poorly constrained.

Recent marine research voyages of the NIWA R/V *Tangaroa* (2012-2015; *TAN1213, TAN1313 TAN1512, TAN1513)* have focused exploration on regions of the Havre Trough (between 36°S to 33°S) including basins near the Colville

Ridge, providing detailed swath bathymetry mapping and rock sampling. These voyages have revealed significant features in the back arc such as; small stratovolcanoes, deep basins, ridges, plateaux, and grabens (Wysoczanski et al., 2012). This study utilises the new bathymetric data and BABB samples collected on these voyages to provide a deeper understanding of morphological and geochemical processes occurring in back arc basins in the KAHT system.

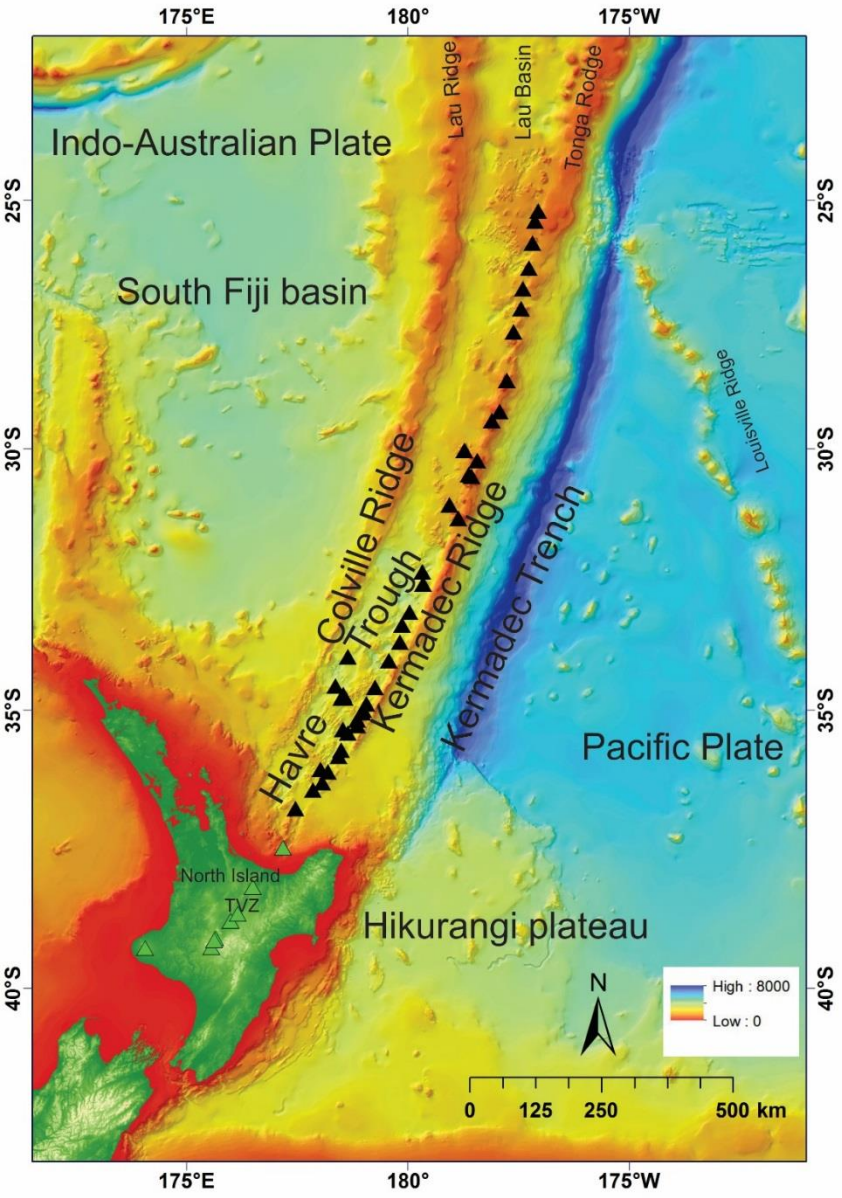

Figure 1.2: Bathymetric map of the KAHT subduction system (NIWA 250 m gridded bathymetry). All arc front and back arc volcanoes are indicated by black triangles. Continental stratovolcanoes are indicated in green triangles. The Taupo Volcanic Zone is represented by TVZ.

1.2 Geodynamic processes and magma genesis at convergent margins

1.2.1 Back arc rifting dynamics

Back arc rifting is initiated through feedback between various processes and may not occur in all arc settings (Molnar and Atwater, 1978). When two plates collide and one plate is negatively buoyant, subduction will occur (Wallace et al., 2009). The transition from collision to subduction causes high pressures to build up on the upper plate, inducing rapid rotation of the forearc microplate (relative to the subducting plate), while shortening is transferred from the trench into the back arc, resulting in rifting in the back arc region (Wallace et al., 2005). Models for back arc rifting are generally two dimensional and propose that extension is likely driven by a combination of asthenospheric processes such as mantle diapirs and/or corner flow, and kinematic boundary conditions such as slab roll back. Slab roll back occurs when the subducting slab migrates in the opposite direction to the plate motion, causing the overriding plate to become stretched, initiating rifting in the back arc to accommodate this (Figure 1.3) (Taylor and Karner, 1983; Wallace et al., 2005; Nakakuki and Mura, 2013).

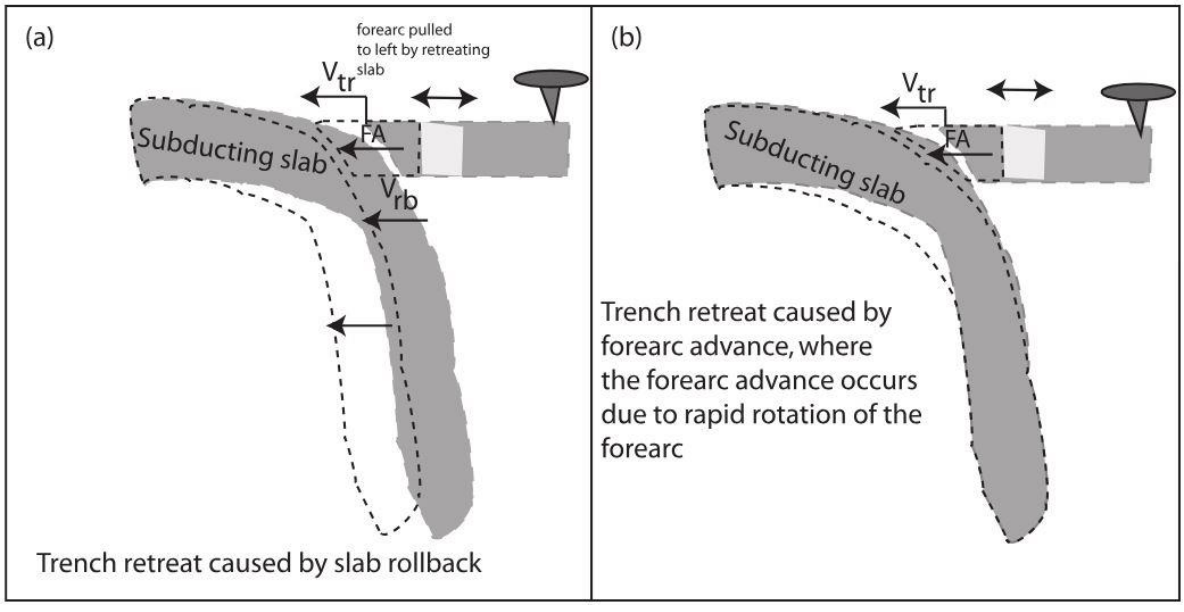

Figure 1.3: Schematic diagram showing (A) Slab roll back causing trench retreat; (B) trench retreat due to rapid rotation and forearc advance. The grey shaded area indicates the early position of the slab and the upper plate and the dashed lines indicate an evolved position of the slab and upper plate. Vtr represents the trench velocity relative to the stable part of the upper plate; Vrb represents the velocity of the slab and FA represents the forearc microplate. Double sided arrows and lightly shaded grey areas represent back arc rifting regions (Wallace et al., 2009).

The well-studied Izu-Bonin-Mariana subduction zone in the NW Pacific exemplifies different stages of back arc evolution and displays irregular spreading rates throughout the basin (e.g. Dewey, 1980, Fryer and Hussong, 1981; Hussong and Fryer, 1983; Carlson and Melia 1984; Garfunkel et al., 1986; Molnar and Atwater, 1986; Beal, 1987; Baker, 1992; Yamazaki et al., 1993; Fryer, 1995; Martinez et al., 1995; Baker et al., 1996; Faccenna et al., 2001). In the north, back arc rifting occurs in the Izu-Bonin arc system, whereas in the Mariana Trough to the south, slow seafloor spreading signifies a more mature (evolved) back-arc system (e.g., Martinez et al., 1995; Gribble et al., 1998, Zhao et al., 2016). Investigations of basalts from the back-arc Mariana Trough have shown a close correlation to island arc lavas with typical arc-like trace element concentrations with some similar to mid ocean ridge basalts (MORB) (Zhao et al. 2016). Studies that have investigated basalts from the Mariana trough have revealed a close relationship between the influence of subduction components to the composition of source magmas and tectonic evolution of the system. Thus, morphology combined with the chemistry of basalts are a useful indictor of the extent of back arc basin evolution (e.g., Elliott et al., 1997; Zhao et al., 2016).

1.2.2 Magma genesis in convergent margins

Magma processes at convergent margins initiate in the descending limb of the subducting plate (Figure 1.4). The subducting plate is comprised of oceanic lithosphere, altered oceanic crust and a sediment veneer that is old, cold and hydrated. When this plate sinks into the mantle, a flow is induced in the overlying mantle wedge (Figure 1.4; 1). Dehydration metamorphic reactions occur in the subducting slab at 150-200km depth, releasing aqueous fluid and silicate melts into the peridotitic mantle wedge, hydrating the mantle and selectively enriching it in these elements (Figure 1.4;2) (e.g., Stern, 2002; Pearce and Stern, 2006; Wysoczanki et al., 2006; Timm et al., 2016).

Sediments that are transported on the subducting slab undergo progressive transformations, increasing in density and decreasing water content of the sediment (Figure 1.4; 3) (e.g., Stern, 2002). In order for clay-rich sediments to melt, temperatures of ~700°C-800°C and pressures corresponding to depths greater than 50km are required to exceed the sediment solidus (e.g., Nicholas et

al., 1996; Johnson and Plank, 1999). Under such P-T conditions, incompatible trace elements immobile in aqueous fluids are likely to become mobile in supercritical fluids or H_2O-rich melts and are then added to the mantle wedge from the subducting slab directly or through diapairs in the mantle wedge that originated at the slab mantle interface (e.g., Pearce and Stern, 2006; Todd et al., 2010; Timm et al., 2016).

As subduction continues and the descending plate flows deeper into the mantle, fluids released lower the solidus of the mantle, triggering volatile flux melting of the overlying mantle wedge, to form volcanic front magmatism (Figure 1.4;4). Melting of the mantle wedge induces a flow as a result of the slab sinking, bringing fresh mantle into the sub-arc front magma generation zone (Figure 1.4;5). However, when a back arc is present, the mantle that is entering the mantle wedge region is first partially melted beneath the back arc before reaching the volcanic front region, and as a result, the mantle that is beneath the arc front is variably depleted in some trace elements compared to the back arc (Figure 1.4;5). Magmatism occurs in the back arc as a response to extension and is manifested as rifts and/or thinned crust, facilitated through adiabatic upwelling. Slab-derived fluids and melts drive partial melting and magma generation in volcanic arcs. In order to distinguish if both components influence the composition of back arc magmas and how this may change across an extending back arc, the geochemical characteristics of back arc basin magmas need to be compared to arc front magmas (Figure 1.4; 6) (e.g., Gamble et al., 1993a; Stern, 2002; Haase et al., 2002; Pearce and Stern, 2006; Wysoczanski et al., 2006; 2010; Timm et al., 2014; 2016; Walowaski et al., 2015).

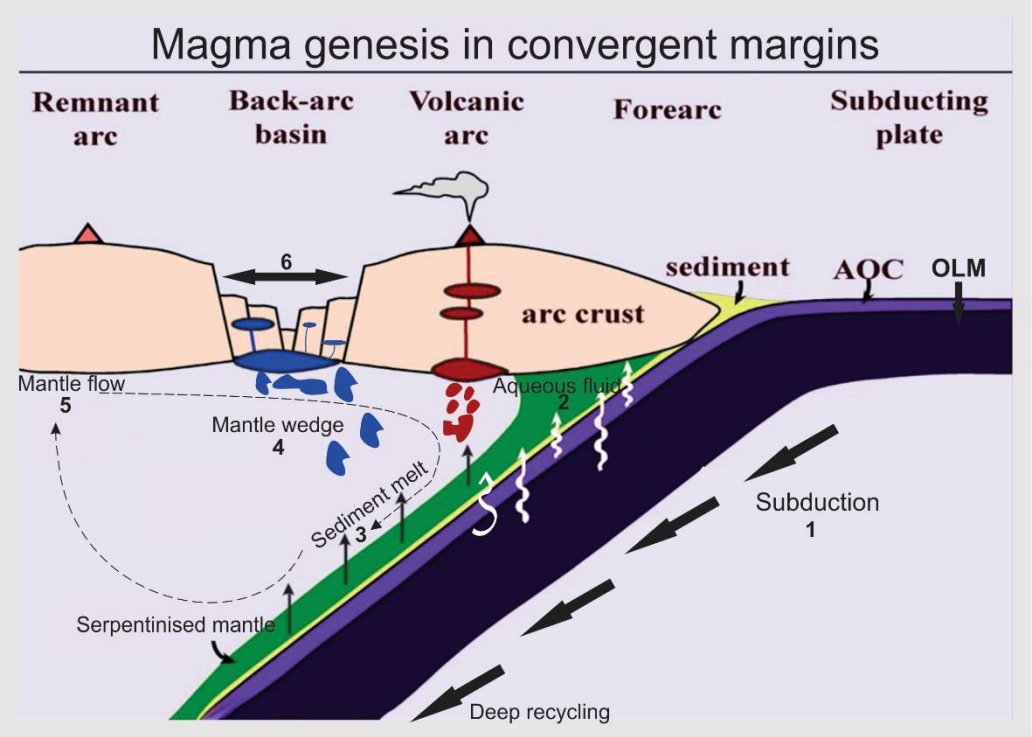

Figure 1.4: Modified schematic diagram of convergent margin systems modified from Wysoczanski et al., 2006. Numbers 1-6 show the processes that occur in subduction zones. **1**: subduction of oceanic lithosphere (OLM), altered oceanic crust (AOC), and a sediment veneer. **2**: dehydration reactions occur along the subducting slab releasing fluid mobile elements and silicate melts into the peridotitic mantle wedge, hydrating the mantle and selectively enriching it in these elements. **3**: sediments melt with changing P-T conditions. **4**: deeper into the mantle volatile fluxing lowers the solidus of the mantle inducing melting of the overlying mantle wedge, to form volcanic front magmatism. **5**: a flow is induced in the mantle wedge from the sinking slab, supplying fresh mantle into the slab-arc front magma generation zone. **6**: extension occurs in the back arc through rifts thinning the crust and magmatism occurs through adiabatic upwelling along rifts and weakened crust.

1.3 Geochemical characteristics of arc and back arc magmas

Analyses of back arc magmas have revealed that they are chemically diverse and range in composition from arc-like to MORB-like reflecting the juxtaposition of decompression and flux melting of a variably depleted mantle wedge (e.g. Hochstaedter et al., 2000; 2001; Haase et al., 2002; Tollstrup et al., 2010; Todd et al., 2010). Pioneering trace element and isotopic studies of Mariana Trough BABB showed that the basalts were derived from a depleted mantle source, analogous to oceanic spreading centres (e.g., Hart, 1972; Pearce and Cann, 1973; Hawkins, 1976). However, analyses of a subset of BABB from the Lau Basin showed significant trace element differences between BABBs and MORB (e.g., Gill, 1976). Several key geochemical characteristics of BABB include elevated water content relative to MORB and variability in subduction components such as high concentrations of large ion lithophile elements (LILE) relative to high field strength elements (HFSE). Higher Sr concentrations coupled with more radiogenic Sr isotope compositions, and a relative depletion in Y (e.g., Gill, 1976; Sinton and Fryer, 1987).

Subsequently, numerous geochemical investigations have confirmed that arc and back arc magmas both result from partial melting of mantle wedge that has been variably fluxed by subducting slab derived components (e.g. Stern et al., 1993; Hochstaedter et al., 2000; 2001; Machida and Ishii, 2003; Tollstrup and Gill, 2005; Machida et al., 2008; Todd et al., 2010; 2011; Tollstrup et al., 2010). Major element trends for both arc and back arc magmas fall into similar magmatic series (tholeiitic and calc-alkaline basalts) and contain geochemical signals that record the recycling of elements through the subduction zone. (e.g. Stern et al., 1993; Hochstaedter et al., 2000, 2001; Machida and Ishii, 2003; Tollstrup and Gill, 2005; Machida et al., 2008; Todd et al., 2010, 2011; Tollstrup et al., 2010).

A study by Pearce and Stern (2006) outlined three main geochemical components in subduction zone magmas that could be distinguished by different element ratios (Figure 1.5):

The mantle component - this represents the mantle entering the subduction system and defines an ambient mantle baseline prior to subduction modification

(proxy ‘A’ in Figure 1.5). The mantle component is exemplified by HFSE which are not fluid-mobile and are highly compatible in refractory mineral phases commonly found in sediments (e.g. rutile, zircon). They are therefore regarded as subduction immobile, and are conservative during subduction processes (e.g., McCulloch and Gamble, 1991; Woodhead et al., 1993; Pearce and Stern, 2006; Todd et al., 2010); A deeper subduction component containing elements mobile in supercritical fluids (a continuum between fluids and melt) or sediment melts released at higher temperatures (proxy ‘C’); A shallow subduction component - representing fluid mobile elements transported from the subducting slab via aqueous fluids (proxy ‘D’). This component can be traced by fluid mobile elements such as LILE (e.g., Pearce and Stern, 2006; Todd et al., 2010). Volatile elements are important in the generation of aqueous fluids and play a key role in facilitating the partial melting of the mantle (e.g. Wallace et al., 2005; Wysoczanski al., 2010). These components can be more simply grouped as two principle components: an ‘ambient mantle’ component (proxy A), with low concentrations of subduction-immobile incompatible elements; and a ‘slab component’ (proxy b in Figure 1.5, comprising both c and d), with enhanced concentrations of subduction-mobile incompatible elements (Pearce and Stern, 2006). Analysing the relative proportions of these different geochemical signals allows element transport mechanisms in subduction zones to be distinguished. 2006).

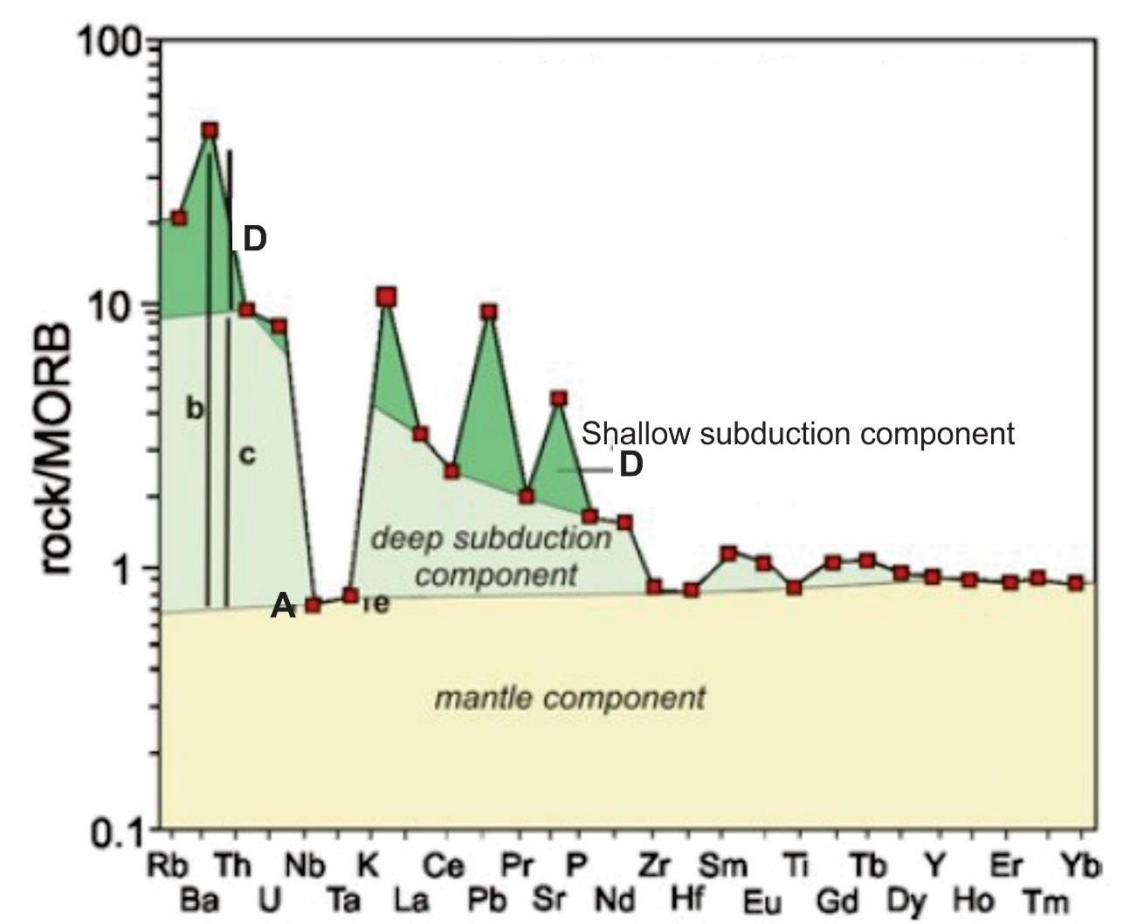

Figure 1.5: MORB normalised multi-element diagram showing subduction input from trace element ratio proxies in a subduction system. Proxy A) is the mantle component measuring mantle fertility and percent of melting using Nb/Yb. Proxy B) is the total subduction component using Ba/Nb. Proxy C) is the deep subduction component using Th/Nb. Proxy D) is the shallow subduction component using Ba/Th and is mobile at higher temperatures is characterised by elements which are mobile at higher temperatures. Elements Ba, Th and Nd are effective fractionation independent proxies for mantle melting (Pearce et al., 2006).

Arc front magmas have a higher fluid component and are therefore more enriched in fluid mobile elements such as LILE. Back arc magmas have lower fluid components and so are less enriched in LILE. Elements that are less soluble in fluids, such as rare earth elements (REE) and Th, may be carried and delivered to the magma generation zone via melting of hydrous silicate sediments. HFSE abundances observed in back arc magmas may provide the best opportunity to see through the contaminating effects of subduction components and thus provides an opportunity to investigate the nature of the (ambient) mantle prior to subduction processing.

Partial melting of the mantle depletes the residual mantle in incompatible trace elements such as HFSE (e.g., Pearce et al., 2006). BABB are generally less depleted in HFSE than volcanic front basalts (Figure 1.5), indicating that BABB has evolved from a more fertile (less depleted) mantle source (Pearce and Stern, 2006; Todd et al., 2010). Furthermore, the HFSE exhibit a range in incompatibility during mantle melting, with Nb and Ta highly incompatible, and Zr, Hf and Ti moderately incompatible. Thus the Nb/Hf will also decrease with increased depletion of the mantle source.

As well as evaluating the contribution of subducting slab components discussed above, the geochemical characteristics of BABB allows us to better constrain the composition of the mantle material that is entering the volcanic front region. This is because the back arc mantle source will have undergone less modification by slab-derived components. The location of the back arc means that it is less exposed to the thermal influence of the cold subducting slab (e.g., Kelley et al., 2006) and therefore more closely reflects any ambient temperature variations in the mantle.

In immature back arc settings, such as the Havre Trough, where magmatism is distributed across the back arc, back arc magmas are generated above the subducting slab at a range of depths and temperatures. Therefore, back arc basalts may be expected to show systematic variations in mantle depletion and subduction components across the back arc and when compared to the volcanic arc (e.g., Todd et al., 2010). Furthermore, correlating variations in the geochemistry of lavas that have erupted along and across strike of the back arc, with structural features of the subduction zone system (e.g. faulting orientation, ridge and basin alignment) should provide insight into lateral variations in the chemistry of the ambient mantle and the proportion of slab component entering the back arc with distance from the arc front.

1.4 Thesis objectives

The primary objective of this thesis is to characterise back arc basins of the KAHT subduction zone system (Figure 1.1 and 1.6). This consists of integrating morphological mapping of the Havre Trough back arc basins with petrography

and whole rock major and trace element geochemistry of selected rock samples previously collected from eleven deep back arc basins (Figure 1.6).

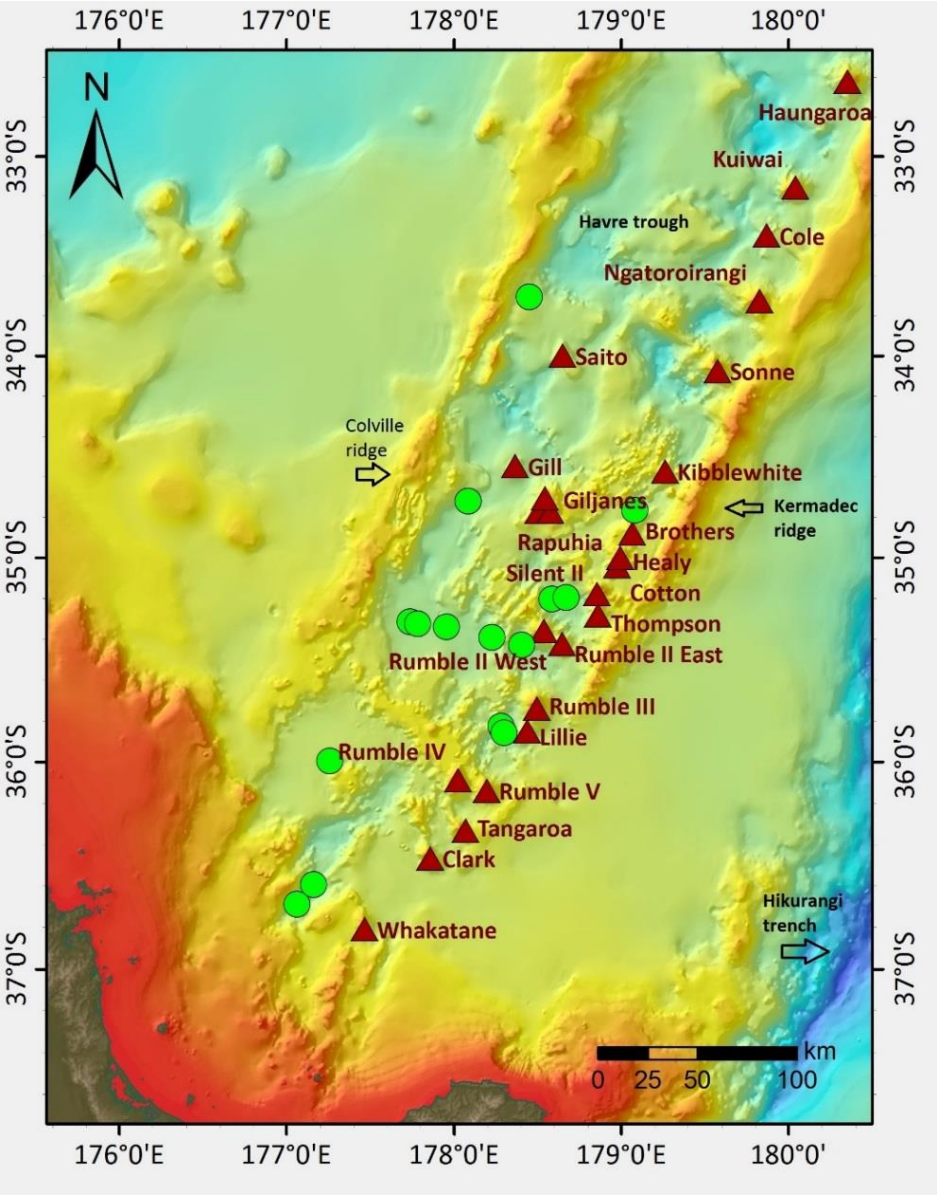

Figure 1.6: Regional bathymetric map of the southern KAHT and remnant Colville arc subduction zone system. Sample sites are indicated in green and volcanoes are indicated in red. Rumble V Ridge is the high extending NW from Rumble V and IV volcanoes to the Colville Ridge. Base map is NIWA 250 m gridded data.

Multibeam echo sounder (MBES) data collected over several research voyages is used to describe the structure and morphology of the basins, giving insight into the morphological nature (i.e. slope angle, and elevation of ridges and cones in the basin), depth, width, asymmetry, and extent of sedimentation of the basins. Together, these features give an indication of how tectonically active the basins have been and the mode of magmatism.

The petrographic and geochemical data provides important insights into back arc magmatism, and the nature of the source ambient mantle wedge as it cycles through the magma generation zones across the subduction zone.

The three research aims of this study are to:

1. Provide the first detailed maps and descriptions of the structural and morphological features of newly mapped back-arc basins of the Havre Trough.
2. Provide the first geochemical and petrological analysis of basalts from these deep Havre Trough basins.
3. Define the composition of the ambient mantle wedge in the KAHT system and the proportion and composition of any slab-derived components using a combination of major and trace element data.

Combining geochemical and morphological analysis of the back-arc samples in this study will contribute to our understanding of subduction system magmatism and the processes associated with magmatism in the Havre Trough. The results presented here also complement previous work on two back-arc basins (Ngatoro Rift and Ngatoroirangi Rift), back arc stratovolcanoes (Gill, Rapuhia, Yokosuka and Giljanes) and studies that have focused on the modern volcanic arc front.

The following techniques have been utilised:

- Digital Terrain Models (DTM) were created for each basin using Arcmap 10.2.1 software. The DTM incorporates features including bathymetry, slope angles and backscatter reflectance to describe basin morphology and structural features (faults).

- Bulk rock petrography using transmitted light microscopy has been described for a subset of samples from each basin.
- Major element compositional data for whole rocks (using X-Ray Fluorescence Spectrometry) and minerals (using electron probe microanalysis (EMPA) are used to define the magmatic processes that have influenced the BABB compositions, such as crystal fractionation and magma mixing.
- Whole rock trace element data, determined using inductively coupled mass spectrometry (ICP-MS), are used to characterise the geochemical variations of the back-arc basin lavas and their mantle source.

1.5 Thesis outline

This thesis is presented in six chapters.

Chapter 1) *Introduction*: An overview of subduction system and back arc processes. This chapter describes the importance and influence of subduction components in the system, and how such components are transported in the subduction factory. A brief introduction to the main objectives of the thesis is also presented.

Chapter 2) *Regional Overview*: A background into the geological setting of the KAHT system, and an overview of back arc opening models proposed from other studies is presented. Also discussed are key geomorphic features of the back arc basins, and the magmatic evolution of the Southern Havre Trough, Kermadec Arc, and Colville Ridge. Details of sample locations are also presented.

Chapter 3) *Analytical Techniques*: A description of the methods used to obtain the morphological, petrographic and geochemical data presented in this thesis.

Chapter 4) *Results*: Presents the results obtained in this study. This chapter is split into several sections corresponding to each type of data obtained: DTMs; petrographic analysis; bulk major element analysis; bulk trace element analysis; in situ mineral analyses.

Chapter 5) *Discussion*: An interpretation of the results presented in Chapter 4, in

terms of basin morphology and nature of magmatism, magmatic evolution of the BABB and variations in the mantle source. Comparisons to the volcanic front, back arc stratovolcanoes, and other intra-oceanic arc settings are also discussed. **Chapter 6)** *Conclusions*: A summary of the key findings of this study and recommendations for future work.

References: A complete list of all references cited in this thesis.

Supplementary Information: A series of appendices are attached including all geochemical and petrographic data collected in the project, and analytical standards used in this study, as well as a list of sample details.

Chapter 2:

Background

2.1. Regional overview

The KAHT subduction zone system, located north of New Zealand, is associated with the oblique westward subduction of the Pacific Plate beneath the Australian Plate. The KAHT system is ~1300 km in length and extends northward from ~37˚S just north of New Zealand to ~25° S (Figure 2.1), where the subduction of the Louisville seamount chain marks the boundary between the northern Kermadec Arc and the Tonga-Tofua Arc system segments (e.g., Lonsdale, 1986). Together the KAHT and Tonga-Tofua arc systems make up an intra-oceanic island arc- back-arc system, characterised by subduction of an old (Cretaceous) and therefore cold, Pacific plate (e.g., Smith and Price, 2006; Graham et al., 2008; Timm et al., 2014).

The Tonga-Kermadec Arc system is regarded as one of the most active volcanic and hydrothermal systems in the world, with 75% of the Kermadec Arc front volcanoes showing signs of hydrothermal activity (e.g., de Ronde et al. 2001; de Ronde et al., 2007). The convergence rates between the Pacific-Australian plates along the Tonga-Kermadec subduction zone increase to the north, coinciding with an increase in distance from the Pacific-Australian pole of rotation (e.g., Wright, 1993; Wallace et al., 2009). Rapid subduction velocities of ~24 cm/yr (highest globally) are observed in the northern Tonga Arc, decreasing southwards to 5 cm/yr in the southern Kermadec Arc (e.g., DeMets et al., 1994; Fujiwara et al., 2001; Ruellan et al., 2001). Associated back-arc widening (or opening) rates are also highest in the north (northern Lau Basin: ~15.8 cm/yr) and decrease to <1 cm/yr in the southern Havre Trough (e.g., Schellart and Sparkman, 2012).

Subduction of the Pacific plate beneath the Tonga-Kermadec Trench is accompanied by the eastward rollback of the Pacific plate moving the trench axis eastwards. In the southern sector of the Kermadec Arc, the trench shallows and

transitions into the Hikurangi Plateau. Further south, the transition from oceanic to continental back-arc opening lies within the Bay of Plenty, northern New Zealand (e.g., Karig, 1970; Wright et al., 1990; Wright, 1993; Gamble et al., 1993; Delteil et al., 2002; Ruellan et al., 2003; Todd et al., 2010; Wysoczanski et al., 2012). This extension into continental crust is associated with intense rifting and extensional faulting, andesitic-rhyolite volcanism, and high heat flow within the Taupo Volcanic Zone (TVZ) (Wright, 1992; Cole et al., 1995; Davey et al., 1995; Wilson et al., 1995; Parson and Wight, 1996; Wright et al., 1996; Taylor et al., 1996; Ruellan et al., 2003).

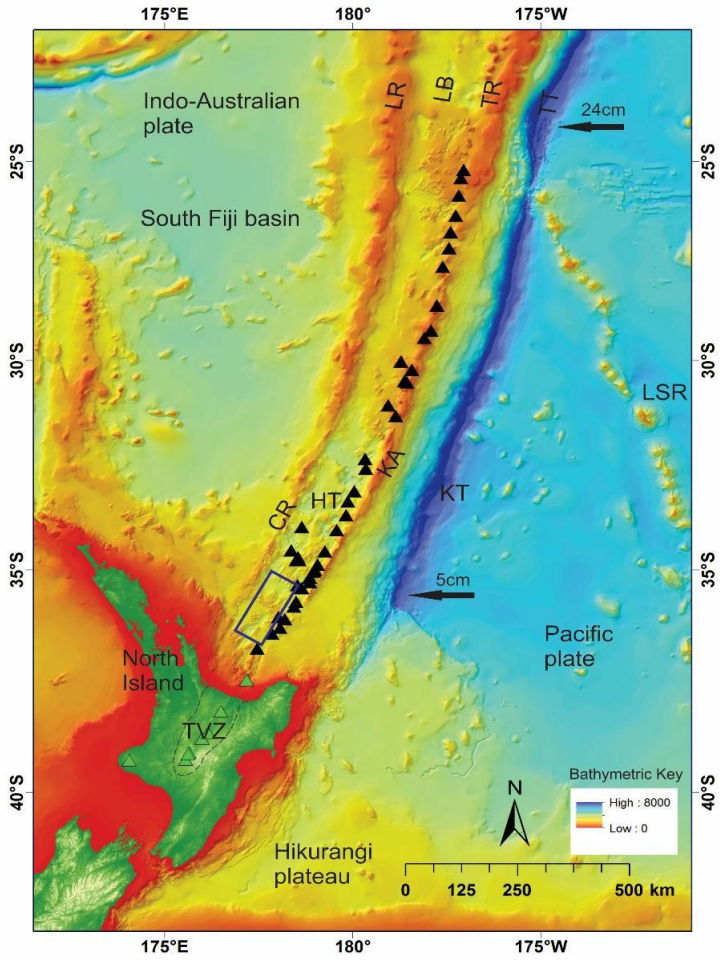

Figure 2.1 Overview showing the regional setting of the Tonga-Kermadec Arc subduction system and Havre Trough. Kermadec Arc (KA), Havre Trough (HT), Colville Ridge (CR), Lau Ridge (LR), Lau Basin (LB), Tonga Ridge (TR), Tonga Trench (TT) and the Louisville Seamount Ridge (LSR). Plate subduction motions are indicated by black arrows, rates are cm/yr (De Mets, 1994). Black triangles indicate arc front volcanoes and back arc stratovolcanoes. Green triangles represent continental volcanoes. Black dashed line outlines the modern TVZ (from Wilson et al., 1995). Dark blue rectangle indicates the region studied here.

The active Kermadec Arc volcanic front is comprised of at least 33 submarine volcanoes and a few partially emergent stratovolcanoes and silicic calderas; Raoul Island, Macauley Island, Herald Island, Curtis Island and L'Esperance Rock (e.g., Smith and Price, 2006; Wright et al., 2006; Wysoczanski and Clark, 2012; Timm et al., 2014). It has been suggested that back arc extension may control the growth of edifices in the southern Kermadec Arc, which is manifested along ridges, faults, in cones and vents, implying that the magmatic evolution of edifices has been modified by cycles of construction and sector collapse (e.g., Wright et al., 2006). Sampling of eruptive units from the Kermadec Arc have revealed lavas are basaltic-andesites, to more evolved dacites to rhyolites in composition. The diversity in lava compositions have been inferred to relate to crustal processes where magmas have undergone prolonged assimilation, crystal fractionation, and differentiation, thus producing dacitic and silicic compositions (e.g., Wright et al., 2006; Haase et al., 2006; Baker, 2012, 2013; Saunders et al., 2010; Timm et al., 2011; Herbert, 2013).

The Havre Trough, ~180 ± 30 km in width, consists of a series of back-arc basins that exhibit a range of different topographical features such as; ridges, plateaux, seamounts/knolls and stratovolcanoes, and rifts comprised of horsts and half-grabens (Wysoczanski et al., 2010; Wysoczanski and Clark, 2012). The location and nature of the back arc basins and their associated stratovolcanoes have been revealed through high-resolution multibeam mapping undertaken by various research voyages over the past two decades (Table 2.1).

Table 2.0-1: Recent marine voyages to the KAHT that have carried out multi-beam mapping and sampling in the southern Havre Trough

Voyage	Year	Voyage leader	Vessel
SO 135	1998	P Stoffers	R/V *Sonne*
TAN 0205	2002	I Wright	R/V *Tangaroa*
YK06-14	2006	R Wysoczanski	R/V *Yokosuka*
SO 192	2007	E Flueh	R/V *Sonne*
TAN1007	2010	G Lamarache	R/V *Tangaroa*
TAN1213	2012	R Wysoczanski	R/V *Tangaroa*
TAN1313	2013	C de Ronde	R/V *Tangaroa*
TAN1512	2015	C de Ronde	R/V *Tangaroa*
TAN1513	2015	R Wysoczanski	R/V *Tangaroa*

The onset of rifting of the previously active Colville Arc resulted in the opening of the Havre Trough, between the remnant Colville Ridge to the west and the Kermadec Ridge to the east (e.g., Mortimer et al., 2010; Wysoczanski et al., 2012). To the north, the boundary between the Havre Trough and the Lau Basin is delineated by a transition from back arc rifting in the Havre Trough to oceanic sea floor spreading in the Lau Basin (Martinez and Taylor, 2006) and where the Louisville Seamount Chain (LSC) intersects the subduction zone, possibly locking the Havre Trough back-arc system (Ruellan et al., 2003). At its southern-most extent, the Ngatoro Rift in the Havre Trough impinges the continental margin of New Zealand.

2.1.1 Back arc opening and disorganised spreading in the Havre Trough

The formation of back arc basins in the southwest Pacific is inferred to have occurred in an episodic manner throughout the past 45 million years (e.g., Sdrolias et al., 2003). However, the timing of opening in the Lau-Havre back arc system is not well constrained. Opening is interpreted to have commenced at ~5 Ma through rifting of older, oceanic arc crust along the eastern margin of the 13-26 Ma South Fiji Basin (e.g., Clift and Dixon, 1994; Parson et al., 1994; Sdrolias et al., 2003; 2004; Crawford et al., 2003; Schellart et al., 2006; Mortimer et al., 2010). Pacific trench roll back is taken up in the back arc domain through back arc extension. Structural analysis carried out along the basin axis reveals that there has been dextral displacement relative to the Australian plate, through left lateral en echelon rifts and/or rifted segments (Delteil et al., 2002).

Early interpretations of aeromagnetic survey data of the Havre Trough suggested active oceanic spreading (~half-spreading rate of 2.7cm^{-}yr) as the mechanism for basin widening in the Havre Trough (e.g., Malahoff, 1982). Subsequent studies that incorporated swath bathymetry, side-scan imagery surveys, airborne magnetic and gravity data, and dredged rock samples documented the presence of oblique en echelon basement structures as well as alternating horst-graben fault systems, but provided no evidence for active oceanic spreading to occur within the Havre Trough (e.g., Pelletier and Louat 1989; Pelletier et al., 1998; Caress 1991; Wright et al., 1996; Balance et al., 1999; Wysoczanski et al., 2010).

The thickness of the Havre Trough ocean crust ranges from ~6 - 15 km (e.g., Wysoczanski et al., 2010; Bassett et al., 2016; Timm et al., 2014; Timm et al., 2016). Prior to formation of the Havre Trough, the separation of the Three Kings Ridge from the western flank of the Colville Ridge, and subduction related tectonic erosion of the Hikurangi Plateau may have caused localised super-thinned arc crust (< 6 km) within the Southern Havre Trough (e.g., Collot and Davey, 1998; Mortimer et al., 2007).

Magmatism in the southern Havre Trough has also been proposed to have occurred through disorganised nascent spreading in the back arc in multiple deep (> 4000 m) rifted systems (Wysoczanski et al., 2010). Such rifting systems

are characterised by failed rifts, rift segmentation and propagation, and deep half graben rifting (Fryer et al., 1996; Wysoczanski et al., 2010). A similar disorganised spreading fabric is observed in the western Lau basin, represented by hummocky terrain, volcanic seamounts and/or knolls in the Lau basin. These features are interpreted to have preceded what would have been the final development of full organised oceanic spreading after the breakup of the arc massif and readjustment and migration of arc volcanoes in a young evolving back arc basin (e.g., Clift and Dixon, 1994; Parson et al., 1994).

The earliest phases of rifting are not well constrained and the initial age of opening in the Lau Basin-Havre Trough remains speculative. The most widely accepted interpretation is that the first stages of rifting occurred in the Lau Basin-Havre Trough at approximately 5.5 - 6 Ma (e.g., Wiedicke and Collier, 1993; Parson and Hawkins, 1994; Hawkins, 1995; Parson and Wright, 1996; Taylor, 1996; Deltiel et al., 2002). This early extension was accompanied by high angle dip-slip boundary faults and crustal thinning, following a southward propagation of en echelon rift segments along the axis of the proto-Kermadec Arc ridge. These features have been suggested to represent simultaneous rifting along the length of the proto-arc from Tonga to New Zealand (Parson and Wright, 1996; Ruellan et al., 2001; Delteil et al., 2002).

A second phase of rifting at ~5 to 4 Ma has been proposed by Ruellan (2003), where the Louisville Seamount Chain began subducting beneath the Tonga arc in the north. Assuming the Tuvalu Seamount Chain was morphologically continuous with the Louisville Seamount Chain, then the Tuvalu Seamount Chain would have arrived at the northern tip, parallel to the Tonga Arc, and subduction of the Tuvalu Seamount Chain would have occurred over its entire length during this phase (Ruellan et al., 2001). Kinematic models (Pelletier and Louat, 1989; Lallemand, 1992) and observations made on the present day structure of the Havre Trough suggest that the subduction of the Louisville Seamount Chain and the oblique collision of the Hikurangi Plateau may be responsible for heterogeneous tectonic fabric and location of back arc opening along the whole length of the system (Ruellan et al., 2003).

During the second phase of rifting, Parson and Wright, 1996 proposed that the Havre Trough was comprised of actively subsiding half and full grabens that were separated by arc massifs. Syntectonic sedimentation and the first phases of active volcanism in the back-arc region were established within these grabens (e.g., Parson and Wright, 1996). The age and duration of this phase, as for phase one and later phases, are poorly constrained. However, interpretations of the Lau Basin and Havre Trough tentatively suggest that rifting during phase two lasted for at least 2-3 million years (Parson and Wright, 1996).

A third phase of rifting in the Havre Trough, commencing at ~3.5 Ma, is characterised by diachronous back arc rifting in the Havre Trough and a transition to oceanic spreading in the Lau Basin along the central axial rift zone of the southern Lau Basin (Valu Fa Ridge). Rifting in the Havre Trough is suggested to have been marked by a series of deep (>3000m), asymmetrical half-grabens, coinciding with a decrease in tectonic activity and magmatism in the flanks of the grabens proximal to the Colville Arc (Parson and Wright, 1996; Ruellan et al., 2003).

Successive episodes of magmatic intrusion into thinned and faulted arc basement has resulted in asymmetric back arc crustal accretion. Spreading along short segmented rifts may be characteristic of arc proximal accretion and slower extension rates such as that observed in the Lau Basin (Wysoczanski et al., 2010).

2.2 Key geomorphic features of the Kermadec Arc-Havre Trough

2.2.1 Definition of geomorphic features

The main geomorphic features which comprise the Kermadec Arc-Havre Trough are summarised in Table 2.2. Each feature is characterised by their structure and distribution throughout the system. The Havre Trough itself is comprised of many deep basins that reach depths of up to 4000 mbsl. These basins make up ~ 27.7% of the entire southern KAHT system by area while only 3.7% of basins comprise the Kermadec Arc. A basal platform lies within the Havre Trough and is characterised by depths of 2500 mbsl, this feature comprises a total of 34.1% of

the Havre Trough surface area. There are two main ridges in the KAHT system, these are the Kermadec Arc and Colville Ridge which are ~20-30 km wide and comprise 29.9% of the total surface area of the entire system, rising above the base of the plateaux and north as the Lau and Tonga Ridges, respectively. Both Ridges exhibit asymmetric profiles, for example steeper trough sides, which are eroded in comparison to the outward slope faces that grade into adjacent basins (e.g., Wright, 1997; Wysoczanski and Clark, 2012). Within the back arc ridges are widely abundant comprising a large proportion of the total surface area.

Seamounts are less common in the back arc region comprising 0.5% of the total area (e.g. Gill volcano) and are generally surrounded by basins (>2500 mbsl). Seamounts comprise a large proportion of the Kermadec Arc surface area (4.1%) most of which are considered hydrothermally active or dormant, with a few larger edifices featuring summit calderas (e.g. Brothers and Healy seamounts) Wysoczanski and Clark, 2012). Other features present in the Havre Trough include obliquely oriented elevated domains, tilted blocks in the basement fabric, and elongated horst and grabens (e.g. Figure 2.2.1, Reullan et al., 2003).

Table 2.0-2: Summary of the main geomorphic features with in the KAHT and the abundance % of each feature. Basal platforms are characterised as basaltic plateaus. (Wysoczanski and Clark, 2012).

Geomorphic structure	**Areal abundance (%)**
Basins (<2500 mbsl) in the Havre Trough	27.7%
Basal platforms (>2500 mbsl) in the Havre Trough	34.1%
Seamounts and/or knolls Kermadec Arc Havre Trough	4.6 % 4.1% 0.5%

Ridges	29.9%
Colville Ridge	16.3%
Kermadec Ridge	13.6%

2.2.2 Distribution of features in the Havre Trough

Basins

In the west, proximal to the remnant Colville Ridge, basins are approximately 3200 mbsl, and are thickly sedimented (e.g., Wright et al., 1996; Fujiwara et al., 2001). Conversely, in the east, proximal to the active Kermadec margin, basins exhibit rugged seafloor topography, shallower bathymetry, volcanic edifices, and actively deforming half graben systems. In the southern sector of the Havre Trough (~36°31'S -36°44'S), basins are generally deeper (up to 4000 mbsl) and consist of complex rift, horst and half graben topography, bounded by multi-terraced rift escarpments (e.g., Wysoczanski et al., 2010) and in the northernmost Havre Trough between 25°30'S and 26° 30'S sedimentary basins are distributed in the back arc (Ruellan et al., 2003). post

Plateau

The back arc region includes a plateau that impinges on the remnant Colville Ridge. The plateau lies at 2500 mbsl, coincident with the depth of the ocean floor either side of the southern KAHT. This plateau is dissected by smaller basins, linear ridges, and lines of knolls, which trend orthogonal to the frontal arc. These structures display a high reflectivity and may therefore reflect young or recent magmatic features (Wysoczanski and Clark, 2012). The plateau itself displays low backscatter reflectivity, which may indicate either: high cover; old, weathered volcanic rock consisting of post-rift magmatic activity; or remnant proto Kermadec Arc, deformed due to rifting (Wysoczanski and Clark 2012).

Ridges

Volcanic ridges are distributed throughout the back arc within deep basins and near constructional edifices. They have been previously interpreted by Wysoczanski et al, (2010) to represent pervasive dyke systems that have penetrated through basement floors. Majority of ridges show strikes at 045°

parallel to the arc front. In the northern and southern Havre Trough ridge fabric show strikes of 040°.

The ridge fabric shows arc-like magmatism has been sufficiently voluminous to produce cross-arc ridges or chains that extend across the back arc perpendicular to the volcanic front (e.g., Wright et al., 1996). A cross arc ridge at ~36°S forms a 40 km wide and 80 km long dissected and morphologically complex 300 – 900 m high basement block (Blackmore and Wright, 1995; Todd et al., 2010). The ridge extends the full width of the Havre Trough between the active arc front at Rumble IV (2000 m isobaths) arc volcano, and the Colville Ridge to the west (Wright et al., 1996). Volcanic ridges that extend from cross arc chains show orientations of 020-030°, as well as kinked orientations, which increase in orientation (clockwise) for northern edges of ridges (Wysoczanski et al., 2010).

Seamounts

Based on their morphology, back-arc seamounts can be subdivided into three main groups: 1) small, circular, isolated cones up to 2 km in diameter and up to 300 m high. These cones are generally present within high sedimented areas; 2) Larger 800-1000 m high circular-elongated cones ~4-8 km across; and 3) Large, > 1000 m high composite cone massifs, ~11-13 km across (Wright et al., 1990), A large (1100 m above seafloor basement) isolated volcanic edifice built on a basement platform ~2500 to 3000 mbsl (Figure 2.2) characterised by highly reflective pillow lavas (e.g., Wysoczanski et al., 2010; Wysoczanski and Clark, 2012). The combination of high back scatter reflectivity and observation of only thin manganese crusts and sediment cover suggests that volcanism of seamounts is young (Wright et al., 1996; Wysoczanski et al., 2010). A back arc stratovolcano, Gill, and the nearby Rapuhia Ridge (e.g. Figure 2.2.3) also yield relatively young ^{40}Ar-^{39}Ar ages (ca. 1170-950 ka and ca. 110-50 ka, respectively; Zohrab, 2016) consistent with the presence of young volcanism in the back arc.

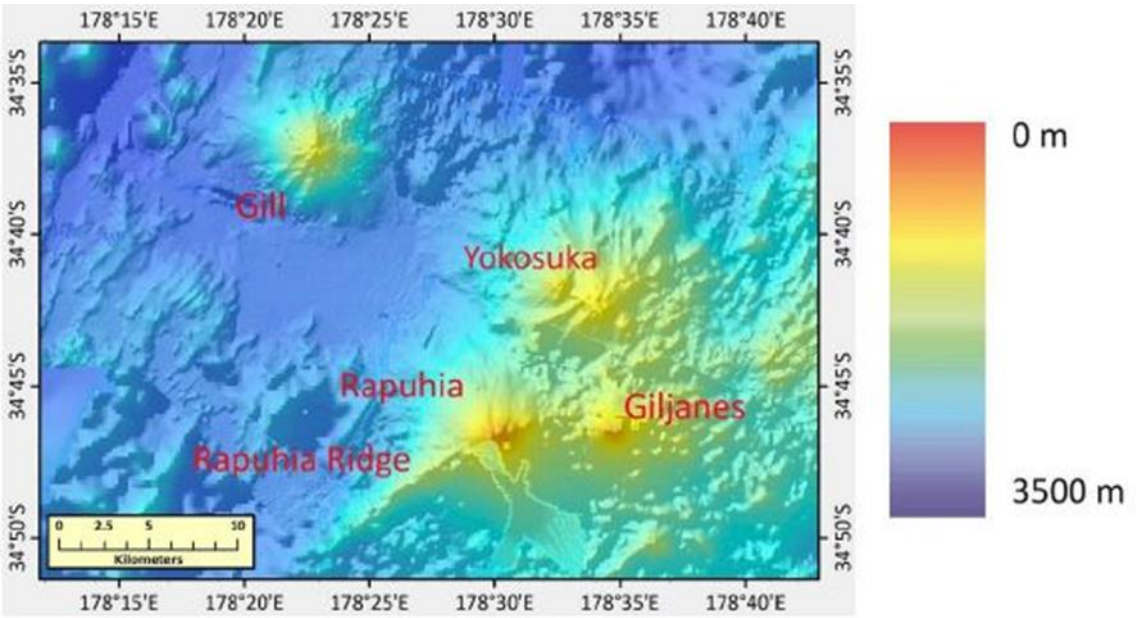

Figure 2.2: Digital topographic map showing the location of back arc stratovolcanoes Gill, Rapuhia, Rapuhia Ridge, Yokosuka, and Giljanes. Image obtained from Zohrab (2016).

Rifts

Deep rifts (spreading systems) of > 4000 mbsl also occur within the back-arc region trending NE-SW subparallel to and impinging on the arc front. Two large rifts have been identified through multi-beam imagery, the Ngatoro Rift located between ~36° 00'S, 176°50'E and ~36° 40'S, 177°50'E (Wright, 1993) and the Ngatoroirangi Rift, located further north between ~33° 29'S, 179°30'E and ~33° 34'S, 179°36'E (Wysoczanski et al., 2012). Manned submersible dives in the Ngatoroirangi Rift (Wysoczanski et al., 2010) revealed stepped graben structures that contain high reflective scarp slopes separated by fault terraces ranging in width from 200-400 m. Rift walls gently dip at 27° and are sediment covered, reflecting an absence of recent volcanism. By contrast, the western walls of the rift consist of alternating constructional pillow basalt ridges separated by sediment covered terraces (Wysoczanski et al., 2010).

An axial ridge lying along the axis of the Ngatoroirangi Rift extends over 5.5 km in length and rises ~ 220 – 240 m above the rift floor. This axial ridge consists of a series of scarps and gently dipping terraces. Dredge sampling of the ridge has revealed well-preserved pillow basalts, tube flows, pillow talus, sparse sediment cover and thin manganese crusts. The less altered nature of the sample lavas

suggests that magmatism may have been more recent here than that observed at the western Ngatoroirangi Rift wall. (Wysoczanski et al., 2010)

2.3 Geochemistry of Havre Trough lavas

The nature of volcanism in the southernmost section of the Havre Trough (35°30'S-36°00'S) is relatively well documented with several studies focusing on large rifts and basins in the Havre Trough. However, the relationship between magmatism, rifting, and extensional processes in the back arc remains a centre of debate (Caress et al., 1991; Benes and Scott, 1995; Parson and Wright, 1996; Wright et al., 1990; 1996; 1997; Balance et al., 1999; Nishizawa et al., 1999; Fuijiwara et al., 2001; Deiteil et al., 2002; Wysoczanski et al., 2010; Todd et al., 2010; Todd et al., 2011). It has been proposed that successive episodes of magmatic intrusion have occurred through active rift-floor, wall extensional magmatism, cross-arc chains and isolated seamounts (Wysoczanski et al., 2010).

2.3.1 Geochemistry of Ngatoro and Ngatoroirangi Rift lavas

The submersible dives within the Ngatoroirangi Rift revealed seafloor outcrops that are tectonically aligned and have been interpreted to represent a loci for young rift magmatism and extension (Wysoczanski et al., 2010). Deep rifts in the southern Havre Trough have been interpreted to resemble the morphology of the southern Valu Fa ridge and western Lau Basin, which are considered to be undergoing nascent 'disorganised' spreading, prior to the development of a mature oceanic spreading such as that observed in the Lau basin (Martinez and Taylor, 2006). The following section summarises previously reported major and trace element geochemistry for southern Havre lavas.

Basalts from Ngatoro Rift in the southern Havre Trough are porphyritic and follow a crystal fractionation sequence consistent with olivine + Cr-spinel + plagioclase + clinopyroxene (Gamble et al., 1994). Whole rock data show SiO_2 contents of ~50 wt. %, MgO contents >7 wt. %, Al_20_3 contents of 15-17 wt. % and K_20 contents ranging between 0.2-0.4 wt.% (Figure 2.3). Lavas from the southern Havre Trough exhibit typical subduction zone trace element enrichments in LILE, LREE and depletions in HFSE relative to N-MORB (Gamble et al., 1996; Wysoczanski et al., 2006)

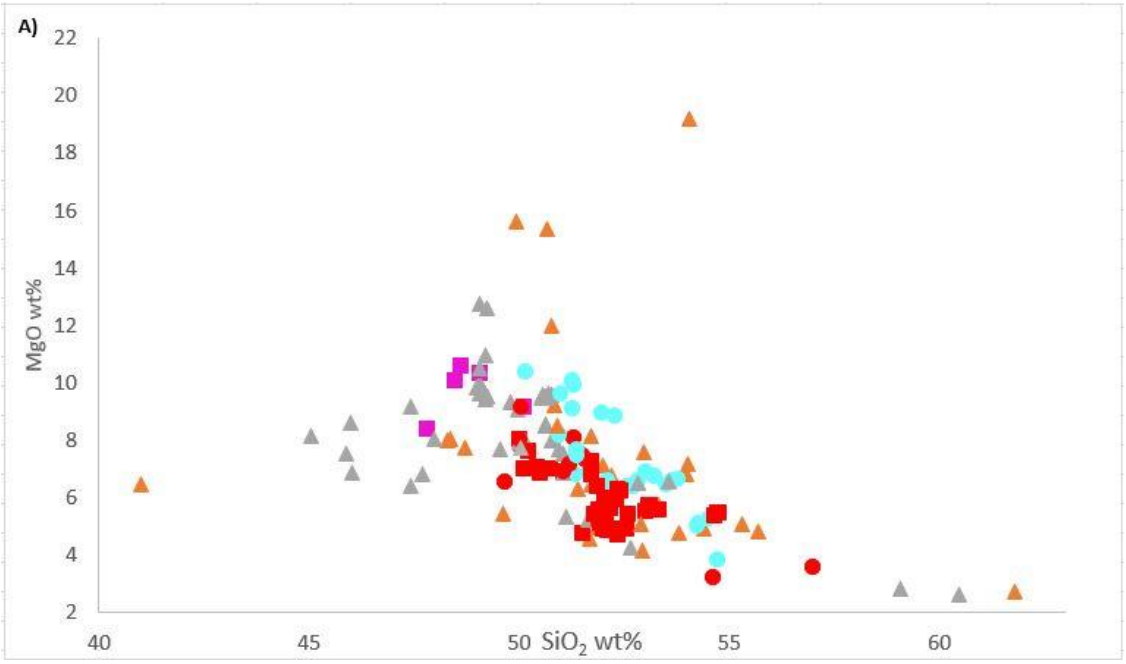

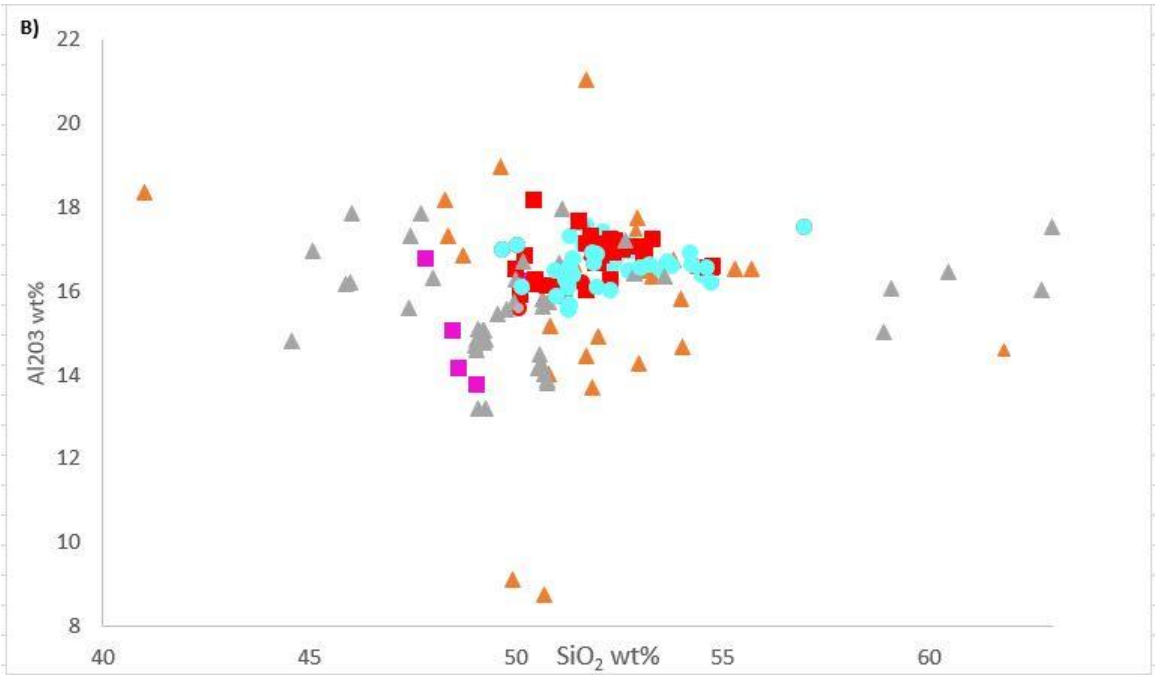

Kermadec arc
Back arc strato volcanoes
Rumble V ridge
Havre Trough basins
Ngatoro basin
Ngatoro rift
Ngatoroirangi rift

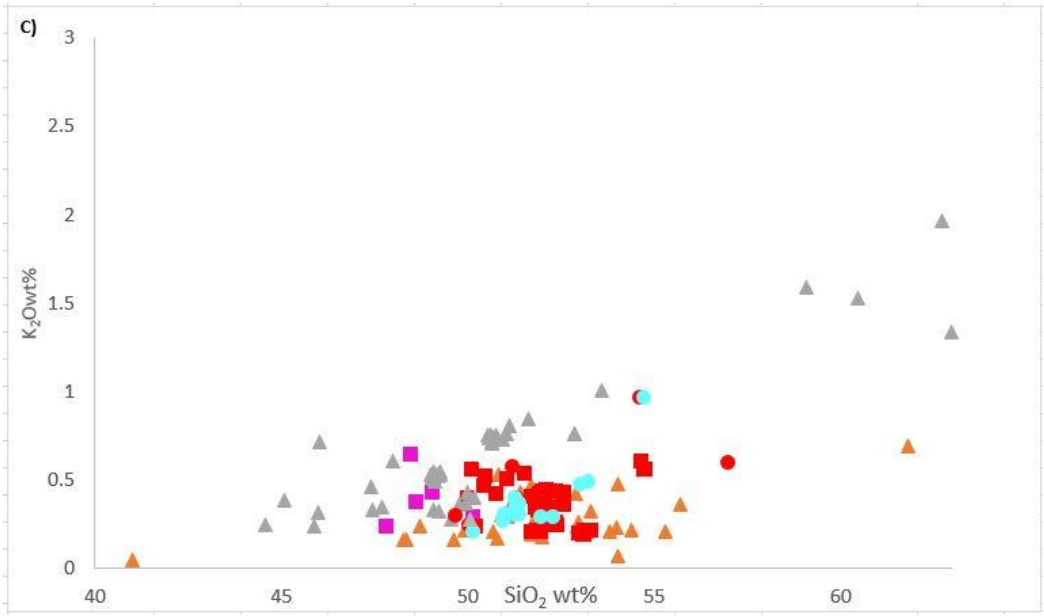

Figure 2.3: Plots showing major element variations **A)** SiO_2 vs MgO **B)** Al_2O_3 vs SiO_2 **C)** K_2O vs SiO_2 between previously analysed Havre Trough basalts, Kermadec Arc samples, southern Havre Trough samples Ngatoro Rift and Ngatoroirangi Rift and back arc stratovolcanoes Gill, Rapuhia, Gilijanes, Yokosuka. Data obtained from Gamble, (1990; 1994); Wright et al., (2002); Haase et al., (2002); Wysoczanski et al., (2006; 2010); Baker et al., (2012); Todd et al., (2011); Timm et al., (2016); Zohrab, (2016).

Rocks recovered from the Ngatoroirangi Rift are olivine-rich basalt-basaltic andesites, interpreted to reflect recent volcanism (Wysoczanski et al., 2012). Samples from the Ngatoroirangi Rift have slightly higher SiO_2 contents (50-55 wt. %) and lower MgO contents (5-6 wt. %) compared to those from the Ngatoro Rift and western Havre Trough basins (Figure 2.4). Whole rock glass compositions indicate that the samples are similar to the other Havre Trough samples as both display higher Na_2O+K_2O for a given SiO_2 than the volcanic front. Higher TiO_2 for a given MgO than the Kermadec Arc, Tonga Arc and the Valu Fa Ridge, but are similar to the Lau spreading centre and Hole 834 amongst the least evolved (high Mg# e.g. 50-60) and most depleted (low TiO2 wt. % e.g. 1-2) from all southern Havre Trough basalts and resemble basalts from the Lau Basin, with exception to rift wall samples that resemble arc front compositions (Figure 2.4).

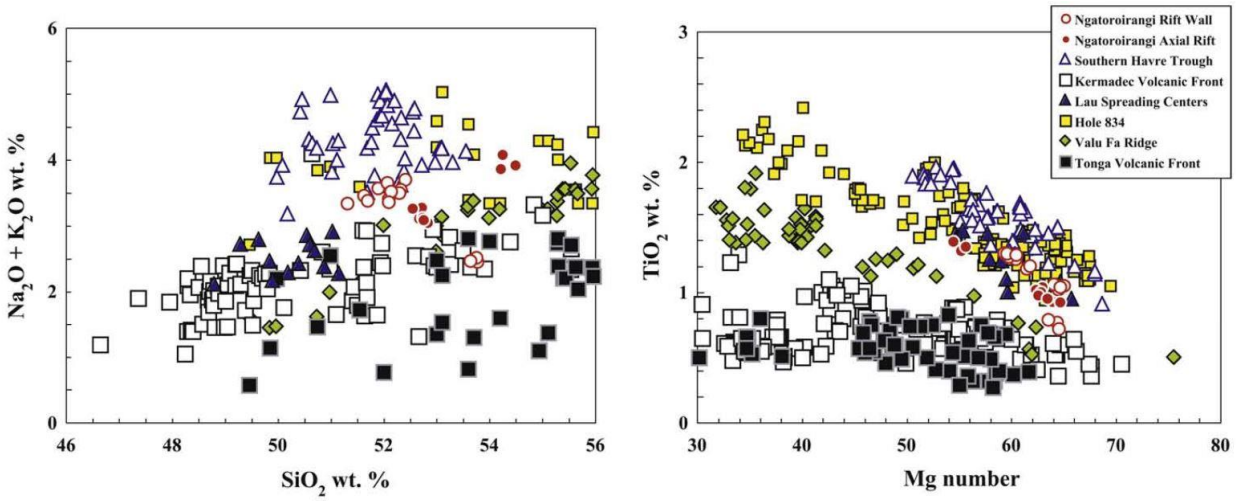

Figure 2.4: Plot showing glass compositions of samples from the Ngatoroirangi Rift compared to previously analysed samples from the southern Havre Trough, Tonga-Kermadec Arc and the Lau basin. A) Total alkali silica diagram and B) TiO2 VS Mg number (Ewart et a., 1994; 1997; 1998; Falloon et al., 1992; Frenzel, 1990; Gamble et al., 1990; 1993; 1994; 1997; Hawkins et al., 1994; Hergt and Nilsson, 1994; Smith et al., 2003; Sunkel et al., 1990; Turner et al., 1997; Vallier et al., 1992; Wysoczanski et al., 2010).

Sr and Nd isotopic systematics are variable in the back arc. Basalts have less depleted $^{87}Sr/^{86}Sr$ ratios (e.g. 0.702556) and low E_{Nd} (e.g. +9.3), values that are significantly lower than arc front basalts, whereas the Ngatoro Rift basalts have less depleted compositions $^{87}Sr/^{86}Sr$ (e.g. 0.7028) low E_{Nd} (e.g. +8.7), resembling basalts from the northern Kermadec Arc (Gamble et al., 1993; 1996; Todd et al., 2010; 2011). Basalts from the Rumble II cross arc chain in the southern Havre Trough have higher $^{87}Sr/^{86}Sr$ (e.g. 0.702991 – 0.705221) and low $^{143}Nd/^{144}Nd$ (0.512756 – 0.513102) isotopic compositions suggesting they were variably modified by a sediment melt component derived from the subducting slab with less influence from a fluid component than arc front lavas (Todd et al., 2011). Variations in the Nd-Hf isotope compositions of the cross-arc lavas reflect systematic changes in the mantle wedge, nature of subduction, and mass fractionation of subduction components (Todd et al., 2011). $^{206}Pb/^{204}Pb$ ratios for the Ngatoro basin show values which extend into and overlap with the least radiogenic rocks from the northern part of the Kermadec Arc. The array of Pb isotope data of the basalts have been suggested to be accounted for by addition of

up to ~5 % sediment to MORB-source (Gamble et al.., 1996).

Back-arc volcanoes

Major and trace element data have been reported for several back arc stratovolcanoes (Wright et al., 2006; Zohrab, 2016). Lavas from Gill, Yokosuka, Giljanes and Rapuhia (Figure 2.3) include basaltic to basaltic andesitic compositions, with phenocrysts assemblages dominated by olivine ± clinopyroxene ± plagioclase, but also extend to more evolved andesitic to dacitic compositions. Phenocryst assemblages in the andesite – dacite lavas consist of plagioclase ± clinopyroxene ± amphibole ± Fe-Ti oxides ± apatite, and reflect assimilation and fractional crystallisation processes (Zohrab, 2016). Yokosuka, Gilijanes and Rapuhia show compositions that lie within the medium-K-series (Wright et al., 2006).

The back arc volcanoes show typical subduction-modified trace element patterns despite their rear-arc setting. The sources of the back arc stratovolcanoes are interpreted to be more affected by sediment-derived melts, based on elevated REE patterns and $(La/Sm)_N$ ratios, rather than by fluid enrichment, which is more prominent in the arc front lavas. Todd et al. (2011) and Zohrab (2016) found that the sediment signal observed in these lavas was not consistent with aqueous fluid transfer or bulk mixing, but through the addition of sediment melts with residual accessory phases monazite ± zircon ± rutile. Analysis of HFSE and REE patterns indicate that basalts from the back arc stratovolcanoes in the southern Havre Trough may be related to compositional mantle anomalies or heterogeneity (Todd et al., 2011; Zohrab et al., 2016).

2.4 Magmatism in the Kermadec Arc

The Kermadec Arc front volcanoes represent the modern, active volcanic arc. The Colville Ridge represents Miocene arc volcanism that occurred prior to the opening of the Lau-Havre Trough. The Colville Ridge is significantly less well studied. The age, composition, and geomorphological features remain uncertain. To date, few geochemical analyses have been published (Mortimer et al., 2010; Todd et al., 2011).

In contrast, the composition of Kermadec Arc lavas are much better understood (e.g. Ewart, 1976; Ewart et al., 1977; Ewart and Hawkeworth, 1987; Gamble et al., 1990; 1991; 1993; 1995; 1996; Ewart et al., 1994; Stoffers et al., 1999; de Ronde et al., 2001; Haase et al., 2002; Barker et al., 2013; Massoth et al., 2003; Smith and Price, 2006; Wright 2006; Wysoczanski et al., 2006; 2012; Timm et al., 2012; 2014; 2016). Lava compositions range from basaltic to rhyolitic and belong mainly to the low-K tholeiitic to medium-K calc-alkaline series (Gill, 1981).

Southern Kermadec Arc lavas are typically porphyritic and vesicular and exhibit high-SiO_2 (~50-60 wt. %), relatively low MgO (~2-4 wt. %) and are K_2O-poor (~0.7-0.4 wt. %) (Figure 2.3), with phenocryst contents ranging from as low as 15% up to 60% (Gamble et al., 1990; 1995; Todd et al., 2011). Exceptions to this are a minor suite of medium- to high-K lavas erupted from Clark volcano, with 1.5-2.25 wt. % K_20 at 52.6 wt. % (Gamble et al., 1997). Whole rock and groundmass glass analyses show Kermadec Arc lavas evolved from parental magmas following fractional crystallisation of olivine + plagioclase + clinopyroxene (Gamble et al., 1991; 1995; Smith and Price, 2006). Major element compositions of magmas have been interpreted as largely driven by fractional crystallisation, with some accumulation of olivine, clinopyroxene and plagioclase and minor crustal anatexis for more evolved silicic magmas (Gamble et al., 1990; 1993a; Smith and Price, 2006; Baker et al, 2012; Wysoczanski et al., 2006; 2012; Timm et al., 2016).

Olivine phenocrysts range from Fo_{91} to Fo_{51} (Gamble et al., 1990, 1993b; Timm et al., 2016) and display weak compositional zoning with high MgO cores and high FeO rims. Olivine compositions suggest that the phenocrysts grew in equilibrium with the host melt (Gamble et al., 1990), except for Rumble II East lavas, which show evidence for olivine accumulation (Timm et al., 2016).

Plagioclase phenocrysts from southern Kermadec Arc lavas are generally anorthite-rich (An_{93}-An_{45}; Gamble et al., 1990; Smith and Brothers, 1998; Timm et al., 2016). Phenocrysts have complex normal, oscillatory, and reversed zoning patterns, and are typically characterised by low K_2O (0.25%) (Gamble et al., 1990). However, more recently higher-K (up to 0.97. wt. %) plagioclase phenocrysts were documented in two samples from Rumble II East and Rumble

II West (Timm et al., 2016), and have been interpreted as having fractionated from a K_2O rich mafic partial melt reservoir or developed during an earlier melting event forming the oceanic crust beneath Rumble II East (Timm et al., 2016). Similarly, lavas from Monowai volcano show evidence for plagioclase ± clinopyroxene accumulation and high An-plagioclase crystals suggesting that crystallisation occurred from a mix of higher H_2O melts with dryer melts during ascent into the arc crust (Timm et al., 2011; Kemner et al., 2015).

Kermadec Arc lavas have arc-like concentrations of fluid mobile LILE including Cs, Rb, Ba, U, K, Pb, and Sr, and MORB-like concentrations in fluid-immobile HFSE (e.g., Haase et al., 2002). Northern Kermadec Arc lavas exhibit enrichments in elements mobile in aqueous fluids, and low LREE and Th relative to HREE and HFSE, which indicates minimal contribution from sediment melt components to their source (Haase et al., 2002). By contrast, southern Kermadec Arc lavas contain a larger contribution from sediment melt slab components, indicated by higher LREE/HREE and Th/HFSE (Gamble et al., 1993; Haase et al., 2002; Wysoczanski et al., 2006; Timm et al., 2016).

Basalts from the northern Kermadec Arc (Herald, Raoul and Macauley Islands) are significantly less radiogenic (Sr and Pb) than basalts from the central (Curtis and L'Esperance) and southern parts (Rumble seamounts) (e.g., Gamble et al., 1993; Timm et al., 2014). Arc lavas containing radiogenic $^{87}Sr/^{86}Sr$ and non-radiogenic $^{143}Nd/^{144}Nd$ indicate a source that has been enriched by crust slab derived components of altered oceanic crust in the north and sediment derived recycled components, particularly in the south (e.g., Haase et al., 2002; Wysoczanski et al., 2006).

Arc front lavas show enrichment in chalcophile and siderophile elements (Cu, Zn, V, Mo, Pb Ba/La, As/Ce) compared to MORB basalts, suggesting the transport of these elements into the mantle wedge via melting of hydrous fluids that are derived from the subducting slab and/or via residual sulphides that have undergone oxidation by fluids in the mantle wedge (e.g., Timm et al., 2012; Keith et al., 2018 Brothers CMP).

Studies which have evaluated the abundances of HFSE ratios (that are not derived from the slab) to indicate relative source depletion, have revealed a broad, systematic change from a strongly depleted mantle source in the northern Kermadec Arc through to less depleted in the southernmost part of the system (e.g., Gamble et al., 1993; Todd et al., 2010; 2011; Timm et al., 2013; Zohrab, 2016). Conversely, a less systemic mantle wedge heterogeneity has been proposed to explain the isotopic variations of aqueous fluid immobile Nd in northern and southern Kermadec Arc lavas (Timm et al., 2014). The arc front mantle has experienced more extensive melt extraction than the back arc region and is therefore depleted in highly incompatible HFSE (Nb, Ta) relative to moderately incompatible HFSE (Zr, Hf) and HREE (e.g. Yb). By contrast, the Havre Trough is considered to be relatively fertile regarding basalt-forming elements with higher Nb, Ta relative to Zr, Hf. However, due to its distance from the main fluid transfer zone of the slab-wedge interface, it is inferred that the source of Havre Trough lavas was not exposed to the same extensive contamination of subduction derived components recorded in the frontal arc magmas. (Gamble et al., 1993).

2.5 Sampling locations

Nine basins within the Havre Trough were selected for this investigation of the back arc system. They cover an along strike distance of ca. 2 degrees latitude (34.7 S to 36.7 S) and extend from near the arc front in the east to abutting the Colville Ridge in the west (Figure 2.5; Table 2.3). Multibeam data and fresh pillow lavas were collected from these basins during several recent marine voyages on the *R.V. Tangaroa* (TAN1213, TAN1313, TAN1512, and TAN1513). Samples were selected from seventeen different dredge sites located in the Havre Trough (Table 2.3)

Table 2.0-3: Back arc basin samples investigated in this study. Table shows voyage name, sample number, latitude and longitude of samples.

Station	Sample Number	Location	Latitude	longitude	Depth (mbsl)
TAN1213-3	2	Basin A Ngatoro rift	-36.6912	177.1598	2774
TAN1213-3	5	Basin A Ngatoro rift	-36.6912	177.1598	2774
TAN1213-6	1	Basin A Ngatoro rift	-36.5965	177.1598	2750
TAN1213-6	3	Basin A Ngatoro rift	-36.5965	177.1598	2750
TAN1213-10	2	Basin E	-35.2051	178.587	3250
TAN1213-10	9	Basin E	-35.2051	178.587	3250
TAN1213-10	13	Basin E	-35.2051	178.587	3250
TAN1213-11	1	Basin E	-35.1985	178.6723	2871
TAN1313-15	1	Basin H	-35.9985	177.2583	
TAN1512-24	1	Basin J	-34.7233	178.0853	
TAN1512-25	1	Basin J	-34.7235	178.0853	
TAN1513-040	1	Basin I	-35.3166	177.7389	2182
TAN1513-041	1	Basin I	-35.3269	177.7823	2120
TAN1513-042	1	Basin I	-35.416	177.9552	2520
TAN1213-47	1	Basin G	-34.77	179.0802	2430
TAN1213-47	2	Basin G	-34.77	179.0802	2430
TAN1213-50	3	Basin C	-34.43	178.404	2943
TAN1213-50	4	Basin C	-34.43	178.404	2943
TAN1213-51	4	Basin D	-35.39	178.2277	2840
TAN1213-51	6	Basin D	-35.39	178.2277	2840
TAN1213-51	7	Basin D	-35.39	178.2277	2840
TAN1213-55	2	Basin B	-35.83	178.2808	2700
TAN1213-56	3	Basin B	-35.83	178.2998	2929
TAN1213-56	Archive	Basin B	-35.83	178.2998	2929
TAN1512 DR10	1	Basin K	-33.7077	178.0853	2950
TAN1512 DR10	2	Basin K	-33.7077	178.0853	2950
TAN1512 DR10	3	Basin K	-33.7077	178.0853	2950
TAN1512 DR10	4	Basin K	-33.7077	178.0853	2950

The back arc basins and rifts are orthogonally aligned to the trend of the Kermadec Trench, and their distribution along and across the back arc has been selected to investigate any latitudinal and longitudinal variation that may be present. The following presents a brief description of each basin as known prior to this study, and context for the dredge site locations. Samples which were analysed in this study are indicated by bold titles.

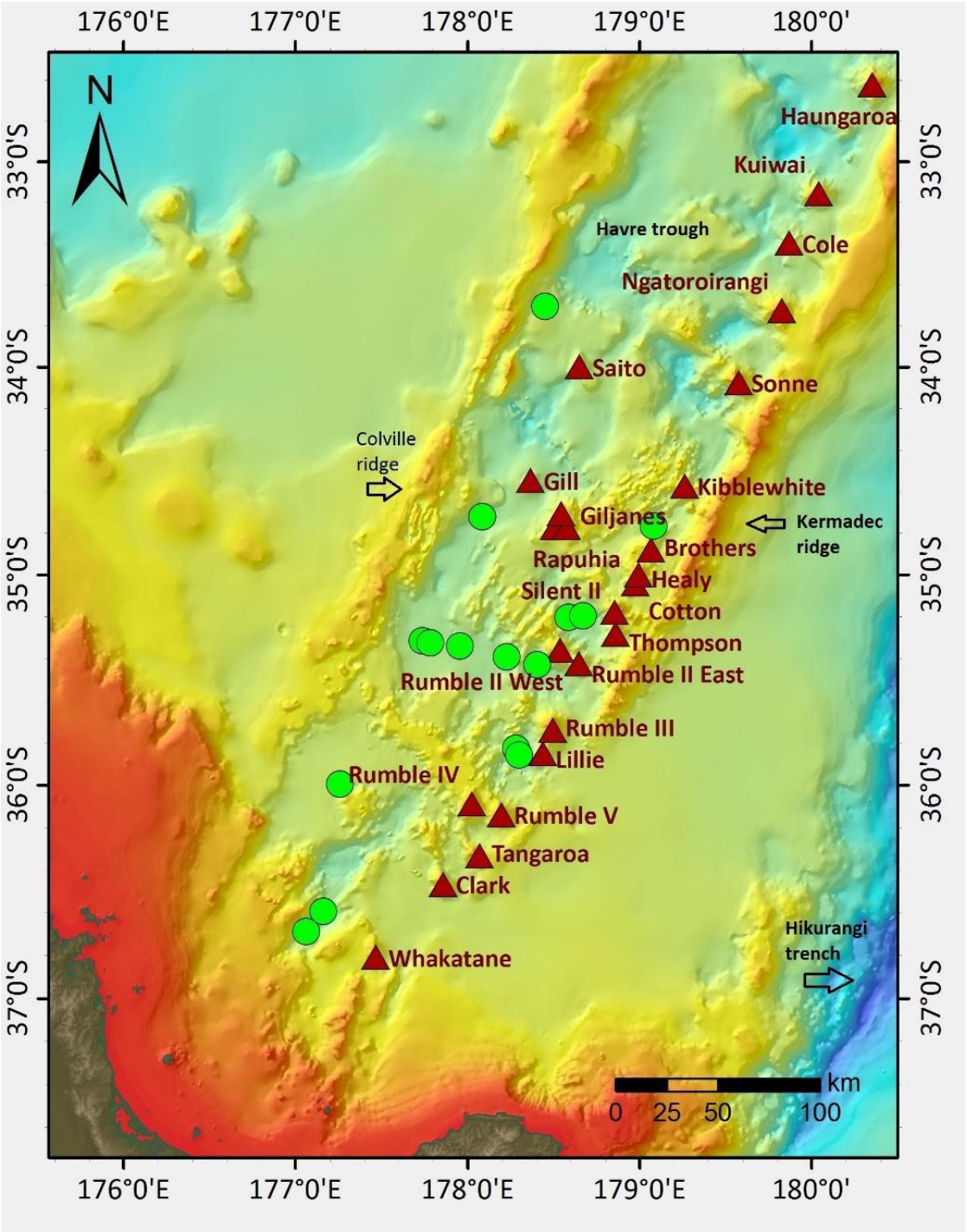

Figure 2.5: Regional tectonic setting of the KAHT and remnant Colville Arc Subduction zone system. Sample sites are indicated by green circles and arc front and back arc volcanoes are indicated by red triangles, Rumble V Ridge is the high extending NW from Rumble V volcano to the Colville Ridge.

Basin A

Basin A (~36°40'S, 177°15'E) is located in the Ngatoro Rift in the southern Havre Trough (Wysoczanski et al., 2010). It is a deep (>4000 mbsl) back arc basin that

progressively narrows towards the south, terminating at the continental margin (Wright, 1993). Samples were collected from Stn 003 (Figure 2.6) located on a ridge in the centre of the basin, and Stn 006 (Figure 2.6) further north of the ridge during the *TAN1213* NIRVANA voyage.

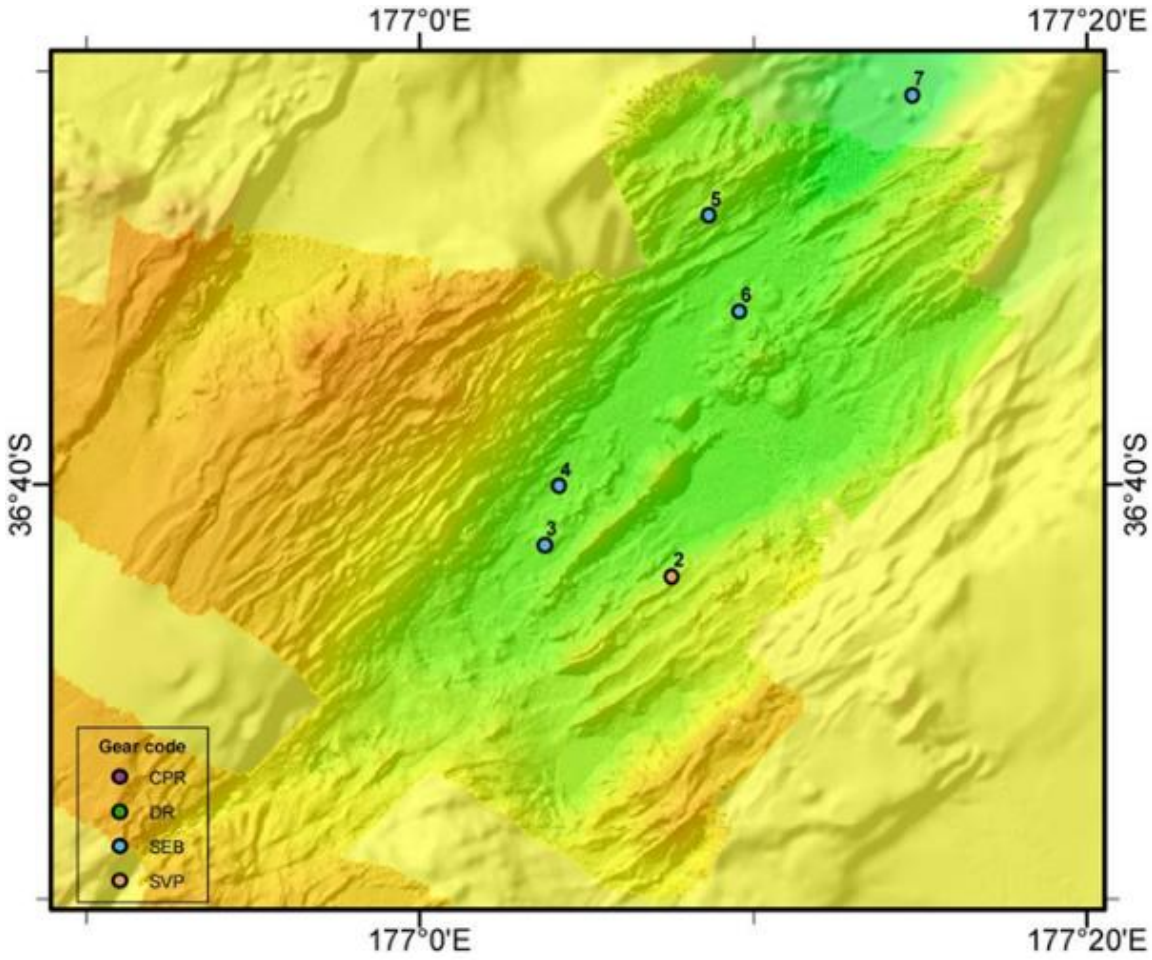

Figure 2.6: Bathymetric map of Basin A, in the southern Havre Trough with sampling locations. Dots represent SEB (Epibenthic Sled), DR (rock dredge), CPR (continuous planktonic recorder), and SVP (sound velocity profiles) (Wysoczanski et al., 2012[b]). Note, rock samples were retrieved via epibenthic sled for sample sites 3 and 6.

Basin B

Basin B, located at ~35°50'S, 178°15'E, lies near several Kermadec Arc front volcanoes: Rumble III and Lillie to the northeast, and Rumble IV and Rumble V to the south. Sampling of Basin B was carried out during *TAN1213* NIRVANA voyage at two stations, Stn 055 and Stn 056 (Figure 2.7), to the southwest of Rumble III and recovered fresh vesicular pillow lavas.

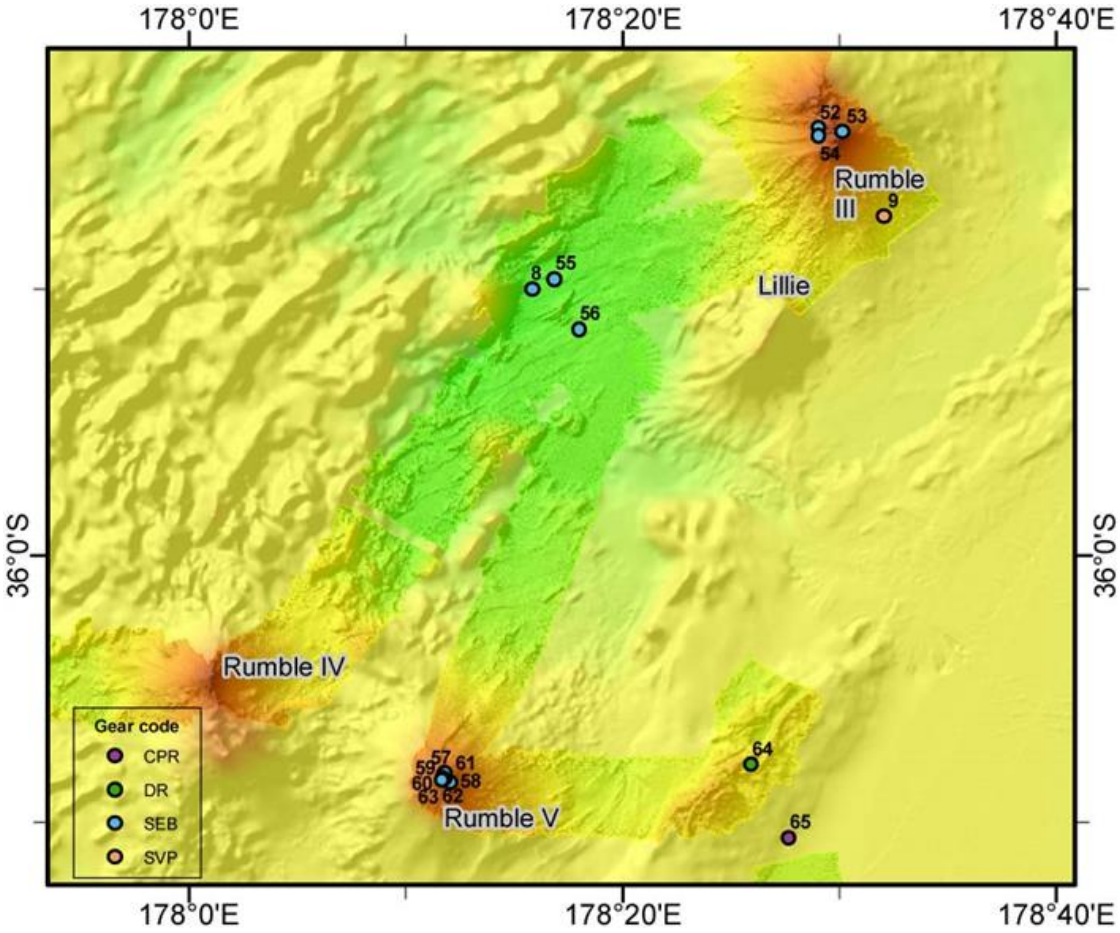

Figure 2.7: Bathymetric map of Basin B, in the southern Havre Trough with sampling locations (Stn 055 and 056) and location of neighbouring back-arc volcanoes (Wysoczanski et al., 2012[b]).

Basin C and Basin D

Basin C (35°25'S, 178°25'E) is situated to the south of back arc volcano Rumble II West and southwest of Rumble II East. Basin D (~35°25'S, 178°15'E) is located west of Basin C. Both sampling sites are located along ridges within the respective basins. Sampling of Basins C and D was carried out during *TAN1213* NIRVANA voyage at stations 050 and 051 (Figure 2.8). Fresh pillow lavas were

recovered from both basins. In addition, altered material was also recovered from Stn 051, as well as several round pumice clasts, but were not analysed as part of this study.

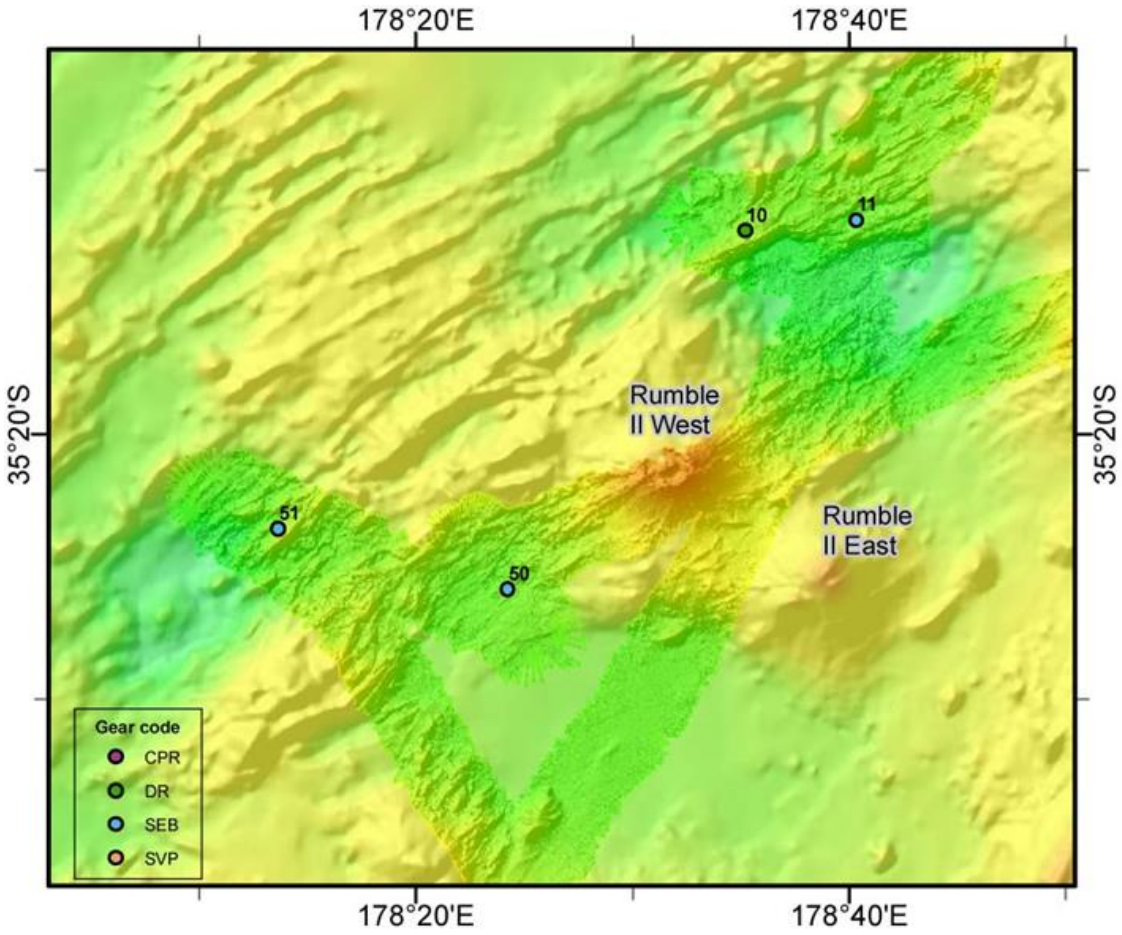

Figure 2.8: Bathymetric map of Basin C and D, in the central Havre Trough with sampling locations (Stn 050 and 051) and neighbouring back-arc volcanoes Rumble II West and Rumble II East (Wysoczanski et al., 2012[b]).

Basin E

Basin E (35°10'S, 178°40'E) is located to the north of Basins C and D and back arc volcanoes Rumble II West and Rumble II East. Sampling of Basin E was carried out during *TAN1213* NIRVANA voyage at stations 010 and 011 (Figure 2.9). Both sampling sites are located along ridges within the basins. Rock dredging at Stn 010 recovered a variety of material including a large amount of cumulative material, serpentinites, and lavas. A large proportion of samples had extensively altered rims. However, their interiors were fresh. Sled sampling at Stn 011 on the

northern wall of basin E recovered angular lava pieces, of which one was selected.

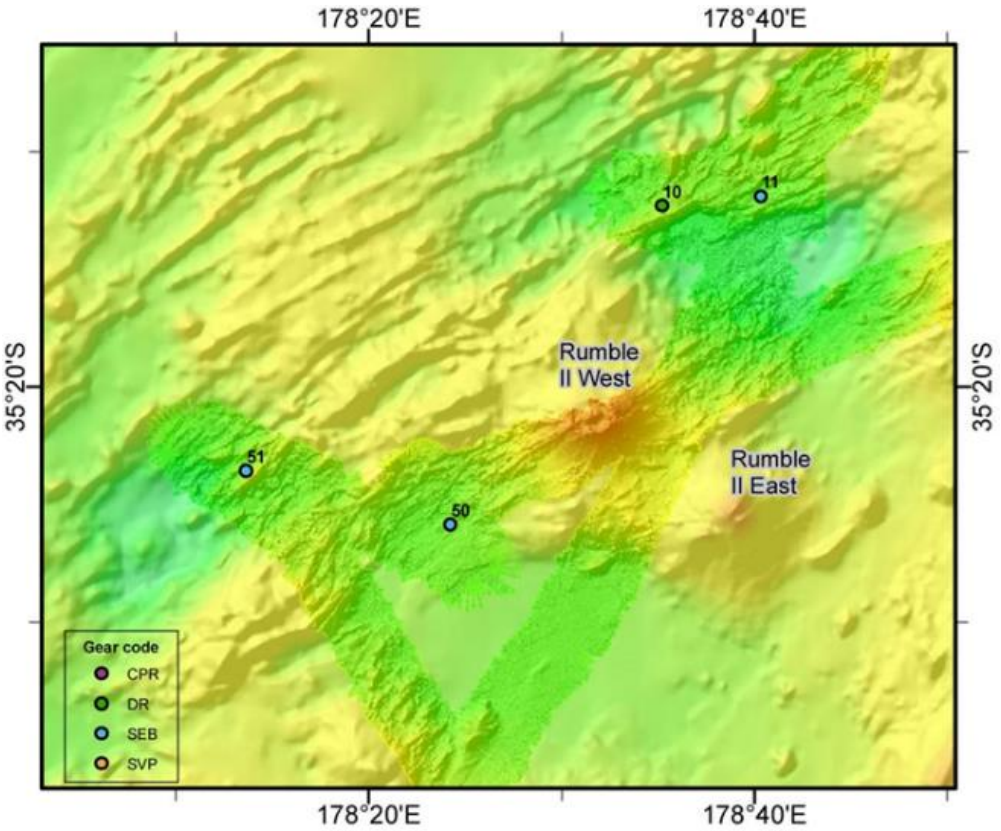

Figure 2.9: Bathymetric map of Basin E, in the central Havre Trough with sampling locations (Stn 10 and 11) and neighbouring back-arc volcanoes Rumble II West and Rumble II East (Wysoczanski et al., 2012[b]).

Basin G

Basin G (~34°45'S, 179°05'E) is located to the north of the Brothers volcano, near to the volcanic front. Sampling was carried out during *TAN1213* Nirvana voyage at station 047 (Figure 2.10) and recovered pillow basalts and rounded pumice clasts. Four fresh basalt samples were selected for this study

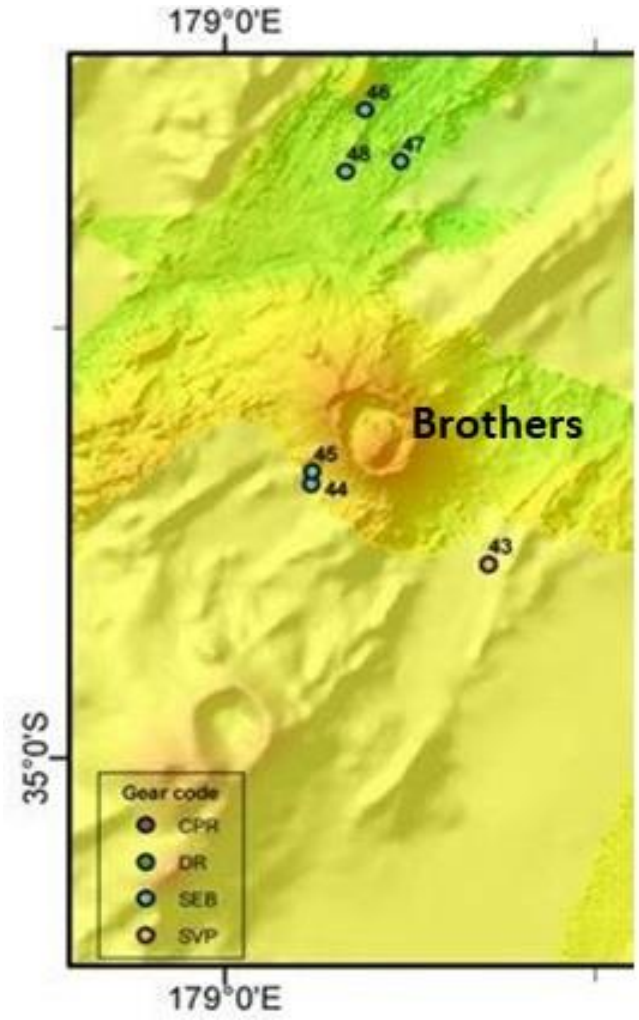

Figure 2.10: Bathymetric map of Basin G, in central eastern Havre Trough with sampling location (Stn 047) and neighbouring Brothers caldera (below) and Kermadec Ridge (right) (Wysoczanski et al., 2012[b]).

Basin H

Basin H (~36°00'S, 177°15'E) is located in the southern Havre Trough, immediately east of the Colville Ridge. Sampling was carried out during *TAN1313* voyage at dredge site DR15 (Figure 2.11) near a small volcanic cone and recovered fragments of pillow lavas and few pumice pebbles.

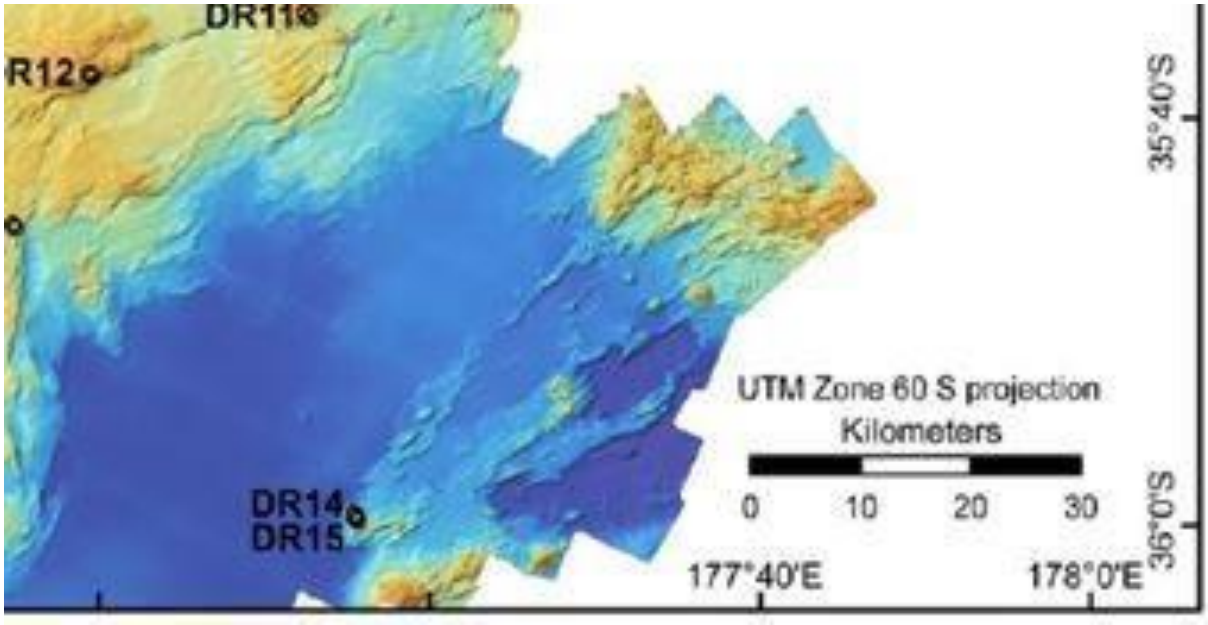

Figure 2.11: Bathymetric map showing the location dredge sites in Basin H (de Ronde et al., 2013).

Basin I

Basin I (~35°20'S, 177°45'E) is located in the western side of the Havre Trough, immediately to the east of Colville Ridge. Sampling was carried out during the *TAN1513* SAMSARA voyage at three dredge sites 40, 41, 42 (Figure 2.12) at depths of >2000 mbsl. The sampling sites were chosen to provide the first back arc basin material from this locality and to compliment previous work carried out during the NIRVANA voyage forming a complete transect of back-arc material across the Havre Trough. Sampling at Stn 40 recovered mafic clasts with Mn crusts, Stn 41 recovered dense vesicular pillow basalts with thin Mn crusts, and mm thick glassy rims. Stn 42 recovered pillow lavas with thin Mn crusts.

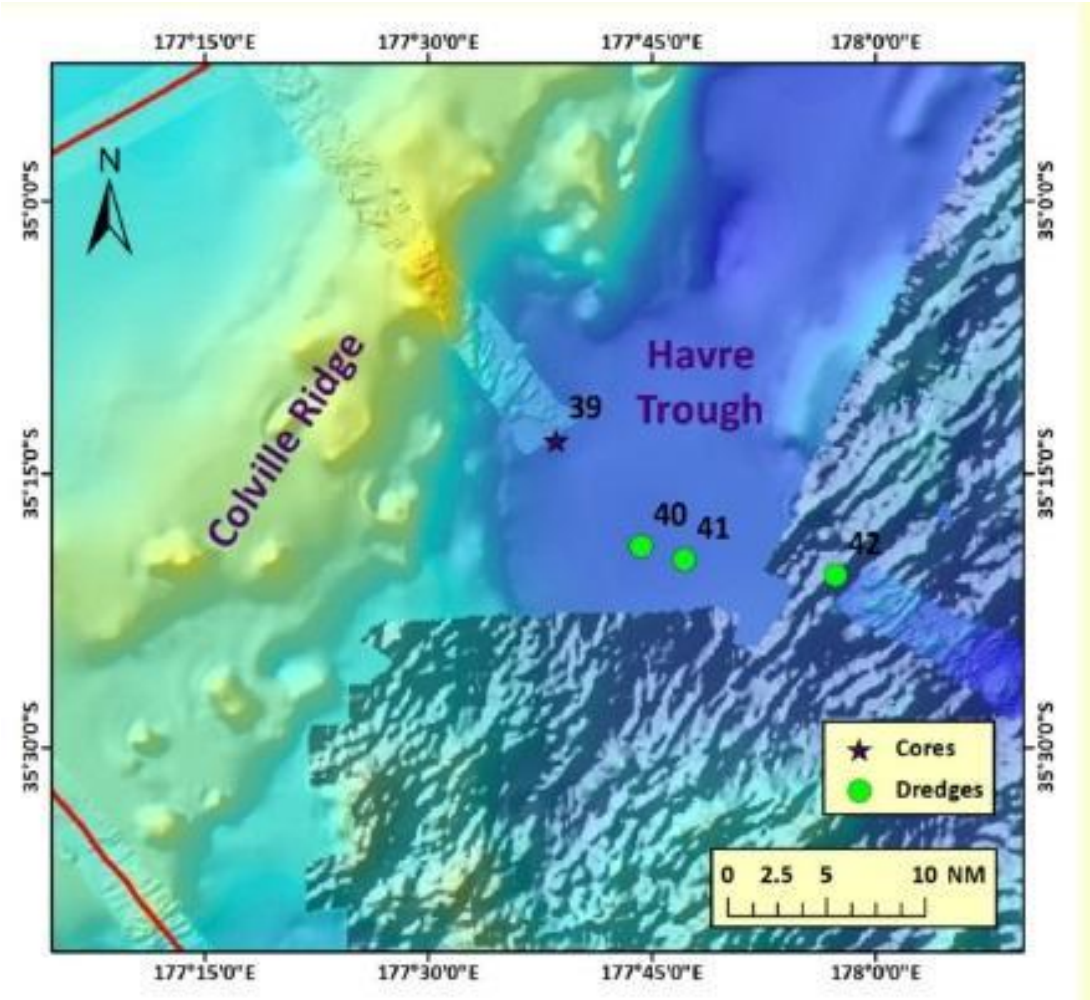

Figure 2.12: Bathymetric map of Basin I in the western Havre Trough showing dredge and core sampling sites during TAN1513 voyage (Wysoczanski et al., 2015)

Basin J

Basin J (~34°45'S, 178°05'E) is located in the west central Havre Trough, immediately to the east of Colville Ridge. Sampling was carried out during the *TAN1512* voyage at dredge site P (Figure 2.13) near a cone and recovered fragments of pillow lavas with up to 25mm thick Mn crusts.

Basin K

Basin K (~33°45'S, 178°30'E) is located in the western Havre Trough, and is the northernmost basin of this study. Sampling was also carried out during the *TAN1512* voyage, at dredge site DR10 (Figure 2.14) near a small seamount. Dredging recovered slightly, to moderately altered vesicular lavas.

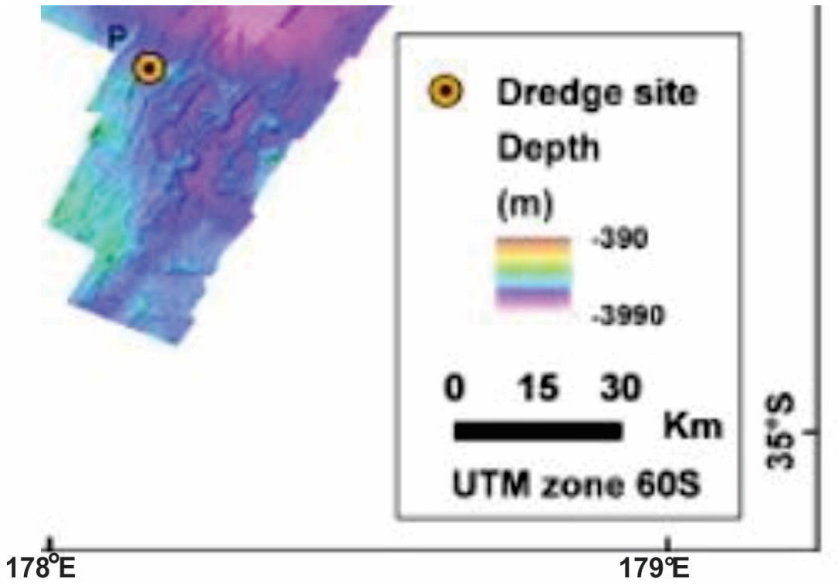

Figure 2.13: Bathymetric map showing dredge site locations in Basin J in the western Havre Trough (de Ronde et al., 2016[b])

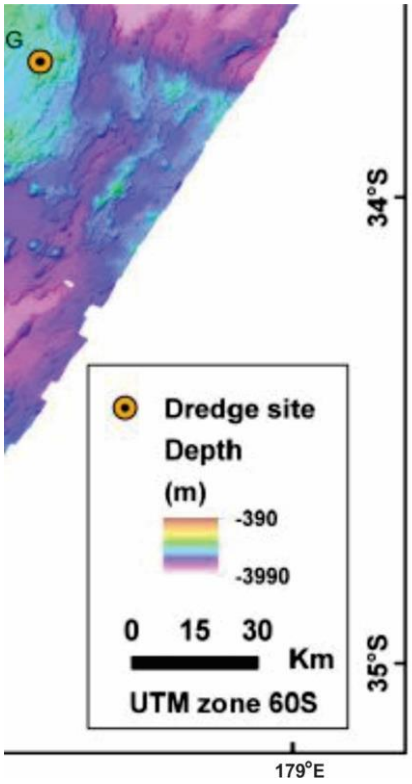

Figure 2.14: Bathymetric map showing Basin K dredge site location in the western Havre Trough (de Ronde et al., 2016b).

Chapter 3:

Analytical Methods

3.1 Morphological analysis

Multibeam echosounder (MBES) data available from NIWA and GNS Science were selected to provide coverage of 10 basins of the Havre Trough (Figure 3.1). The collected were data using 30 kHz EM300 and 12 kHz SEABEAM MBES systems.

ArcMap 10.2.1 software was used to create a Digital Terrain Model for each basin. The DTM incorporated features including bathymetry, slope angles and backscatter reflectance. Each DTM was used to describe the basin's geomorphologic and structural (e.g. faults) features. Backscatter reflectance, combined with subsurface profiles (e.g. Topas data) where available, allow the sediment fill for each basin to be evaluated.

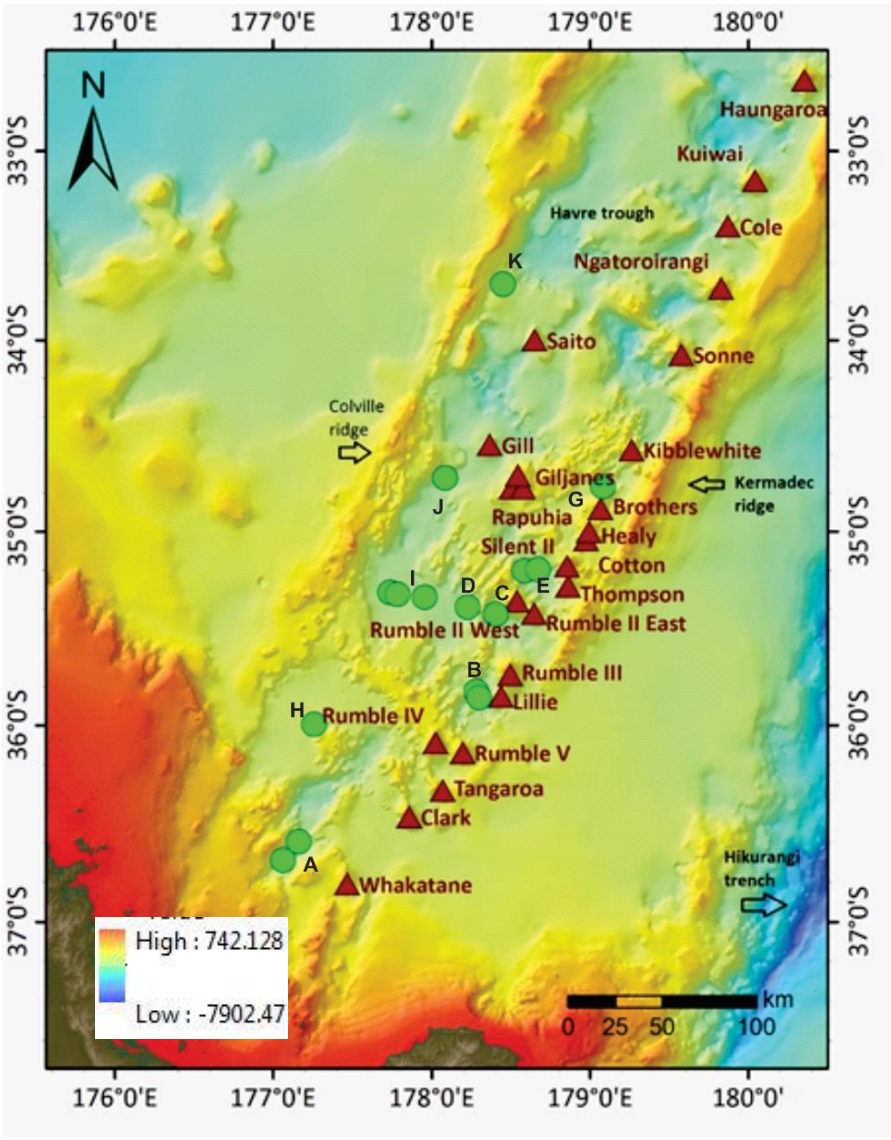

Figure 3.1: Bathymetry map showing location of 10 basins analysed in this study denoted by letters A-K (NIWA 250m gridded bathymetry)

3.2 Geochemical analysis

3.2.1 Samples selected for analyses

29 samples of fresh lavas from 15 locations were selected for this study. Of these, bulk major and trace element data were available for 21 samples; a further 9 samples were prepared and analysed for trace elements and 18 for major elements (Table 3.1).

Table 3.0-1: Samples used in this study including sample name, location, type of analysis and where analysis was carried out. VUW = 1 refers to samples analysed prior to this study at VUW. GNS=2 refers to samples that were analysed prior to this study at ALS and OGL laboratories. VUW=refers to samples analysed during this study.

Sample	Location	Major Elements	Trace Elements	Microanalysis
TAN1213-3 -2	Ngatoro Basin	3	1	
TAN1213-3-5	Ngatoro Basin	3	1	
TAN1213-6-1	Ngatoro Basin	3	3	
TAN1213-6-3	Ngatoro Basin	3	3	3
TAN1213-10-2	Basin E	3	3	3
TAN1213-10-9	Basin E	3	1	
TAN1213-10-13	Basin E	3	1	
TAN1213-11-1	Basin E	3	1	
TAN1213-50-3	Basin C	3	1	
TAN1213-50-4	Basin C	3	1	
TAN1213-50-4 Dup	Basin C	3	1	
TAN1213-51-4	Basin D	3	1	
TAN1213-51-6	Basin D	1	1	
TAN1213-51-7	Basin D	3	1	
TAN1213-55-2	Basin B	3	3	3
TAN1213-56-1	Basin B	3	1	
TAN1213-56-3	Basin B	3	1	
TAN1213-56-3 (Archive)	Basin B	3	1	
TAN 1513 040	Basin I	1	1	3
TAN 1513 041	Basin I	1	1	
TAN 1513 042	Basin I	1	1	
TAN1213-47-1	Basin G	2	2	3
TAN1213-47-2	Basin G	2	2	3
TAN1313 DR-15-1	Basin H	2	2	
TAN1512-DR-24-1	Basin J	2	2	
TAN1512-DR 25-1	Basin J	2	2	
TAN1512-DR 10-1	Basin K	2	2	
TAN1512- DR10-2	Basin K	2	2	3
TAN1512- DR-10-3	Basin K	3	3	
TAN1512 -DR 10-4	Basin K	3	3	
VUW=1				
GNS (ALS and OGL)=2				
VUW (This study)=3				

3.2.2 Analytical methods employed for data obtained prior to this study

Samples analysed prior to this study were carried out at VUW and followed the same procedures used for the samples analysed in this study. For data analysed externally, samples *TAN1213*-47-1, 47-2 were analysed at ALS laboratories in Vancouver, Canada. Samples *TAN1313*-15 and *TAN1512*-DR10-1, DR10-2, DR25-1 were analysed at Ontario Geoscience labs in Sudbury, Canada. These samples were collected during Voyages *TAN1007*-2010 and *TAN1104*-2011.

Samples selected for geochemical analysis were broken into small sub-centimetre fragments, only saw blade cut surfaces were selected and cleaned in an ultrasonic bath in 18.2 MΩ water three times in order to eliminate any contamination from sea water. Samples were then crushed to powder using an agate mill. Whole rock powders were taken into solution using different methods at both laboratories, although optimized to provide 100% digestion to analyse major and trace elements. Samples that were analysed at OGL were digested in closed vessels for 72 hours with a mix of nitric, hydrofluoric, perchloric and hydrochloric acid. At ALS, the samples were taken into solution using lithium metroborate fusion. Major elements were analysed by inductively coupled mass spectrometry (ICP-MS) and X-Ray Fluorescene (XRF; OGL). Trace and REE were analysed by ICP-MS at both laboratories. The relative deviations of standards measured are <5.7%, except for Ho (6.6%), Tl (8.25), and U (13.8%) (Timm et al., 2016).

3.2.3 Sample preparation

All samples are highly vesicular and were collected from the seafloor. Consequently, saltwater and sediment can percolate through small interconnected vesicles throughout even fresh lava samples. Therefore, the samples have undergone meticulous preparation and cleaning methods to remove seawater and minimise sediment contamination.

Whole rock samples were first cut into small sections (~5 cm in length and ~2 cm thick) using a diamond-blade saw. Sections that contained altered surfaces and weathered material were removed, ensuring only fresh samples were chosen for further processing. The fresh blocks were polished using a diamond lap, to

remove any metal contamination that may have been introduced during rock cutting.

A representative block from each sample was cut into a domino for thin section preparation. Samples were then crushed into smaller chips using a tungsten carbide hydraulic press. During this process, the hydraulic press was meticulously cleaned using ethanol before any crushing was undertaken and between each sample to remove any chance of cross contamination.

To remove seawater contamination, the sample chips were washed and boiled in glass beakers using ultra-pure H_2O (resistivity >18.2 MΩ). The beakers were then boiled for 60 minutes on a hot plate and then transferred to an ultra-sonic bath and heated for another 60 minutes per sample. During each cycle of washing, the concentration of total dissolved solids (TDS) of the boiled water was measured using an Okaton® Eco Testr TDS low tester. After boiling, the H_2O and any loose material was discarded and replaced with fresh Milli-Q H_2O. This was repeated until the concentration of TDS of the boiled water resembled that of the fresh ultra-pure H_2O (0-10 ppm). Each sample underwent numerous cycles of washing, to ensure that all the salt and sedimentary material had been removed. Once samples had met these requirements they were then dried in an oven at approximately 60 °C for 24 hours.

After the samples had been cleaned and dried, approximately 60 g of fresh material was selected for crushing to produce powders for geochemical analysis. The samples were crushed to 1-2 mm sized grains using a Rocklab Boyd crusher. The Boyd crusher was cleaned using ethanol and compressed air before any crushing began, to remove any material from prior crushing, and between crushing of each sample, reducing any possibility of cross contamination. All crushed material was collected and used to ensure the final milled sample was an accurate representation of the bulk rock. The crushed material for each sample was then milled to a fine powder (grain size ca. 75 μm) using an agate puck and ring mill.

To reduce the possibility of contamination from previously milled samples, 60-80 g of pure silica sand was milled prior to use and the mill head cleaned with ethanol and compressed air between samples.

3.3 Whole rock major element geochemistry

A total of 20 samples (Table 3.2) were prepared for major element analysis using a Panalytical Minipal-4 X-Ray fluorescence (XRF) spectrometer at the National Institute of Water and Atmospheric Research (NIWA). Glass disks were formed by mixing whole rock powders with a 1.2:2.2 mixed lithium tetraborate and lithium metaborate flux, using a sample: flux ratio of 1:10. This mixture was heated to 1050°C for 25 minutes and then cooled into a glass disk.

The XRF calibration curve was based on 12 international silicate standards. To monitor accuracy and precision two certified international USGS basalt standard reference materials (SRMs) BHVO-2 and BCR-2 were also measured during the analysis session. Two standard deviations (2SD) for each element were determined from three replicate analysis of BHVO-2 and four of BCR-2, and all are generally <2% relative. Average values for each standard were in close agreement with the certified values (<1-2% offset).

Table 3.0-2: List of preferred values for element abundances of whole rock powdered standard BHVO-2 used for major element analysis. Reference values were obtained from the GeoRem database (Jochum et al., 2016). All values are given in wt. %.

Standard	**BHVO-2 563**				
Oxide	**Whole rock powder conc**		Mean	2 SD	2 SD%
SiO2	49.61	49.64	49.63	0.02	0.03
TiO2	2.70	2.70	2.70	0.00	0.007
Al2O3	13.26	13.30	13.28	0.02	0.04
Fe2O3	12.33	12.30	12.31	0.02	0.03
MnO	0.17	0.17	0.17	0.00	0
MgO	7.19	7.16	7.17	0.01	0.02
CaO	11.44	11.41	11.42	0.02	0.03
Na2O	2.50	2.53	2.51	0.02	0.03
K2O	0.51	0.50	0.50	0.00	0.001
P2O5	0.30	0.30	0.30	0.00	0
S ppm	235.76	211.9	223.84	11.92	23.84
Cl ppm	209.28	131.1	170.19	39.09	74.18

Table 3.0-3: List of preferred values for element abundances of whole rock powdered standard BCR-2 used for major element analysis. Reference values were obtained from the GeoRem database (Jochum et al., 2016). All values are given in wt. %.

Standard	**BCR-2 562**				
Oxide	**Whole rock powder conc**		Mean	2 SD	2 SD%
SiO2	54.10	54.17	54.14	0.03	0.06
TiO2	2.34	2.33	2.33	0.01	0.01
Al2O3	13.36	13.40	13.38	0.02	0.03
Fe2O3	14.00	13.98	13.99	0.01	0.02
MnO	0.19	0.19	0.19	0.00	0
MgO	3.49	3.47	3.48	0.01	0.02
CaO	7.17	7.15	7.16	0.01	0.01
Na2O	3.17	3.17	3.17	0.00	0.01
K2O	1.86	1.85	1.86	0.01	0.01
P2O5	0.31	0.30	0.30	0.00	0.00
S ppm	306.5	329.2	317.85	11.39	22.78
Cl ppm	108.1	77.27	92.68	15.41	30.82

3.4 Whole rock trace element geochemistry

3.4.1 Sample preparation

Samples selected for trace element analysis in this study were prepared in the ultra-clean geochemistry laboratory facility at Victoria University of Wellington. The ultra-clean chemical separation laboratory contains four class 10 laminar flow workstations and is positively pressured with air filtered to class 100 to minimise the risk of contamination.

Ultra-pure water (>18.2 MΩ) was used for all sample preparation and beaker cleaning. All acids used for final beaker cleaning, and for sample dilution and digestion were Optima™ ultra-pure grade acids (all key metals <10 ppt). Analytical reagent (AR) grade acids were used during early stages of sample beaker cleaning.

Prior to sample preparation, 23 ml Savillex Teflon™ beakers were cleaned following standard procedures: each beaker was thoroughly rinsed and wiped down with ethanol and soaked in 6M HCl for a minimum of 24 hours at 120°C on a hotplate, then rinsed three times water. Beakers were then soaked in 7M HNO_3 on a hotplate for a further 24 hours and rinsed three times in water. For final cleaning, beakers were refluxed for a minimum of 24 hours, using 4-5 mL of 6-7M sub-boiled AR HNO_3, followed by three rinses in water. This step was then repeated with 6-7M Optima™ ultra-pure grade HNO_3 and the beakers rinsed (3x water) and air dried in a laminar flow hood.

Approximately 50-60 mg of powdered sample and international SRMs (BHVO-2 and BCR-2) were weighed on a high precision balance to +0.0001 g and transferred to pre-cleaned 23 mL Savillex screw top Teflon beakers. Each sample batch included SRMs BHVO-2 and BCR-2 and a full blank.

The samples were dissolved using conventional open-beaker acid digestion methods. Ca. 2 mL of concentrated hydrofluoric acid (29 M HF) and ca. 0.5 mL nitric acid (16 M HNO_3) were added to the samples in sealed Savillex beakers and heated on a hotplate to 120°C for 3-4 days. The solutions were then evaporated

to incipient dryness. Care was taken to ensure that samples were not overly dried, as this may cause sample loss and the formation of insoluble fluorides.

The sample residues were evaporated twice in ca. 2 mL of concentrated HNO_3 at 120°C to ensure that any residual HF was removed from the solution. Next, sample solutions were refluxed in 4 mL of half concentrated hydrochloric acid (6M HCl) at 120°C overnight. The samples were then visually checked to ensure that they were fully in solution, and the HCl was evaporated to dryness. The sample cakes were covered in concentrated HN03 and evaporated, to convert the samples back to nitric form. Each sample was then refluxed for a further 1-2 days in 9 mL of 1M HNO_3 at 120°C, to bring up fully in solution for the final dilutions.

The sample solutions were 100% transferred into pre-cleaned 10 mL polyethylene centrifuge-tubes and precisely weighed using a high precision balance (± 0.000 g). The samples were centrifuged at 2000 rpm for 10 minutes, and checked visually to ensure that no solids or precipitants were present. To form a dilution of the sample, 60 µL aliquot was transferred and precisely weighed into another clean 10 mL centrifuge-tube. Each aliquot was topped up with ca. 10 mL of 1% HNO_3 and weighed again, so a final dilution of the sample could be accurately calculated.

3.4.3 ICP-MS analysis

Trace element concentrations were measured on the diluted samples using a ThermoScientific Element 2 inductively coupled plasma mass spectrometry (ICP-MS) at Victoria University of Wellington. Sample solutions were introduced using an attached Elemental Scientific Inc. (ESI) auto sampler, and passed through a micromist neubuliser. The ICP-MS was tuned using a 1 ppb multi-element standard solution, where instrument parameters such as torch position and carrier/make-up gas flow were adjusted to obtain the lowest relative standard deviation (RSD), and to optimise sensitivity. This step was repeated for the calibration standard BVHO-2 and BCR-2. Oxide and doubly charged ion generation were monitored using measured ratios of BaO^+:Ba^+ (0.1-0.2%), Ba^{++}:Ba^+ (5.3-6.3%), and UO^+:U^+ (4.1-7.0%)

ICP-MS analysis was performed using low mass resolution for the majority of masses, but the resolution was increased to medium resolution for selected masses (Mg, Al, Ca, Sc, V, Cr, Mn, Co, Ni, Cu, Zn, Ga) to ensure that element counts were not affected by spectral interferences, or that elemental counts were reduced for particularly abundant masses that may otherwise overload the detector (e.g. ^{27}Al).

Following analysis of each sample, the ICP-MS and auto-sampler lines were washed using 1% optima-grade HNO_3 for 240 seconds. Analytical runs were performed in a looping sequence starting with the primary standard (BVHO-2), and secondary standard (BCR-2), six samples, repeated and finishing with the primary standard. Background counts were measured periodically throughout each sequence before each primary standard and after each secondary standard using a 1% Optima HNO_3 acid blank.

The concentrations for each sample were calculated by sample standard bracketing using the USGS standard BHVO-2 as a calibration standard. USGS BCR-2 was measured as a secondary standard to evaluate accuracy. Element abundances for both standards were obtained from the GeoReM database of preferred values (Jochum et al., 2017). Count rates for each mass were

determined by subtracting the background counts per second (CPS) values of acid blanks from the CPS value for each sample and standard, using backgrounds analysed closest to the sample or standard. Concentrations were then calculated for the background-subtracted CPS, relative to the bracketing calibration standard, BHVO-2, using Equation 1.

Equation 1: $\text{Sample } C_i = (\text{SampleCPS}/\text{BHVO}_{CPS}) \times (\text{Sample}_{Dil}/\text{BHVO}_{Dil}) \times \text{Ref}$

Where Ci represents the concentration of the element of interest, Xcps is the background-subtracted CPS of the element of interest, Xdil is the concentration of material in the dilution aliquots, and Ref is the reference value of the BHVO-2 standard. For each sample, the measured Ca was used as an internal standard, using the wt. % of CaO determined from XRF analysis (Section 3.3). This allows for any loss of material during preparation to be identified and corrected for using equation 2.

Equation 2: Sample Ci (Ca corrected) = eq. (1)×(CCa XRF/CCa ICP−MS)

Where CCa is the measured concentration of Ca.

Trace element analysis of secondary standard BHVO-2 and BCR-2 were accurate to ≤ 3 % of preferred values, except for B, Sr, Zr, Mo, Ba, MgO, Sc, V, Cr, Cr, MnO (wt.%), Co, Ni, Cu, Zn, Ga (Table 3.4 and 3.5).

Table 3.0-4: List of preferred values for element abundances of whole rock powdered standard BCR-2 used for trace element analysis. Reference values were obtained from the GeoRem database (Jochum et al., 2016). All values are given in ppm.

Element	Standard n=5	SD	2SD	Ref
	BHVO-2 mean concentration			
MgO (wt%)	98.58	186.22	372.44	7.25
Al2O3 (wt%)	11.31	5.8	11.5	13.44
CaO (wt%)	7.96	4.6	9.1	11.4
MnO (wt%)	0.14	0.1	0.1	0.169
Li	4.54	0.1	0.1	4.5
Be	1.06	0.1	0.3	1.076
B	2.00	0.8	1.7	2.95
Sc	3090.54	6117.4	12234.7	31.80
V	8535.97	16437.7	32875.5	318.2
Cr	269.07	43.7	87.3	*287.2*
Co	83.08	76.4	152.8	44.89
Ni	249.05	254.9	509.7	119.8
Cu	517.80	775.3	1550.6	129.3
Zn	166.42	124.7	249.5	103.9
Ga	26.87	11.4	22.7	21.37
Rb	9.32	0.2	0.5	9.261
Sr	397.36	10.0	20.0	394.1
Y	25.98	0.5	0.9	25.91
Zr	172.24	4.2	8.4	171.2
Nb	18.22	0.4	0.7	18.1
Mo	4.08	0.1	0.2	4.07
Cd	0.17	0.0	0.0	0.152
Cs	0.10	0.0	0.0	0.10
Ba	132.57	3.7	7.4	130.9
La	15.31	0.4	0.8	15.2
Ce	37.75	0.9	1.8	37.35
Pr	5.39	0.1	0.3	5.33
Nd	24.53	0.8	1.6	24.27
Sm	6.03	0.2	0.4	6.023
Eu (151)	2.07	0.1	0.2	2.043
Gd	6.33	0.3	0.6	6.207
Tb	0.95	0.0	0.0	0.94
Dy	5.40	0.2	0.4	5.28
Ho	0.99	0.0	0.1	0.99
Er	2.53	0.1	0.2	2.51
Tm	0.33	0.0	0.0	0.3
Yb	2.00	0.1	0.1	1.99
Lu	0.28	0.0	0.0	0.28
Hf	4.50	0.2	0.3	4.47
Ta	1.16	0.0	0.1	1.15
W	0.25	0.0	0.0	0.25
Tl	0.01	0.0	0.0	0.02
Pb	1.02	0.8	1.6	1.65
Bi	0.43	0.5	1.0	0.01
Th	0.75	0.6	1.2	1.22
U	0.72	0.4	0.8	0.41

Table 3.0-5: List of preferred values for element abundances of whole rock powdered standard BCR-2 used for trace element analysis. Reference values were obtained from the GeoRem database (Jochum et al., 2016). Al l values are given in ppm.

Element	Standard n=5	SD	Ref
	Whole rock powder BCR-2 mean concentration		
MgO (wt%)	3.45	0.09	3.60
Al2O3 (wt%)	12.93	0.3	13.48
CaO (wt%)	6.83	0.1	7.11
MnO (wt%)	0.19	0.0	0.20
Li	7.43	3.1	9.13
Be	-1.53	6.5	2.17
B	116.76	214.2	4.40
Sc	32.07	0.8	33.53
V	398.31	13.7	417.60
Cr	15.02	0.5	15.85
Co	36.87	0.3	37.33
Ni	11.64	0.3	12.57
Cu	17.04	0.2	19.66
Zn	118.77	2.1	129.50
Ga	21.44	1.0	22.07
Rb	44.97	2.1	46.02
Sr	342.63	27.2	337.40
Y	31.39	5.2	36.07
Zr	162.45	33.5	186.50
Nb	18.13	11.0	12.44
Mo	190.33	89.6	250.60
Cd	2.26	2.8	0.69
Cs	16.48	28.0	1.16
Ba	576.62	167.6	683.90
La	29.16	8.7	25.08
Ce	43.13	15.8	53.12
Pr	6.61	0.1	6.83
Nd	23.34	8.1	28.26
Sm	6.38	0.1	6.57
Eu	2.05	0.1	1.99
Gd	6.69	0.2	6.81
Tb	1.12	0.2	1.08
Dy	6.04	0.5	6.42
Ho	1.26	0.0	1.31
Er	3.14	0.8	3.67
Tm	0.52	0.0	0.53
Yb	3.15	0.1	3.39
Lu	0.63	0.3	0.50
Hf	4.31	1.0	4.97
Ta	0.62	0.2	0.79
W	0.36	0.2	0.47
Tl	0.22	0.1	0.27
Pb	8.07	3.5	10.59
Bi	1.26	2.2	0.05
Th	4.57	2.1	5.83
U	2.45	1.5	1.68

3.6 In situ major element geochemistry

Sixteen samples were selected and prepared into 40 μm polished thin sections for major element analysis using a JEOL JXA 8230 Superprobe Electron Micro Analyser (EPMA) at Victoria University of Wellington. To select samples for EMPA analysis, petrographic descriptions were carried out on thin sections of at least two representative samples per basin. The selected thin sections were coated with a ca. 25 nm film of carbon prior to analysis. For each sample, in situ major and minor element compositions were measured for olivine and clinopyroxene phenocrysts, as well as spinel and melt inclusions where present within olivine phenocrysts.

The JEOL JXA 8230 Superprobe is equipped with five wavelength dispersive spectrometers (WDS) that are used for quantitative analysis of minerals to produce spot analyses and element concentration maps. The EMPA also contains two energy dispersive X-Ray spectrometers (EDS) which are useful for rapid qualitative analysis of minerals and several detectors that allow the collection of backscattered electrons (BSE) and secondary electrons (SE). Both BSE and BE detectors generate images of the sample surface, compositional zoning and grain morphology.

Quantitative analysis for each mineral was carried out using WDS with a focused beam, a 1-2 μm spot diameter, an accelerating voltage of 15 kV, and a beam current of 12 na. Both cores and rims were analysed for all minerals, including those that did not exhibit greyscale compositional zoning in BSE images. For minerals that contained melt or spinel inclusions, cores, rims and inclusions were analysed and BSE images were taken.

3.6.1 Standard calibration and raw data processing

For calibration and monitoring of data quality, calibrated natural and synthetic standards were periodically run 2-3 times each for every 20-30 sample measurements. Standards were analysed during each analytical run, at the

beginning and end of each analytical season to monitor for instrumental drift and to determine the precision and accuracy of each sample.

Natural mineral standards used for elements with high abundance (>1 wt %) were selected that had similar compositions to the minerals being analysed (Table 3.6.1). To calibrate elements that were low in abundance (<1 wt %), synthetic oxide standards were used.

All major element concentrations were calculated using the ZAF correction method (matrix effects of mass number, atomic absorbance and fluorescence are corrected for).

For olivine, all elements were normalised to San Carlos Olivine. For clinopyroxene, all elements were normalised to Kakanui Augite and for spinel, elements Mg, Cr and Al were not normalised, as a synthetic oxide Cr_2O_3 was used. Approximately 2SD relative analytical precisions are generally <5% for elements which occur in concentration >1 wt%. However, for elements that occur in low concentrations, the precision and accuracy decreases with decreasing relative concentration. It is also worth noting that data that showed totals below 98% were not used in the results.

Table 3.0-6: List of standards used to calibrate during analysis. EMPA calibrated to standard reference values from Jarosweich et al. (1980) for San Carlos and Klügel et al. (2005) for Kakanui Augite.

Mineral	**Matrix-matched standards**	**Synthetic oxides**
Clinopyroxene	Kakanui Augite (Si, Al, Mg, Na, Ca, Fe, Ti)	
Olivine	San Carlos (Si, Mg, Fe)	
Spinel		Cr_2O_3 (Al, Fe, Mn)

Chapter 4:

Results

4.1 Morphological analysis of basins

To provide the first detailed maps and descriptions of the morphological and structural features of back arc basins in the Havre Trough, high resolution multibeam (EM300 and SEABEAM) data collected from each basin were processed to produce DTMs. Outlines for 10 basins were developed (Figure 4.1) and their key morphological features summarised for each basin in Table 4.1. Morphologies in the back arc are defined by their apparent shapes according to slope, contour, and bathymetric maps. Ridges are defined by their elongation, knolls are defined as circular constructs less than 2km in size, cones are defined as circular constructs greater than 2 km in size, and basin floors are defined as areas with a lack of structures. All basins are comprised of varying proportions of features. The depth of bathymetry exceeding 2500 mbsl and the location of constructional features provided a means of confining the parameters of each basin (Table 4.1). However, constraining basins is difficult as a significant amount of ridge morphology and basin floors continue into nearby basins, in particular for basins on the eastern side of Havre Trough, which also contain arc front volcanoes. Basins A, B, C, D, E, and G have been previously used on marine voyage (e.g. Rovark). Names for Basins H, J and K have been defined in this study. Maps for each basin are presented in figures 4.2 – 4.4, with dredge sample locations also indicated. Basins are grouped by location south to north and east to west (Figure 4.1). Results for each basin are described in the following order:

1) Eastern basins closest to the arc front with increasing distance to the north; Basins B, C, E, and G.

2) Central basins grouped by increasing distance from the trench; Basins A, D, I.

3) Western basins which are closest to the Colville Ridge, with increasing distance to the north.

Table 4.0-1: Table showing the location of each basin, the size, depth and percentage of each feature.

Basin	Latiude	Longitude	Area km^2	Depth (mbsl)	Ridges	Cones	Basin floor
A	36°45'0"S- 36°31'30"S	177°10'30"E-177°16'30"E	369	4000	35	5	60
B	36°30'0"S- 35°29'30"S	178°11'30"E-178°45'30"E	396	3000	25	15	60
C	35°45'0"S- 35°20'30"S	178°11'30"E-178°47'30"E	1050	3000	20	5	75
D	35°35'0"S- 35°14'30"S	178°3'0"E-178°39'30"E	1200	3000	85	5	10
E	35°28'0"S- 35°56'30"S	178°28'0"E-179°5'0"E	600	3000	50	15	35
G	35°15'0"S- 35°40'30"S	178°40'0"E-179°20'0"E	900	3000	25	30	45
H	36°47'0"S- 35°45'0"S	177°0'0"E-177°35'0"E	3800	2500	5	15	80
I	35°29'30"S- 35°14'30"S	177°32'0"E-177°25'0"E	2400	3000	30	10	60
J	35°15'0"S- 34°43'0"S	177°38'0"E-178°34'0"E	3400	3000	10	25	65
K	34°27'30"S- 34°38'0"S	177°3'0"E-179°5'0"E	3750	2500	20	10	70

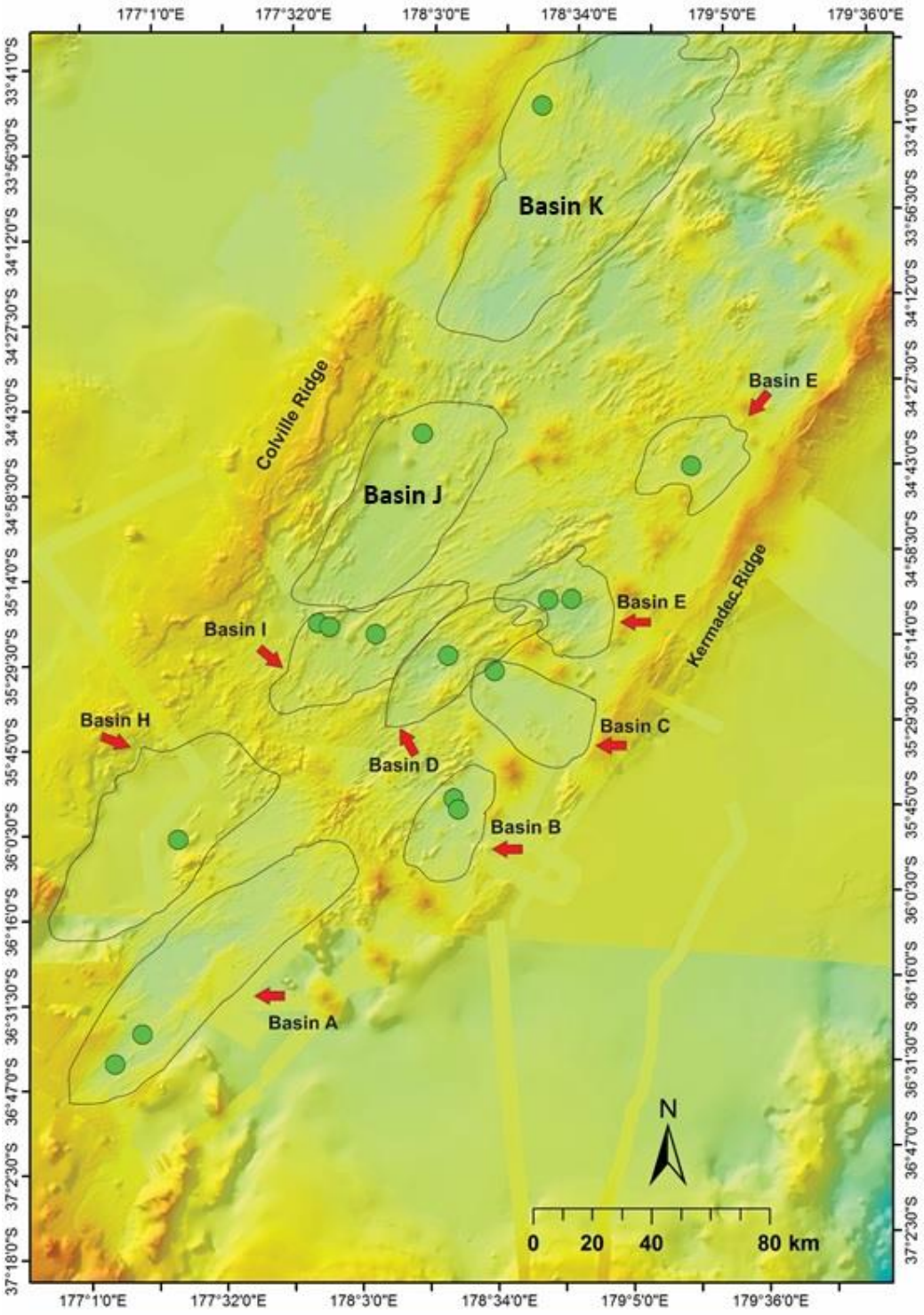

Figure 4.1: Bathymetric map showing a general outline distinguished for each basin in this study. Green circles signify dredge sample locations.

4.1.2 Eastern Basins

Basin B, the southernmost eastern basin is approximately 3000 mbsl, 33 km long, 12 km wide in the centre, 10 km wide at its south end and 7.9 km wide at its north end. It lies 10 km from Lille volcano, 20 km from Rumble III volcano, 45 km from Rumble V, and 28 km from the Kermadec Ridge 60% of this basin contains no structure and/or is flat, which is indicated by the lack of steep contour lines and low slope angles between 0-7° (Figure 4.2). Structural features that are present in Basin B are concentrated in the southern end of the basin. Between sample locations 55 and 56, a 1.8 km long and 1.2 km wide ridge is present. The ridge has a slope angle of 13-17° at the top then flattens out to 10-13° near the bottom (Figure 4.2; a). The height of the ridge is approximately 130 m.

To the west of the sample locations are wide ridges (~2.5-4 km long and 2-3 km wide) that are oriented at 045° and 060° and are broadly curved (Figure 4.2; b). Curved ridges are oriented at 060° and straight ridges are oriented at 045° (parallel to the Kermadec Ridge). In the southernmost extremity of the basin, a cluster of ridges is present that are ~6 km long and ~3-4 km wide (Figure 4.2; c). Ridges in this cluster are oriented both north to south as well as at 045°, 060° and 070°. Ridges are wider closer to Rumble V and to the edge of the basin in the west. All ridges have a slope angle that is relatively steep, ranging between 21-45° and an elevation of ~60 m. A cluster of cones is present in the basin (Figure 4.2; d). The cones are ~4-5 km long and ~5-7 km wide with steep slope angles ranging between 21-45°. Basin floors comprise a total of 60% of the basin area (Figure 4.2; e) and contain no structures, highlighted by low slope angles 0°-7° on the slope analysis map.

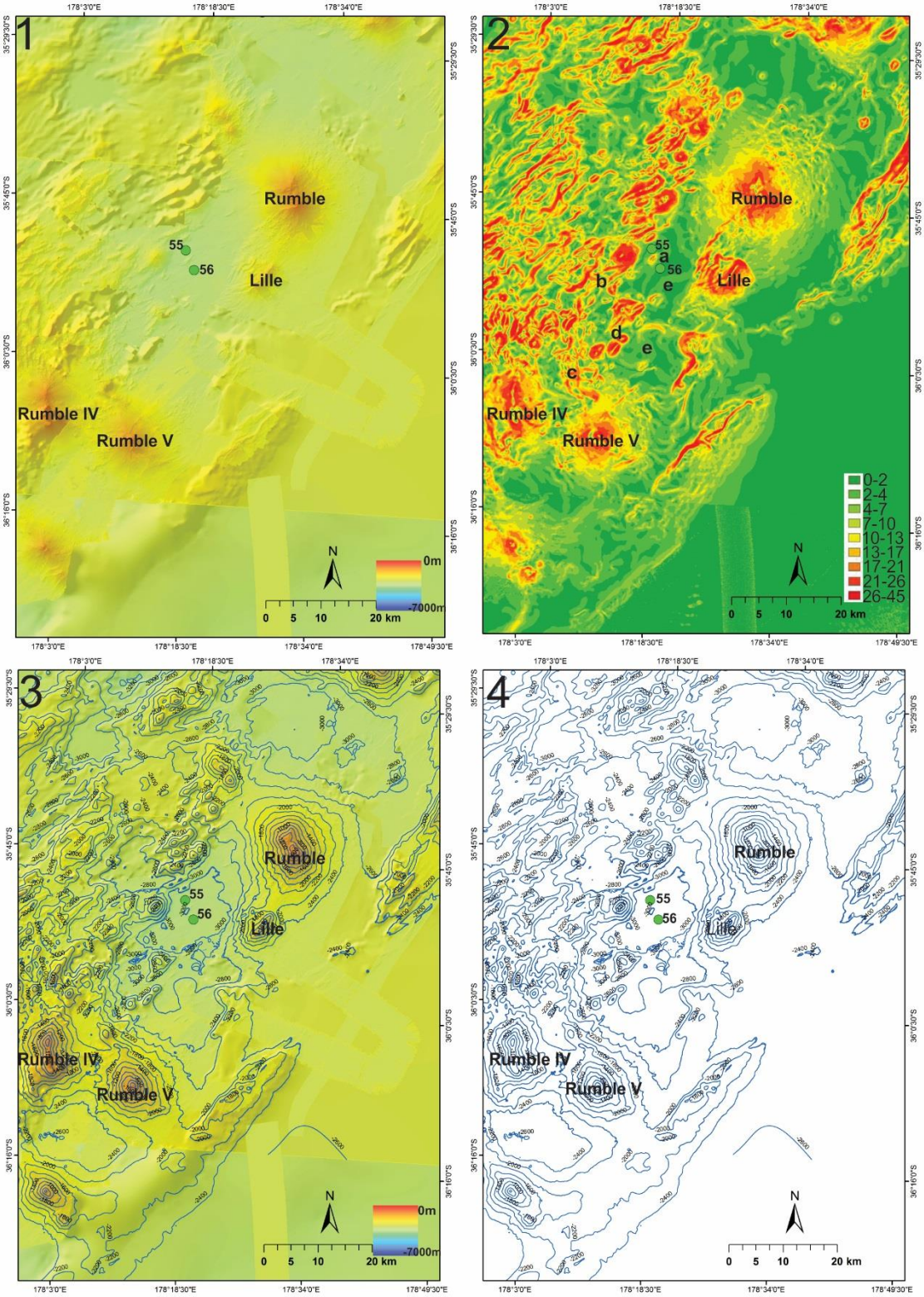

Figure 4.2: Digital topographic maps of Basin B, **1)** high resolution bathymetry map **2)** Map showing slope angles and labels of features described in text (a-e) **3)** high resolution bathymetry map with contours overlaid **4)** contour map. All maps show sampling numbers and locations.

Basin C is 44 km long, 28 km wide and approximately 3000 mbsl. Bordering Basin C are arc front volcanoes Rumble II East, Rumble II West and Rumble II. The basin lies approximately 5 km from the Kermadec Ridge. There are scattered ridges along the edge of the basin (Figure 4.3; a) that appear to be discontinuous, thin, long, broadly curved, and are oriented at 040°, 045°, 050°, and 060°. In the south-western section of the basin (Figure 4.3; b), the ridges form dendritic-like noses that are wider at the northern end, and appear to be shorter and thicker than that observed in the eastern and northern sections between Rumble II West and Rumble II East. These ridges have peak elevations ranging from 60-100 m and a slope angle of 21-26°. Directly adjacent to Rumble III on the northern side are thin long ridges that have a slope angle ranging from 7-13° and a few stepper ridges ranging from 17-21° (Figure 4.3; c). These ridges extend several km into the centre of Basin C. Several knolls are present in the basin (Figure 4.3; e) and have slope angles ranging between 10-13°. The basin consists of predominantly no structures (80% of the total basin area) (Figure 4.3; f) and is relatively flat indicated by a 0-7° slope angle and widely spaced contour lines. This is likely due to a lack of high resolution multi-beam data.

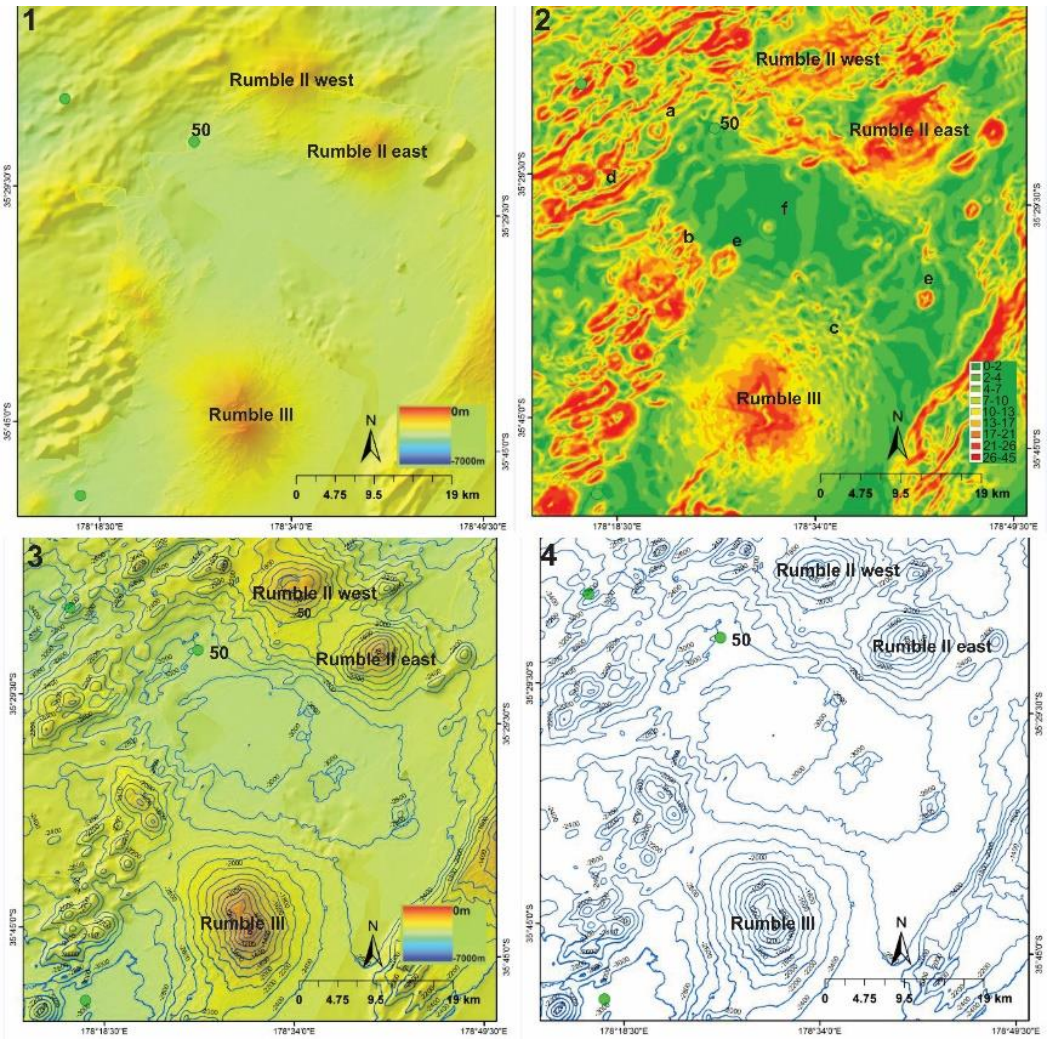

Figure 4.3: Digital topographic maps of Basin C, **1)** high resolution bathymetry map **2)** Map showing slope angles and labels of features described in text (a-e) **3)** high resolution bathymetry map with contours overlaid **4)** contour map. All maps show sampling numbers and locations.

Basin E is approximately 2500-3000 mbsl, 20 km wide and 30 km long and lies ~8 km Rumble II West, ~12 km Rumble II East, ~4 km from Thompson and ~28 km from the Kermadec Ridge. Basin E consists of a large continuous ridge located near the sampling sites 10 and 11 (Figure 4.4; a). The ridge is ~500 m-1 km wide and ~10-15 km long, and is steep indicated by tight contour lines, a slope angle ranging between 26-45° and an elevation up to 50 m. To the north of and between Rumble II West and Rumble II East is a large cluster of ridges (Figure 4.4; b) that are ~400 m-2 km wide and ~8-10 km long, and are steep with slope angles ranging between 26-45°. Several smaller ridges are also present in the basin and appear to be less steep than larger ridges in the basin, with slope angles that are between 10-17° (Figure 4.4.; c). Several large cones are also present in the basin northwest of both sampling sites and are approximately 2-4 km wide and 3-5 km long with slope angles ranging from 21-45°. Adjacent to ridge and cone features are basin floors with no structural features (Figure 4.4; d) highlighted by widely spaced contours and 0-7° slope angles. This area is approximately 15-20 km wide and comprises 35% of the total basin area.

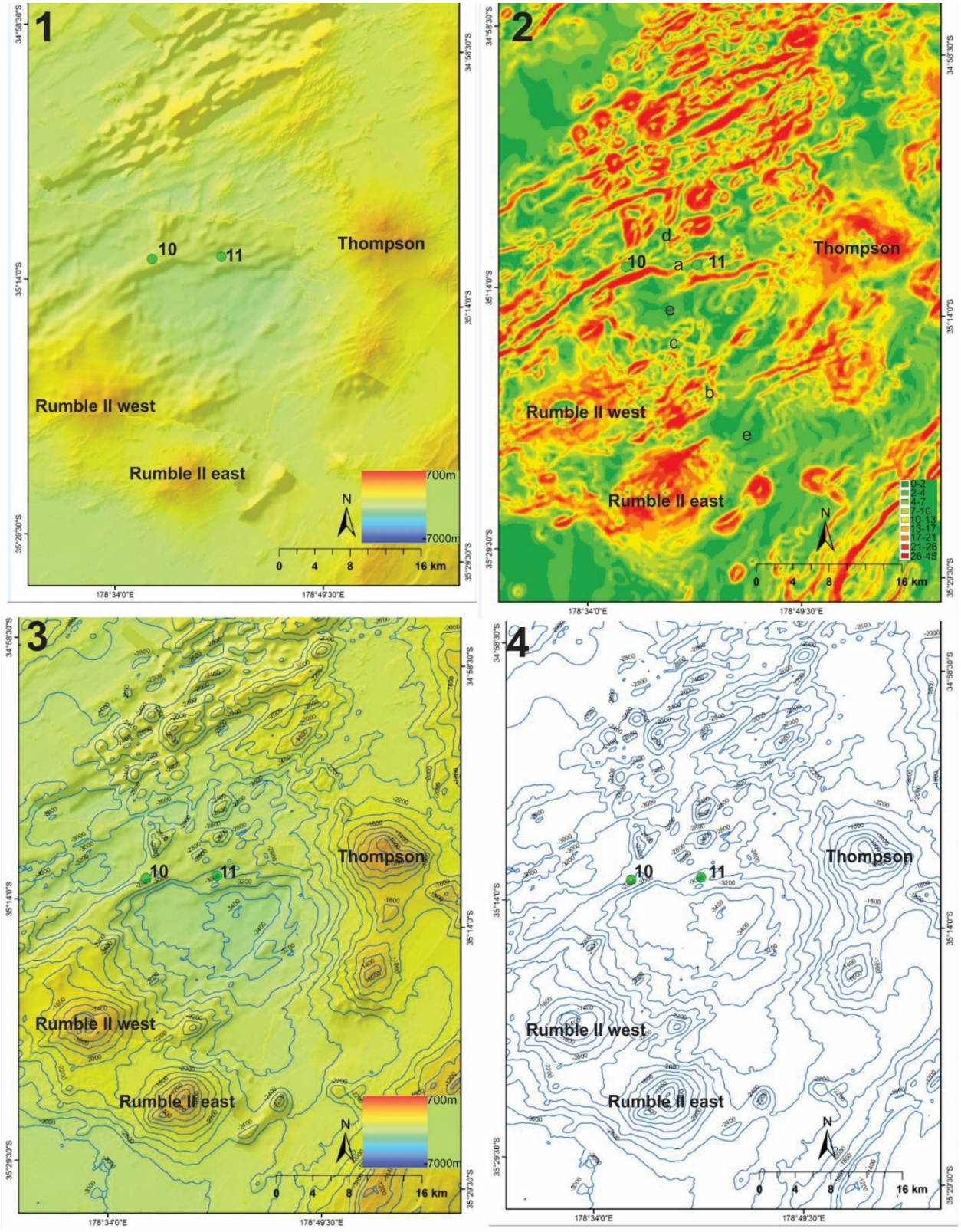

Figure 4.4: Digital topographic maps of Basin E, **1)** high resolution bathymetry map **2)** Map showing slope angles and labels of features described in text (a-e) **3)** high resolution bathymetry map with contours overlaid **4)** contour map. All maps show sampling numbers and locations.

Basin G is approximately 2500-3000 mbsl, ~37 km wide, 63 km long and lies ~6 km from Brothers, ~10 km from Healy and ~20 km from the Kermadec Ridge. A cluster of ridges is present below sample site 47 (Figure: 4.5; a) that vary in slope angle from 10-13° at the edges, to 26-45° at the top. To the northwest of the sample site is a large series of ridges that are steep and appear to be wider to the west (up to 5 km in width) (Figure: 4.5; b), have slope angles ranging from 21-45° and elevations ranging from 8-10 m. In the southern section of the basin and adjacent to the sample site are a series of long thin discontinuous ridges (Figure: 4.5; c).

These ridges are moderately steep with slope angles ranging from 10-26° and are approximately 5-10 m high. Several cones and knolls are present in the basin (Figure 4.5; d; e; f; g). Cone d is approximately 5 km wide and 10 m- 20 m in height, is the largest of the two cones and two knolls in the north, and has a 2 km long ridge on its eastern side. Cone e is approximately 3 km wide and knolls f and g are approximately 1 km wide. All cones and knolls range in slope angle from 26-45°. To the southwest and northeast of the sampling site and adjacent to the Kermadec Arc are basin floors that lack structures (Figure: 4.5; g). Here contours are widely spaced and slope angles range between 0-7°. Bathymetry for the westernnnmost extremity of the basin contains less high-resolution data therefore, bathymetric maps appear to be blurry.

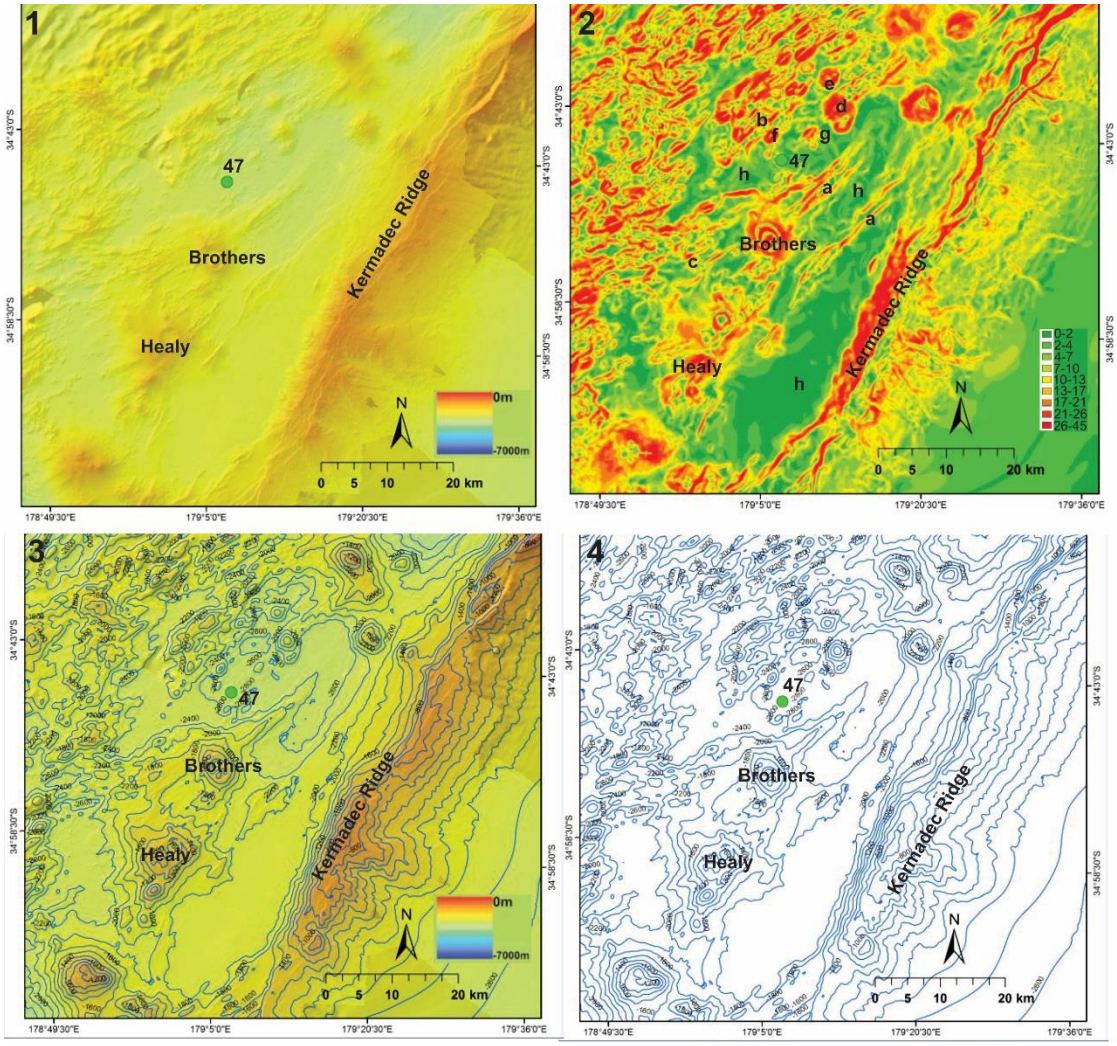

Figure 4.5: Digital topographic maps of Basin G, **1)** high resolution bathymetry map **2)** Map showing slope angles and labels of features described in text (a-e) **3)** high resolution bathymetry map with contours overlaid **4)** contour map. All maps show sampling numbers and locations.

4.1.3 Central basins

Basin A (southern Ngatoro Rift) is one of the deeper back arc basins >4000 mbsl (Figure 4.6) in the Havre Trough. The basin is 11.4 km wide, 32.4 km long and lies approximately 62 km from the Kermadec Ridge and ~35 km from Whakatane volcano. Basin A contains the large Ngatoro Axial Ridge and several clusters of narrow ridges which are best highlighted on the slope angle map (e.g. Figure 4.6.2). Ngatoro Axial Ridge extends ~9.35 km in length and is oriented at 45° parallel to the arc front. It ranges in width from 1.4 km in the south increasing to the north where it is 2.28 km wide (Figure 4.6; a).

To the north of sample site 006, a series of thin ridges are present ranging in width from 200-500 m, that are ~10 km in length, have slope angles between 10-21° and are oriented at 045° (Figure: 4.6; b). To the southeast of sample site 006 is a series of curved ridges oriented north-south, east- west and 045° (Figure 4.6; c). They are approximately 1-2 km long, 500 m wide and ~200 m high. To the northeast of sample site 3 and the west of Ngatoro Axial Ridge is a series of narrow ridges approximately 200 m wide and 1.5 km long (Figure 4.6;d). However, these ridges are best highlighted on the slope map.
On the western flank of basin A, a series of ridges that are widely spaced occupy the basin. The ridges are up to 260 m in elevation indicated by tight contour lines, slope angles of 21-26° for inner ridges and 26-45° for large outer ridges (Figure: 4.6; e). On the eastern flank of basin A ridges are steeper and are tightly spaced, indicated by extremely tight contour lines and range in elevation up to ~100 m (Figure: 4.6; f). A large cone is present in the basin, north of Ngatoro Axial Ridge and is best highlighted in the slope angle map. This cone is approximately 2.4 km wide and 2 km long with a slope of 13-26° (Figure: 4.6; g).

Within the basin a total of 30% of the basin area is comprised by structureless basin floor (e.g. Figure 4.6; h). This is indicated by a lack of contours and a slope angle of 0-7°. Sections of bathymetry (e.g. Figure 4.6; h) are blurry as there is less high-resolution mapping carried out here and some of the data for these sections were not available to use in this study.

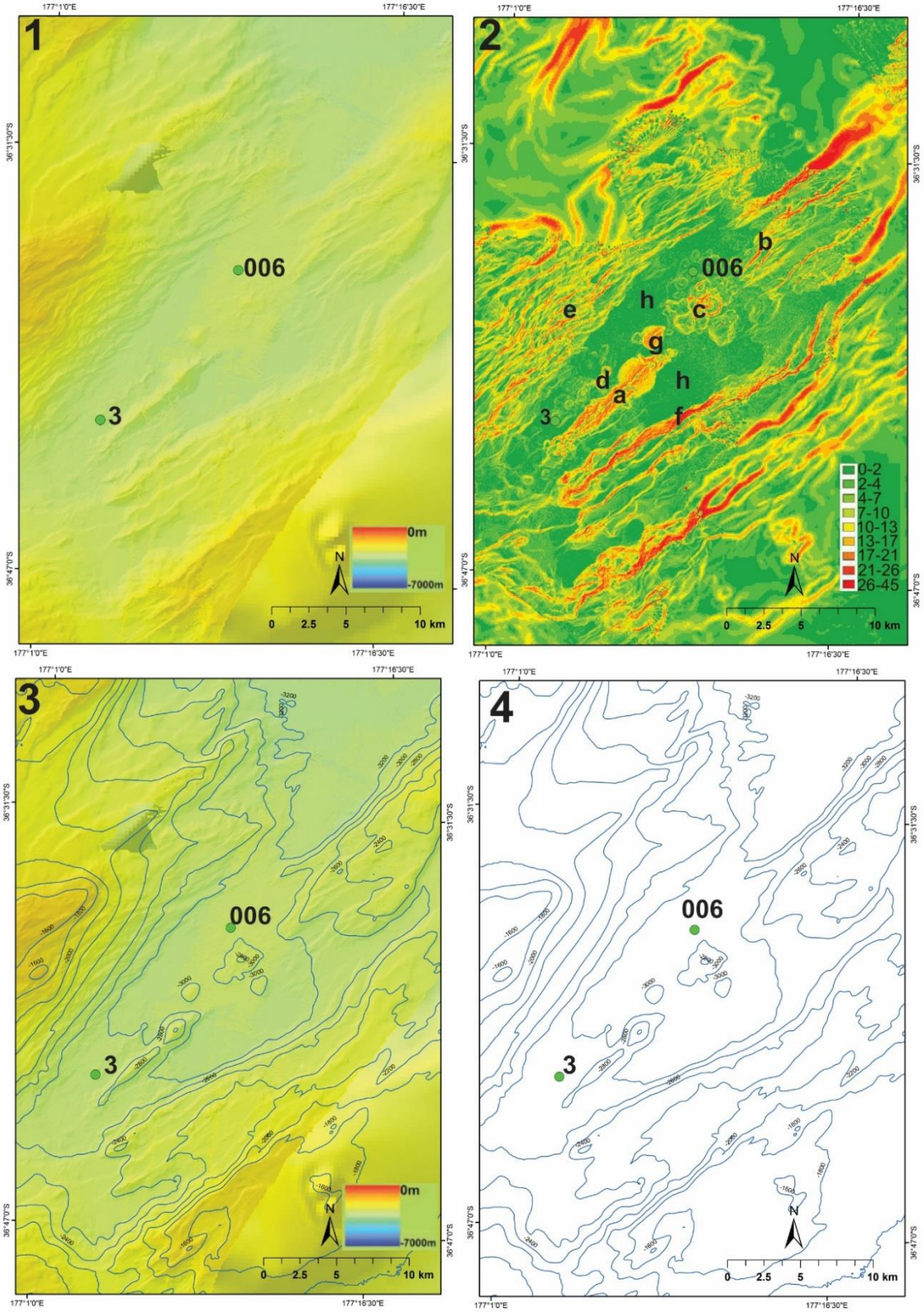

Figure 4.6: Digital topographic maps of Basin A, **1)** high resolution bathymetry map **2)** Map showing slope angles and labels of features described in text (a-e) **3)** high resolution bathymetry map with contours overlaid **4)** contour map. All maps show sampling numbers and locations.

Basin D is approximately 2500-3000 mbsl, ~59 km long, ~20 km wide and lies ~45 km from Rumble II, ~20 km from Rumble II West, ~30 km from Rumble II East, and ~49 km from the Kermadec Ridge. In the northern part of the basin (on and near the sampling site) extensive ridges are present which are predominantly oriented at 045°, and a few oriented at 040°, 050° and up to 080° (Figure 4.7;a). In general, the elevation of the ridges ranges from 60-80 m and are also relatively steep indicated by tight contour lines, as well as slope angles between 17-45°. However, most range between 17-26°. The largest ridge or series of ridges in the basin are approximately 6.6 km long and 1.8-2.5 km wide, with a peak elevation of ~100 m and a slope angle of 26-45° (Figure 4.7; b). In the west a series of ridges are also present that appear to be discontinuous (Figure 4.7; c). These ridges are oriented at 45° and 35° and range in size from 500 m-1 km in width and 4-5 km in length.

Few small cones are present in the western part of the basin (Figure 4.7; d). These are approximately 2 km wide and 3-5 km long and have steep slopes ranging from 26-45°and range in elevation to ~200 m. Adjacent to ridges and cones and to the west of the sample site in the basin are pockets of basin floors, which contain no structural features, comprising a total of 10% of the total basin area. The location of basin floors is indicated by widely spaced contour lines and slope angles ranging between 0-7° (Figure 4.7; e) and are best highlighted on slope angle and bathymetric contour maps.

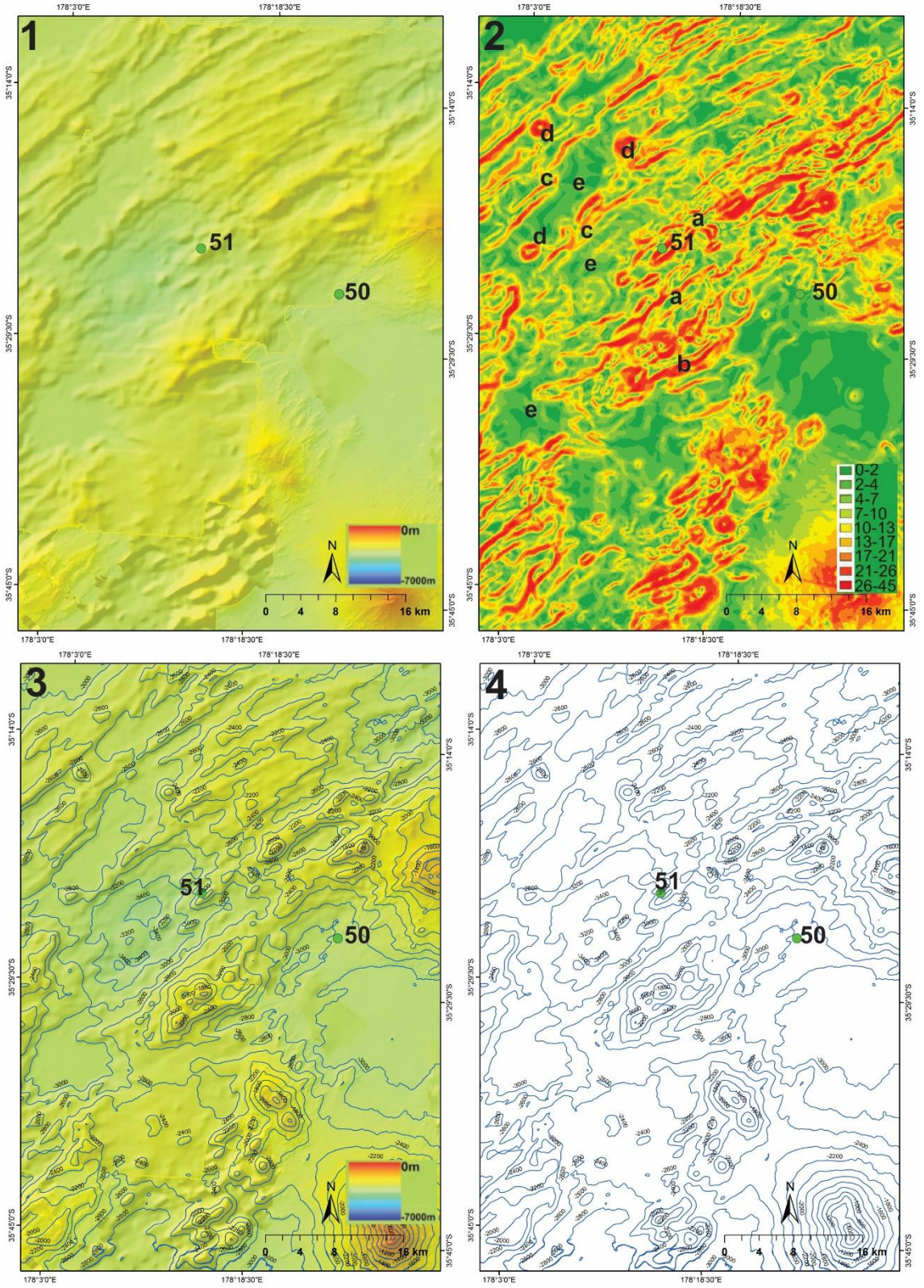

Figure 4.7: Digital topographic maps of Basin D, **1)** high resolution bathymetry map **2)** Map showing slope angles and labels of features described in text (a-e) **3)** high resolution bathymetry map with contours overlaid **4)** contour map. All maps show sampling numbers and locations including sampling site for basin C.

Basin I is approximately 3000 mbsl, ~59 km wide, ~37 km long and is located ~15 km from the Colville Ridge, 68 km from the Kermadec Ridge and the northern parameter of Basin I extends into Basin J in the west. The western side of the basin also appears to become slightly shallower indicated by a colour change in bathymetry, and slightly thicker indicated by the tightness in contour lines and steeper slope angles.

There are four main ridges in Basin I, three of which are where sampling was carried out (Figure 4.8; a; b; c). The large ridges all have a slope angles between 21-45° and range in elevation (Sample 040) 21 m, (sample 041) 45 m (higher on the east side) and (sample 042) ~100-200 m. Ridge a is 2 km wide and 3 km long, ridge b is 1.5 km wide and 9 km long and ridge c is 1 km wide and 18 km long. Two ridges are present in the middle of sample site 041 and 042 (Figure 4.8; d; e). Ridge d is ~21 km long and ~1.5 km wide. Ridge is ~8.5 km long and 1.5 km wide. Both ridges have slope angles of 21-45° and are approximately 60 m high. Northeast of sample site 042 is a series of ridges that are ~3-5 km long, 1-2 km wide, and a slope of 17-26° (Figure 4.3; f). To the north of sample sites 040 and 041 are a series of discontinuous ridges which are oriented both east to west and north to south. These ridges are up to 4 km in length and 1 km in width and are relatively steep with slope angles of 21-26° (Figure 4.3.3.2.g). In the southernmost section of the basin are discontinuous ridges oriented at 45° that range in size from 500 m-1 km in length and 500 m in width and show slope angles of 13-17° (Figure 4.8; h)

Several cones are present in the basin (e.g. Figure 4.8; i) that range in size from 2-2.5 km, with a slope of 26-45° that are best highlighted on slope angle maps. Adjacent to the ridges and cones are basin floors which contain no structures, a slope angle of 0-7° and widely spaced contour lines. (Figure 4.8; j). Basin floors comprise a large portion of the basin (60% of the total basin area).

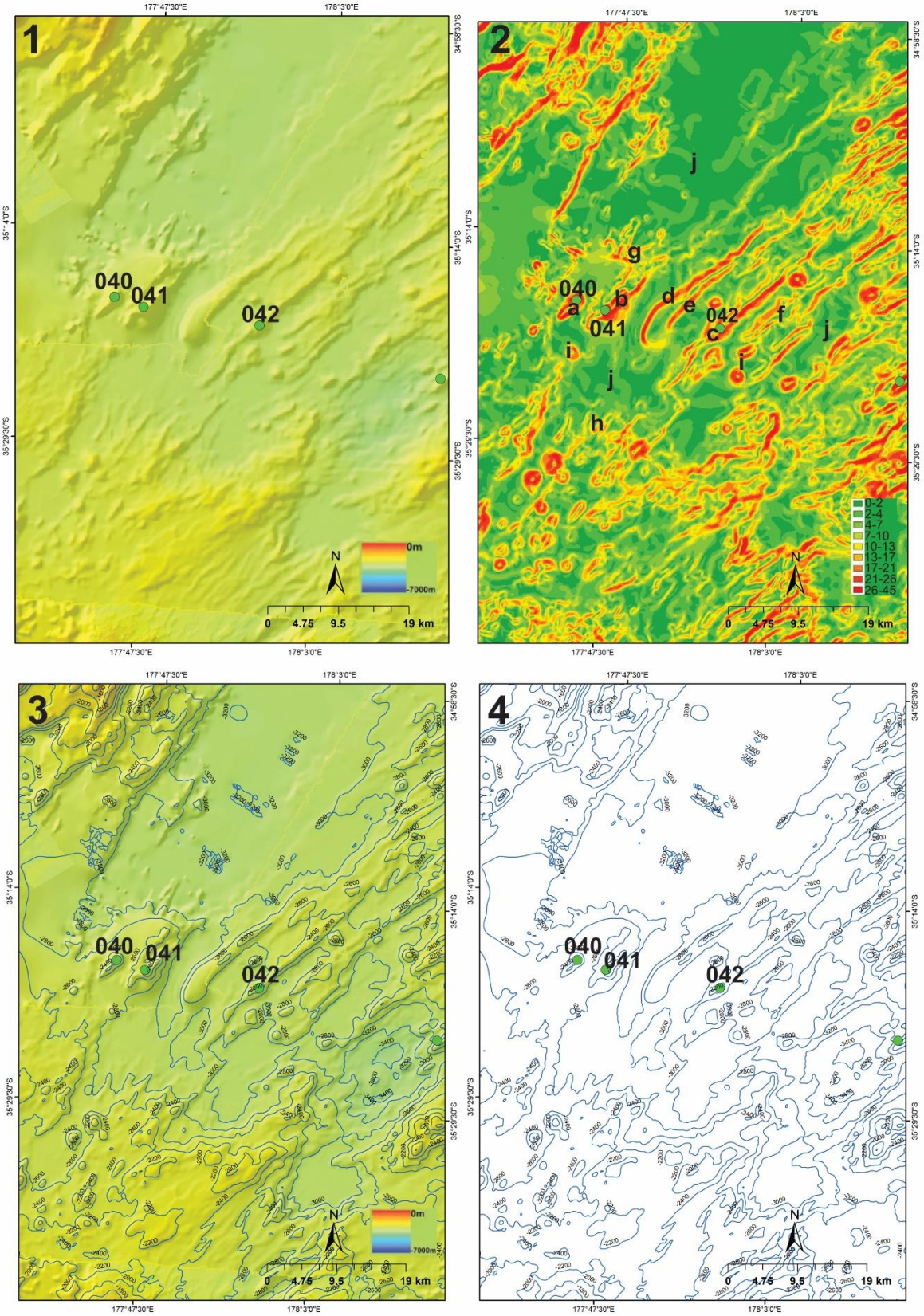

Figure 4.8: Digital topographic maps of Basin I, **1)** high resolution bathymetry map **2)** Map showing slope angles and labels of features described in text (a-e) **3)** high resolution bathymetry map with contours overlaid **4)** contour map. All maps show sampling numbers and locations.

4.1.4 Western basins

Basin H is approximately 2000-2500 mbsl, is ~45 km wide and ~90 km long, and lies ~15 km from the Colville ridge, ~104 km from the Kermadec Ridge. The structures that are present are focussed around the eastern side of the basin. A short ridge located at the sampling site is ~4 km wide, has an elevation of 80 m and a slope angle of 17-26° (Figure 4.9; a). North of the sample site is another longer, thin ridge (Figure 4.9; b) that has a slope angle of 13-17°. South of the sampling site is a series of small curved discontinuous ridges ranging in length from 3-7.5 km and width of up to 1.5 km. The ridges are oriented at 040° and 070° and are fairly steep ranging in slope angle from 10-21° (Figure 4.9; c). In the northeast there is a cluster of discontinuous ridges that are oriented predominantly at 045° with few oriented at 060°. The ridges have lengths of ~5 km and widths of 1 km (Figure 4.9; d).

There are at least 6 cones present in the basin that vary in size from 2-5 km. The largest cone (Figure 4.9; e) to the southeast of the sample site is ~4.5 km wide and has an elevation of ~140 m and a slope angle between 17-45°. Cone f (e.g. Figure 4.9; .f) is ~2 km wide. Cone g (e.g. Figure 4.9; g) is ~3 km wide and Cone h (e.g. Figure 4.9; h) is ~2 km wide and appears to transition into a ridge on its western side. Cone i (e.g. Figure 4.9; i) is ~5 km wide and also appears to transition into two ridges on its southern side. Both ridges are 3 km long and 1.5 km wide. Cone J (e.g. Figure 4.9; j) located at the northernmost extremity of the basin is approximately 2.5 km wide. Two knolls are also present in the basin (e.g. Figure 4.9; k) both knolls are ~1 km-1.5 km wide. All cones and knolls have similar slope angles ranging between 21-45° and elevations ranging between 20-100 m.

Approximately 80% of the total basin contains no structures which is highlighted best in slope angle maps and contour maps showing very widely spaced and a lack of contour lines, and slope angles between 0-7° (e.g. Figure 4.9; l).

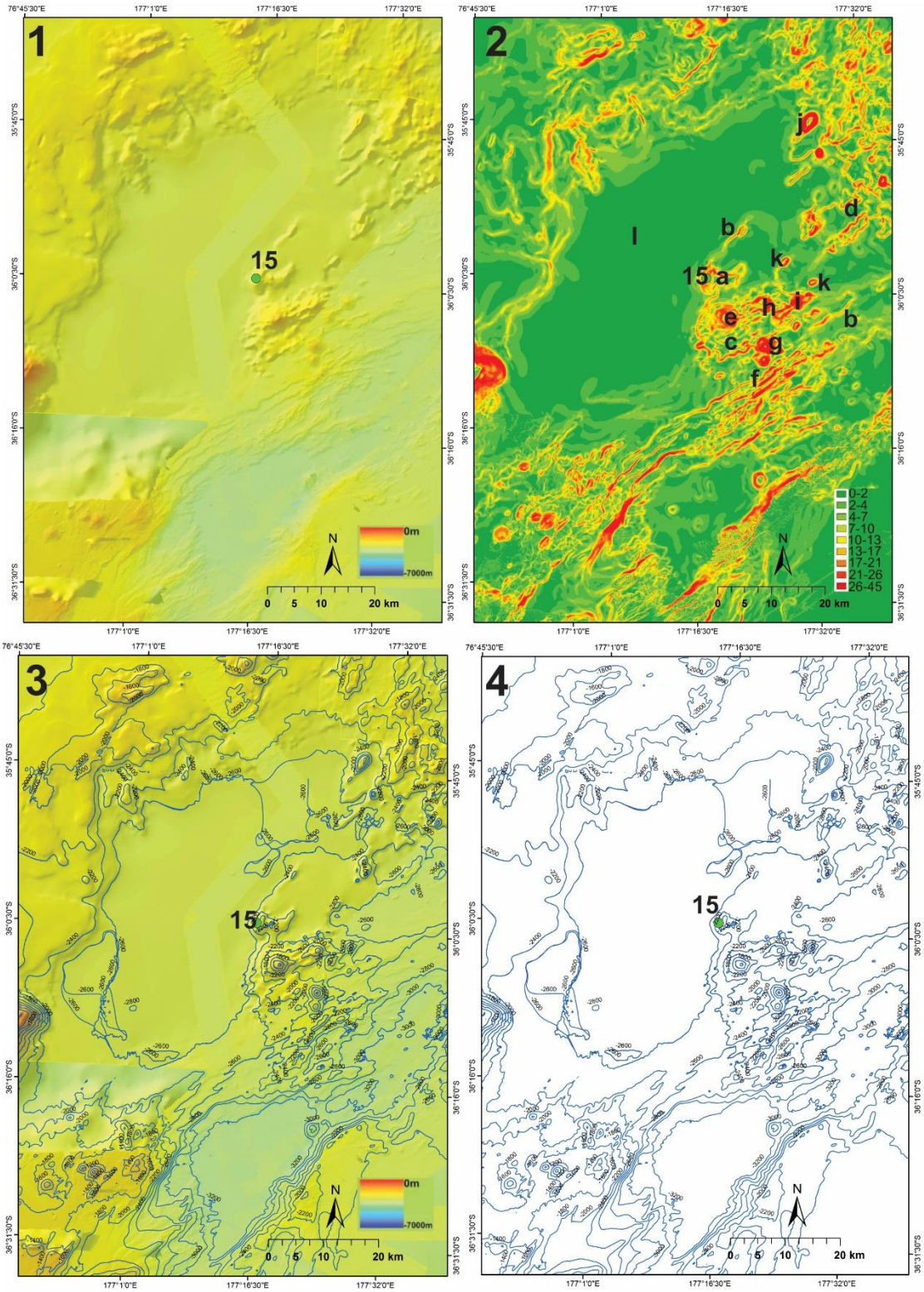

Figure 4.9: Digital topographic maps of Basin H, **1)** high resolution bathymetry map **2)** Map showing slope angles and labels of features described in text (a-e) **3)** high resolution bathymetry map with contours overlaid **4)** contour map. All maps show sampling numbers and locations.

Basin J is approximately 3000 mbsl, ~74 km wide ~118 km long, and lies ~30 km from Rapuhia, ~35 km from Yokosuka, ~5 km from Gill, and ~19 km from the Colville Ridge and 88 km from the Kermadec Ridge. The basin contains scattered ridges (Figure 4.10; a) which are ~2.5 km in length, ~1.5 km in width and are oriented north to south, east to west, 045° and 050°. To the north of these ridges are a series of longer ridges (~7.5 km long and ~1.5 km wide). The ridges are oriented at 20°and are relatively steep ranging from 17-26° (Figure 4.10; b). Northeast of the sampling site are a series of discontinuous ridges, which range from 2-4 km in length and up to 3 km in width for ridges that are closer to the sample site. The ridges are also relatively steep, showing slope angles of 17-45° (Figure 4.10; c). A small cluster of ridges are present in the north which are approximately 1-2 km in length, 1 km in width, oriented at 10° almost north-south and show a slope of 17-26° (Figure 4.10; d). Another small cluster of ridges is present in the easternmost side of the basin, oriented both north-south and at 45°. The length of the ridges ranges from 1-2.5 km and widths from 500 m-1 km (Figure 4.10; e).

There are several clusters of cones throughout the basin. The first cluster is seen to the east of the sampling site (Figure 4.10; f; g; h; I; j; k; l; m). The cones varying in size from 2-4.5 km in width and show slope angles ranging between 21-45°. The cone which is farthest north (Figure 4.10; m) is approximately 60-70 m high. The second cluster of cones are present in the northern part of the basin adjacent to Gill stratovolcano that range in size from 2-4.5 km. The cones are spaced closely compared to cones that are on the eastern side. All cones are steep (slope angles form 26-45°) and are approximately 60 m high (Figure 4.10; n).

70% of the total basin area is comprised of basin floors and areas with no structures (Figure 4.10; o). This is portrayed best in slope angle maps and contour maps that show slope angles of 0-7° and widely spaced contours.

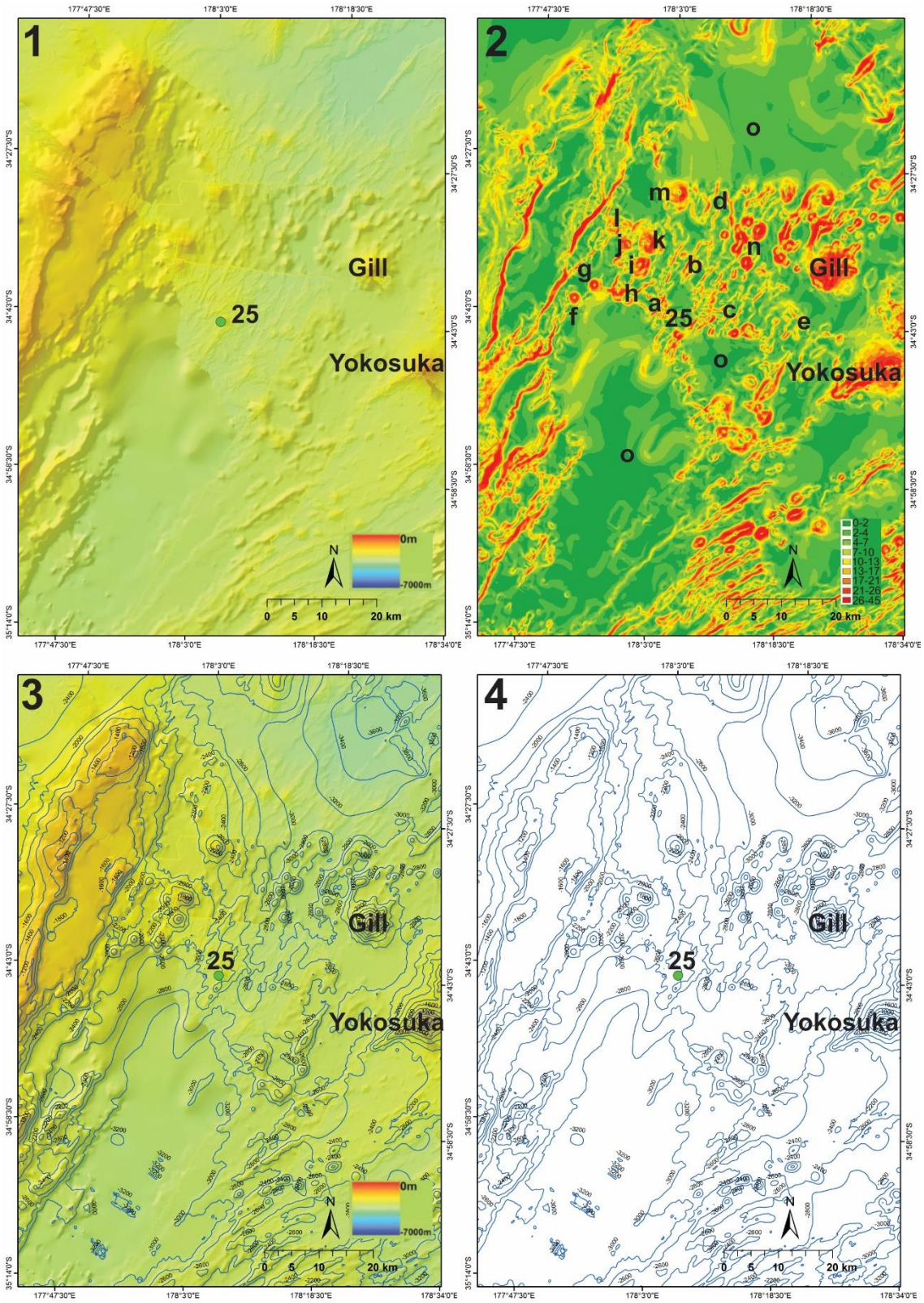

Figure 4.10: Digital topographic maps of Basin J, **1)** high resolution bathymetry map **2)** Map showing slope angles and labels of features described in text (a-e) **3)** high resolution bathymetry map with contours overlaid **4)** contour map. All maps show sampling numbers and locations.

Basin K is approximately 2500-3000 mbsl, is ~49 km wide ~143 km long, and lies ~1.8 km from the Colville Ridge, ~5 km from Saito Seamount and ~90 km from the Kermadec Ridge. There is a concentration of thin, discontinuous ridges to the north and south of the sample site (Figure 4.11; a). These ridges are similar in size ~1.5 km long and up to 1 km wide. The northern ridges are oriented north to south, in contrast to the southern ridges which are oriented at 40° and east to west. Both sets of ridges show similar steepness from 26-45°. On the eastern side of the basin are also another two sets of ridges that appear to be more continuous. The ridges in the north are approximately 5 km in length and 1.5-2 km in width and are oriented at 030°, 040°, and 060° (Figure 4.11; c). The central eastern ridges are longer (2.5-22 km long) and are ~2-3.5 km wide. The orientation of these ridges is 045° and show slope angles of 26-45° (Figure 4.11; d).

Cones and knolls are scattered throughout the basin, with a small cluster of cones and knolls present in the centre and north of the basin. Cone b (e.g. Figure 4.11; b) is approximately 2.5 km in size. Cone e (e.g. Figure 4.11; e) is approximately 4km in size. Cone f (e.g. Figure 4.11; f) is approximately 3 km in size. Knoll g (e.g. Figure 4.11; g) is approximately 1.2 km in size. The first cluster of cones (e.g. Figure 4.11; h) are ~2 km in size and appear to be connected together by a few short ridges. The second cluster of knolls (e.g. Figure 4.11; i) range in size from 1-1.5 km and are also connected by short ridges. In the easternmost side of the basin a cone is present and is approximately 2 km in size (Figure 4.11; j). All cones and knolls are relatively steep and show slope angles of 26-45°.

Basin floors are present in the south and north, as well as between all structures in the basin. Basin floors comprise a total of 70% of the basin area, represented by slope angles between 0-7° and widely spaced contour lines (e.g. Figure 4.11; k).

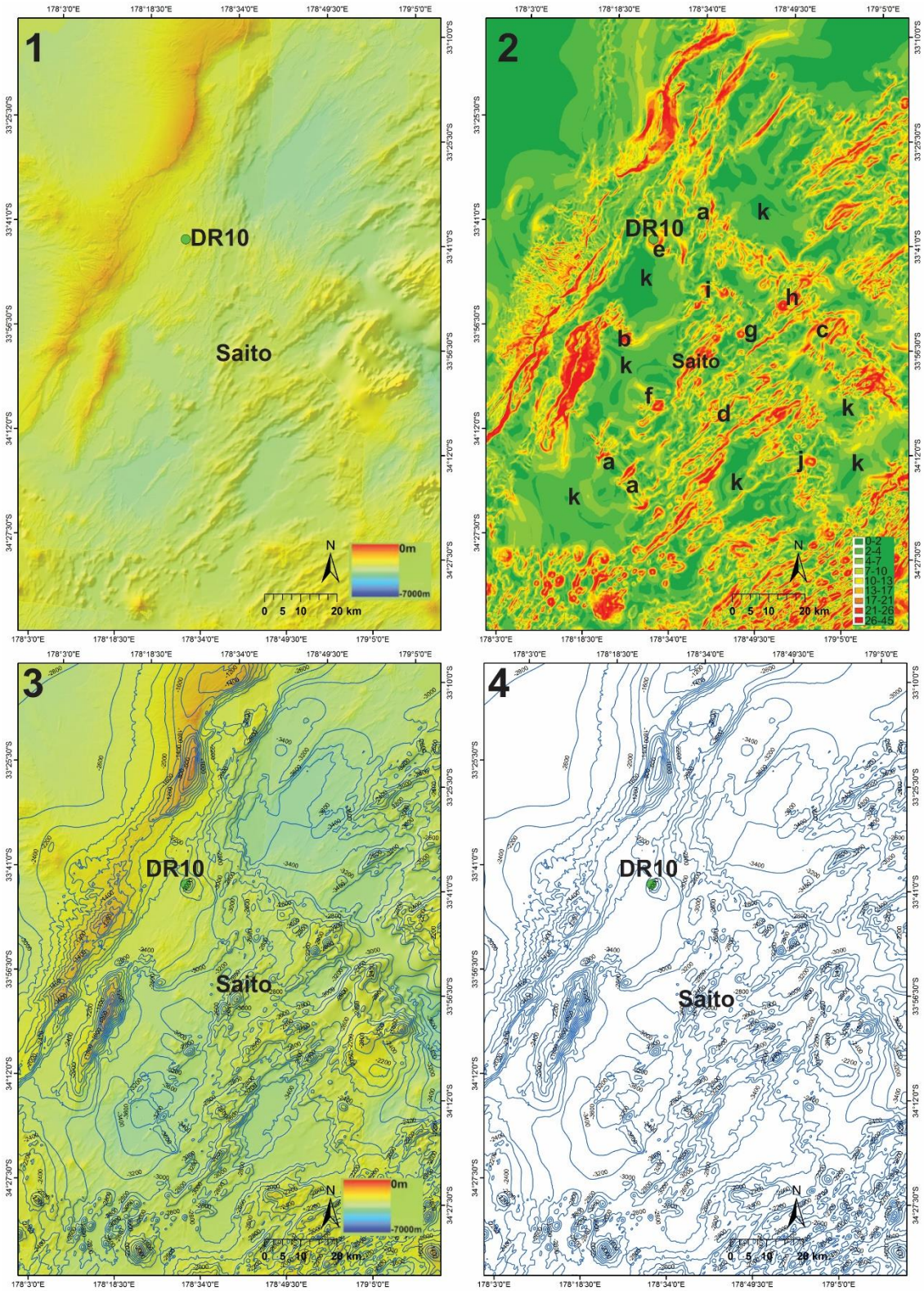

Figure 4.11: Digital topographic maps of Basin K, **1)** high resolution bathymetry map **2)** Map showing slope angles and labels of features described in text (a-e) **3)** high resolution bathymetry map with contours overlaid **4)** contour map. All maps show sampling numbers and locations.

In general, basins on the western side appear to contain a higher percentage of structureless basin floors and few scattered ridge and knoll morphology. The cones and knolls that are present tend to form in clusters and are generally connected by shorter ridges. The ridges within western basin are typically oriented north to south, east to west, 030°, 040° and 060° rather than at 045°. Basin floors within western basins appear to be shallower than eastern basins. In contrast, eastern and central basins appear to contain a higher percentage of ridges and overall less cones than the western side. Ridges are more continuous and are predominantly oriented at 045° parallel to the arc front, with few basins showing arc perpendicular orientations. The widths and lengths of basins are more confined on the eastern side due to large constructional edifices (i.e. back arc and arc front volcanoes).

4.2 Petrography

Petrographic descriptions have been made for 17 samples selected from 8 back arc basins. Two basins were not included in the petrographic analysis due to a lack of rock samples available. The samples were subdivided into four different litho-types (1-4) on the basis of the overall mineral assemblage present, the dominant phenocryst mineral (from olivine rich to plagioclase rich), and the size, shape, and textures present in phenocrysts. In this section, the petrographic features of each litho-type are summarised, with specific petrographic descriptions for each sample included in Appendix A2.

4.2.1 Type 1 (olivine and plagioclase phyric)

Type 1 rocks are moderately porphyritic with ≤20% phenocrysts, ca.40% groundmass and < 45% vesicles. The phenocryst assemblage consists of ca. 20-60% olivine, ca. 25-70% plagioclase and ≤2% clinopyroxene. Orthopyroxene is absent. Examples of type 1 rocks were described from 3 Basins (B, D, and G) with photomicrographs of typical sections shown in Figure 4.12.

Olivine phenocrysts are generally subhedral- euhedral, a few are skeletal, and are commonly fractured. Olivine phenocrysts typically range from 0.5 to 1.5 mm and are commonly present in clusters where crystal rims are touching each other (e.g. Figure 4.12; A and C). Chromium spinel is common in Type 1 rocks, forming inclusions ≤ 50 μm within olivine phenocrysts or as (<60 μm) crystals immediately adjacent to olivine phenocrysts. Melt inclusions (<100 μm) are also present in the olivine phenocrysts and are typically crystallised. Uncrystallised melt inclusions are rare.

Plagioclase phenocrysts are most commonly acicular and up to 0.5 mm in size, displaying simple twining. 10% are tabular and euhedral with weak compositional zoning. Rare plagioclase crystals show dissolution textures, e.g. in samples from basin D. Plagioclase commonly occurs as glomerocrysts with olivine and clinopyroxene, with the glomerocrysts ranging in size from 0.4 mm-1 mm (e.g. Figure 4.12; D)

Clinopyroxene phenocrysts range in size from 0.5-1.5 mm and occur as subhedral-euhedral, and long tabular crystals. Twinning and opaque inclusions are common in clinopyroxene phenocrysts (e.g. Figure 4.12; F).

The framework groundmass is dominated by microcrystalline acicular plagioclase with minor olivine and pyroxene, medium brown glass and Fe-Ti oxides. A transition into darker glass at the rims is common for Type 1 rocks.

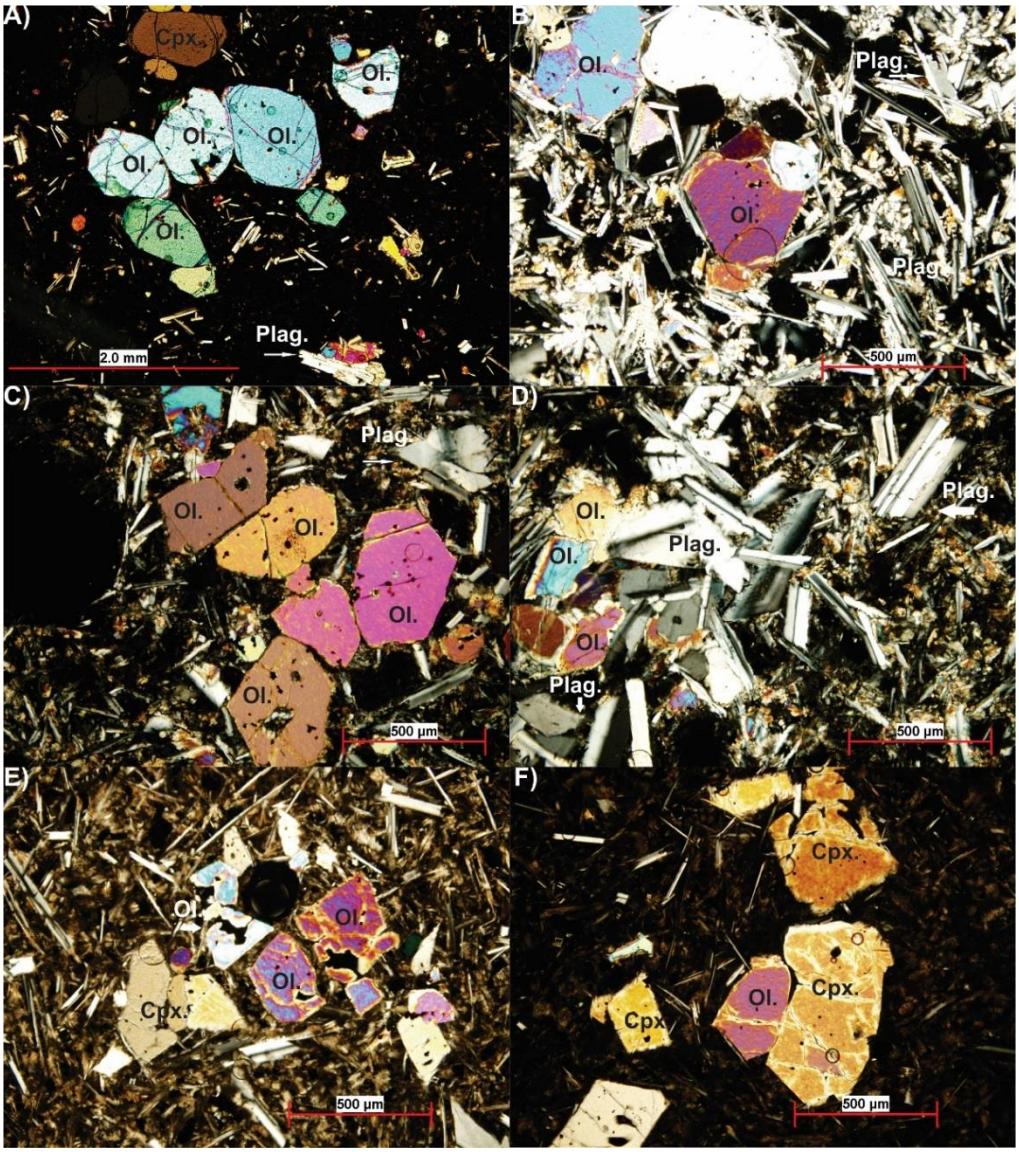

Figure 4.12: Photomicrographs in cross polarised light of representative phenocrysts from various samples. **A)** Sample TAN1213-47-2 note small plagioclase and olivine glomerocryst in bottom right corner. **B)** Sample TAN1213-56-1. **C) and D)** TAN1213-51-4. **E) and F)** TAN1213-56-3 note small amount of clinopyroxene present. Crystal phases shown are olivine (Ol.), plagioclase (Plag.) and clinopyroxene (Cpx.).

4.2.2 Type 2 (olivine and clinopyroxene phyric)

Type 2 rocks are moderately porphyritic basalts consisting of 15-25% phenocrysts, ca. 40% groundmass and <45% vesicles. Olivine phenocrysts are volumetrically dominant in Type 2 rocks comprising 60% of the phenocryst population, clinopyroxene comprises 38%, and plagioclase comprises <1%. Orthopyroxene is absent. This lithotype was described for 1 sample from Basin I (Figure 4.13).

Olivine phenocrysts are commonly present as well formed subhedral to euhedral phenocrysts ranging in size from 0.5-1.7 mm. Fractures are common. Chromium spinel is highly abundant within and adjacent to olivine phenocrysts, ranging in size from 50-70 μm (e.g. Figure 4.13; A; B). Melt inclusions are commonly present in olivine phenocrysts as crystallized inclusions, ranging in size from 500-200 μm. Uncrystallised inclusions are less common and range in size from 150-300 μm.

Clinopyroxene phenocrysts occur as tabular, subhedral phenocrysts, ranging in size from 0.3-1 mm (e.g. Figure 4.13; C). Clinopyroxene phenocrysts typically occur in clusters or as glomerocrysts with olivine. Few phenocrysts show weak growth zoning, simple twinning is common.

Plagioclase is very sparse in Type 2 rocks, present as acicular and tabular stumpy crystals up to 0.2 mm in size.

The groundmass in Type 2 rocks is comprised of microcrystalline plagioclase, olivine, clinopyroxene, brown glass and minor amounts of Fe-Ti oxides.

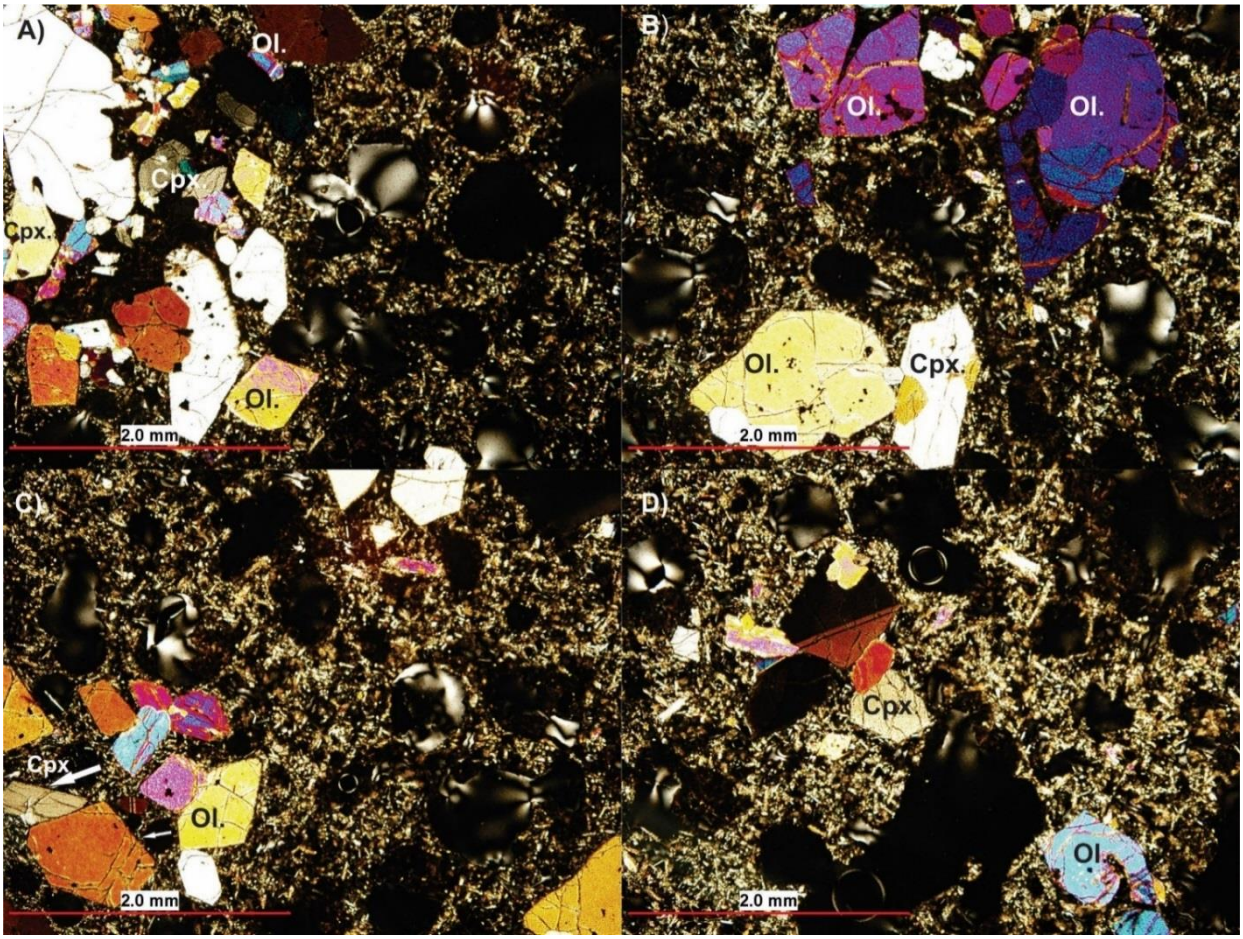

Figure 4.13: Photomicrographs in cross polarised light of representative phenocrysts from sample TAN1513-040-02 (Basin I) **(A-D).** Crystal phases shown are olivine (Ol.) and clinopyroxene (Cpx.). Note a lack of plagioclase in this sample, which is only present in the groundmass.

4.2.3 Type 3 (olivine, plagioclase and clinopyroxene phyric)

Type 3 rocks are the most abundant variety sampled from the basins in this study. This type consists of olivine + clinopyroxene + plagioclase phenocryst assemblages, varying in proportions, textures and sizes from basin to basin. Type 3 rocks consist of 10-25% phenocrysts, 40-60% groundmass, and 30-50% vesicles. Olivine (30-50%) and plagioclase (45-65%) are the dominant phenocrysts in all samples with up to 10% of the crystal assemblage being clinopyroxene. The Type 3 samples differ from type 1 in the overall groundmass, vesicle and phenocryst abundance. Type 1 rocks contain a very small amount of clinopyroxene. While type 3 rocks contain a combination of larger phenocrysts, a higher abundance of clinopyroxene and larger glomerocrysts. Five samples were

described from basins (C, I, K, and E). Examples of photomicrographs of Type 3 rocks are shown in Figure 4.14.

Olivine phenocrysts occur in a variety of shapes such as; well-formed subhedral to euhedral phenocrysts, skeletal, dissolved and compositionally zoned phenocrysts. The olivine phenocrysts are most commonly <1 mm but range up to 2.5 mm in the northernmost basin, L. Chromium spinel is present in the majority of Type 3 rocks, except samples from basin C, and range between 30-50 μm, occurring within and adjacent to olivine phenocrysts. Recrystallized melt inclusions are present in olivine from all samples, uncrystallised melt inclusions were only observed in sample 11 from basin E. Melt inclusions range in size from 300-400 μm. Olivine phenocrysts commonly occur as clusters and glomerocrysts with clinopyroxene and plagioclase, the entirety of glomerocrysts range in size from 0.5-2.5 mm.

Clinopyroxene phenocrysts comprise 10% of the phenocryst population in Type 3 rocks, ranging in size from 0.2-1.5 mm and occur as tabular and subhedral phenocrysts (e.g. Figure 4.14; D) Simple twinning and opaque inclusions are common features in clinopyroxene phenocrysts.

Plagioclase phenocrysts occur most commonly as acicular, tabular and euhedral phenocrysts, ranging in size from <1 mm to 3 mm. Plagioclase phenocrysts show a range of different textures, twinning, compositional zoning and fragmented rims are common, fractures and dissolution textures are a less common feature and were only found in samples from Basin K (e.g. Figure 4.14; E). Plagioclase phenocrysts commonly occur as clusters and glomerocrysts with olivine and clinopyroxene. Plagioclase clusters range in size up to 3.5 mm.

Groundmass is predominantly comprised of microcrystalline acicular plagioclase, olivine and clinopyroxene, and light-medium brown glass, with minor amounts of Fe-Ti oxides. Black glassy rims are also common in Type 3 rocks.

Figure 4.14: Photomicrographs in cross polarised light of representative phenocrysts from various samples.

Crystal phases shown are olivine (Ol.), clinopyroxene (Cpx.) and plagioclase (Plag.) and groundmass texture (G-mass texture). **A)** Sample TAN1213-50-1 (Basin C) note phenocrysts are small and are present mainly as glomecrysts. **B) And C)** Sample TAN1213-50-3 note zoning in plagioclase phenocryst (B) and large plagioclase phenocryst (C). **D**) Sample TAN1513-041-03 (Basin I) note large glomerocrysts of clinopyroxene and olivine. **E)** Sample TAN1512-DR10-2 (Basin K) note large plagioclase glomerocrysts. **F)** Sample TAN1213-11-1 (Basin E) note lack of large plagioclase phenocrysts in this sample.

4.2.4 Type 4 (orthopyroxene bearing)

Type 4 rocks were documented from three of the basins (A, E and G). This type is distinguished by minor orthopyroxene in the phenocryst assemblage, in addition to olivine, clinopyroxene and plagioclase, and the presence of amygdales within vesicles. Phenocryst proportions range from 10-30%, groundmass 30-45%, and vesicles 40-65%. Sizes and textures of phenocrysts vary from basin to basin. Plagioclase and olivine dominate the phenocryst assemblage in Type 4 rocks, with 40-75% plagioclase, 20-55% olivine, 10-15% for clinopyroxene and <5% for orthopyroxene. Examples of photomicrographs of Type 4 rocks are shown in (Figure 4.15)

Olivine phenocrysts range in habit, size, and texture between basins. Phenocrysts in samples from basin A occur as well-formed euhedral to circular crystals. Olivine commonly feature as glomerocrysts with acicular and tabular plagioclase. Olivine phenocrysts range from 0.5-1 mm. Chromium spinel, and recrystallized melt inclusions are common in basin A olivines. Sizes of melt inclusions range 100 μm to 1000 μm.

Olivine phenocrysts in samples from basin A display a variety of shapes including euhedral, equant, and skeletal (e.g. Figure 4.14; C; D; H). Phenocrysts range in size from 0.5-1.5 mm, a large proportion of phenocrysts are broken. Glomerocrysts are common, and occur with olivine and acicular plagioclase, ranging in size up to 0.7 mm. Chromium spinel inclusions are common and range in size up to 60 μm.

Olivine phenocrysts in sample 10-2, from basin E, occur as both subhedral and skeletal crystals, ranging in size from 0.5-1 mm. Glomerocrysts are less common and occur with acicular plagioclase, ranging in size up to 0.7 mm. Chromium spinel inclusions are common.

Olivine phenocrysts in sample 47-2, from basin G commonly occur as subhedral to euhedral, and skeletal crystals, ranging in size from 0.5-1.5 mm. Chromium spinel inclusions are common within olivine phenocrysts, and range in size up to 70 μm. Melt inclusions were not observed in this sample.

Plagioclase phenocrysts also show a wide range of habit, size and texture between basins. Phenocrysts in samples from all three basins occur as acicular, euhedral and tabular crystals with simple and multiple twinning. Few phenocrysts show compositional zoning and dendritic patterns. However, dissolution textures are a more common feature in Type 4 rocks (e.g. Figure 4.2.4; B and F). Plagioclase phenocrysts range from 0.5-1 mm.

Clinopyroxene phenocrysts (<0.5-7 mm) occur as tabular, equant and skeletal crystals. Few clinopyroxene form glomerocrysts, which range in size from 0.5-1 mm.

Orthopyroxene phenocrysts occur as subhedral-euhedral crystals, 0.5 mm in size, and rarely contain opaque inclusions (e.g. Figure 4.15; A).

Type 4 rocks groundmass consists of microcrystalline acicular plagioclase, minor olivine and pyroxenes, and medium-light brown glass. Black glassy rims are present on basin A samples. Vesicles from basin G samples are large ranging up to 1.5 mm in size and are the largest of all Type 4 rocks. Scattered amygdales are present in samples 3-5 from basin A and 47-2 from basin G in the interior of vesicles and secondary fractures.

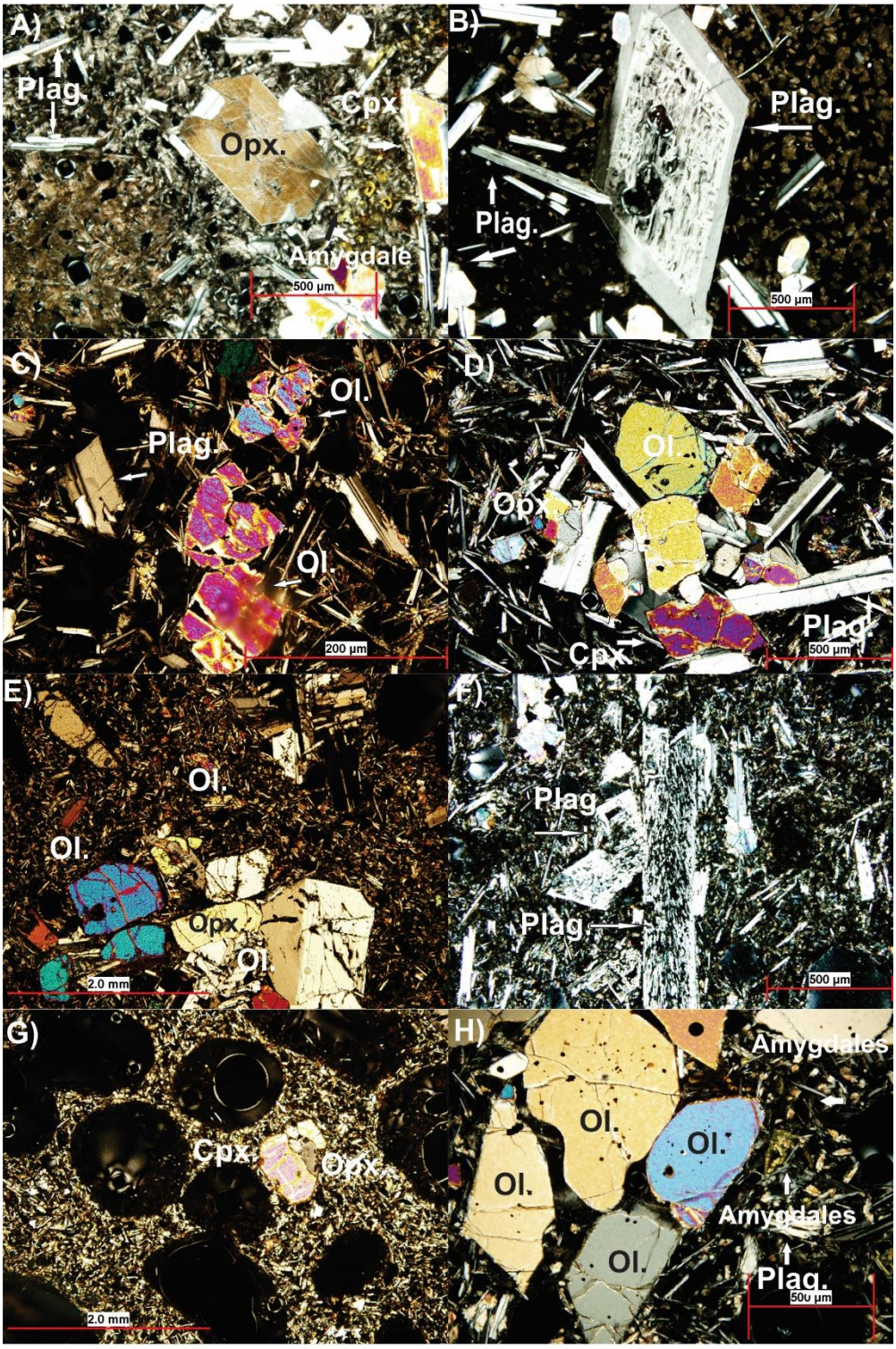

Figure 4.15: Photomicrographs in cross polarised light of phenocrysts in various samples.

Crystal phases shown are olivine (Ol.), plagioclase (Plag.), clinopyroxene (Cpx.), and orthopyroxene (Opx.) **A and B)** Sample *TAN1213*-3-5 (Basin A) note moth eaten texture and zoning in plagioclase (B). **C and D)** Sample *TAN1213*-006-3 (Basin A). **E and F)** Sample *TAN1213*-10-1, 10-2 (Basin E) note sieve-like texture in plagioclase (F). **G and H)** Sample *TAN1213*-47-2 (Basin G) note size of vesicles in (G).

4.3 Whole rock major geochemistry

Major element data for each sample are presented in Appendix B and trace element data in Appendix C. The key features of the data are summarised in the following sections.

4.3.1 Classification of back arc lavas

The Havre Trough back arc basin samples are basalts (i.e. ca. 46-53 wt. % SiO_2) except for two samples from basin A and C that are basaltic-andesitic in composition as defined on the total-alkali-silicon (TAS) diagram (Figure 4.16; Le Maitre et al., 1989).

The key difference amongst the various basins is that the eastern basins' (B, C, E, and G) lavas are all more evolved (SiO_2 50.5-53 wt. %) than the central basins' (A, D and I) (47-52 wt. %) and western basins' (H, J and K) (SiO_2 46-50 wt. %). Basalts from all basins show typical fractionation trends with a positive correlation between K_2O wt. % and SiO_2 wt. % and all plot within the low-K series, showing a range in K_2O from ca. 0.2-0.7 wt. % (Figure 4.17). Samples from basin A (006) and basin C (50) have higher Na_2O+K_2O and are more evolved relative to basin B, G and E with similar SiO_2 contents. Basin K has higher Na_2O+K_2O values relative to basin I, J and D for similar SiO_2 contents.

Central and eastern basin lavas (A, B, D, E, G and I) are lie along the boundary between tholeiitic and calc-alkaline compositions whereas western and south eastern basin samples (C, H, J and K) plot more clearly within the tholeiitic field (Figure 4.18).

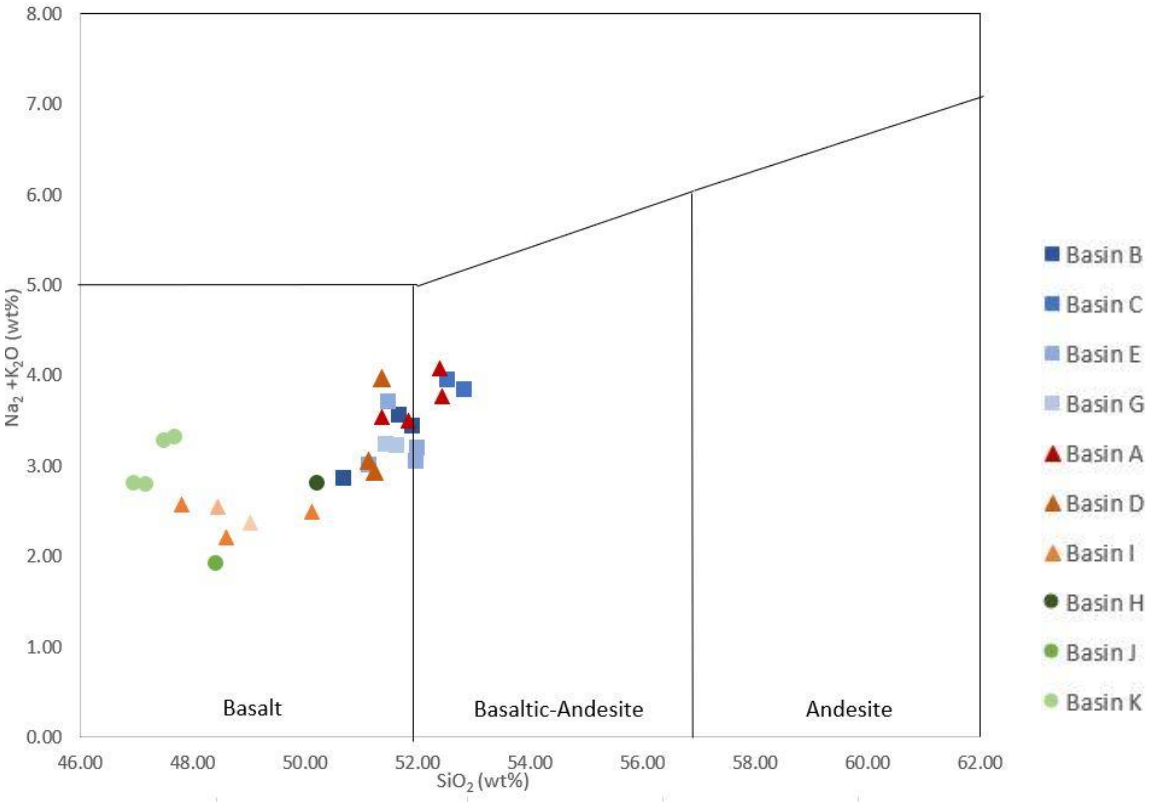

Figure 4.16: Plot showing whole rock wt. % of total alkali (TAS) of lavas in this study. Compositional boundaries come from Le Maitre et al. (1989).

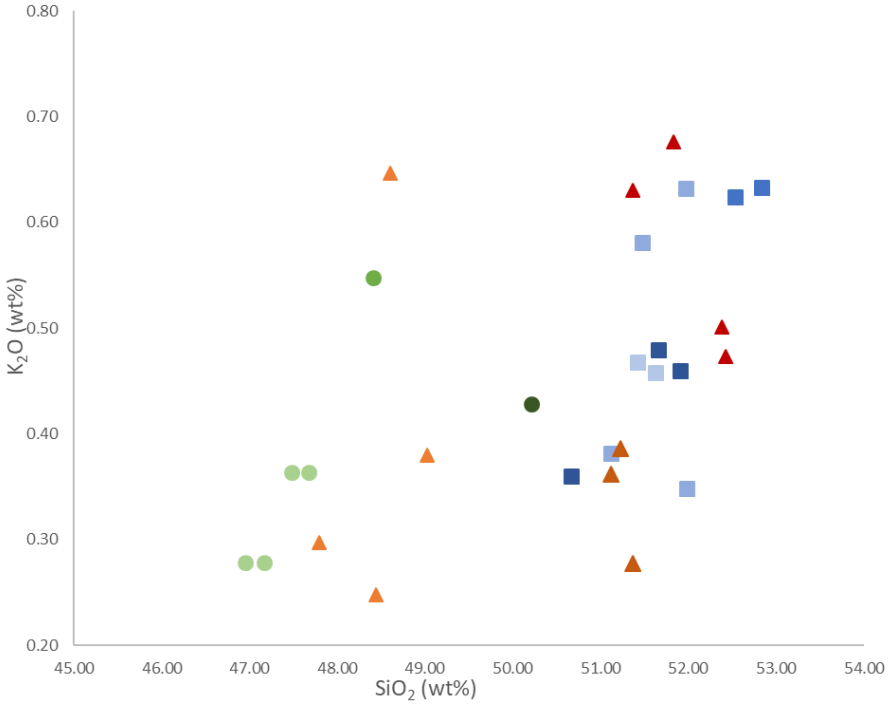

Figure 4.17: Diagram showing the range in SiO2 vs K2O contents from individual samples from each basin. Compositional boundaries were taken from Miyashiro. (1974).

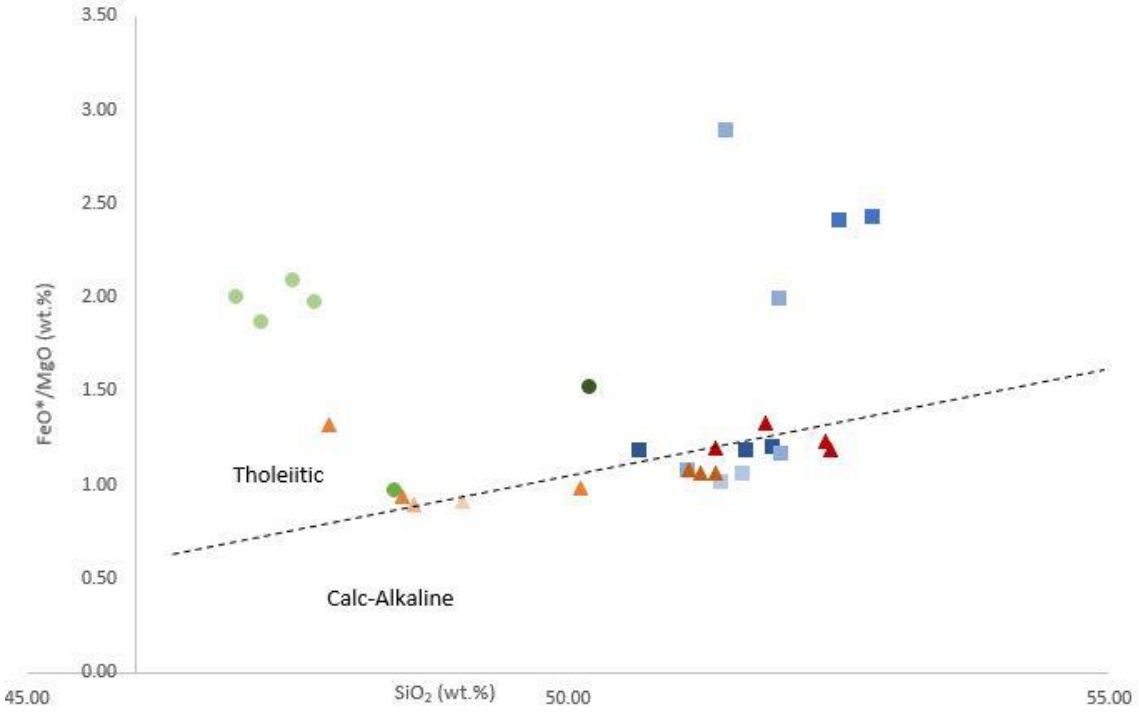

Figure 4.18: Diagram showing SiO_2 vs FeO/MgO (wt. %) for individual samples from each basin. The dashed line delineates the boundary between calc-alkaline and tholeiitic groups. Boundaries were taken from Miyashiro. (1974). Symbols are the same for all plots.

4.3.2 Major element characteristics

In general, the samples from all basins display broad trends of increasing SiO_2 concentrations with decreasing MgO concentrations (e.g. Figure 4.19). However, basalts from Basin K differ from this with low SiO_2 and low MgO concentrations. This basin lies in the western Havre Trough, close to the Colville ridge and is the northernmost basin analysed in this study.

All TiO_2 contents increase with decreasing MgO contents, the highest value is observed in basins close to the Kermadec Arc (basin C, E and A) (e.g. Figure 4.19). All basins show a slight decrease P_20_3 content with decreasing MgO contents. However, Basin K, the northernmost basin contains the highest P_20_5 concentrations (e.g. Figure 4.19).

The observed trend for Na_2O shows increasing concentrations with decreasing MgO contents. Eastern basins, with exception of basin A and basin K, all exhibit the highest Na_2O contents relative to central and western basins. Central basins (D and I) show a systemic decrease in Na_2O with increasing distance away from

the arc front (e.g Figure 4.19). All K_2O concentrations show a positive correlation with increasing SiO_2. The highest K_2O concentrations are observed in eastern basins C and E, which are close to the Kermadec Arc (e.g. Figure 4.19). All basins show a general increase in Al_2O_3 with decreasing MgO concentrations and basins that are in the southern and eastern side of the Havre Trough show higher Al_2O_3 values (e.g. Figure 4.19).. There are two general trends for CaO concentrations these are, a decrease in concentration with decreasing MgO contents and samples from western basins have higher CaO at a given MgO compared with the eastern basin lavas (e.g. Figure 4.19). All samples show a trend of increasing Fe_2O_3 concentrations with decreasing MgO concentrations with western basins exhibiting lower TiO_2 contents for a given MgO (e.g. Figure 4.19).

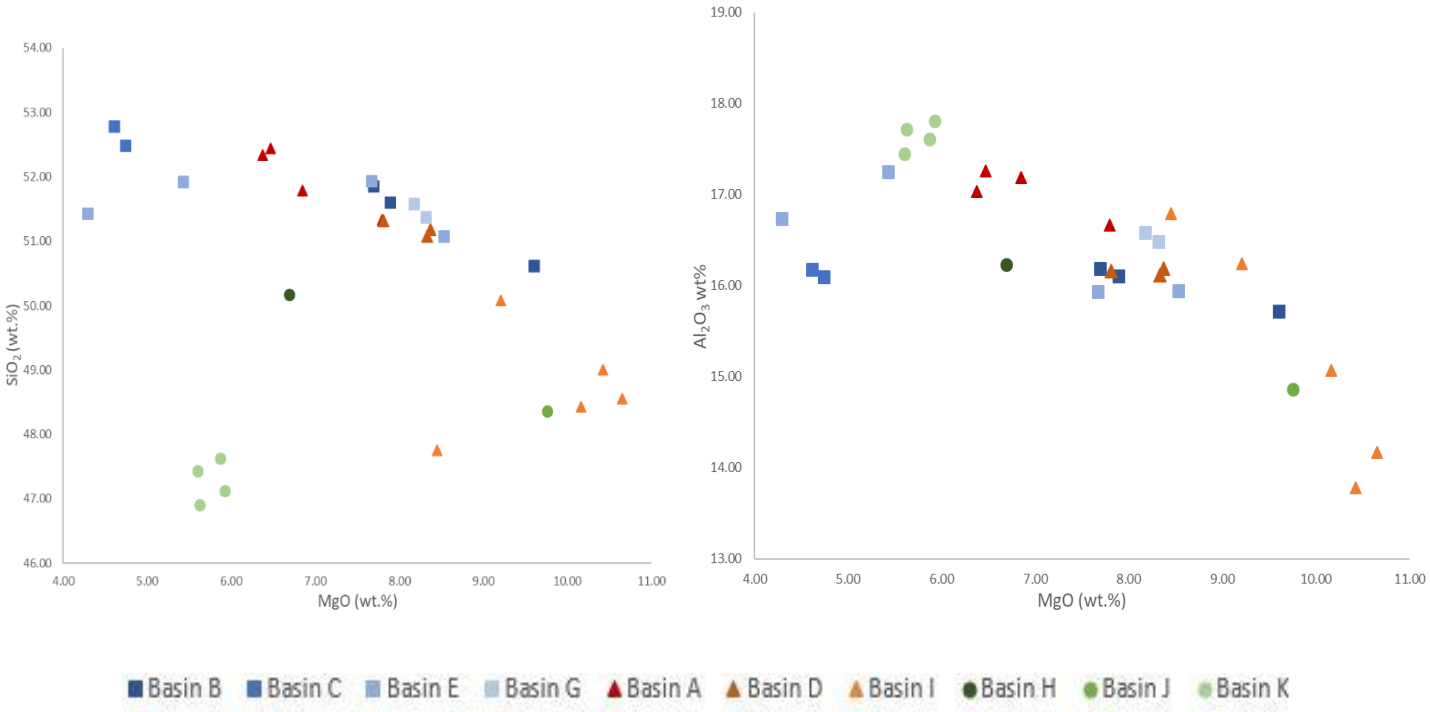

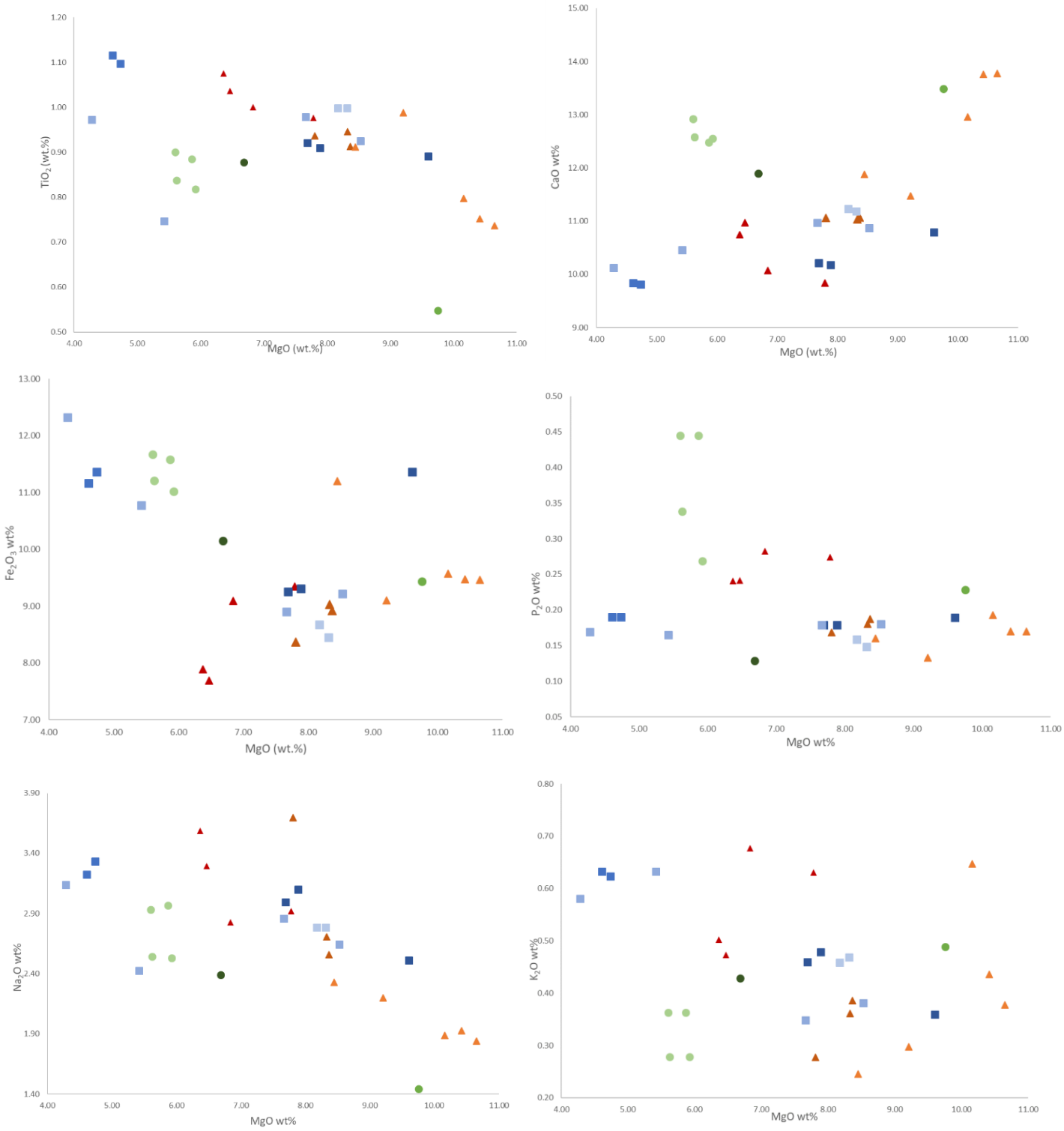

Figure 4.19: Plots showing variation in major element oxides for all basin samples. Symbols for all basins are the same.

4.4 Whole rock trace element geochemistry

All samples analysed in this study are characterised by greater concentrations in LILE, which are fluid-mobile (e.g. Cs, Rb, Ba, U, Pb and Sr), and LREE with respect to N-MORB values (Figures 4.20). All samples show lower concentrations in HFSE (e.g. Nb, Zr, Hf and Ta) and HREE when compared to LILE and LREE. These trace element patterns are typical subduction-modified arc magma trends (e.g. Pearce and Peate, 1995). Western basin lavas are overall more enriched in all elements when compared to eastern and central basin lavas. Central basin lavas show a larger Nb and positive Eu anomaly when compared to N-MORB, eastern and western basin lavas. All basins correlate well on a REE plot and show a shallow chondrite/rock REE pattern (e.g. Figure 4.21). Basalts from the western basins are slightly LREE depleted (relative to MREE) in contrast to eastern samples which are moderately LREE enriched – this is illustrated best with ratios: $(La/Yb)_n$ (2.1-3.7 for eastern samples, 3.2-10.14 for central samples and 2.5-7.6 for western samples).

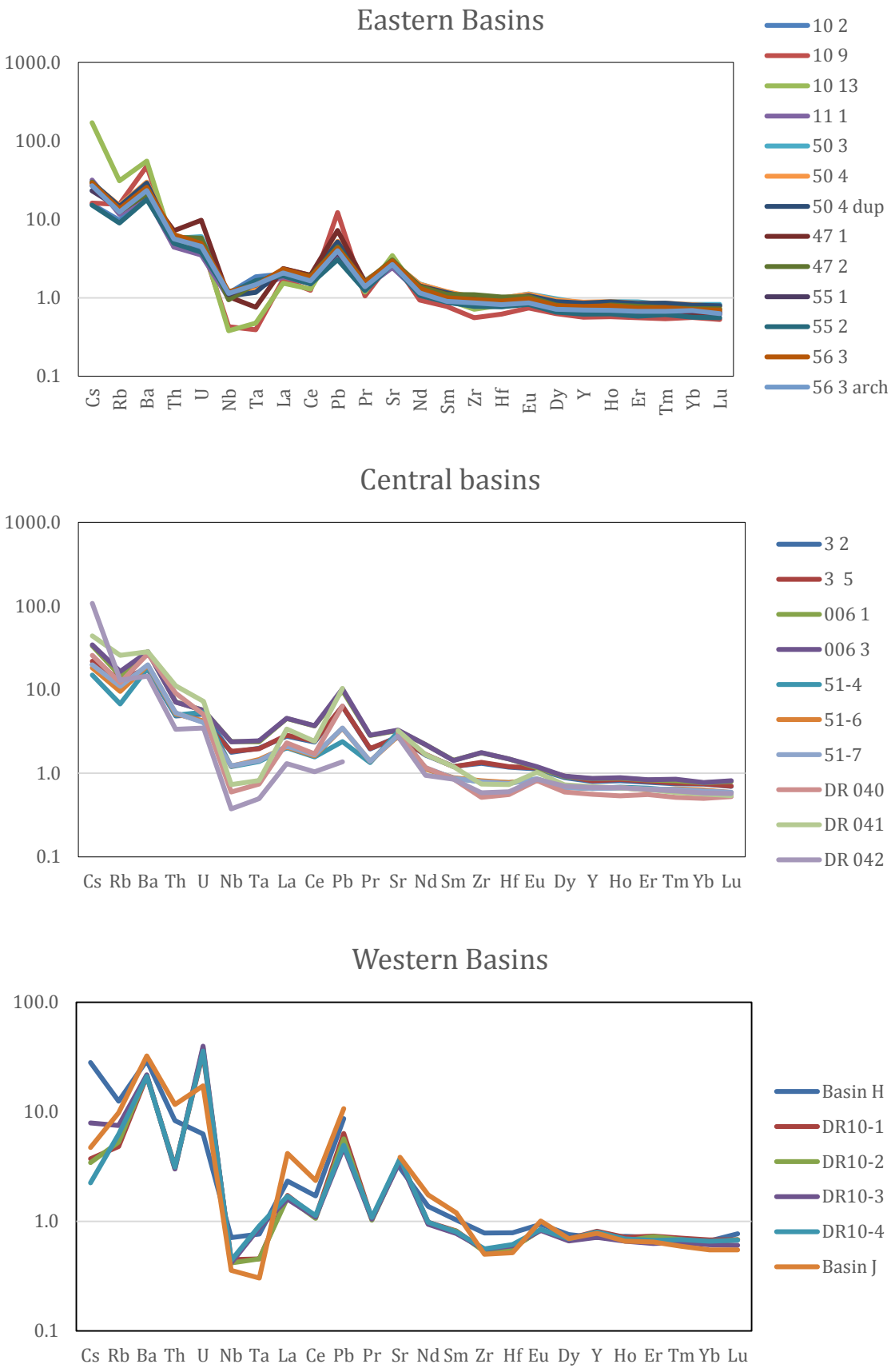

Figure 4.20: N-MORB normalised multi-element plot of all basin samples grouped as eastern, central and western basins. N-MORB values were obtained from Sun and McDonough. (1989).

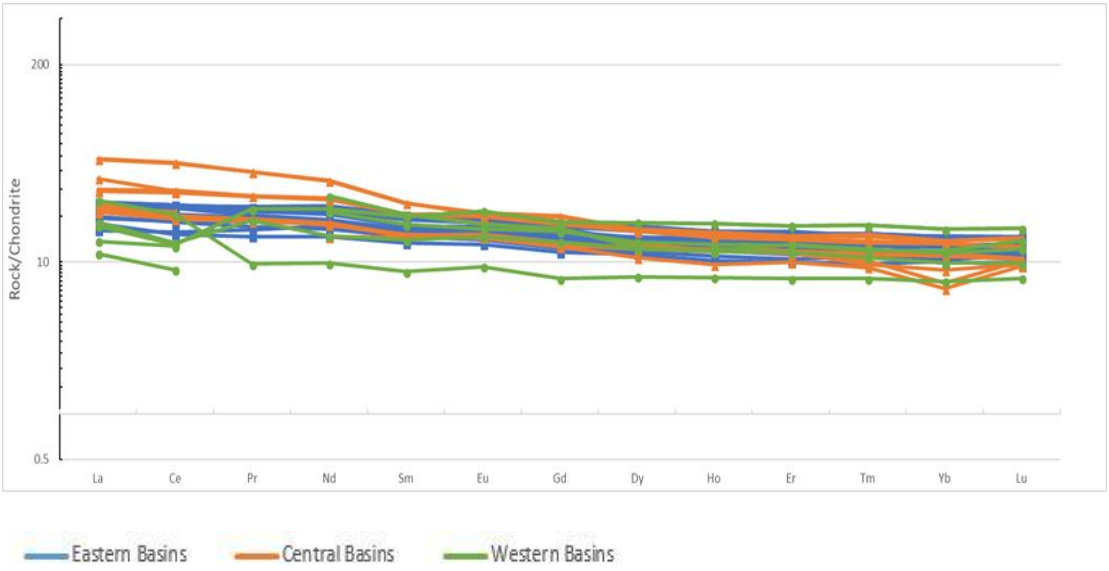

Figure 4.21: Chondrite normalised REE plot of all basin samples. N-chondrite values were obtained from Sun and McDonough. (1989).

Trace elements that generally behave compatibly in mafic magmatic systems (e.g. Cr, Ni) show strong positive correlations with MgO, with increasing scatter observed at higher MgO contents (e.g. Figure 4.22). By contrast, incompatible trace elements (e.g. Pb, La, Yb and Hf) show more scatter versus MgO and trends are less clear (e.g. Figure 4.22).

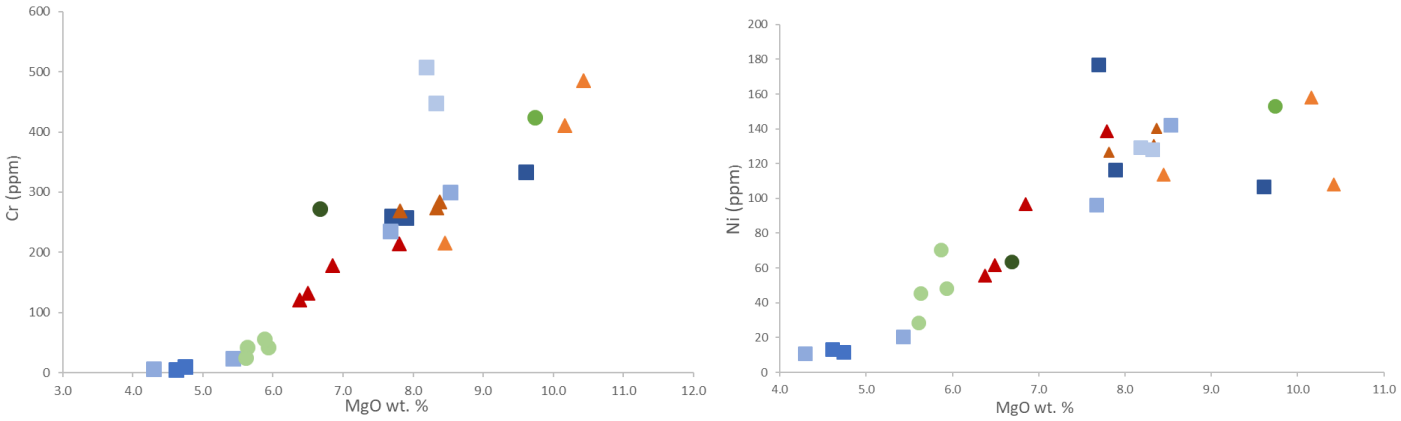

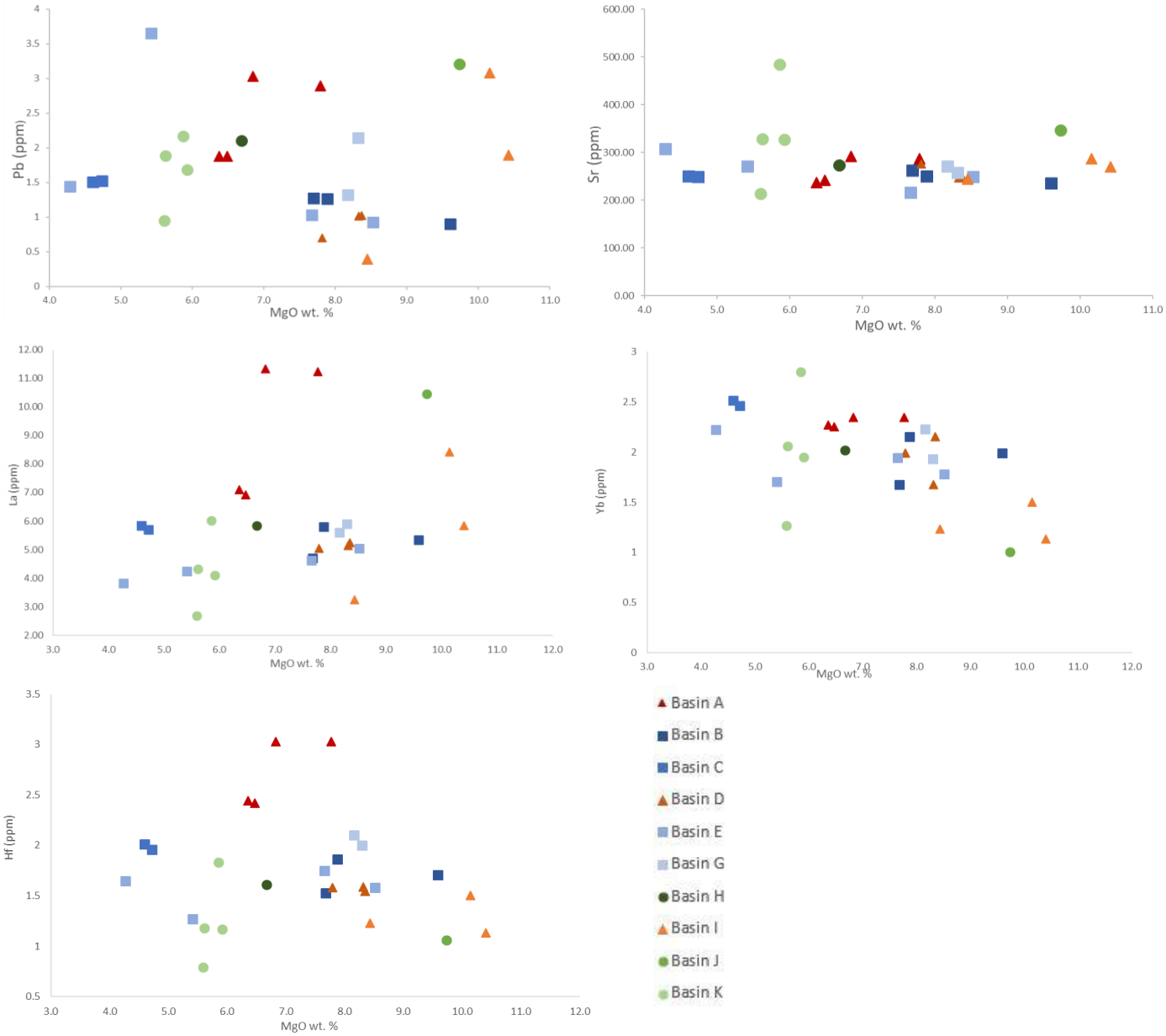

Figure 4.22: Plots showing selected trace element concentrations against MgO content of samples from all basins.

4.5 Mineral chemistry

Table 4.2 lists the samples for which phenocryst assemblages were analysed for major element compositions and the full data are given in Appendix D. Descriptions of each analysed crystal phase are given in the following sections.

4.5.1 Olivine

The majority of the olivine phenocrysts contain spinel inclusions, recrystallized melt inclusions, with rare uncrystallised glassy inclusions. Compositional zoning is present in most olivine phenocrysts, where cores are Mg-rich and range in composition from 42-49 MgO wt. % and 34-38 MgO wt. % seen in samples from Basin C, and rims are Fe-rich ranging between 10-28 FeO wt.% (Figure 4.23). Olivine phenocrysts show Fo contents ranging between Fo_{65-90}, with the majority ranging between Fo_{75-90}, except for the southernmost basins A and B which range down to Fo_{65-70} content, and the highest Fo content seen in samples from basin, B, E, G and I Fo_{88} (Figure 4.24). All basins generally exhibit a consistent increase in Fo content with increasing whole rock Mg#.

In general olivine phenocrysts display positive NiO trends when plotted against Fo content (Figure 4.25), all basins follow this trend expect for basin C that has very low NiO content (0-10 wt.%) and the highest seen in samples from basin A (0.37 wt.%). When plotting Fo content against CaO wt% (Figure 4.26) majority of the basins show the same concentration in Cao ranging between 0.13-0.60 wt.%. Basin I from across the back arc is slightly more enriched overall in CaO than the other basins analysed.

Table 4.0-2: Mineral assemblages for each basin and whole rock MgO wt. %

Sample	Whole Rock MgO (wt. %)	Mineral assemblage
Basin A (3-5)	6.36	Olivine+ clinopyroxene
Basin A (006-3)	6.83	Olivine+ spinel
Basin B (55-2)	9.59	Olivine+ clinopyroxene+ spinel
Basin B (56-3)	7.68	Olivine+ clinopyroxene+ spinel
Basin C (50-3)	4.59	Olivine+ clinopyroxene
Basin D (51-4)	7.80	Olivine+ clinopyroxene+ spinel
Basin E (10-2)	8.51	Olivine+ clinopyroxene
Basin E (11-1)	7.65	Olivine+ clinopyroxene+ spinel
Basin G (47-1)	8.3	Olivine+ clinopyroxene+ spinel
Basin G (47-2)	8.16	Olivine+ clinopyroxene+ spinel
Basin I (040-2)	10.40	Olivine+ clinopyroxene
Basin I (041-3)	10.14	Olivine
Basin K (DR10-2)	5.61	Olivine

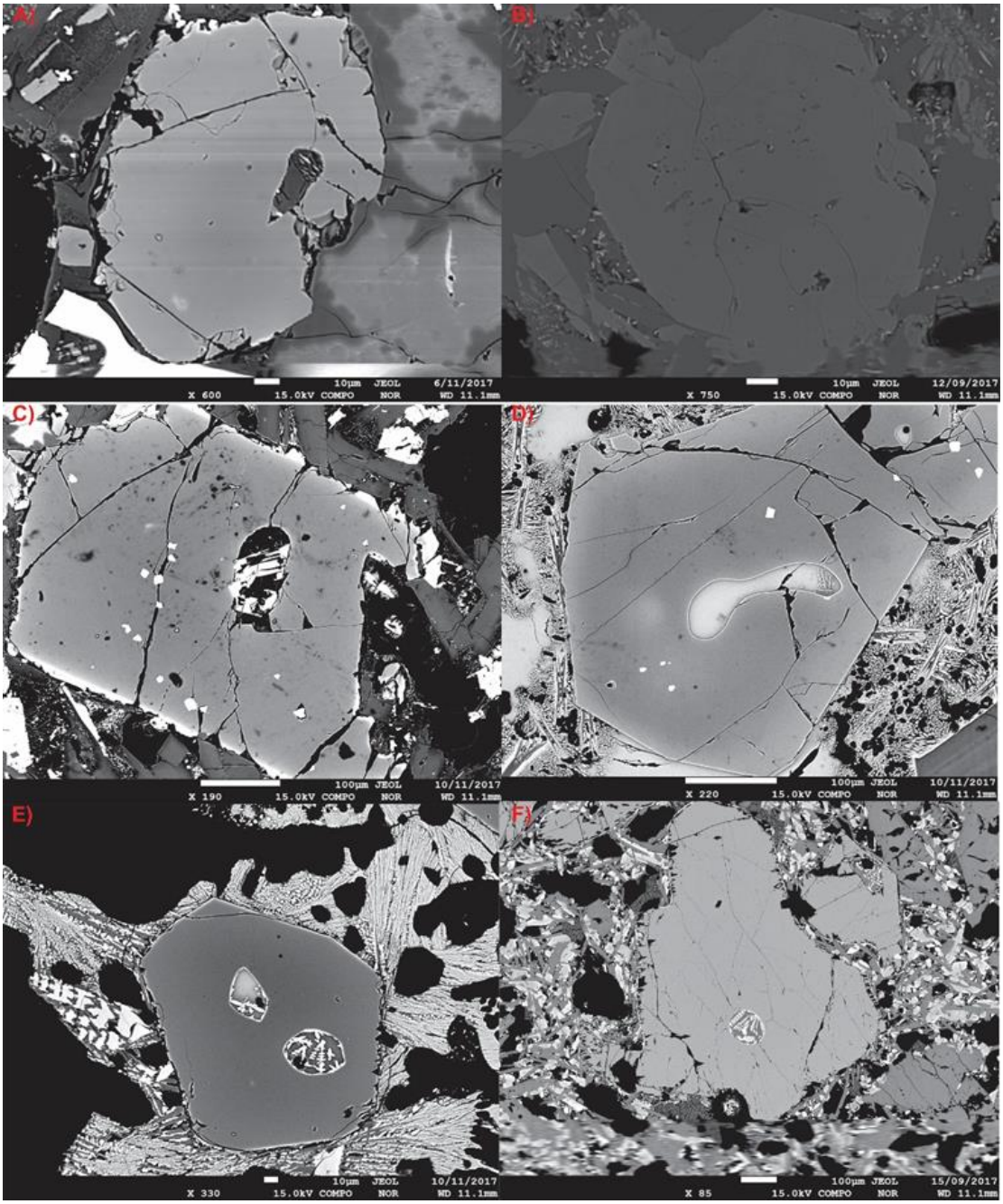

Figure 4.23: Back-scattered electron images (BSE) of olivine phenocrysts found in basin samples **(A)** TAN1213-50-3, note recrystallized melt inclusion within olivine phenocryst. **(B)** TAN1213-10-2, **(C)** TAN1213-11-1, note small spinel inclusions and large recrystallized melt inclusion within olivine phenocryst **(D)** TAN1213-47-1, note large melt inclusion and small spinel inclusions **(E)** TAN1513-040, note two large semi and recrystallized melt inclusion and thin Fe-rich rim **(F)** TAN1512-DR10-2, note small recrystallized melt inclusion. Shading in greyscale is relative to compositional changes where lighter shades correspond to higher FeO content in mafic minerals, darker shades represent higher MgO content.

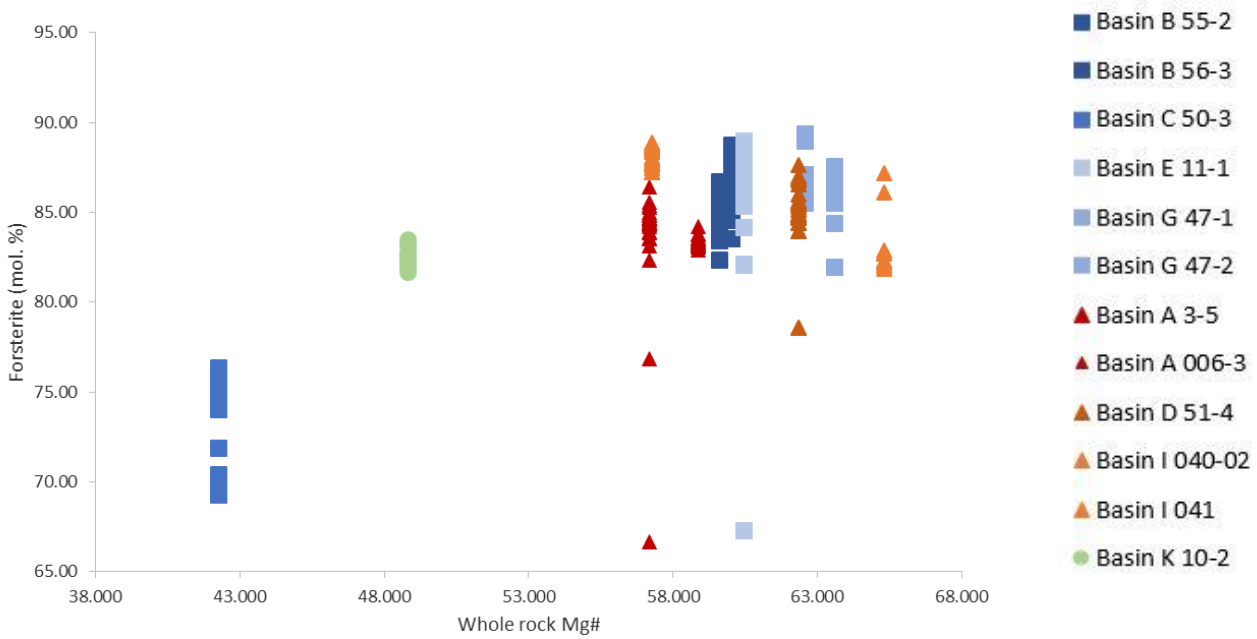

Figure 4.24: Graph showing the relationship between Olivine (Fo) content and whole rock Mg# for back arc basin samples.

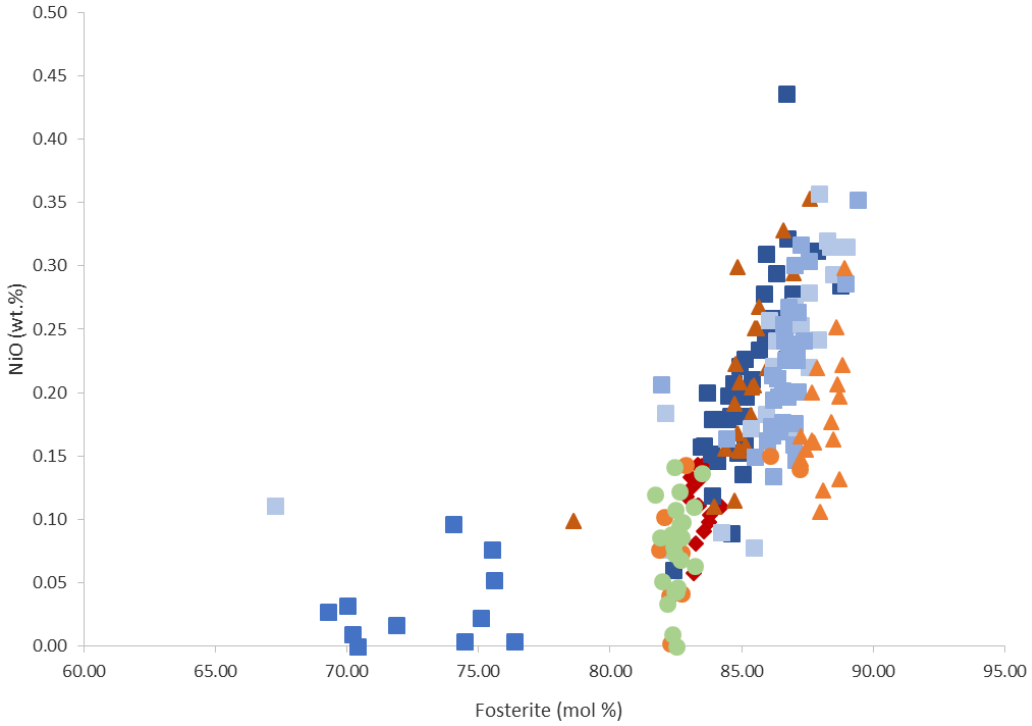

Figure 4.25: Graph showing the relationship between NiO wt. % and Forsterite content for back arc basin samples.

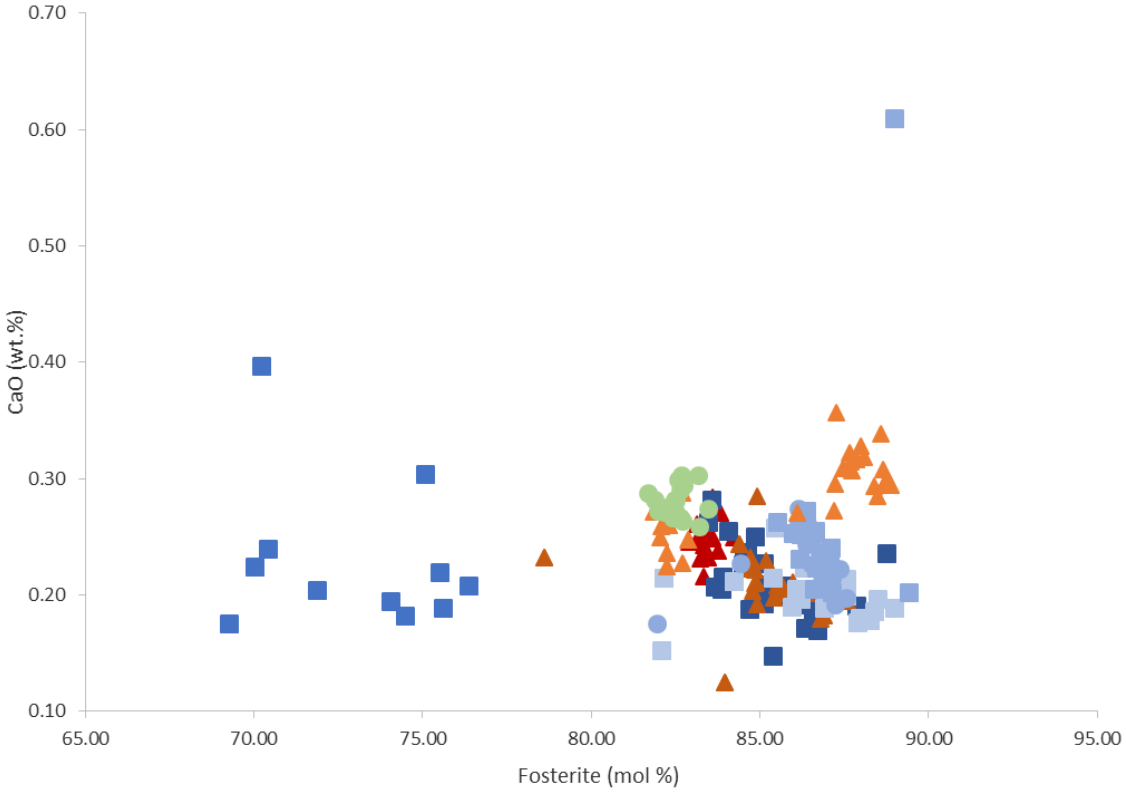

Figure 4.26: Graph showing the relationship between CaO wt. % and Forsterite content for back arc basin samples.

4.5.2 Clinopyroxene

Clinopyroxene phenocrysts often display compositional zoning, where the rims are slightly more enriched in FeO content compared to the cores (Figure 4.27). Clinopyroxene phenocrysts exhibit similar compositions, ranging from $En_{0\text{-}20}$ and $En_{20\text{-}40}$ (from two basins Figure D and E), $Wo_{50\text{-}65}$ $Fs_{30\text{-}50}$ (Figure 4.28). There are two distinctive compositional trends seen in clinopyroxene phenocrysts. The first group are Mg-rich (16-21 wt. % MgO) dominant in samples from basins A, B, C, G, E, I, with lower FeO contents (2-4 wt. %). The second population of clinopyroxene contain lower MgO (8-15 wt. %), and are richer in Fe (3-11 wt. %), present in samples from basins E and K.

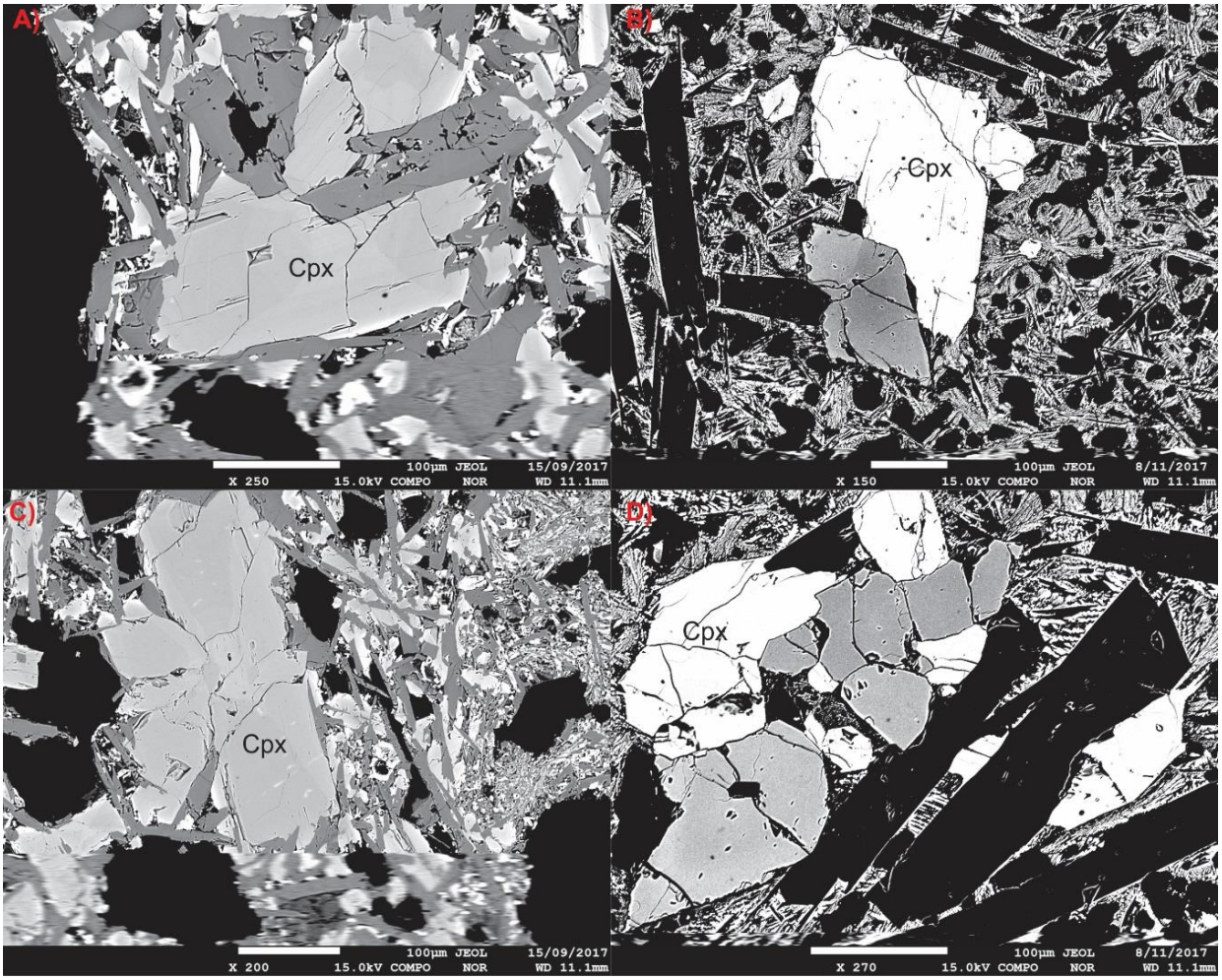

Figure 4.27: Back-scattered electron images (BSE) of clinopyroxene phenocrysts found in basin samples. **(A)** and **(C)** TAN1512- DR10-2 note compositional zoning where rims are slightly lighter **(B)** and **(D)** TAN1213-3-5. Shading in greyscale is relative to compositional changes where lighter shades indicate higher FeO content in mafic minerals and CaO content in plagioclase.

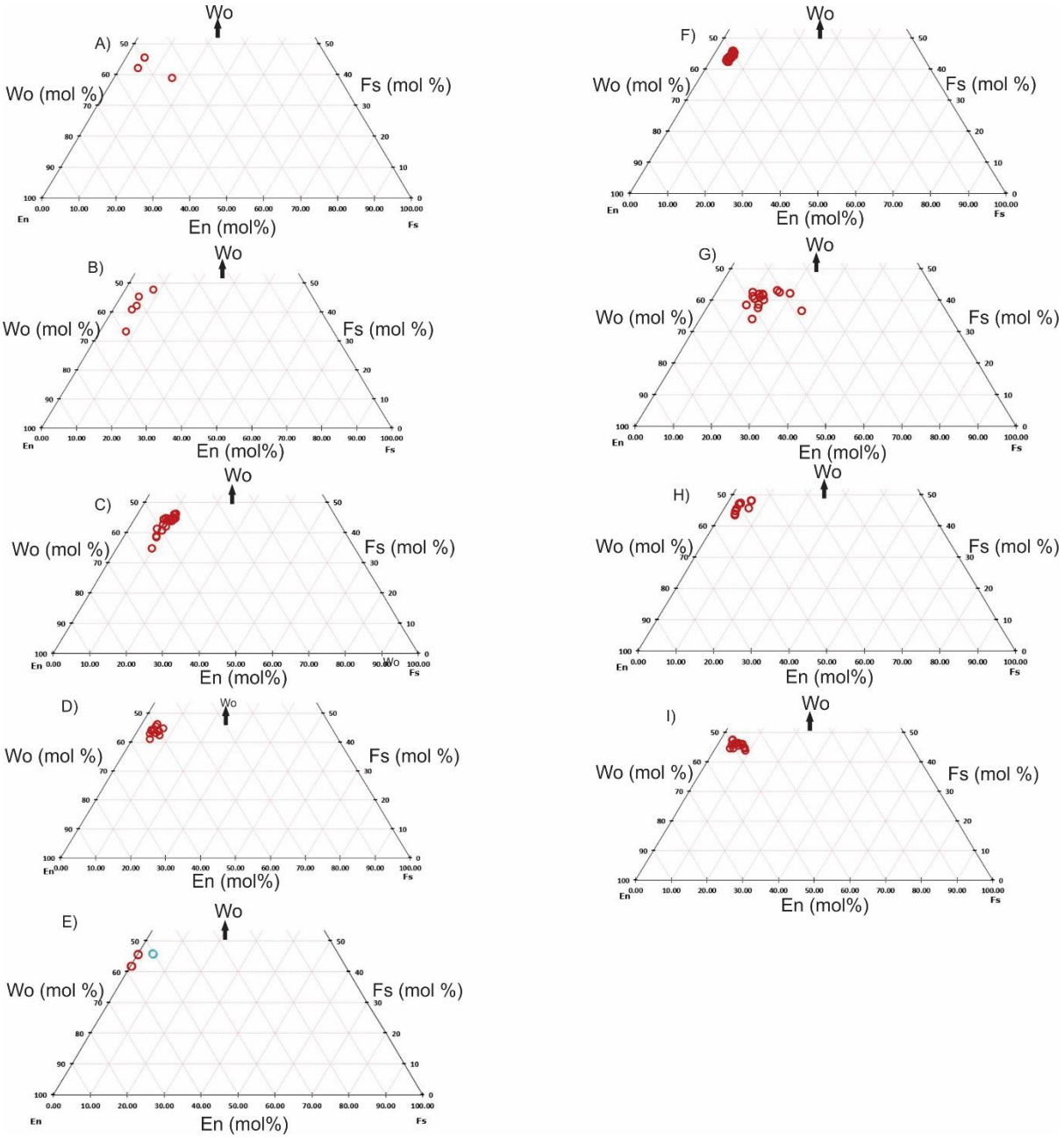

Figure 4.28: Enstatite (En), Ferrosilite (Fs) and Wollastonite (Wo) ternary diagrams stacked by location-south to north. **A)** basin B 56-3, **B)** basin C 50-3, **C)** basin E 10-2, **D)** 11-1, **E)** basin G 47-1 and 47-2 (on the same plot) and east-west across the back arc. **F)** basin A 3-5, **G)** basin D 51-4, **H)** basin I 040 **I)** basin I 041 showing the composition of clinopyroxene phenocrysts in representative samples.

4.5.3 Spinel

Chromium spinel inclusions in olivine are a common feature in back arc samples except for several samples from basins; A (3-5), E (10-2), and K (DR10-2) which contained no spinel inclusions. When comparing Cr# of spinel inclusions in olivines from each basin, samples generally range between 0.55-0.80 Cr# and Fo_{83-88} (Figure 2.29). Overall the most variation in both Cr# and Fo content is seen in central basins. Basin I contain the highest Cr# (0.8-0.75), while the lowest Cr# is seen in samples from basin A and D (Cr# 0.55). Eastern basins show less variation (0.60-0.75).

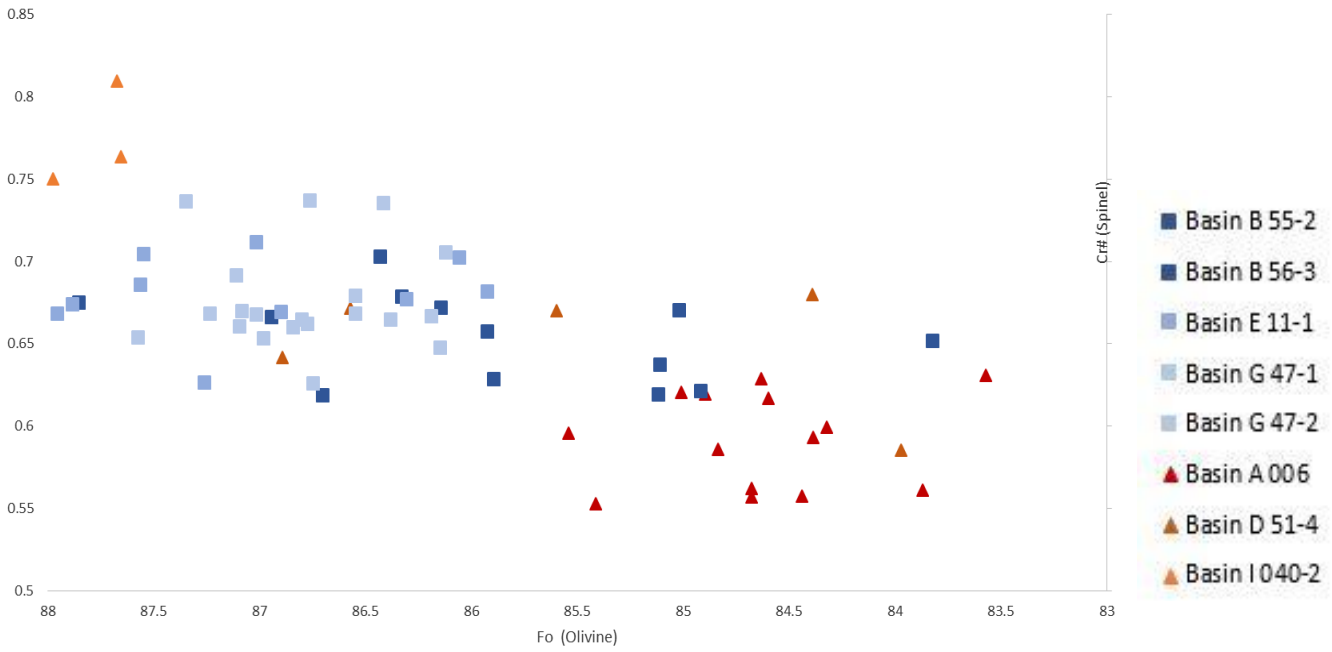

Figure 4.29: Plot showing the relationship between Cr# of spinel and Forsterite content of olivine from several different basins.

Chapter 5:

Discussion

The primary aim of this study is to detail the broad scale geomorphic features of the back arc basins of the Havre Trough and the geochemical composition of the basalts erupted within them. The discussion which follows is in four main sections. First, the morphologies within the basins are described, including their relationship to the structural regimes previously proposed for the Havre Trough. Second, the magmatic processes and potential mechanisms for generating the sampled back arc lavas are discussed, including comparisons between basin locations and with other features within the back arc. Third, the influence of slab derived components on the back arc mantle is considered and how this may vary along and across the back arc. Fourth, the composition of the ambient mantle wedge (the composition of the mantle prior to the addition of subduction components) and the source of the back arc magmas are discussed. Finally, these four components are summarised using a tectono-magmatic model.

5.1 Basin morphology

The perimeters of each basin appear to be relatively well defined in the high-resolution bathymetry maps of the Havre Trough. However, when considering the slope maps, these boundaries become less distinct and the fabric of structures throughout the back arc appear more pervasive, even cutting through and across apparently distinct basins. From the slope maps, there are no clear distinctions where basins start, or end and a large proportion of basins appear to continue into each other, particularly on the eastern side of Havre Trough. Therefore, defining the exact location and size of basins within the Havre Trough is complex.

A combination of ridges, cones, and basin floors comprise the basins, but the proportions of each vary between each basin and are unevenly distributed. There is a strong structural and magmatic control for the abundance and types of morphologies present in each basin. Rifting and/or spreading in the back arc has

been proposed previously to occur in a disorganised manner (Wysoczanski et al., 2010). Where there is a high abundance of ridge and cone morphologies in basins, this may reflect more volcanically active areas where multiple episodes of pervasive magmatic intrusions through thinned and weakened crust have occurred, and/or reflect changes within the mantle wedge as the subduction influence varies across the back arc (Dunn and Martinez, 2011). Basins that lack or contain minimal structures may reflect either zones of higher sedimentation cover or variations in the mantle wedge which control the amount of partial melting beneath basins.

Despite consistent NW-SE structural trends across the back arc, when looking at slope maps basins C and E appear to trend NE-SW. This apparent orientation may be an artefact of the ridge and cone morphologies that occupy, and cross cut these basins, causing the basins to appear to trend in the opposite direction (Figure 5.1).

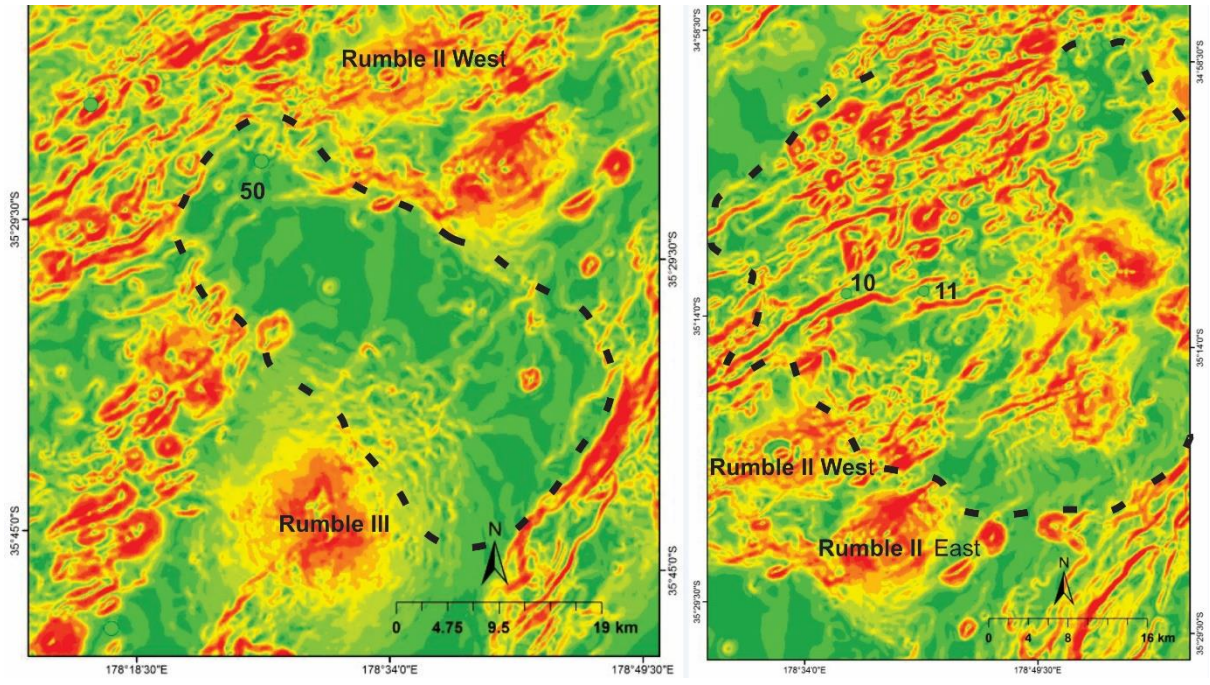

Figure 5.1: Slope maps showing E-W orientation of basin C (left) and basin E (right). Sample numbers and neighbouring volcanoes are also indicated.

The structural fabric of the Havre Trough has been previously divided into two regimes that alternate throughout the back arc (Wysoczanski et al., 2010). A rift regime is characterised by deep basins and ridge formation and is associated with rifting and decompression melting. An arc regime is defined by thicker crust and constructional edifices (e.g. back arc stratovolcanoes, cross arc chains such as the Rumble V ridge) and characterised by arc-like magmatism with variable additions of subduction related slab derived components (Wysoczanski et al., 2010; Todd et al., 2011). Within the back arc, segments of rift regime (pull-apart basins) and arc regime (arc-like volcanic constructs) alternate at approximately 100 km intervals and have been proposed to reflect a NW-SE variation in melt productivity (Wysoczanski et al., 2010; Todd et al., 2010; 2011). In other settings such as NE Japan, a hot finger model has been suggested in order to explain the formation of a series of cross-arc chains, where mantle melting and magma production is controlled by hot regions within the mantle wedge at 50 km intervals (Tamura et al., 2002). Todd et al (2011) suggested that arc-type basalts forming constructional edifices crossing the Havre Trough perpendicular to the front are also the result of thermal anomalies in the mantle wedge.

All basins examined in this study lie within the areas distinguished as rift regime, except for two basins (J and G), which lie within an arc regime. Basin J is in close proximity to constructional edifices Gill and Rapuhia volcanoes, and basin G lies at a similar latitude to Gill, Rapuhia and Giljanes volcanoes. Of the basins examined, basins G and J have the highest proportion of cones (30% of total area in basin G and 25% of the total area in basin J) (refer to table 4.1), which may be due to a higher melt productivity associated within the arc-regime and associated constructional features.

Basins on the western side of the Havre Trough (e.g. basins H, J and K) appear to be broader and longer than the eastern basins (e.g. basins B, E, and G) and contain significantly less ridge and cone morphologies (< 5-30% of the total area, versus 5-85% of the total area). This may be an artefact of higher sediment cover for these basins. Wider and more continuous ridge segments characterise the eastern basins in comparison with the western basins. The eastern basin ridges have similar orientations to the arc front at 045°, but also range from 040-060°

predominantly in basins C, E and G, and are of moderate size (up to 100 m high, 13 km long and 5 km wide). Ridges are less prevalent in the western basins and are short (<5 km long), discontinuous and appear to be deformed (e.g. Figure 5.2). The distances between ridges are wider in the western basins compared with those in the east.

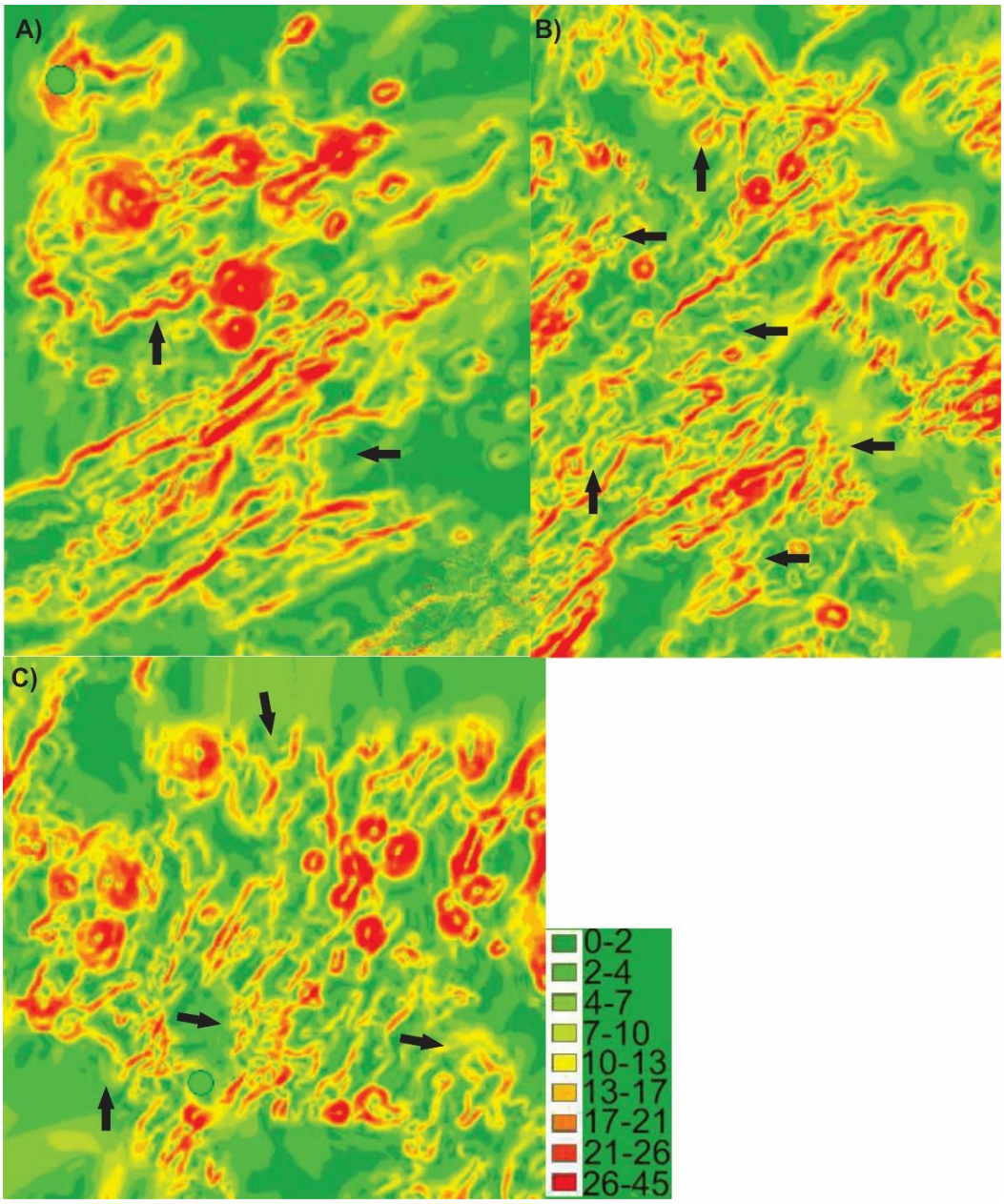

Figure 5.2: Slope angle maps showing deformed ridges in western basins **A)** is basin H **B)** is basin J and **C)** is basin K.

Cones and knolls within basins (not including back arc stratovolcanoes) are also less prevalent in the western basins. Those that are present are relatively large (60-70 m high and 1-5 km wide) and generally form in clusters. Ridges generally comprise the edges of the cones and also connect several cones together in clusters. This suggests that ridges may initially develop in zones where there may be more rifting or the structure of the crust (i.e. thinner) and more partial melting of the mantle has allowed pathways for magmas to ascend easier and over time, through repeated episodes of volcanism, constructional volcanoes or volcanic highs have developed in the centre of the ridges.

Studies which was analysed the structure and composition of ridges in the back arc (e.g., Wysoczanski et al., 2010) have inferred that ridges may reflect dyke systems which have penetrated and replaced the original arc crust with newly accreted intrusives. Leading the authors to suggest that the Havre Trough back arc crust is composed of extended arc basement that has been pervasively penetrated by basaltic intrusives (Wysoczanski et al., 2010).

The western basins also appear to be more thickly sedimented than the eastern basins. Seismic reflections running north from the Ngatoro basin (Line 7; Figure 5.3) show a flat seafloor which is underlain by a sedimentary sequence comprised of 3 units. 1) An uppermost unit that is highly stratified and approximately 350 m thick. 2) A thin acoustically transparent layer. 3) The lowest unit which is incoherent and overlies an acoustic basement (Wysoczanski et al., 2015). Within the seismic profile along line 7 (Figure 5.3), sedimentary Unit 1 appears to be relatively deformed and most of the upper two units are missing in the Ngatoro Basin. A series of blocks are down faulted to the east delineating the transition from the Ngatoro basin to the Colville basin where both upper units return. At the end of the seismic line, the profile shows a well layered sedimentary sequence that is approximately 450 m thick. (Wysoczanski et al., 2015). The seismic profiles for the Colville basin (e.g. line 8 Figure 5.3) show a highly stratified upper sedimentary unit, approximately 450 m to 1 km thick, and 2) a lower unit which onlaps onto an acoustic basement (Wysoczanski et al., 2015).

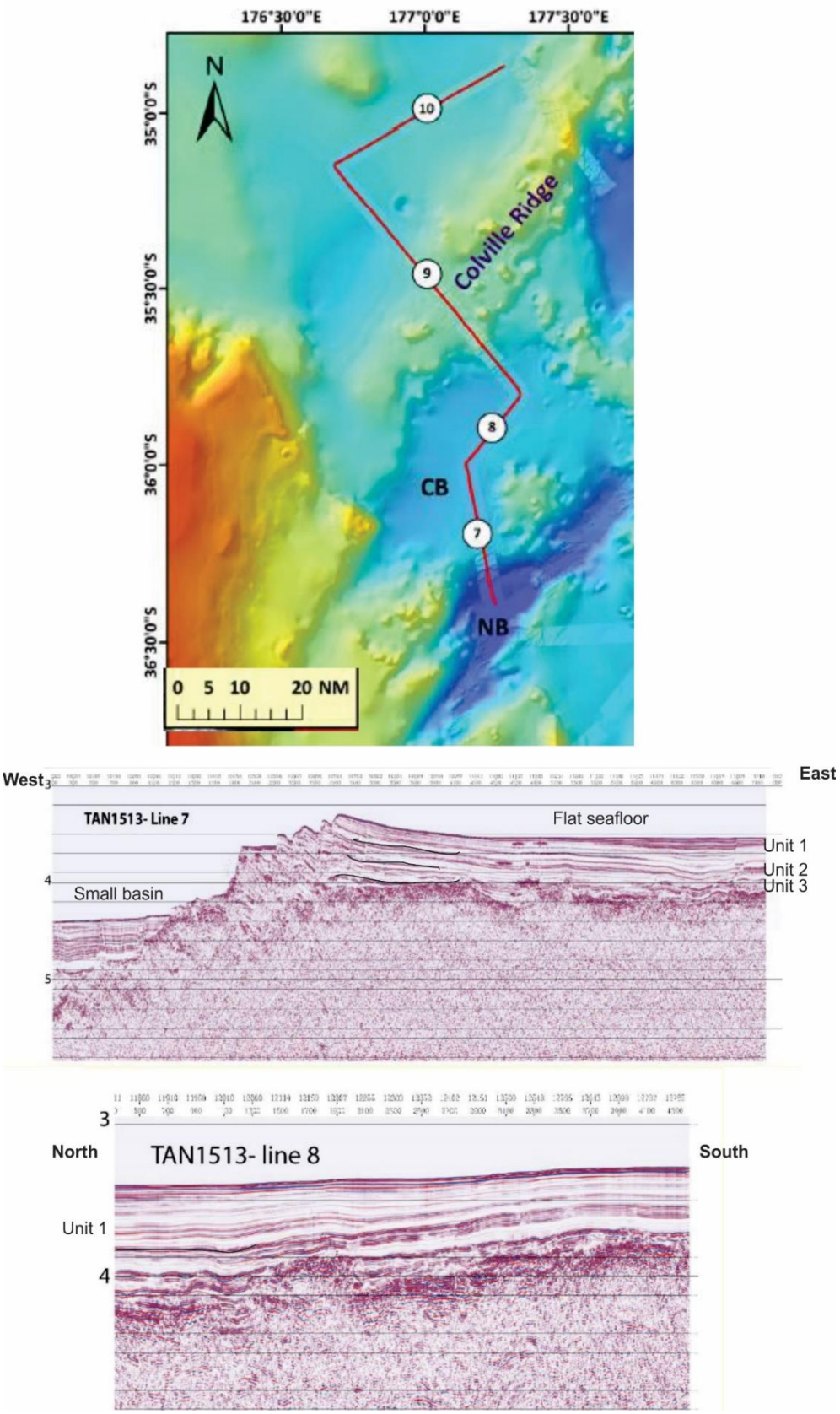

Figure 5.3: Bathymetry map (top) showing location of seismic profile lines carried out during voyage SAMSARA TAN1513 (Wysoczanski et al., 2015). NB is the Ngatoro basin and CB is the Colville basin. Scale is measured in nautical miles.

The seismic profiles suggest that structures underlying the thick sediment cover represent older rift structures that were associated with early basin formation, while the structures that are present above the basin floors could reflect younger rifting features that have penetrated through sediment and are associated with nascent 'disorganised' spreading (Wysoczanski et al., 2010). This may be the case for all basins on the western side that are also broad and appear relatively structureless.

The Ngatoro Basin contains a few long, continuous ridges but is predominantly structureless which may be due to a higher sediment cover resembling western basins. This basin appears to extend north beyond these ridges until it intersects the Rumble V ridge cross arc chain. It is interpreted that this basin overlies older rift structures (axial ridges) that propagate into the central southern Havre Trough, whereas the emergent ridges and cones represent younger, <1 Ma, rift related volcanism (Wysoczanski et al., 2010). In contrast, basins on the eastern side of the Havre Trough, whilst also broad, have undergone more extensive ridge and edifice construction and constructional volcanism, including the Kermadec Arc front volcanoes. They therefore appear to be smaller and narrower in width than the western basins. The higher concentration of ridges and cones on the eastern side and close proximity of basins to the arc front, may reflect higher melt productivity in these basins due to higher volumes of flux melting from the subducting slab resulting in more and/or larger volcanic features (Todd et al., 2011).

5.1.2 Associations between morphology and magmatism

Where the seafloor is deep, the crust is likely thinned through rifting process, less evolved lavas are expected to be sampled from the basin floors than at cones or ridges where there may have been more potential for magma stalling within the thicker crust. In order to evaluate the effect of rifting and differing types of morphology on the composition of lavas, a comparison between lavas sampled from each morphology-type was made.

Overall, the major element compositions of the lavas follow broad correlations versus MgO, with variable degrees of scatter and overlap (Figure 5.4). Lavas from

ridges and basin floors, generally more closely follow correlations between the major element oxides, except for basin K samples, which show distinctively different major element compositions to those from ridges and basin floors (all other basins). Ridges show the largest spread in MgO (e.g. 10.46 - 4.27 wt. %) and SiO_2 (e.g. 47 - 51.4 wt. %,) the lowest Al_20_3 (e.g. 13.80 wt. %), CaO (9.85 wt. %) and K_20 (0.25 wt. %) contents (Figure 5.4) relative to basin floors. However, in detail there is variation in the composition of the lavas from each morphology-type by basin. Basin A and C contain the most evolved lavas of all back arc samples. However, these were sampled from basin floors, which are expected to be less evolved compared to ridges, and appear to be more primitive (e.g. samples from basin I ridges.) Therefore, there is no compelling evidence for any clear difference between morphology types and magma chemistry and any trends observed may be an artefact of a small sample size.

Basins that are located within the proposed rift regimes (basins A, B, C, D, E, H, and I) have similar major element concentrations to samples from arc regime basins G and J. There are no clear major element distinctions between compositions of arc-type basalts and rift-type basalts, therefore suggesting the magmatic processes are very similar between these two regimes.

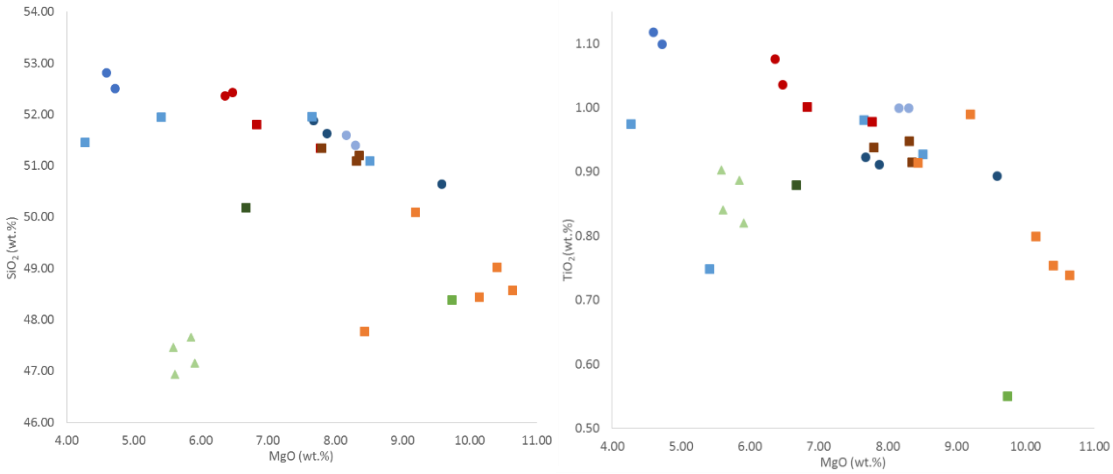

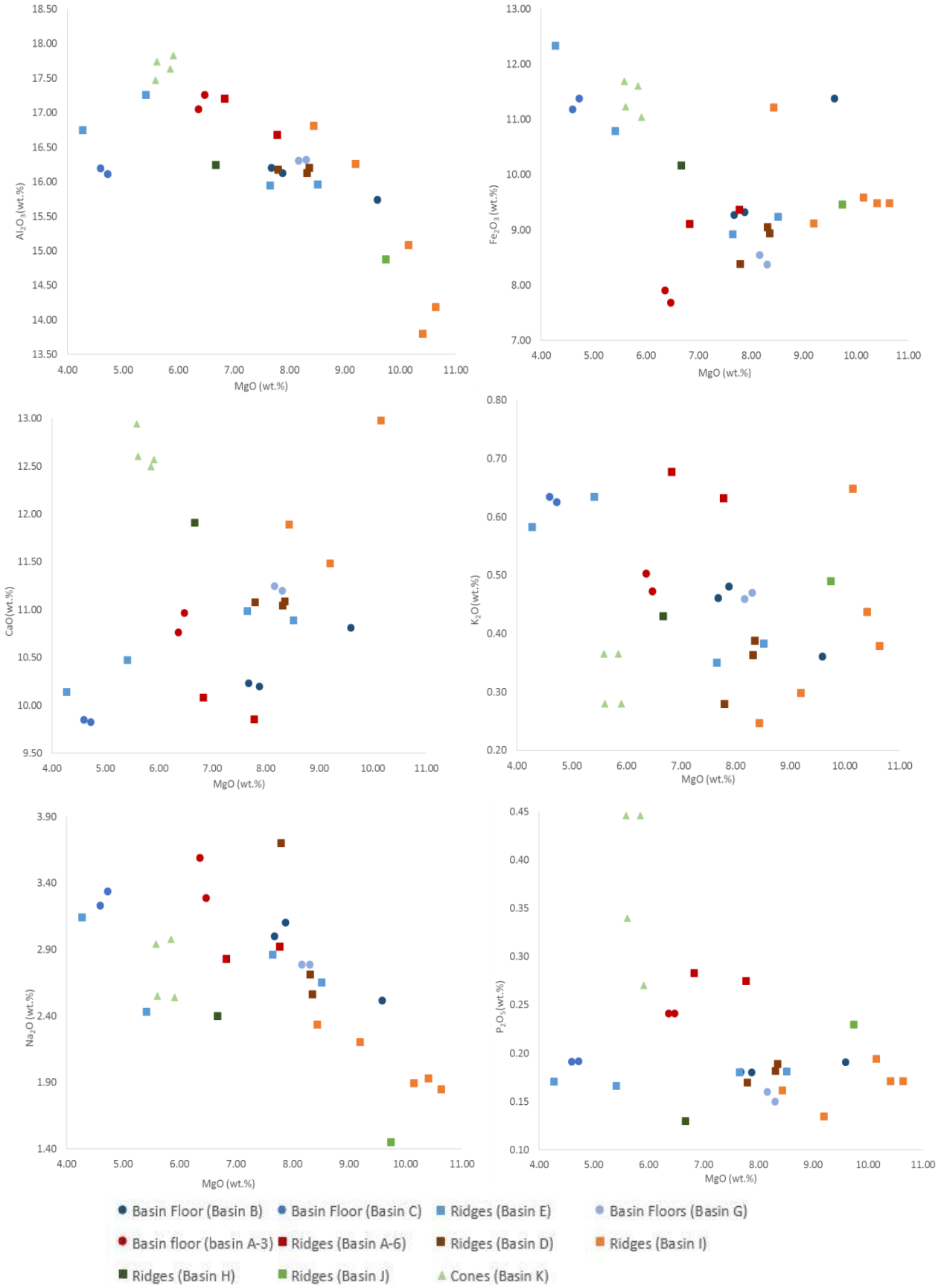

Figure 5.4: Plots showing major element comparisons between ridges, basin floors and cones for each basin.

The possible exception to this are the basalts from Basin K, which have very distinct compositions in SiO_2 vs MgO, and have notably high P_2O_5 contents. However, rather than distinctive magmatic processes, this more likely to reflect secondary alteration, as discussed below.

Effects of alteration on magma composition

Several samples analysed in this study display evidence for alteration and secondary infiltration from clay/minerals (e.g. >1 wt. % and up to 4 wt. % L.O.I for the most affected samples) and the presence of amygdales. The affected samples are from Basin A (006-1 and 006-3), Basin E (10-9), Basin I (040, 041 and 042) and all Basin K samples (DR10-1, 10-2, 10-3 and 10-4). However, two of the four Basin K samples (DR10-3 and DR10-4) were analysed at VUW and the other two (DR10-1 and DR10-2) were analysed at OGL and ALS indicating that their differences in bulk rock compositions are not attributed to any differences in sample preparation or analytical protocols.

Amygdales were present in samples from basin A (3-5) and basin G (47-2). Basin K samples have the highest L.O.I. contents, ≤ 4 wt. %, higher CaO and markedly elevated P_2O_5 contents for a given MgO content (Figure 5.4). High P_2O_5 and CaO could be consistent with apatite accumulation, however, apatite was not observed petrographically. They also display highly variable concentrations in LILE (e.g. Cs, Rb, and U) and elevated concentrations in Li (refer to multi-element plot, Figure 4.7.1:A) that are clearly distinct from the more systematic patterns of the other back arc samples, suggesting that these elements may have been affected by secondary alteration.

For samples that contained amygdales in the petrographic analysis, only rock chips that were free of filled vesicles were selected for powdering for geochemical analysis, and bulk geochemical data for these samples show no evidence for alteration (e.g. <1 wt. % L.O.I.). Of the samples that underwent the rigorous boiling method but still showed relatively elevated L.O.I. contents (1.06-4.01) the major elements, including P_2O_5, and the fluid-mobile LILE and Li follow the same patterns as samples with <1% L.O.I. (Figure 5.4) and their analyses are considered to be reliable. However, it may be that subtle alteration effects have

added to some of the scatter in the major element plots. Finally, although a few fluid mobile trace elements and several major elements were affected by alteration in samples from Basin K, the less mobile elements appear unaffected (e.g. REE and HFSE) and therefore these components of the Basin K samples, but not the major elements and LILE, have been included in the following discussions.

5.2 Magmatic processes and petrology

All basin lava samples examined carry a phenocryst assemblage dominated by olivine + clinopyroxene ± plagioclase ± orthopyroxene. Orthopyroxene phenocrysts were only observed in lavas from basins A, E and G, classed as type 4 rocks. These samples were from both ridges and basin floors.

Type 1 rocks are characterised by an olivine + plagioclase + minor clinopyroxene phenocryst assemblage and were observed in lavas from ridges and floors from basins B, D and G. Type 2 rocks, which only contain olivine and clinopyroxene phenocrysts, were sampled from ridges only, whereas type 3 rocks, characterised by olivine + plagioclase + clinopyroxene were from ridges and cones only, and contained more clinopyroxene phenocrysts than type 1 rocks. The phenocryst mineralogy is therefore not tightly constrained to a particular morpho-type as most phenocryst assemblages are present in at least one example of each morpho-type.

Overall, the back arc basin lavas are moderately mafic to mafic in composition, MgO contents typically range from 4-9 wt. % with samples from basins I and J ranging up to 11 wt. %. The highest SiO_2 contents are seen in basaltic andesite lavas from basins A and C, which contain olivine + plagioclase + pyroxene phenocryst assemblages (Types 3 and 4). The occurrence of olivine, clinopyroxene and plagioclase in the lavas, combined with increasing SiO_2 and decreasing MgO, Ni, Cr_2O_3, CaO and Al_2O_3 contents, suggests the fractionation of these mineral phases controlled the magmatic evolution. Al_2O_3 and TiO_2 increase with decreasing MgO initially, but level off at MgO contents around 8.5 – 9 wt. % (Figure 5.5). This is consistent with the fractionation of olivine and clinopyroxene initially, as both Al_2O_3 and TiO_2 are incompatible in these mineral phases, and the

later onset of crystallisation of plagioclase (and oxides). The phenocryst assemblages observed in the samples support this order of crystal fractionation.

The samples with the most mafic compositions, exemplified by the highest MgO contents (MgO 10.14-10.64 wt. %), come from basin I. These are all type 2 basalts, which are characterised by a phenocryst assemblage comprising olivine and clinopyroxene (see section 4.5). Plagioclase is absent as a phenocryst phase. This is consistent with the observed high MgO and CaO contents, and low Al_2O_3 contents, and early crystallisation of olivine + clinopyroxene. The phenocryst assemblage changes from olivine-clinopyroxene dominant to plagioclase-olivine dominant with decreasing MgO content. For example, Basin G samples (8.16 - 8.30 wt. % MgO, 16.5 - 16.6 wt.% Al_2O_3) are type 3 and 4 lavas with plagioclase comprising 40-75% of the phenocryst assemblage, and Basin A samples (6.36 - 7.78 wt. % MgO, 16.68 - 17.27wt. % Al_2O_3) are petrographically type 3 and 4 with plagioclase a significant component of the phenocryst assemblage (20 – 55%).

Lavas from the back arc stratovolcanoes and arc front overlap with the back arc basin samples on major element plots, but also extend to andesite and dacite compositions (Figure 5.5). Speculating that the back arc magmatism may have followed comparable magmatic processes for both rift and constructional magmatism with the large constructional features providing opportunity for magmas to stall and evolve to more felsic compositions. Overall, the major element chemistry of the back arc samples also follows the same trends as previously reported for Kermadec Arc front and back arc stratovolcano lavas, with only minor variations such as slightly higher TiO_2, K_2O and P_2O_5 contents for comparable MgO contents (Figure 5.5).

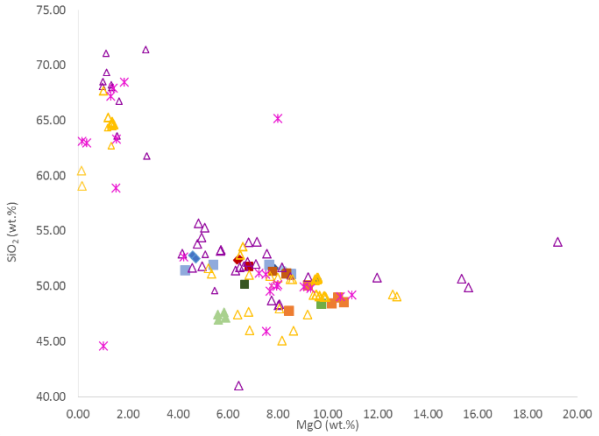
75.00
70.00
65.00
60.00
55.00
50.00
45.00
40.00
SiO2 (wt.%)
0.00
2.00
4.00
6.00
8.00
10.00
12.00
14.00
16.00
18.00
20.00
MgO (wt.%)

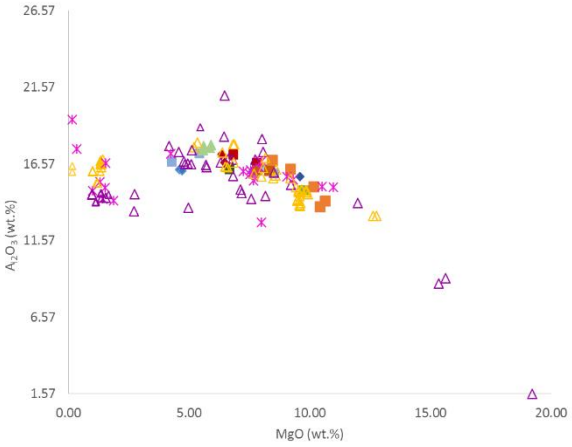
26.57
21.57
16.57
11.57
6.57
1.57
A2O3 (wt.%)
0.00
5.00
10.00
15.00
20.00
MgO (wt.%)

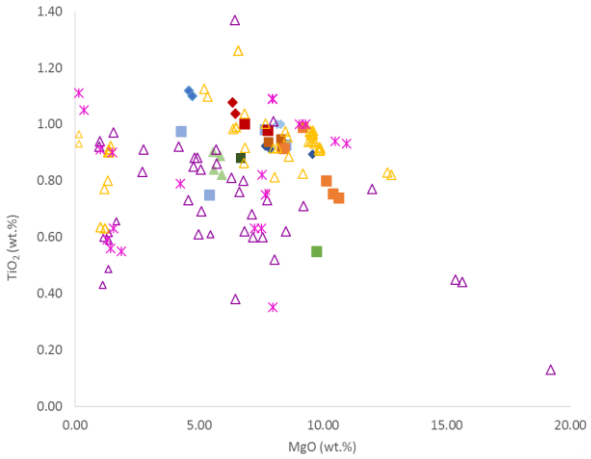
1.40
1.20
1.00
0.80
0.60
0.40
0.20
0.00
TiO2 (wt.%)
0.00
5.00
10.00
15.00
20.00
MgO (wt.%)

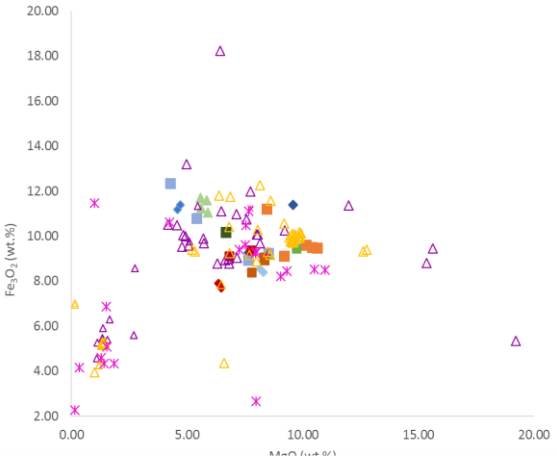
20.00
18.00
16.00
14.00
12.00
10.00
8.00
6.00
4.00
2.00
Fe2O3 (wt.%)
0.00
5.00
10.00
15.00
20.00

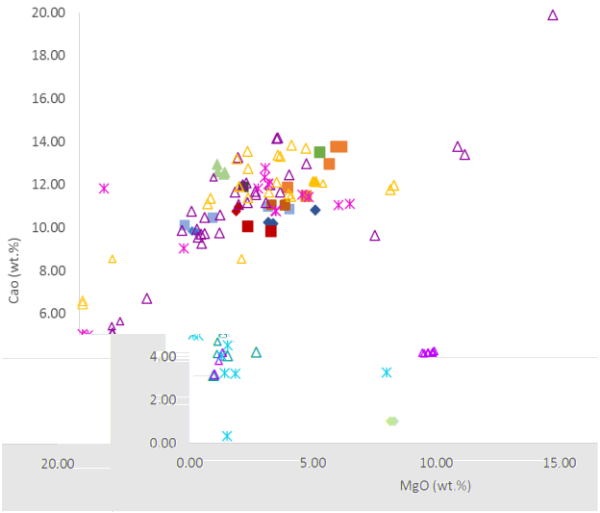
20.00
18.00
16.00
14.00
12.00
10.00
8.00
6.00
Cao (wt.%)
4.00
2.00
0.00
20.00
0.00
5.00
10.00
15.00
MgO (wt.%)

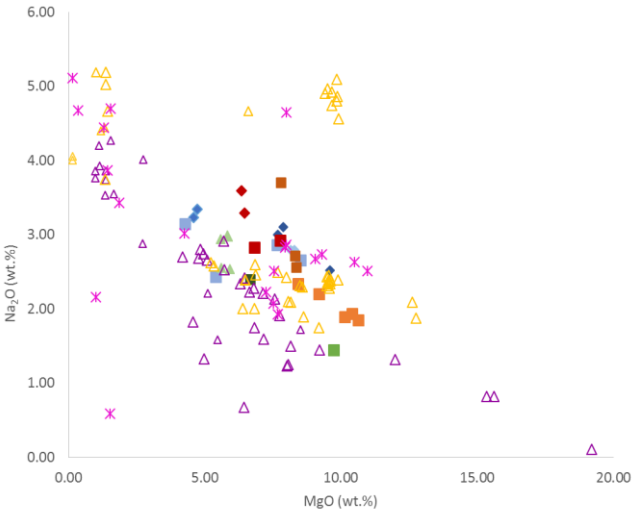
6.00
5.00
4.00
3.00
2.00
1.00
0.00
Na2O (wt.%)
0.00
5.00
10.00
15.00
20.00
MgO (wt.%)

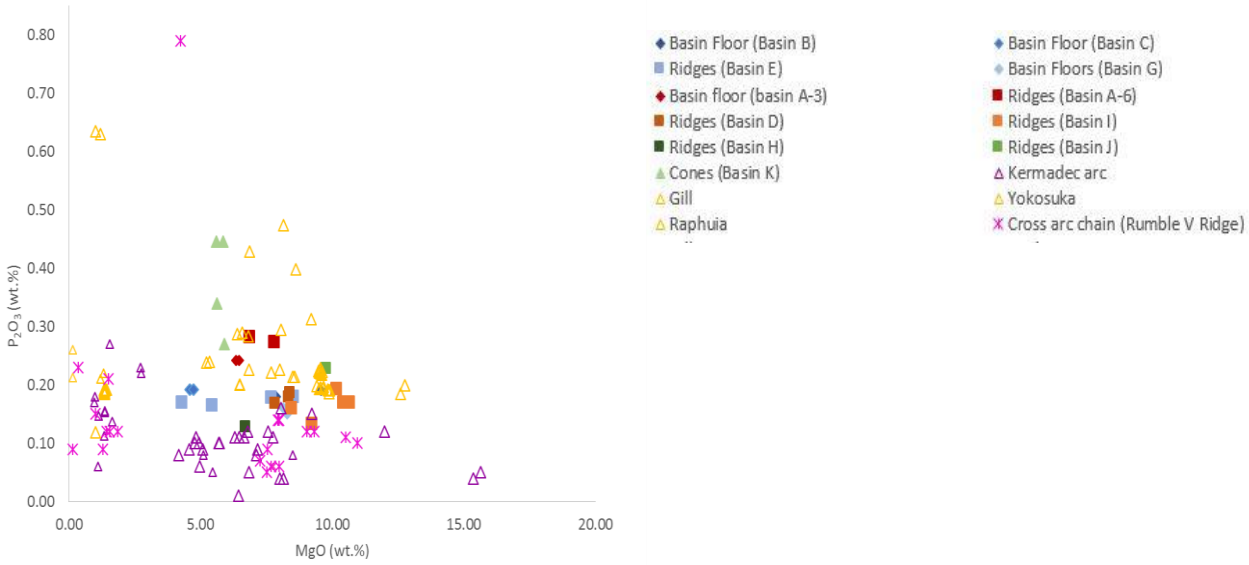

Figure 5.5: Plot showing the comparison of major element compositions for back arc basins basalts and Kermadec Arc lavas and back arc stratovolcanoes. Data for Kermadec Arc lavas were obtained from (Gamble et al. (1990; 1993a; 1993b, 1994; 1996), Haase et al. (2002), Wysoczanski et al. (2006; 2010), Todd et al. (2010; 2011) Barker et al., (2012), Timm et al. (2016), Zohrab. (2016).

5.2.1 Clues from mineral textures

The majority of plagioclase phenocrysts in the back arc basin samples show evidence for complex growth histories (moderate compositional zoning and sieve-textures), suggesting that they may have been in magma(s) of contrasting compositions and/or changing pressure and temperature conditions during ascent and decompression as the magma rises toward the surface (e.g., Pearce et al., 1987).

Olivine phenocrysts that also show variations in growth history (zoning, skeletal textures, and fragmented phenocrysts) are only observed in type 3 and 4 rocks. In both these types, plagioclase phenocrysts are present and also show compositional zoning and sieve/dissolution type textures. Skeletal crystals form during large supercooling and indicate disequilibrium. They form by preferential growth of the corners of crystals, a diffusion-controlled growth process. Combined, the olivine and plagioclase textures observed in these rock types it may be inferred that the crystals formed significantly prior to being erupted and may not have been in equilibrium with the melt that they had travelled in.

In general, clinopyroxene phenocrysts show an overall increase in FeO content in rims by 1 wt.% and up to 2 wt.% in some samples (basin D) compared to cores, suggesting that they had crystallised in an evolving magma. Several clinopyroxene phenocrysts show reverse zoning however, where rims are lower in FeO than cores (basin I). This may reflect an influx of primitive magmas, suggesting diverse magmatic conditions in the basin's magmatic systems.

5.2.2 Magmatic evolution and equilibrium

Olivine phenocrysts from the back arc basin samples show a range of Fo contents (83 –87%) which could indicate that different olivine populations were incorporated into the melt at different depths during magma evolution and ascent or may simply reflect fractionation of a magma in a magma chamber. In order to determine whether olivine phenocrysts were in equilibrium with the host melt at the time of crystallization, the olivine-liquid equilibria test of Roeder and Emslie (1970) was applied to crystals from all basins (Figure 5.6). Most olivine phenocrysts appear to be in equilibrium with the whole rock compositions and are likely to have crystallised from the melt they were carried in.

Olivine phenocrysts from basin I sample 042 contain lower Fo content for a given whole rock Mg#, therefore, did not crystallise in its melt and were likely incorporated into the magma during evolution and ascent. Olivine populations that contain Fo contents higher than that predicted for a given whole rock Mg#, such as those from basin E; Figure 5.6, may have formed through several possibilities; 1) Crystallisation of olivine occurred in more primitive magmas at higher temperatures, 2) Olivine had crystallised in the magma chamber and was incorporated into the melt which produced them. 3) Olivine crystals were entrained in the melt from an unrelated rock showing disequilibrium in olivine phenocrysts. Note, olivine from basin K is also above the equilibrium lines, however the bulk rock chemistry (Mg#) may have been compromised by alteration.

Olivine phenocrysts that contain high Fo contents may indicate crystallization at high temperatures (Table 5.1) although accurate temperature estimates are

difficult to constrain without pressure or H_2O estimates. Using the Sobolev and Danyushevsky (1994) linear regression equation, temperature estimates obtained from olivines range from 837° in basin C with the lowest Fo content to 1250°C in basin E with the highest Fo content..

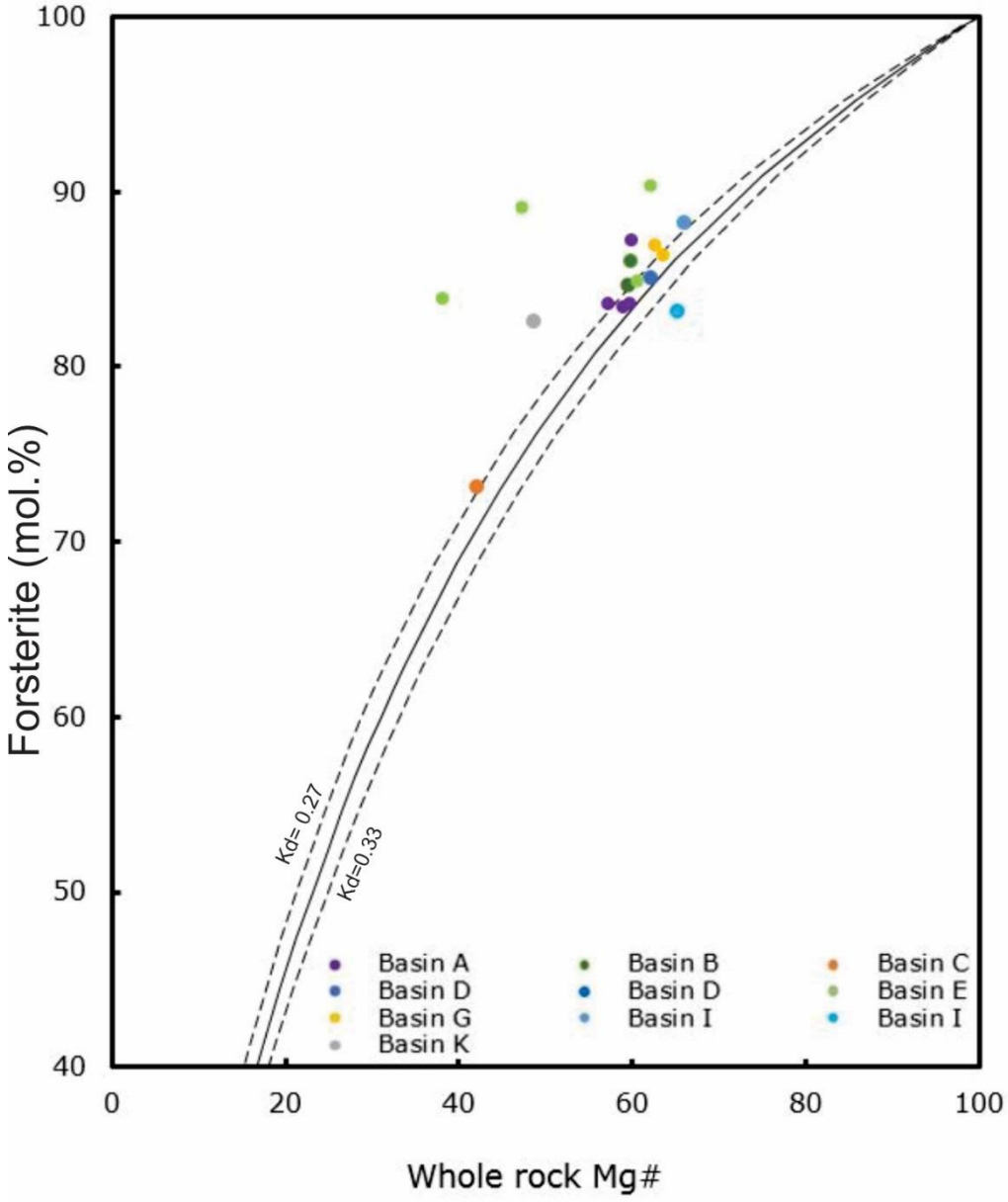

Figure 5.6: Plot showing the composition of olivine crystals from basins in chemical equilibrium with the host melt. Olivine forsterite (Fo) content is plotted against whole rock Mg# for a select few basins. The dashed lines indicate the minimum and maximum uncertainty for olivine phenocrysts forming in chemical equilibrium in the host melt, based on the olivine-liquid equilibrium test of Roeder and Emslie (1970).

.

Table 5.0-1: Temperature ranges (± 50°) for selected basins based on Fo content of olivine crystals in equilibrium with their host melt shown in figure 5.5. Temperatures were obtained using the Sobolev and Danyushevsky (1994) method

Basin	**Temperature (°C)**
Basin A 3 2	1175
Basin A 3 5	1085
Basin A 006-1	1090
Basin A 006-3	1090
Basin B 55-2	1145
Basin B 56-3	1115
Basin C 50-3	840
Basin D 51-4	1125
Basin E10 2	1250
Basin E 10 9	1220
Basin E10 13	1095
Basin E 11 1	1120
Basin G 47-1	1155
Basin G 47-2	1170
Basin I TAN1513-040	1200
Basin I TAN1513-041	1080
Basin K TAN1512 DR10-2	1065

5.3 Influence from slab derived components

Back arc basin samples are enriched in LILE and LREE with respect to N-MORB (Figure 4.20), suggesting that their mantle source has been variably modified by slab derived components. The extent and variability of enrichment from subducting slab components can be ascertained by comparing ratios of elements that are variably mobile in aqueous fluids and sediment melts to those that are immobile (Pearce and Stern, 2002). The trace element ratio of Ba/Nb is commonly used to assess the total subduction component, Ba/Th to assess enrichment from aqueous fluids and La_N/Sm_N as a proxy for deeper subduction components associated with sediment melts or supercritical fluids (e.g. Davis and Stevenson, 1992; Elliot et al., 1997; Pearce and Stern, 2002; Sinton et al., 2003; Wysoczanski et al., 2006).

5.3.1 Aqueous fluid components

Samples from the back arc basins do not show any systematic variations in Ba/Th across the back arc or along strike of the arc, except for two samples from basin E which are substantially higher than all other basins (Figure 5.7). This basin lies 40km to the west of the Kermadec Ridge close to the trench where aqueous fluids are more likely added to the mantle wedge (e.g., Ruenke et al., 2004). However, basins which are located closer to the arc front do not show such high Ba/Th ratios, and similarly not all samples from basin E display high Ba/Th. It is not clear why these two samples have anomalously high Ba values (47.7-55-273) compared to all other samples. However, they are at the same general distance from the trench as the volcanic front volcanoes that show the highest Ba/Th values (Figure 5.7), consistent with this region seeing higher, but variable, fluxes of aqueous fluid.

The back arc basin stratovolcanoes have similar low Ba/Th values to the adjacent back arc basins (Figure 5.7) and both back arc basin lavas and back arc stratovolcanoes overall show lower Ba/Th ratios than the Kermadec Arc front volcanoes: typically < 60-124 (basin E), compared with 47–233 reported for Kermadec Arc volcanoes (Figure 5.7) (e.g. Gamble et al., 1990; Haase et al., 2002;Wysoczasnki et al., 2006; Baker et al., 2010; Timm et al., 2016). This is

consistent with the mantle source for the back arc having undergone less flux from aqueous fluids derived from the subducting slab than the Kermadec Arc front mantle source (e.g. Wysoczanski et al., 2006; Haase et al., 2002; Todd et al., 2010; 2011). Thus, overall the influence of slab-derived aqueous fluids is highest at the volcanic front and lower and fairly consistent throughout the back arc region.

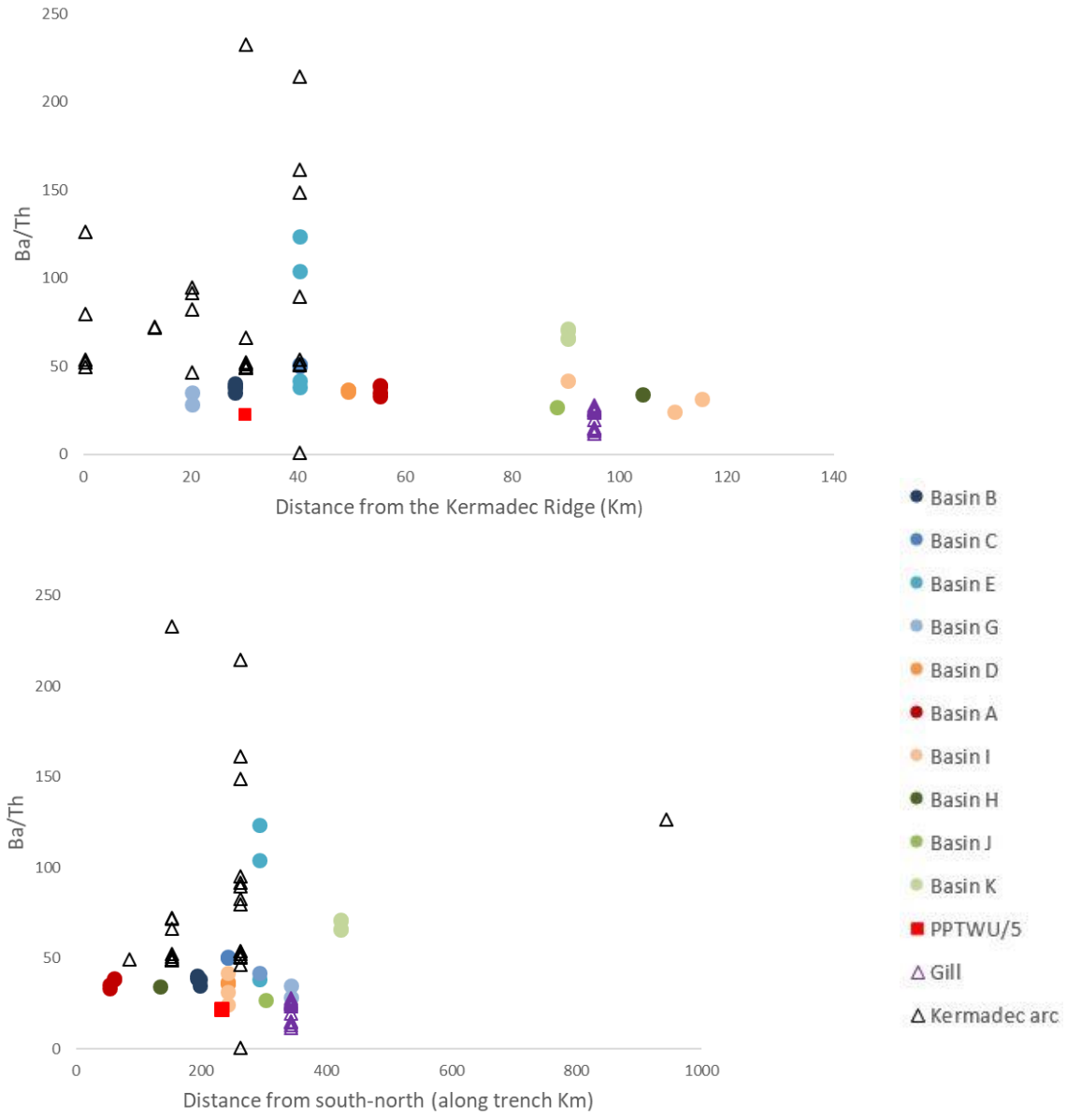

Figure 5.7: Plot showing Ba/Th ratios of back arc basins, back arc stratovolcanoes and AMW sample PPTUW/5 and arc front volcanoes their relationship to varying distance from the arc front and along strike of the arc front. Data for Back arc stratovolcano Gill obtained from Todd et al. (2011), Zohrab. (2016) Data for PPTWU/5 obtained from Haase et al. (2002), Wysoczanski et al. (2012). Data for arc front volcanoes was obtained from Gamble et al. (1990; 1993a; 1993b; 1996), Baker et al. (2012), Todd et al. (2011), Timm et al. (2016). Note only basaltic lavas were used as comparisons for back arc and arc front volcanoes.

Experimental studies carried out on basaltic eclogites suggest that aqueous fluids are transferred into the mantle wedge at relatively low temperatures (700-800°C) and shallow depths, <180 km (4 Gpa) (Kessel et al., 2005). The subducting slab beneath Gill Volcano has been modelled to be at 280 km depth (Syracuse et al., 2010; Todd et al., 2010), which exceeds the critical threshold for which aqueous fluids are stable in equilibrium with eclogite-bearing mineral phases (Hermann et al., 2006). Aqueous fluids therefore have more likely been added to the back arc via supercritical fluids released from the subducting slab at pressures exceeding 4 Gpa, (Kessel et al., 2005; Hermann et al., 2006). Experimental studies on fluids for saturated eclogitic basalt containing cpx + garnet ± rutile at 6.0 GPa indicate the presence of supercritical fluids at a wider temperature range (800–1000°C), but below 4.0 GPa liquids from altered oceanic crust (AOC) are either aqueous fluids (< 900°C) or melts at temperatures that exceed 1000°C (Kessel et al., 2005).

5.3.2 Sediment melt component

The back-arc basin samples show similar La_N/Sm_N along strike of the subduction zone with broad variations across the back arc. In general, there is a positive increase in La_N/Sm_N with increasing distance from the arc front, exemplified by samples from basin I which increase in La_N/Sm_N with further distance away from the arc front (Figure 5.8). Therefore, there is a greater and more variable modification of the mantle wedge from deeper subduction components with increasing distance from the volcanic front.

Lavas from basin A have among the highest La_N/Sm_N and are the most evolved of the back arc basin samples. Their increased sediment melt component could be attributed to fractional crystallization processes as La/Sm slightly negatively correlates with MgO. This could indicate that the sediment melt component is more significant in basin A lavas.

Back arc stratovolcanoes have similar (Gill volcano) to larger (Rapuhia ridge and Giljanes volcano) additions of a deep subduction component as characterised by La_N/Sm_N (Figure 5.8). Notably, samples from basin J have similar La_N/Sm_N as the back arc stratovolcanoes Gill and Yokosuka, which are close to basin J (within

approximately 30 km). This suggests that the addition of a deep, sediment melt slab component to the mantle is mainly related to distance from the volcanic front and is similar for both rift basin and constructional regions of the back arc.

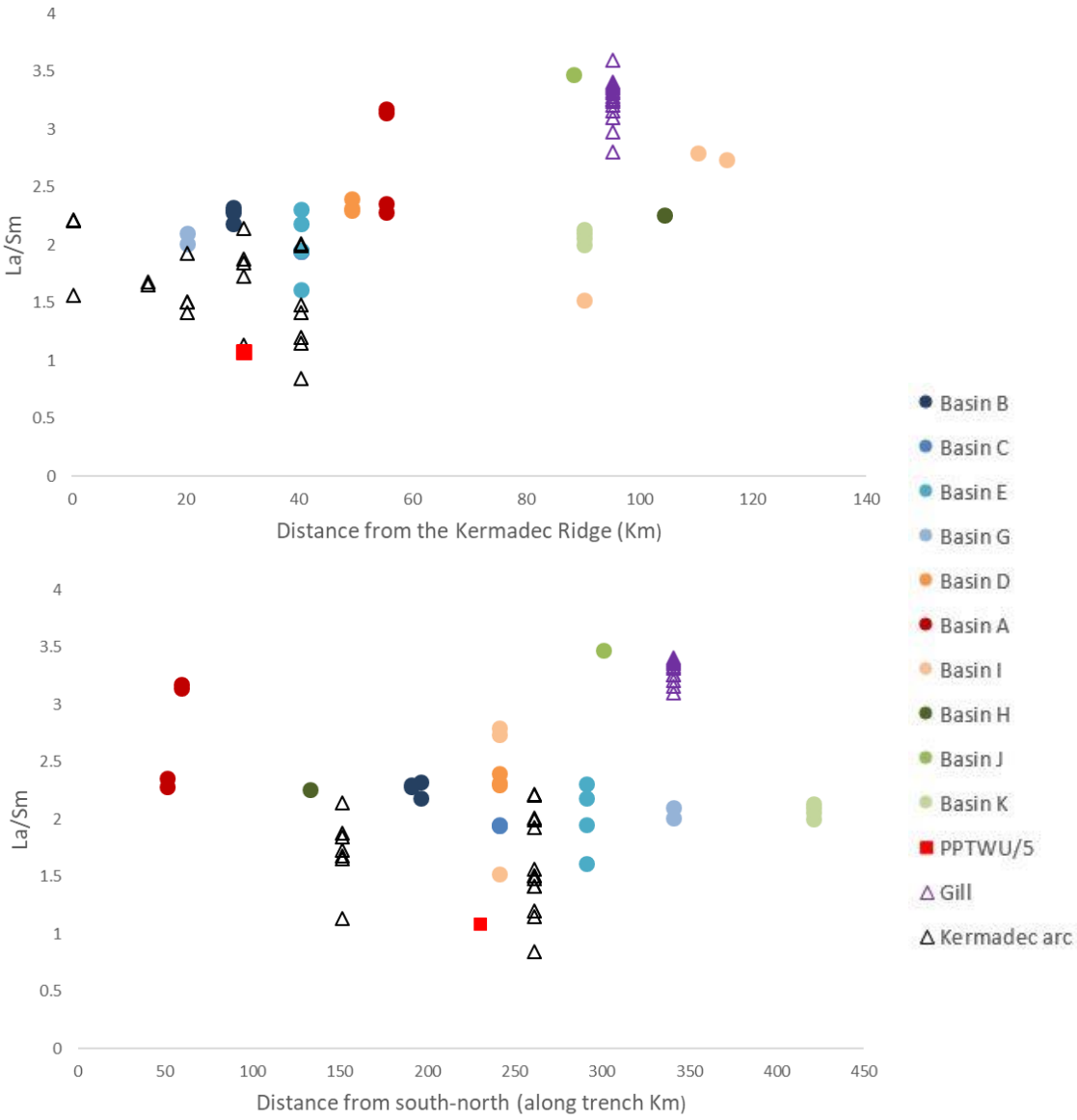

Figure 5.8: Plot showing La/Sm ratios of back arc basins, back arc stratovolcanoes and AMW sample PPTUW/5 and arc front volcanoes their relationship to varying distance from the arc front and along strike of the arc front. Data for Back arc stratovolcano Gill obtained from Todd et al. (2011), Zohrab. (2016) Data for PPTWU/5 obtained from Haase et al. (2002), Wysoczanski et al. (2012). Data for arc front volcanoes was obtained from Gamble et al. (1990; 1993a; 1993b; 1996), Baker et al. (2012), Todd et al. (2010; 2011), Timm et al. (2016). Note only basaltic lavas were used as comparisons for back arc and arc front volcanoes.

In order to modify the mantle by sediment melts, partial melting of subducting sediment requires temperatures over 650°C, in order to exceed the water saturated solidus of sediments. This is facilitated by slow subduction rates (<7 cm/year for the southernmost Kermadec Arc), and a thick sediment cover on the subducting slab such as is observed for the southern Kermadec subduction zone (Carter et al., 1996).

Todd et al. (2010) inferred that residual mineral phase's rutile, zircon, monazite, and apatite were present in the source of the deep slab component observed in the Rumble V Ridge lavas. Observed Hf isotope trends in the Rumble V Ridge lavas could be explained by the addition of 0.05% - 2% sediment melt with residual trace zircon, monazite and rutile to the mantle wedge source (Todd et al., 2010).

Fractionation of HFSE from REE requires partial melting of sediment rather than crystal fractionation or bulk sediment addition, which will not significantly fractionate Hf from REE. Low observed Hf/Hf* (where $Hf/Hf^* = Hf_N / \sqrt{[Nd_N \times Sm_N]}$) in Rumble V Ridge basalts therefore also requires addition of partial melts of sediment that contains refectory zircon (Todd et al., 2010). However, eastern Rumble V ridge basalts contained smaller negative Hf anomalies (Hf/Hf* up to 0.93) compared to western Rumble V ridge basalts (Hf/Hf* ~ 0.8), consistent with increased sediment melt component in the west. When variations in Hf isotopic compositions were also taken into account, Todd et al, (2010) suggested the amount of residual zircon in the sediment melt source decreased with further distance from the subducting slab, and with increasing temperature and depth of the subducting slab resulting in more partial melting sediment and less residual zircon. Hf anomalies for back arc stratovolcanoes are negative ranging between Hf/Hf* = 0.6 – 0.9, which were inferred to reflect partial melting of subducting sediment with residual zircon (Zohrab, 2016). Calculated Hf anomalies for the back arc basin lavas studied here range from Hf/Hf* of 0.78 for eastern basins, to ~ 0.72 in the central basins and ~ 0.64 for western basins, following the same broad pattern as observed in the Rumble V ridge basalts.

Th/Nb is another common measure for the amount of sediment melt or deep subduction component added and is interpreted to reflect addition of a sediment

melt component with residual rutile. The back arc basin samples contain similar, if slightly lower, Th/Nb ratios compared to the back arc stratovolcanoes (e.g. 0.14-0.78 vs 0.38-1.37). Basins also slightly increase in Th/Nb values with distance from the arc front (e.g. values from basin G are 0.23 vs 0.70 and 0.78 in basins I and J). The differences between basins and back arc stratovolcanoes are moderate however. In particular, basins that are near to Gill volcano and Rapuhia Ridge show higher ratios (0.3-1.2 in the back arc stratovolcanoes and 0.32-0.35 in back arc basins). As sediment melt addition reflects flux from deep in the mantle wedge, the sediment signature may be transported into the mantle melting zone via sediment diapairs (e.g. Behn et al., 2011)

5.4 Composition of the ambient mantle wedge

The ambient mantle wedge (AMW) is defined as the mantle wedge prior to being modified by subduction-derived components (e.g. Todd et al., 2010). The ambient mantle is heterogeneous, relatively fertile mantle that is progressively depleted by partial melting during advection to the volcanic front and re-enriched via fluids or melts derived from the subducting plate (Todd et al., 2010; Woodhead et al., 2011).

Previous work has suggested that back arc basin magmas in the southern Havre Trough are derived from a mantle wedge comprising a mixture of depleted MORB mantle source (DMM) of the East Pacific Rise and enriched components proposed by Hanan and Graham (1996). The enriched component has been variably modified by partial melting events and the addition of subduction components with respect to the more uniform DMM source (Todd et al., 2010).

Early studies used a single depleted basalt from the Havre Trough (sample PPTUW/5) as representative of the ambient mantle, owing to a scarcity of back arc basin samples (Gamble et al., 1993a; Gamble and Wright, 1995; Gamble et al., 1996; Woodhead et al., 2001). Subsequently, Todd et al., (2010) reported data for six samples from the Havre Trough (two samples from the south Fiji basin, and four samples from north of 30°S that they proposed provided a good representation of the AMW as these samples did not appear to have been significantly modified by subduction components. These samples were characterised, for example, with Hf/Hf* ≥ 1.0, Ce/Pb ≥ 13.0, $^{143}Nd^{144}Nd$ >0.51305

and $La_N/Yb_N \leq 1.3$ (Todd et al., 2010). This study provides new data for a larger number of back-arc samples spanning a wide region of the Havre Trough, thus providing the opportunity to revisit the composition of the Havre Trough AMW.

The previous section showed that across and along the back arc basin, the sampled lavas display a range in trace element ratios that are characteristic of slab-derived component addition (e.g. La_N/Sm_N, Ba/Th), but with a fairly consistent lower baseline to this range throughout the trough (e.g. Figures 5.6 and 5.7).

PPTUW/5 and the AMW samples proposed by Todd et al. (2010), plot along this baseline (Figures 5.9). Therefore, with the extended sampling of the basin, these samples appear to be representative of the southern Havre Trough AMW.

MORB-normalised Nb/Yb ratios (Nb_N/Yb_N) are a useful proxy in determining the relative enrichment and depletion of the ambient mantle source as 1. both elements are relatively immobile during subduction processes and therefore will not be modified by addition of subduction-derived components to the mantle source, and 2. vary according to the degree of melting with Nb behaving significantly more incompatibly than Yb (Pearce and Stern, 2006). Globally, back arc basin samples are generally less depleted (higher Nb_N/Yb_N) than their respective arc front lavas (lower Nb_N/Yb_N), which is consistent with trench orthogonal flow from the back arc toward the arc front, where the mantle is progressively depleted in the back arc before reaching the arc front (Pearce and Stern, 2006) (Figure 5.9).

The back arc basin samples analysed in this study however show a more complex spatial pattern of fertility (or depletion). Nb_N/Yb_N does broadly decrease toward the arc front, but in two apparent trends: 120 to 80 km from the Kermadec Ridge, then 60 – 0 km from the Kermadec Ridge. It should be noted however, that the samples span an along-strike distance of some 400 km. Samples from basin I, however, provide a sampling that is aligned orthogonal to the Kermadec Ridge and have Nb_N/Yb_N values that decrease from 1.5, 115 km from the arc front to 0.9 values at 90 km from the arc front (Figure 5.9), consistent with the conventional trench orthogonal flow model. However, basins D and C are also along the same

general alignment as basin I, closer to the Kermadec Ridge, but follow the second trend of trenchward decreasing Nb_N/Yb_N (Figure 5.9) indicating a more complex relationship than the simple conventional trench orthogonal flow and progressive depletion.

There is a broad trend of decreasing Nb_N/Yb_N (increasing depletion) along strike of the arc, from south to north for the back arc basin samples (Figure 5.9). Basin A, in the south, has the highest Nb_N/Yb_N and is the most fertile, with the basin samples becoming progressively depleted towards the north, with low Nb_N/Yb_N seen in basin K and J samples (Figure 5.9). When comparing back arc basins basalt – basaltic andesites to basalt – basaltic andesites from the back arc stratovolcanoes (Gill, Rapuhia, Yokosuka and Giljanes Volcanoes), particularly at the same location (e.g. Basin G and J), the basins overall have lower Nb_N/Yb_N than back arc stratovolcanoes. This suggests that there are differences in the source for magmas supplying the back arc volcanoes compared to adjacent basins. If the back arc stratovolcano sources are characterised by higher Nb_N/Yb_N and are hence more fertile, this would facilitate higher degrees of partial melting beneath the volcanoes (Zohrab, 2016. However, small degrees of partial melting of mantle peridotite can also result in elevated Nb/Yb ratios (Keleman et al., 1993), which would suggest that Gill volcano magmas involved similar to higher degrees of partial melting than the adjacent back arc basin lavas.

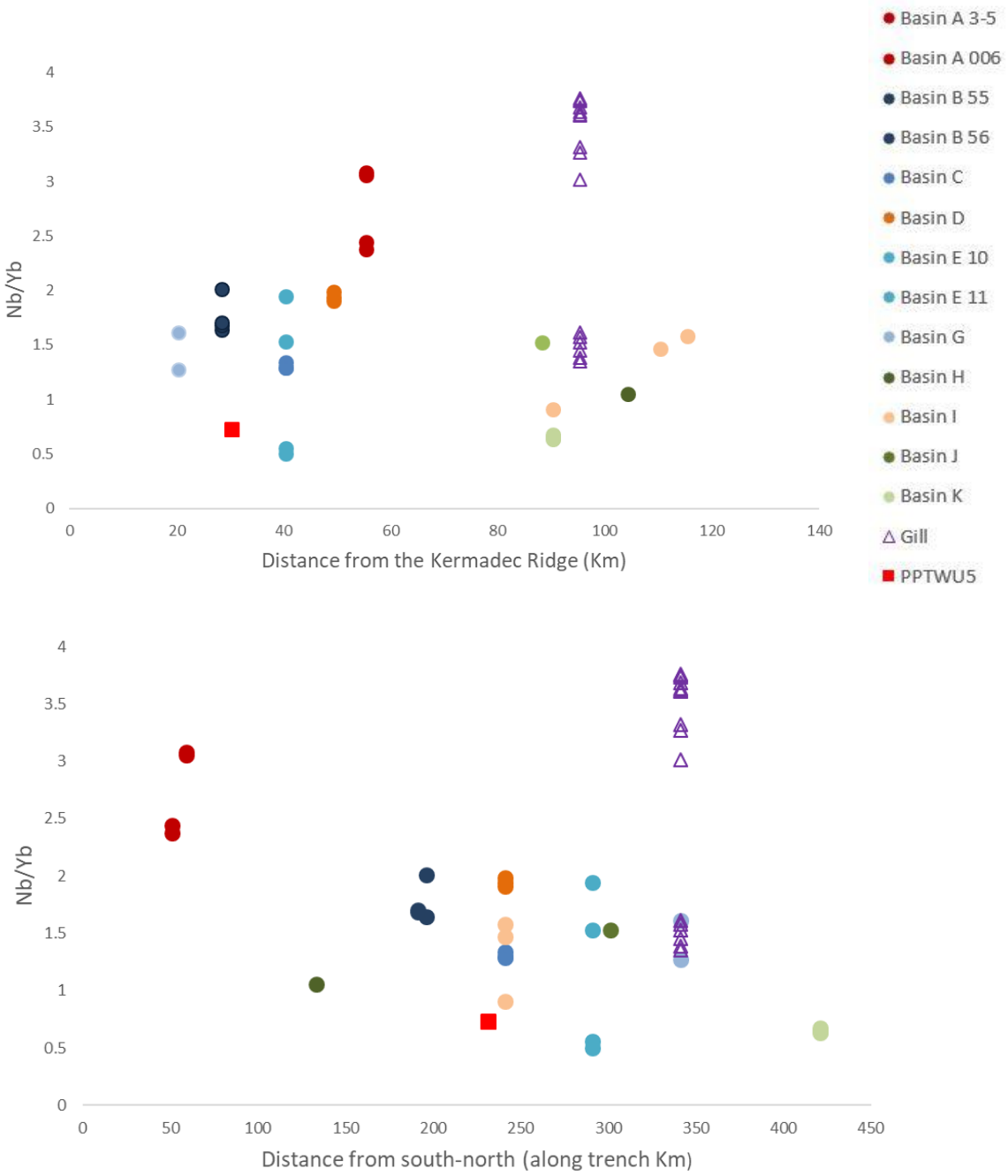

Figure 5.9: Plot showing Nb/Yb ratios of back arc basins and back arc stratovolcanoes and AMW sample PPTUW5 their relationship to varying distance from the arc front and along strike of the arc front. Data for Back arc stratovolcano Gill obtained from Todd et al. (2011), Zohrab. (2016) Data for PPTWU/5 obtained from Haase et al. (2002).

There are three key variations in Nb_N/Yb_N values across and along the back arc: 1) Trench-wards depletion in Nb_N/Yb_N orthogonal to trench; 2) an along-strike, northward depletion in Nb_N/Yb_N in the basin samples; and 3) deviation of the constructional back arc volcanoes from this along-strike trend to higher Nb_N/Yb_N. Several different possibilities may explain different aspects of these observations.

First, pre-existing heterogeneity in the mantle that is underlying the Australian plate entering into the subduction zone, consistent with observations from other back arc systems (e.g. Izu-Bonin Arc: Hochstaedter et al., 2000). This could explain, for example, the higher Nb_N/Yb_N in the source of the back arc stratovolcanoes compared to the lower values from adjacent deep basins. The south-north gradient observed would require a larger scale compositional gradient in the incoming mantle.

Second, mantle flow dynamics where the conventional model of trench orthogonal flow or trenchward advection of the mantle may cause progressive depletion towards the east and arc front, as previously suggested to account for the observed patterns in Nb_N/Yb_N in western Rumble V ridge lavas (e.g. Todd et al., 2010). Similar patterns are also observed in other back arc settings (e.g. Mariana arc; Pearce et al. (2005)). Trench orthogonal flow is consistent with conventional subduction zone models where subduction induces a flow in the mantle which is first sampled in the back arc, if one is present, before reaching the arc front.

Third, a trench parallel mantle flow, superimposed upon the orthogonal flow, may cause the observed variations of depletion increasing to the north. Trench parallel flow in the mantle beneath the central Tonga-Kermadec Arc system has been previously suggested by Timm et al., (2013). They combined estimations of the timing of fluid release with absolute plate motions models that indicated an anticlockwise rotation in the subducted Louisville seamount chain to suggest primarily trench normal mantle flow beneath the central Tonga-Kermadec system.

In other subducting systems seismic anisotropy, measuring parameters of shear wave splitting (delay time and fast polarization direction) have been used to identify orientations of aligned olivine fast-axes in the mantle wedge (e.g. Kneller et al., 2007; Hoernle et al., 2008). Seismological studies from shear wave splitting of teleseismic events, indicate that preferred lattice orientations of olivine crystals in the upper mantle, follow past deformation in the lithosphere or current strain orientations in the mantle related to the flow of the mantle wedge (e.g. review by Savage. (1999). Seismic anisotropy in the mantle wedge showing strong evidence for along-arc alignment of olivine fast axes, combined with systematic along-arc trends in radiogenic isotopes in volcanic front magmas were used to suggest arc parallel flow of the mantle wedge in the Costa Rica subduction zone (Hoernle et al., 2008). Strong arc parallel anisotropy has also been reported in the Mariana and Andean subduction systems (e.g. Kneller and Keken, 2007). In that study, the authors found that shear wave splitting measurements provided strong evidence for trench parallel alignment of olivine fabric close to the trench and abruptly rotating to trench perpendicular with distance away from the arc. They suggest a three-dimensional flow of the mantle which may be controlled by variations in the strain field due to variations in the slab dip (Kneller and Keken, 2007).

Whilst no mantle shear wave splitting studies have been published for the southern Havre Trough back arc, several studies (e.g. Gledhill and Gubins, 1996; Marson-Pidgeon and Savage, 1997; Marson-Pidgeon and Savage, 2004; Marson-Pidgeon et al., 1999; Matcham et al., 2000; Greve et al., 2008; Greve and Savage, 2009) have been conducted immediately to the south (38°'S) in central – eastern North Island, New Zealand. The south to north Nb_N/Yb_N depletion trend for the Havre back arc basin samples is most strongly recorded in basins that are on the eastern side of the back arc, nearest the trench, which aligns with the eastern Central Volcanic Region of continental North Island where shear wave splitting is most pronounced (Figure 5.10) (Greve et al., 2008; Greve and Savage, 2009). The shear-wave splitting observed beneath the Central Volcanic Region was attributed as being best explained by a combination of local (shallow) trench perpendicular and deeper trench parallel mantle flow, and pockets of melt aligned in bands (Greve et al., 2008).

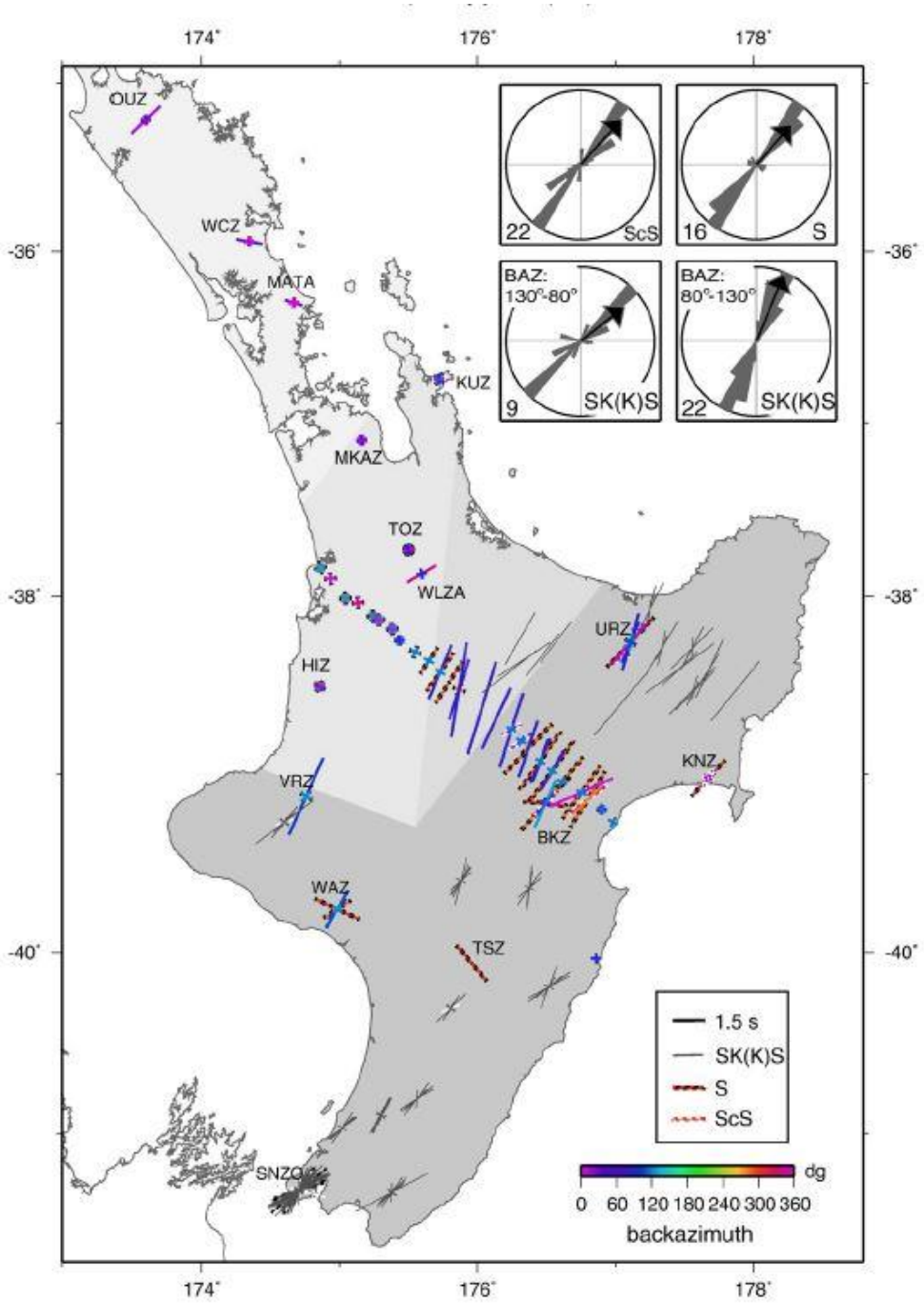

Figure 5.10: Shear wave splitting measurements of available data for the central volcanic region in New Zealand showing the preferred orientation of olivine minerals (Audoine et al., 2004; Cochran, 1999; Gledhill and Gubbins, 1996; Marson-Pidgeon and Savage,1997; Marson-Pidgeon et al.,1999; Marson-Pidgeon and Savage, 2004). Figure obtained from (Greve et al., 2008).

Fourth, some of the heterogeneity observed in the mantle sources may have been inherited from earlier phases of back arc magmatism prior to mixing with recent hydrous sediments and material from the Hikurangi Plateau (Todd et al., 2010; Timm et al., 2016).

5.5 Tectono-magmatic model for back arc basins in the Havre Trough

A model for back arc basin evolution is proposed depicting key features for the back arc basins in the southern Havre Trough (Figure 5.11). Arc perpendicular variations in Havre Trough ridge morphology are observed predominantly in the eastern Havre Trough combined with greater constructional volcanism and may reflect a volcanic-magmatic swell in the eastern margin facilitating the development of constructional volcanism (Wysoczanski et al., 2010). In the west, basins are wider, and ridge and cone morphologies are present in clusters concentrated at the margins of basins.

The distribution of ridge and cone morphologies in the west could be attributed an eastward migration of an extensional melting with rift progression and older prolonged extension in the west, combined with higher sedimentation cover in these basins (Wysoczanski et al., 2010). Rift ridge and cone morphologies present in the western basins either reflect the caps of older large extrusive features formed during early basin formation or are newly accreted volcanics that have been able to penetrate through thicker sedimentation cover. Similar types of 'chaotic fabric' have been observed in the western Lau basin, which are interpreted as older structures derived from analogous nascent disorganised spreading (Wysoczanski et al.,2010).

The variation in trends of ridges in the back arc is consistent with previous observations of block rotation at the Kermadec-Hikurangi arc front margin at ~37°S (Collot et al., 1996) and clockwise rotation of the Kermadec ridge microplate (Delteil et al., 2002). A contrast in the crustal thickness and buoyancy within the subducting slab between normal Pacific Ocean crust and the Hikurangi Plateau are inferred to drive this rotation (Collot and Davey, 1998; Wallace et al., 2005).

The ambient mantle wedge shows evidence for largely trench perpendicular flow, with a possible component of trench parallel flow, reflected in a general northward depletion in the mantle (e.g. Figure 5.11). Along strike variations in geometry of the slab (e.g. slab curvature and dip angle) will cause along strike variations in pressure as well as slab roll back. Furthermore, the Havre Trough is essentially locked in the north by the incoming Louisville seamount chain and in the south of the Tongariro National park hindering 'saloon door-like' opening as observed in the Lau Basin. Together these may contribute to drawing wedge material towards the north (e.g. Kneller et al., 2007; Hoernle et al., 2008; Timm et al., 2013).

Basin J and G basalts display similar subduction component enrichments to nearby back arc stratovolcano, Gill Volcano, while basins B and E lavas show similar enrichments to adjacent cross arc chain and arc front volcanoes (Rumble II east and Rumble II west). Thus, overall the mantle beneath the back arc has less fluid enrichment than the mantle beneath the arc front, whether beneath basins or constructional edifices. As basins near back arc stratovolcanoes show similar general trends in subduction component enrichments, the overall influence of subduction components throughout the back arc appears to be fairly consistent. However, the larger or more constructional features reflect localised zones of higher melt productivity and greater degrees of partial melting of the mantle wedge (Wysoczanski et al., 2010).

Todd et al. (2011) suggested that the manifestation of constructional cross arc chains at both the Rumble V ridge and at 34°S, which includes Gill volcano, Rapuhia Ridge, Giljanes volcano, and basins G and J, reflects arc-regime type basalts. They suggested that anomalously higher temperature regions in the mantle wedge (e.g. hot fingers; Tamura et al., 2002) could facilitate higher degrees of partial melting in order to generate the voluminous magmas that have produced both back arc stratovolcanoes and cross arc chains (Todd et al. 2011). By contrast, lower temperature regions between the hot fingers would underlie the rift-type regimes. As the mantle source of the basins and that of adjacent back arc volcanoes locally show no significant differences in slab component, and the overall morphology trends throughout the back arc appear to be relatively

consistent, the cause of the construction back arc structures is not obviously related to differences in fluxing (re-enrichment) of the source or structural features in the overriding plate. Thus, thermal anomalies within the mantle wedge may be the most likely cause for the distribution of the constructional 'arc regime' structures in the back arc. In addition, the higher Nb_N/Yb_N observed for the backarc stratovolcanoes at 34°S (including Gill Volcano) compared with the back-arc basin trends, suggests the larger volumes of magmas produced to form at least some of the constructional features may also relate to locally more fertile mantle.

In order to measure if thermal anomalies are present in the mantle, measured temperatures that were calculated from olivine geothermobarometry (Table 5.1) were correlated to distances from the Kermadec Ridge (Figure 5.12). In general, there appears to be no significant difference in temperatures between basins, and back arc stratovolcanoes (Gill and Rapuhia Ridge). Basin E lavas however, show the highest temperatures at 1210°C, while basin C lavas are anonymously lower at 840° C than other basins analysed. Therefore, there is no significant evidence suggesting thermal anomalies in the mantle may generate voluminous magmas. However, the data set for measured temperatures is small therefore, more sampling is needed to provide sufficient evidence for thermal anomalies in the mantle.

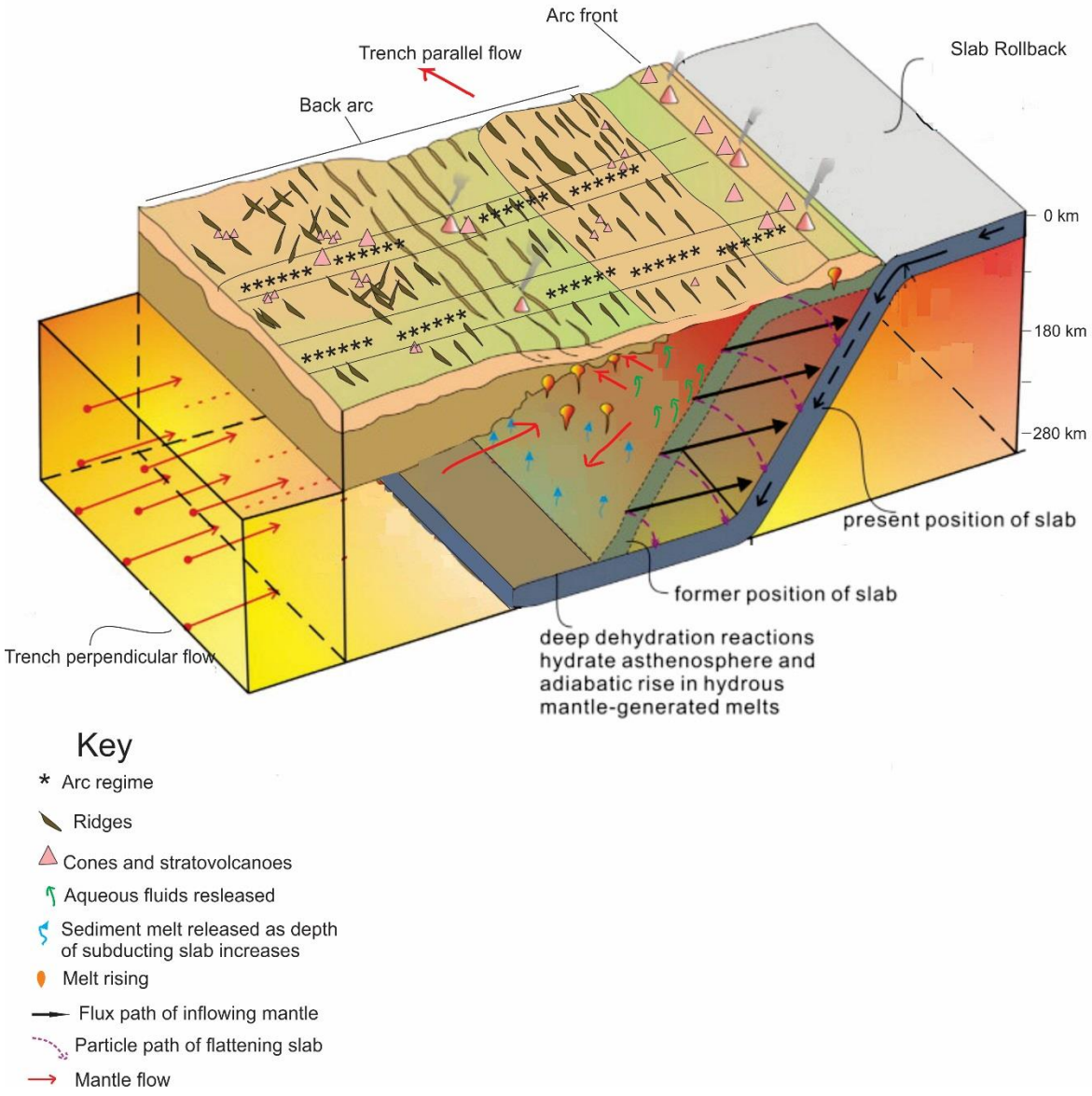

Figure 5.11: Schematic diagram showing key features within the subduction system for the southern Havre Trough. Modified from (Kusky et al., 2014). Trench perpendicular flow is indicated by red arrows. The mantle would be coming in orthogonal in the upper part of the mantle wedge, below the upper plate, and then turn at the corner and follow down the subducting slab. Depths of the subducting slab underneath the volcanic front were obtained from Syracuse et al., 2010).

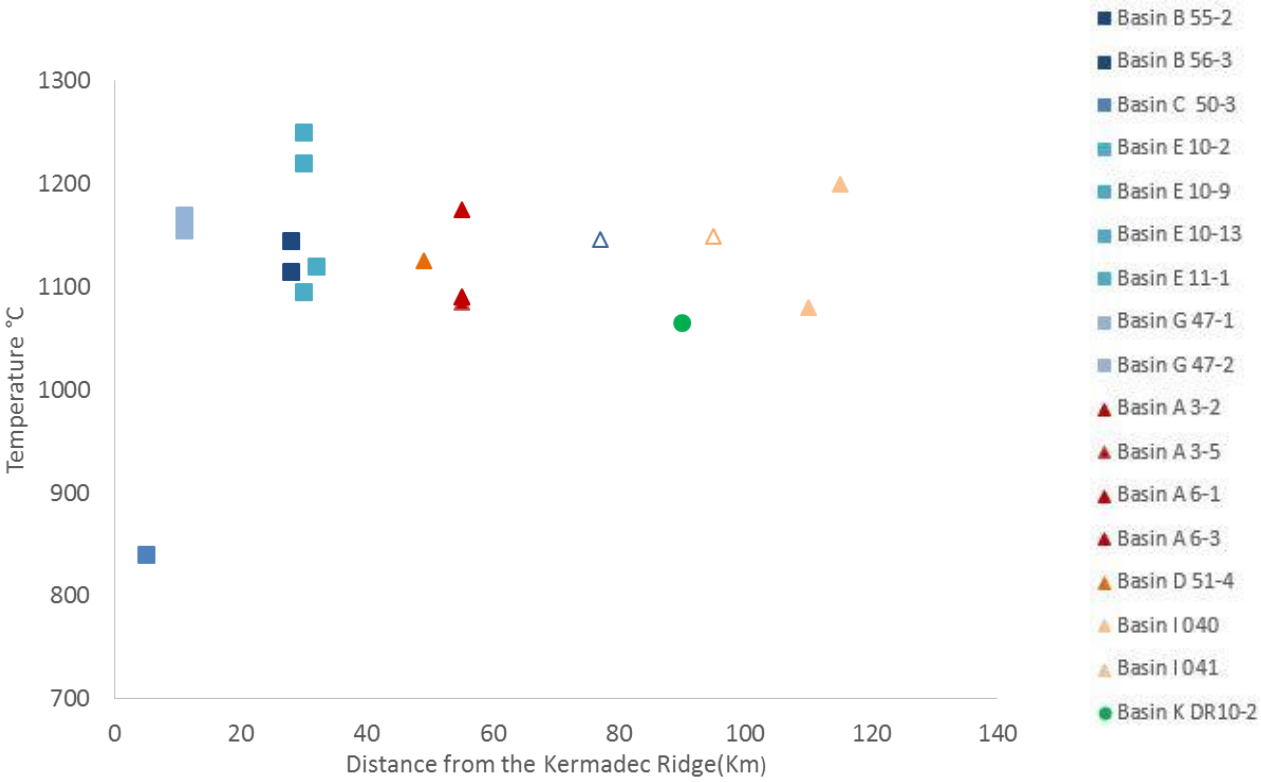

Figure 5.12: Plot showing measured temperatures using the Sobolev and Danyushevsky (1994) method against distances from the Kermadec Ridge (Km).

Chapter 6:
Conclusions

6.1 Key findings in this study

The focus of this study was to analyse the structure and geochemical composition of deep basins in the Havre Trough. The key findings of this study are summarised in the following section.

1. The back arc basins and the morphologies within them form through repeated episodes of magmatic intrusion through pervasive dyke systems due to structural controls and weaknesses in the crust (Wysoczanski et al., 2010). These systems may originate as ridges and over time develop into volcanic cones reflecting higher degrees of partial melting in the mantle wedge necessary to form larger volcanic features. As constructional features (cones and ridges) are more common in the eastern margin and centre of the back arc, this may reflect localised recent volcanism, while fewer emergent cone and ridge features in the western basin suggest recent volcanism may be more broadly distributed throughout the western section of the back arc.

2. The composition of the ambient mantle wedge as defined by back arc basalts is enriched with variable additions of slab derived components relative to N-MORB source, in particular with sediment melts of increasing importance with distance from the arc front.

3. The mantle beneath the back arc in general shows evidence for two broad flow patterns; 1) typical trench perpendicular depletions where depletion is the highest closest to the arc front and 2) a component of trench parallel flow based on a pattern of broadly increasing depletion to the north. Pre-existing heterogeneity with small scale variations may also explain the more fertile pockets feeding into the source of Gill volcano and other back arc stratovolcanoes. A pre-existing larger scale south-north fertility gradient in the

mantle entering the subduction system however, is considered to be a less likely alternative explanation of the south-north variations in fertility observed for the mantle wedge.

4. All samples in this study show major element and trace element compositions that follow consistent magmatic processes of fractional crystallisation of olivine, clinopyroxene and plagioclase with no obvious systematic differences among the different basins or different morphologies (cones, ridges and basin floors). The basin samples overall are not as evolved as lavas from back arc stratovolcanoes and arc front volcanoes, which likely results from basin samples having erupted through thinner crust and therefore, did not have time to stall and undergo assimilation and further differentiation.

5. Overall, the contribution of aqueous fluids and sediment melt components from the subducting slab follow typical enrichments with relation to distance from the trench. Back arc basins are characterised by enrichments in sediment melts La_N/Sm_N compared to arc front lavas, which show a greater influence from aqueous fluids. The back arc basins lavas have similar contributions of slab components as adjacent back arc stratovolcanoes, suggesting that the addition of slab components are fairly consistent throughout the back arc.

6. The similarity in the source characteristics between the rift regime back arc basin basalts and the arc regime constructional features are consistent with previously suggested thermal anomalies within the mantle wedge to explain the spatial variations between both rift and arc regimes and the generation of constructional edifices in the back arc (Todd et al., 2010). According to this interpretation, anomalously higher temperatures in the mantle result in higher degrees of melting and more (constructional) magmatism, resulting in the development of cross arc chains at 36°S and 34°S (at 100 km intervals) whereas rift type basalts are suggested to have been produced by lower degrees of partial melting situated in cooler regions in the mantle wedge (Todd et al., 2010; 2011).

6.2 Suggestions for future studies

This study provided the first geomorphic and geochemical analysis of under-explored, deeper back arc basins in the southern Havre Trough. Due to the location and scale of the back arc, sampling and surveying of the basins is still limited. This study has raised interesting questions related to the structural and chemical nature of the back arc. Suggestions for future studies are presented below.

1) In order to understand the back arc system better more sampling of each basin is needed, in particular targeted dredging of different morphologies within each basin and more extensive coverage throughout the Havre Trough. This would allow for better comparisons to be made between each morphology and each basin.

2) There are limited seismic profiles across back arc basins in the western Havre Trough, therefore, more seismic imaging would allow evaluation of the sediment cover of these basins and whether older magmatic structures are present underneath the sediment cover. This would aid in determining if structures in western basins relate to older basin formation or reflect recent pervasive dyke systems.

3) It has been suggested that a south to north flow may be present in the mantle beneath the eastern Havre Trough in particular. In order to test this further, shear wave measurements in the back arc would be useful for defining mantle flow dynamics, as would further trace element analysis of back arc basin samples and isotopic analyses.

4) Olivine hosted melt inclusions were observed in several samples. Magmatic processes could be better constrained by analysis of melt inclusions. This would give insight into early magma evolution, volatile (water) contents, and the amount of degassing associated with the basin magmas.

5) Further geophysical surveying (e.g. Seismic tomography and gravity modelling) of the thermal structure in back arc basins may help explain the

development of higher concentrations of structures present in basins as well as cross arc chains and back arc stratovolcanoes better constraining the observations of “rift-regimes” and “arc regimes”.

6) Expanding the study of these samples to radiogenic isotopes (Sr, Nd, Hf, Pb) would better characterise the roles of the subduction components in the back arc mantle source. (e.g. such as Todd et al., 2010 for the Rumble V ridge samples).

7. Compiling detailed geological maps including inferred faults, ridge orientations, sediment basins, exposed lava flows, and the locations of cones, would provide a greater insight into the overall structure of the Havre Trough.

8. $^{40}Ar/^{39}Ar$ age analysis of basins located close to previously dated stratovolcanoes may provide a greater insight into the age of the back arc and may better constrain the time of opening commenced in the Havre Trough.

References

Audione, E., Savage, M.K., GLedhil, k. (2004). Anisotrophic structure, under a back-arc spreadig region, the Taupo Volcanic Zone, New Zealand. . *Journal of Geophysical Research, 109*(11).

Baker, E., Feely, R., De Ronde, C., Massoth, G., & Wright, I. (2003). Submarine hydrothermal venting on the southern Kermadec volcanic arc front (offshore New Zealand): Location and extent of particle plume signatures. *Geological Society, London, Special Publications, 219*(1), 141-161.

Barker, S., Wilson, C., Baker, J., Millet, M.-A., Rotella, M., Wright, I., & Wysoczanski, R. (2012). Geochemistry and petrogenesis of silicic magmas in the intra-oceanic Kermadec Arc. *Journal of Petrology, 54*(2), 351-391.

BAS, M. L., Maitre, R. L., Streckeisen, A., Zanettin, B., & Rocks, I. S. o. t. S. o. I. (1986). A chemical classification of volcanic rocks based on the total alkali-silica diagram. *Journal of Petrology, 27*(3), 745-750.

Blackmore, N., & Wright, I. (1995). *Southern Kermadec Volcanoes*: New Zealand Oceanographic Institute, National Institute of Water and Atmospheric Research Limited.

Caress, D. W. (1991). Structural trends and back-arc extension in the Havre Trough. *Geophysical Research Letters, 18*(5), 853-856.

Carlson, R., & Melia, P. (1984). Subduction hinge migration. *Tectonophysics, 102*(1-4), 399-411.

Carter, L., Carter, R., McCave, I., & Gamble, J. (1996). Regional sediment recycling in the abyssal Southwest Pacific Ocean. *Geology, 24*(8), 735-738.

Clift, P. D., & Leg, O. (1994). Volcanism and sedimentation in a rifting island-arc terrain: an example from Tonga, SW Pacific. *Geological Society, London, Special Publications, 81*(1), 29-51.

Cole, J., Darby, D., & Stern, T. (1995). Taupo Volcanic Zone and Central Volcanic Region backarc structures of North Island, New Zealand *Backarc Basins* (pp. 1-28): Springer.

Collot, J.-Y., Delteil, J., Lewis, K. B., Davy, B., Lamarche, G., Audru, J.C., Lallemand, S. (1996). From oblique subduction to intra-continental transpression: Structures of the southern Kermadec-Hikurangi margin from multibeam bathymetry, side-scan sonar and seismic reflection. *Marine Geophysical Researches, 18*(2-4), 357-381.

Contreras-Reyes, E., Grevemeyer, I., Watts, A. B., Flueh, E. R., Peirce, C., Moeller, S., & Papenberg, C. (2011). Deep seismic structure of the Tonga subduction zone: Implications for mantle hydration, tectonic erosion, and arc magmatism. *Journal of Geophysical Research, 116*(B10).

Crawford, A., Meffre, S., & Symonds, P. (2003). 120 to 0 Ma tectonic evolution of the southwest Pacific and analogous geological evolution of the 600 to 220 Ma Tasman Fold Belt System. *Special Papers-Geological Society of America*, 383-404.

Davey, F., Henrys, S., & Lodolo, E. (1995). Asymmetric rifting in a continental back-arc environment, North Island, New Zealand. *Journal of Volcanology and Geothermal Research, 68*(1-3), 209-238.

Davies, J. H., & Stevenson, D. J. (1992). Physical model of source region of subduction zone volcanics. *Journal of Geophysical Research: Solid Earth, 97*(B2), 2037-2070.

de Ronde, C., Baker, E., Massoth, G., Lupton, J., Wright, I., Sparks, R., Greene, R. (2007). Submarine hydrothermal activity along the mid-Kermadec Arc, New Zealand: Large-scale effects on venting. *Geochemistry, Geophysics, Geosystems, 8*(7).

de Ronde, C. E., Caratori, T.., Timm, C., Merle, S.G. . (2013). *Colville I '13 OS2020 cruise to the southern Colville Ridge*.

de Ronde, C. E., Caratori, T.., Timm, C., Merle, S.G. . (2016). *Colville '15 OS2020 cruise to the southern Colville Ridge*.

de Ronde, C. E. J., Walker, S. L., Ditchburn, R. G., Tontini, F. C., Hannington, M. D., Merle, S. G., Stoffers, P. (2014). The Anatomy of a Buried Submarine Hydrothermal System, Clark Volcano, Kermadec Arc, New Zealand. *Economic Geology, 109*(8), 2261-2292.

Delteil, J., Ruellan, E., Wright, I., & Matsumoto, T. (2002). Structure and structural development of the Havre Trough (SW Pacific). *Journal of Geophysical Research: Solid Earth, 107*(B7), ETG 7-1-ETG 7-17.

DeMets, C., Gordon, R. G., Argus, D. F., & Stein, S. (1994). Effect of recent revisions to the geomagnetic reversal time scale on estimates of current plate motions. *Geophysical Research Letters, 21*(20), 2191-2194.

Dunn, R. A., & Martinez, F. (2011). Contrasting crustal production and rapid mantle transitions beneath back-arc ridges. *Nature, 469*(7329), 198-202.

Elliott, T., Plank, T., Zindler, A., White, W., & Bourdon, B. (1997). Element transport from slab to volcanic front at the Mariana arc. *Journal of Geophysical Research: Solid Earth, 102*(B7), 14991-15019.

Elliott, T., Plank, T., Zindler, A., White, W., & Bourdon, B. (1997). Element transport from slab to volcanic front at the Mariana arc. *Journal of Geophysical Research: Solid Earth, 102*(B7), 14991-15019.

Erdmann, S., Scaillet, B., Martel, C., & Cadoux, A. (2014). Characteristic Textures of Recrystallized, Peritectic, and Primary Magmatic Olivine in Experimental Samples and Natural Volcanic Rocks. *Journal of Petrology, 55*(12), 2377-2402.

Ewart, A. (1976). Mineralogy and chemistry of modern orogenic lavas—some statistics and implications. *Earth and Planetary Science Letters, 31*(3), 417-432.

Ewart, A., Collerson, K. D., Regelous, M., Wendt, J. I., & Niu, Y. (1998). Geochemical Evolution within the Tonga-Kermadec-Lau Arc-Back-arc Systems: the Role of Varying Mantle Wedge Composition in Space and Time. *Journal of Petrology, 39*(3), 331-368.

Ewart, A., & Hawkesworth, C. (1987). The Pleistocene-Recent Tonga-Kermadec Arc lavas: interpretation of new isotopic and rare earth data in terms of a depleted mantle source model. *Journal of Petrology, 28*(3), 495-530.

Ewart, A., Hergt, J., & Hawkins, J. (1994). *29. Major element, trace element, and isotope (Pb, Sr, and Nd) geochemistry of Site 839 basalts and basaltic andesites: implications for arc volcanism.* Paper presented at the Proceedings of the Ocean Drilling Program, Scientific Results.

Fryer, P. (1995). Geology of the Mariana Trough *Backarc Basins* (pp. 237-279): Springer.

Fryer, P. (1996). Evolution of the Mariana convergent plate margin system. *Reviews of Geophysics, 34*(1), 89-125.

Fujiwara, T., Yamazaki, T., & Joshima, M. (2001). Bathymetry and magnetic anomalies in the Havre Trough and southern Lau Basin: from rifting to spreading in back arc basins. *Earth and Planetary Science Letters, 185*(3-4), 253-264. Fujiwara, T., Yamazaki, T., & Joshima, M. (2001). Bathymetry and magnetic anomalies in the Havre Trough and southern Lau Basin: from rifting to spreading in back-arc basins. *Earth and Planetary Science Letters, 185*(3-4), 253-264.

Gamble, J. A., Smith, I. E., Graham, I. J., Kokelaar, B. P., Cole, J. W., Houghton, B. F., & Wilson, C. J. (1990). The petrology, phase relations and tectonic setting of basalts from the Taupo Volcanic Zone, New Zealand and the Kermadec Island Arc-Havre Trough, SW Pacific. *Journal of Volcanology and Geothermal Research, 43*(1-4), 253-270.

Gamble, J., Smith, I., McCulloch, M., Graham, I., & Kokelaar, B. (1993)[A]. The geochemistry and petrogenesis of basalts from the Taupo Volcanic Zone and Kermadec Island Arc, SW Pacific. *Journal of Volcanology and Geothermal Research, 54*(3-4), 265-290.

Gamble, J. A., Wright, I. C., & Baker, J. A. (1993)[B]. Seafloor geology and petrology in the oceanic to continental transition zone of the Kermadec-Havre-Taupo Volcanic Zone arc system, New Zealand. *New Zealand Journal of Geology and Geophysics, 36*(4), 417-435.

Gamble, J. A., Wright, I. C., Woodhead, J. D., & McCulloch, M. T. (1994). Arc and back-arc geochemistry in the southern Kermadec Arc-Ngatoro Basin and offshore Taupo Volcanic Zone, SW Pacific. *Geological Society, London, Special Publications, 81*(1), 193-212.

Gamble, J., & Wright, I. (1995). The Southern Havre Trough geological structure and magma petrogenesis of an active backarc rift complex *Backarc basins* (pp. 29-62): Springer.

Gamble, J., Woodhead, J., Wright, I., & Smith, I. (1996). Basalt and sediment geochemistry and magma petrogenesis in atransect from oceanic island arc to rifted continental margin arc: the Kermadec—Hikurangi Margin, SW Pacific. *Journal of Petrology, 37*(6), 1523-1546.

Gamble, J. A., Christie, R. H., Wright, I., & Wysoczanski, R. J. (1997). Primitive K-rich magmas from Clark Volcano, southern Kermadec Arc; a paradox in the K-depth relationship. *The Canadian Mineralogist, 35*(2), 275-290.

Garfunkel, Z., Anderson, C., & Schubert, G. (1986). Mantle circulation and the lateral migration of subducted slabs. *Journal of Geophysical Research: Solid Earth, 91*(B7), 7205-7223.

George, R., Turner, S., Morris, J., Plank, T., Hawkesworth, C., & Ryan, J. (2005). Pressure–temperature–time paths of sediment recycling beneath the Tonga–Kermadec Arc. *Earth and Planetary Science Letters, 233*(1-2), 195-211.

Gill, J. B. (1976). Composition and age of Lau Basin and Ridge volcanic rocks: Implications for evolution of an interarc basin and remnant arc. *Geological Society of America Bulletin, 87*(10), 1384-1395.

Gill, J. B., Tollstrup, D., & Todd, E. (2006). Hf mobility and immobility in subduction zones. *Geochimica et Cosmochimica Acta, 70*(18), A203.

Gledhill, K., & Gubbins, D. (1996). SKS splitting and the seismic anisotropy of the mantle beneath the Hikurangi subduction zone, New Zealand. *Physics of the Earth and Planetary Interiors, 95*(3-4), 227-236.

Gorczyk, W., Gerya, T. V., Connolly, J. A. D., & Yuen, D. A. (2007). Growth and mixing dynamics of mantle wedge plumes. *Geology, 35*(7), 587.

Graham, I. J., Reyes, A. G., Wright, I. C., Peckett, K. M., Smith, I. E., & Arculus, R. J. (2008). Structure and petrology of newly discovered volcanic centres in the northern Kermadec–southern Tofua arc, South Pacific Ocean. *Journal of Geophysical Research: Solid Earth, 113*(B8).

Greve, S. M., Savage, M. K., & Hofmann, S. D. (2008). Strong variations in seismic anisotropy across the Hikurangi subduction zone, North Island, New Zealand. *Tectonophysics, 462*(1-4), 7-21.

Greve, S. M., & Savage, M. K. (2009). Modelling seismic anisotropy variations across the Hikurangi subduction margin, New Zealand. *Earth and Planetary Science Letters, 285*(1-2), 16-26.

Gribble, R. F., Stern, R. J., Newman, S., Bloomer, S. H., & O'Hearn, T. (1998). Chemical and isotopic composition of lavas from the northern Mariana Trough: Implications for magmagenesis in back-arc basins. *Journal of Petrology, 39*(1), 125-154.

Haase, K. M., Worthington, T. J., Stoffers, P., Garbe-Schönberg, D., & Wright, I. (2002). Mantle dynamics, element recycling, and magma genesis beneath the Kermadec Arc-Havre Trough. *Geochemistry, Geophysics, Geosystems, 3*(11), 1-22.

Hanan, B., & Graham, D. (1996). Lead and helium isotope evidence from oceanic basalts for a common deep source of mantle plumes. *Science, 272*(5264), 991-995.

Hart, S., Glassley, W., & Karig, D. (1972). Basalts and sea floor spreading behind the Mariana island arc. *Earth and Planetary Science Letters, 15*(1), 12-18.

Hawkins, J. W. (1976). Tectonic setting and petrology of Samoa-Tonga-Fiji region. *SOPAC Technical Bulletin, 2*, 141-152.

Hawkins, J., Parson, L., & Allan, J. (1994). *4. COMPOSITION AND ORIGIN OF VOLCANICLASTIC SEDIMENTS IN THE LAU BASIN (SOUTHWEST PACIFIC), LEG 135 (SITES 834-839).* Paper presented at the Proceedings of the Ocean Drilling Program: Scientific results.

Herbert, K. R. (2013). Temporal distribution and frequency of explosive volcanism in the Kermadec Arc, SW Pacific: Insights from marine cores.

Hermann, J., Spandler, C., Hack, A., & Korsakov, A. V. (2006). Aqueous fluids and hydrous melts in high-pressure and ultra-high pressure rocks: implications for element transfer in subduction zones. *Lithos, 92*(3-4), 399-417.

Hermann, J., Zheng, Y. F., & Rubatto, D. (2013). Deep Fluids in Subducted Continental Crust. *Elements, 9*(4), 281-287.

Hochstaedter, A. G., Gill, J. B., Peters, R., Broughton, P., Holden, P., & Taylor, B. (2001). Across-arc geochemical trends in the Izu-Bonin arc: Contributions from the subducting slab. *Journal of Geochemistry, Geophysics, Geosystems, 2*(7).

Hochstaedter, A. G., Gill, J. B., Taylor, B., Ishizuka, O., Yuasa, M., & Monta, S. (2000). Across-arc geochemical trends in the Izu-Bonin arc: Constraints on source composition and mantle melting. *Journal of Geophysical Research: Solid Earth, 105*(B1), 495-512.

Hoernle, K., Abt, D. L., Fischer, K. M., Nichols, H., Hauff, F., Abers, G. A., Protti, M. (2008). Arc-parallel flow in the mantle wedge beneath Costa Rica and Nicaragua. *Nature, 451*(7182), 1094.

Hussong, D. M., & Fryer, P. (1983). Back-arc seamounts and the SeaMARC Ⅱ seafloor mapping system. *Eos, Transactions American Geophysical Union, 64*(45), 627-632.

Jarosewich, E., Nelen, J., & Norberg, J. A. (1980). Reference samples for electron microprobe analysis. *Geostandards and Geoanalytical Research, 4*(1), 43-47.

Jarrard, R. D. (1986). Relations among subduction parameters. *Reviews of Geophysics, 24*(2), 217.

Jochum, K. P., & Nohl, U. (2008). Reference materials in geochemistry and environmental research and the GeoReM database. *Chemical Geology, 253*(1-2), 50-53.

Jochum, K., & Enzweiler, J. (2013). Reference materials in geochemical and environmental research. *Treatise on Geochemistry: Second Edition*.

Johnson, M. C., & Plank, T. (1999). Geochemistry Geophysics Geosystems.

Karig, D. E. (1970). Ridges and basins of the Tonga-Kermadec Island Arc System. *Journal of Geophysical Research, 75*(2), 239-254.

Keith, M., Haase, K. M., Klemd, R., Smith, D. J., Schwarz-Schampera, U., & Bach, W. (2018). Constraints on the source of Cu in a submarine magmatic-hydrothermal system, Brothers volcano, Kermadec island arc. *Contributions to Mineralogy and Petrology, 173*(5), 40.

Kelemen, P. B., Shimizu, N., & Dunn, T. (1993). Relative depletion of niobium in some arc magmas and the continental crust: partitioning of K, Nb, La and Ce during melt/rock reaction in the upper mantle. *Earth and Planetary Science Letters, 120*(3-4), 111-134.

Kelley, K. A., Plank, T., Grove, T. L., Stolper, E. M., Newman, S., & Hauri, E. (2006). Mantle melting as a function of water content beneath back-arc basins. *Journal of Geophysical Research, 111*(B9).

Kelley, K. A., & Cottrell, E. (2009). Water and the oxidation state of subduction zone magmas. *Science, 325*(5940), 605-607.

Kemner, F., Haase, K. M., Beier, C., Krumm, S., & Brandl, P. A. (2015). Formation of andesite melts and Ca-rich plagioclase in the submarine Monowai volcanic system, Kermadec Arc. *Geochemistry, Geophysics, Geosystems, 16*(12), 4130-4152.

Kessel, R., Schmidt, M. W., Ulmer, P., & Pettke, T. (2005). Trace element signature of subduction-zone fluids, melts and supercritical liquids at 120–180 km depth. *Nature, 437*(7059), 724.

Klügel, A., Hansteen, T. H., & Galipp, K. (2005). Magma storage and underplating beneath Cumbre Vieja volcano, la Palma (Canary Islands). *Earth and Planetary Science Letters, 236*(1), 211-226.

Kneller, E. A., & van Keken, P. E. (2007). Trench-parallel flow and seismic anisotropy in the Mariana and Andean subduction systems. *Nature, 450*(7173), 1222-1225.

Kogiso, T., Omori, S., & Maruyama, S. (2009). Magma genesis beneath Northeast Japan arc: A new perspective on subduction zone magmatism. *Gondwana Research, 16*(3-4), 446-457.

Kusky, T. M., Windley, B. F., Wang, L., Wang, Z., Li, X., & Zhu, P. (2014). Flat slab subduction, trench suction, and craton destruction: Comparison of the North China, Wyoming, and Brazilian cratons. *Tectonophysics, 630*, 208-221.

Leat, P. T., Pearce, J. A., Barker, P. F., Millar, I. L., Barry, T. L., & Larter, R. D. (2004). Magma genesis and mantle flow at a subducting slab edge: the South Sandwich arc-basin system. *Earth and Planetary Science Letters, 227*(1-2), 17-35.

Machida, S., & Ishii, T. (2003). Backarc volcanism along the en echelon seamounts: The Enpo seamount chain in the northern Izu-Ogasawara arc. *Geochemistry, Geophysics, Geosystems, 4*(8).

Machida, S., Ishii, T., Kimura, J. I., Awaji, S., & Kato, Y. (2008). Petrology and geochemistry of cross-chains in the Izu-Bonin back arc: Three mantle components with contributions of hydrous liquids from a deeply subducted slab. *Geochemistry, Geophysics, Geosystems, 9*(5).

Malahoff, A., Feden, R. H., & Fleming, H. S. (1982). Magnetic anomalies and tectonic fabric of marginal basins north of New Zealand. *Journal of Geophysical Research, 87*(B5), 4109.

Marson-Pidgeon, K., & Savage, M. K. (1997). Frequency-dependent anisotropy in Wellington, New Zealand. *Geophysical Research Letters, 24*(24), 3297-3300.

Marson-Pidgeon, K., Savage, M. K., Gledhill, K., & Stuart, G. (1999). Seismic anisotropy beneath the lower half of the North Island, New Zealand. *Journal of Geophysical Research: Solid Earth, 104*(B9), 20277-20286.

Marson-Pidgeon, K., & Savage, M. K. (2004). Modelling shear wave splitting observations from Wellington, New Zealand. *Geophysical Journal International, 157*(2), 853-864.

Martínez, F., Fryer, P., Baker, N. A., & Yamazaki, T. (1995). Evolution of backarc rifting: Mariana Trough, 20–24 N. *Journal of Geophysical Research: Solid Earth, 100*(B3), 3807-3827.

Martinez, F., & Taylor, B. (2006). Modes of crustal accretion in back-arc basins: Inferences from the Lau Basin. *Back-arc spreading systems: geological, biological, chemical, and physical interactions*, 5-30.

Massoth, G. J., De Ronde, C. E., Lupton, J. E., Feely, R. A., Baker, E. T., Lebon, G. T., & Maenner, S. M. (2003). Chemically rich and diverse submarine hydrothermal plumes of the southern Kermadec volcanic arc (New Zealand). *Geological Society, London, Special Publications, 219*(1), 119-139.

Matcham, I., Savage, M., & Gledhill, K. (2000). Distribution of seismic anisotropy in the subduction zone beneath the Wellington region, New Zealand. *Geophysical Journal International, 140*(1), 1-10.

McCulloch, M. T., & Gamble, J. (1991). Geochemical and geodynamical constraints on subduction zone magmatism. *Earth and Planetary Science Letters, 102*(3-4), 358-374.

Mortimer, N., Herzer, R. H., Gans, P. B., Laporte-Magoni, C., Calvert, A. T., & Bosch, D. (2007). Oligocene–Miocene tectonic evolution of the South Fiji Basin and Northland Plateau, SW Pacific Ocean: Evidence from petrology and dating of dredged rocks. *Marine Geology, 237*(1-2), 1-24.

Mortimer, N., Gans, P., Palin, J., Meffre, S., Herzer, R., & Skinner, D. (2010). Location and migration of Miocene–Quaternary volcanic arcs in the SW Pacific region. *Journal of Volcanology and Geothermal Research, 190*(1-2), 1-10.

Nakakuki, T., & Mura, E. (2013). Dynamics of slab rollback and induced back-arc basin formation. *Earth and Planetary Science Letters, 361*, 287-297.

Nichols, G. T., Wyllie, P. J., & Stern, C. R. (1996). Experimental melting of pelagic sediment, constraints relevant to subduction. *Subduction top to bottom*, 293-298.

Nishizawa, A., Takahashi, N., & Abe, S. (1999). Crustal structure and seismicity of the Havre Trough at 26°S. *Geophysical Research Letters, 26*(16), 2549-2552.

Parson, L., Rothwell, R., & MacLeod, C. (1994). *Tectonics and sedimentation in the Lau Basin (southwest Pacific).* Paper presented at the Proceedings of the Ocean Drilling Program, Scientific Results.

Parson, L. M., & Wright, I. C. (1996). The Lau-Havre-Taupo back-arc basin: A southward-propagating, multi-stage evolution from rifting to spreading. *Tectonophysics, 263*(1-4), 1-22.

Pearce, J. A. (2008). Geochemical fingerprinting of oceanic basalts with applications to ophiolite classification and the search for Archean oceanic crust. *Lithos, 100*(1-4), 14-48.

Pearce, J. A., & Cann, J. (1973). Tectonic setting of basic volcanic rocks determined using trace element analyses. *Earth and Planetary Science Letters, 19*(2), 290-300.

Pearce, J. A., Stern, R. J., Bloomer, S. H., & Fryer, P. (2006). Geochemical mapping of the Mariana arc-basin system: Implications for the nature and distribution of subduction components. *Geochemistry, Geophysics, Geosystems, 6*(7).

Pelletier, B., Calmant, S., & Pillet, R. (1998). Current tectonics of the Tonga–New Hebrides region. *Earth and Planetary Science Letters, 164*(1-2), 263-276.

Ramillien, G., & Wright, I. C. (2000). Predicted seafloor topography of the New Zealand region: A nonlinear least squares inversion of satellite altimetry data. *Journal of Geophysical Research: Solid Earth, 105*(B7), 16577-16590.

Rapp, R. P., Irifune, T., Shimizu, N., Nishiyama, N., Norman, M. D., & Inoue, T. (2008). Subduction recycling of continental sediments and the origin of geochemically enriched reservoirs in the deep mantle. *Earth and Planetary Science Letters, 271*(1-4), 14-23.

Regelous, M., Gamble, J. A., & Turner, S. P. (2010). Mechanism and timing of Pb transport from subducted oceanic crust and sediment to the mantle source of arc lavas. *Chemical Geology, 273*(1-2), 46-54.

Rodríguez-González, J., Billen, M. I., & Negredo, A. M. (2014). Non-steady-state subduction and trench-parallel flow induced by overriding plate structure. *Earth and Planetary Science Letters, 401*, 227-235.

Roeder, P., & Emslie, R. (1970). Olivine-liquid equilibrium. *Contributions to mineralogy and petrology, 29*(4), 275-289.

Ruellan, E., Delteil, J., Wright, I., & Matsumoto, T. (2003). From rifting to active spreading in the Lau Basin - Havre Trough backarc system (SW Pacific): Locking/unlocking induced by seamount chain subduction. *Geochemistry, Geophysics, Geosystems, 4*(5), n/a-n/a.

Rüpke, L. H., Morgan, J. P., Hort, M., & Connolly, J. A. (2004). Serpentine and the subduction zone water cycle. *Earth and Planetary Science Letters, 223*(1-2), 17-34.

Saunders, K., Baker, J., & Wysoczanski, R. (2010). Microanalysis of large volume silicic magma in continental and oceanic arcs: Melt inclusions in Taupo Volcanic Zone and Kermadec Arc rocks, South West Pacific. *Journal of Volcanology and Geothermal Research, 190*(1-2), 203-218.

Savage, M. (1999). Seismic anisotropy and mantle deformation: what have we learned from shear wave splitting? *Reviews of Geophysics, 37*(1), 65-106.

Schellart, W., & Spakman, W. (2012). Mantle constraints on the plate tectonic evolution of the Tonga–Kermadec–Hikurangi subduction zone and the South Fiji Basin region. *Australian Journal of Earth Sciences, 59*(6), 933-952.

Sdrolias, M., Roest, W. R., & Müller, R. D. (2004). An expression of Philippine Sea plate rotation: the Parece Vela and Shikoku basins. *Tectonophysics, 394*(1-2), 69-86.

Sdrolias, M., & Müller, R. D. (2006). Controls on back-arc basin formation. *Geochemistry, Geophysics, Geosystems, 7*(4).

Sinton, J. M., & Fryer, P. (1987). Mariana Trough lavas from 18 N: Implications for the origin of back arc basin basalts. *Journal of Geophysical Research: Solid Earth, 92*(B12), 12782-12802.

Smith, G. P., Wiens, D. A., Fischer, K. M., Dorman, L. M., Webb, S. C., & Hildebrand, J. A. (2001). A complex pattern of mantle flow in the Lau backarc. *Science, 292*(5517), 713-716.

Smith, I. E. M., & Price, R. C. (2006). The Tonga–Kermadec Arc and Havre–Lau back-arc system: Their role in the development of tectonic and magmatic models for the western Pacific. *Journal of Volcanology and Geothermal Research, 156*(3-4), 315-331.

Sobolev, A. V., & Danyushevsky, L. V. (1994). Petrology and geochemistry of boninites from the north termination of the Tonga Trench: constraints on the generation conditions of primary high-Ca boninite magmas. *Journal of Petrology, 35*(5), 1183-1211.

Stern, R. J. (2002). Subduction zones. *Reviews of Geophysics, 40*(4).

Stoffers, P., Wright, I., De Ronde, C., Hannington, M. D., Herzig, P. M., & Villinger, H. (1999). Longitudinal transect of the Kermadec-Havre Trough back-arc system: initial results of the R/V Sonne cruise SO-135. *InterRidge News, 8*(1), 45-50.

Sun, S.-S., & McDonough, W.-s. (1989). Chemical and isotopic systematics of oceanic basalts: implications for mantle composition and processes. *Geological Society, London, Special Publications, 42*(1), 313-345.

Syracuse, E. M., van Keken, P. E., & Abers, G. A. (2010). The global range of subduction zone thermal models. *Physics of the Earth and Planetary Interiors, 183*(1-2), 73-90.

Tamura, Y., Tatsumi, Y., Zhao, D., Kido, Y., & Shukuno, H. (2002). Hot fingers in the mantle wedge: new insights into magma genesis in subduction zones. *Earth and Planetary Science Letters, 197*(1-2), 105-116.

Tatsumi, Y. (2000). Slab melting: Its role in continental crust formation and mantle evolution. *Geophysical Research Letters, 27*(23), 3941-3944.

Tatsumi, Y. (2005). The subduction factory: how it operates in the evolving Earth. *GSA today, 15*(7), 4.

Tatsumi, Y., Furukawa, Y., & Yamashita, S. (1994). Thermal and geochemical evolution of the mantle wedge in the northeast Japan arc: 1. Contribution from

experimental petrology. *Journal of Geophysical Research: Solid Earth, 99*(B11), 22275-22283.

Taylor, B., Zellmer, K., Martinez, F., & Goodliffe, A. (1996). Sea-floor spreading in the Lau back-arc basin. *Earth and Planetary Science Letters, 144*(1-2), 35-40.

Timm, C., Graham, I. J., de Ronde, C. E., Leybourne, M. I., & Woodhead, J. (2011). Geochemical evolution of Monowai volcanic center: New insights into the northern Kermadec Arc subduction system, SW Pacific. *Geochemistry, Geophysics, Geosystems, 12*(8).

Timm, C., de Ronde, C. E. J., Leybourne, M. I., Layton-Matthews, D., & Graham, I. J. (2012). Sources of Chalcophile and Siderophile Elements in Kermadec Arc Lavas. *Economic Geology, 107*(8), 1527-1538.

Timm, C., Bassett, D., Graham, I. J., Leybourne, M. I., De Ronde, C. E., Woodhead, J., . . . Watts, A. B. (2013). Louisville seamount subduction and its implication on mantle flow beneath the central Tonga–Kermadec Arc. *Nature communications, 4*, 1720.

Timm, C., Davy, B., Haase, K., Hoernle, K. A., Graham, I. J., de Ronde, C. E., . . . Gamble, J. A. (2014). Subduction of the oceanic Hikurangi Plateau and its impact on the Kermadec Arc. *Nat Commun, 5*, 4923.

Timm, C., Leybourne, M. I., Hoernle, K., Wysoczanski, R. J., Hauff, F., Handler, M., de Ronde, C. E. J. (2016). Trench-perpendicular Geochemical Variation Between two Adjacent Kermadec Arc Volcanoes Rumble II East and West: the Role of the Subducted Hikurangi Plateau in Element Recycling in Arc Magmas. *Journal of Petrology, 57*(7), 1335-1360.

Todd, E., Gill, J. B., Wysoczanski, R. J., Handler, M. R., Wright, I. C., & Gamble, J. A. (2010). Sources of constructional cross-chain volcanism in the southern Havre Trough: New insights from HFSE and REE concentration and isotope systematics. *Geochemistry, Geophysics, Geosystems, 11*(4).

Todd, E., Gill, J. B., Wysoczanski, R. J., Hergt, J., Wright, I. C., Leybourne, M. I., & Mortimer, N. (2011). Hf isotopic evidence for small-scale heterogeneity in the mode of mantle wedge enrichment: Southern Havre Trough and South Fiji Basin back arcs. *Geochemistry, Geophysics, Geosystems, 12*(9),

Tollstrup, D. L., & Gill, J. B. (2005). Hafnium systematics of the Mariana arc: Evidence for sediment melt and residual phases. *Geology, 33*(9), 737.

Tollstrup, D., Gill, J., Kent, A., Prinkey, D., Williams, R., Tamura, Y., & Ishizuka, O. (2010). Across-arc geochemical trends in the Izu-Bonin arc: Contributions from the subducting slab, revisited. *Geochemistry, Geophysics, Geosystems, 11*(1).

Wada, I., Behn, M. D., & Shaw, A. M. (2012). Effects of heterogeneous hydration in the incoming plate, slab rehydration, and mantle wedge hydration on slab-derived H 2 O flux in subduction zones. *Earth and Planetary Science Letters, 353-354*, 60-71.

Wallace, P. J. (2005). Volatiles in subduction zone magmas: concentrations and fluxes based on melt inclusion and volcanic gas data. *Journal of Volcanology and Geothermal Research, 140*(1-3), 217-240.

Wallace, L. M., Ellis, S., & Mann, P. (2009). Collisional model for rapid fore-arc block rotations, arc curvature, and episodic back-arc rifting in subduction settings. *Geochemistry, Geophysics, Geosystems, 10*(5).

Wallace, L. M., Reyners, M., Cochran, U., Bannister, S., Barnes, P. M., Berryman, K., Ellis, S. (2009). Characterizing the seismogenic zone of a major plate boundary subduction thrust: Hikurangi Margin, New Zealand. *Geochemistry, Geophysics, Geosystems, 10*(10).

Walowski, K. J., Wallace, P. J., Hauri, E., Wada, I., & Clynne, M. A. (2015). Slab melting beneath the Cascade Arc driven by dehydration of altered oceanic peridotite. *Nature Geoscience, 8*(5), 404.

Wiedicke, M., & Collier, J. (1993). Morphology of the Valu Fa spreading ridge in the southern Lau Basin. *Journal of Geophysical Research: Solid Earth, 98*(B7), 11769-11782.

Wilson, C., Houghton, B., McWilliams, M., Lanphere, M., Weaver, S., & Briggs, R. (1995). Volcanic and structural evolution of Taupo Volcanic Zone, New Zealand: a review. *Journal of Volcanology and Geothermal Research, 68*(1-3), 1-28.

Wood, D., Marsh, N., Tarney, J., Joron, J., Fryer, P., & Treuil, M. (1981). 33. GEOCHEMISTRY OF IGNEOUS ROCKS RECOVERED FROM A TRANSECT ACROSS THE MARIANA TROUGH, ARC, FORE-ARC, AND TRENCH, SITES 453 THROUGH 461, DEEP SEA DRILLING PROJECT LEG 601. *Hussong DM, Uyeda S. et al., Init. rep. of the Deep Sea Drilling Project, XL.–Washington, US Gov. Print. Off*, 611-642.

Woodhead, J., Eggins, S., & Gamble, J. (1993). High field strength and transition element systematics in Island arc and back-arc basin basalts: evidence for multi-phase melt extraction and a depleted mantle wedge. *Earth and Planetary Science Letters, 114*(4), 491-504.

Woodhead, J., Hergt, J., Greig, A., & Edwards, L. (2011). Subduction zone Hf-anomalies: Mantle messenger, melting artefact or crustal process? *Earth and Planetary Science Letters, 304*(1-2), 231-239.

Wright, I., Carter, L., & Lewis, K. (1990). GLORIA survey of the oceanic-continental transition of the Havre-Taupo back-arc basin. *Geo-marine letters, 10*(2), 59-67.

Wright, I. C. (1993). Pre-spread rifting and heterogeneous volcanism in the southern Havre Trough back-arc basin. *Marine Geology, 113*(3-4), 179-200.

Wright, I. (1996). Volcaniclastic processes on modern submarine arc stratovolcanoes: sidescan and photographic evidence from the Rumble IV and V volcanoes, southern Kermadec Arc (SW Pacific). *Marine Geology, 136*(1-2), 21-39.

Wright, I. C., Parson, L. M., & Gamble, J. A. (1996). Evolution and interaction of migrating cross-arc volcanism and backarc rifting: An example from the Southern Havre Trough (35°20′-37°S). *Journal of Geophysical Research: Solid Earth, 101*(B10), 22071-22086. Wright, I. C. (1997). Morphology and Evolution of the Remnant Colville and Active Kermadec Arc Ridges South of 33°30′ S. *Marine Geophysical Researches, 19*(2), 177-193.

Wright, I. C., Worthington, T. J., & Gamble, J. A. (2006). New multibeam mapping and geochemistry of the 30°–35° S sector, and overview, of southern Kermadec Arc volcanism. *Journal of Volcanology and Geothermal Research, 149*(3-4), 263-296.

Wysoczanski, R. J., Wright, I. C., Gamble, J. A., Hauri, E. H., Luhr, J. F., Eggins, S. M., & Handler, M. R. (2006). Volatile contents of Kermadec Arc–Havre Trough pillow glasses: Fingerprinting slab-derived aqueous fluids in the mantle sources of arc and back-arc lavas. *Journal of Volcanology and Geothermal Research, 152*(1-2), 51-73.

Wysoczanski, R. J., Todd, E., Wright, I. C., Leybourne, M. I., Hergt, J. M., Adam, C., & Mackay, K. (2010). Backarc rifting, constructional volcanism and nascent disorganised spreading in the southern Havre Trough backarc rifts (SW Pacific). *Journal of Volcanology and Geothermal Research, 190*(1-2), 39-57.

Wysoczanski, R. J., & Clark, M. R. (2012). Southern Kermadec Arc–Havre Trough Geohabitats and Biological Communities *Seafloor Geomorphology as Benthic Habitat* (pp. 853-867): Elsevier.

Wysoczanski R., M. J., Barton, S., Black, J., Boschen, R.., Kaiser, S., Khong, L., Mitchell J., Pallentin, A., Stewart, R., Timm, C., Wilcox S., & Woelz, S. (2012). *NIRVANA - TAN1213 R.V. Tangaroa Research Voyage Report. NIWA Internal Report*. Retrieved from Wellington New Zealand.

Wysoczanski R., L., G., Carey, R., Davey, N., Davey, F., Higgs, B., Ikegami, F., Nichols, A., S., Woelz, Wilcox S., Wilkinson, S., & Zohrab, A. (2015). *SAMSARA - TAN1513,*

R/V Tangaroa Research Voyage Report. Retrieved from Wellington New Zealand

Yamazaki, T., Murakami, F., & Saito, E. (1993). Mode of seafloor spreading in the northern Mariana Trough. *Tectonophysics, 221*(2), 207-222.

Zhao, G., Luo, W., Lai, Z., Tian, L., & Xu, C. (2016). Influence of subduction components on magma composition in back-arc basins: A comparison between the Mariana and Okinawa troughs. *Geological Journal, 51*(S1), 357-367.

Zohrab, A. (2016). The Petrology, Geochemistry and Geochronology of Back-Arc Stratovolcanoes in the Southern Kermadec Arc-Havre Trough, SW Pacific.

Appendices

Appendix A: Sample information

Table A.0-1: Details of samples analysed in this study.

Sample	Location	XRF	ICP-MS	EMPA
TAN1213-3 -2	Ngatoro Basin	x		
TAN1213-3-5	Ngatoro Basin	x		
TAN1213-6-1	Ngatoro Basin	x	x	
TAN1213-6-3	Ngatoro Basin	x	x	x
TAN1213-10-2	Basin E	x	x	x
TAN1213-10-9	Basin E	x		
TAN1213-11-1	Basin E	x		x
TAN1513 040-2	Basin I			x
TAN1513 041-3	Basin I			x
TAN1513 042-2	Basin I			
TAN1213-47-1	Basin G	x		x
TAN1213-47-2	Basin G	x		x
TAN1213-50-3	Basin C	x		x
TAN1213-50-4	Basin C	x		
TAN1213-51-4	Basin D	x		x
TAN1213-51-6	Basin D	x		
TAN1213-51-7	Basin D	x		
TAN1213-55-1	Basin B		x	
TAN1213-55-2	Basin B	x	x	x
TAN1213-55 Dup	Basin B		x	
TAN1213-56-1	Basin B	x	x	
TAN1213-56-3	Basin B	x		x
TAN1213-56-3 (Archive)	Basin B	x		
TAN1313 DR-15-1	Basin H			
TAN1512-DR-24-1	Basin J			
TAN1512-DR 25-1	Basin J			
TAN1512-DR 10-1	Basin K			
TAN1512- DR10-2	Basin K			x
TAN1512- DR-10-3	Basin K		x	
TAN1512 -DR 10-4	Basin K		x	

Appendix B: Petrographic descriptions

TAN1213 3-5

Basaltic Andesite. 40% groundmass, 20-30% phenocrysts, 30-40% vesicles. Phenocrysts consist of 60% acicular plagioclase (0.5-2 mm) 30% olivine (0.1-0.8 mm), 10% pyroxenes (0.2-0.5 mm), are non-foliated and few glomecrysts are present consisting of predominantly plagioclase and olivine. Groundmass consists of 60% acicular plagioclase, 20% glass, 10% olivine and <5% Fe-Ti oxides. Vesicles range in size from 0.3-0.7 mm and are sub-angular to sub-rounded, and are generally singular.

TAN1213 006-3

Basaltic Andesite. 45% groundmass, 25% phenocrysts, 40% vesicles. Phenocrysts consist of 70% plagioclase (0.6-2 mm), 90 % acicular, 10% euhedral with zoning and moth-eaten sieve-like textures. 20% olivine (<0.8 mm) some with opaque inclusions and 5% pyroxenes (<0.5 mm) and all are non-foliated. Few glomecrysts consisting of plagioclase, olivine and clinopyroxene. Vesicles range in size (0.5-2 mm) and are generally singular, and sub-rounded. Groundmass consists of 60% acicular plagioclase, 50% olivine, 5% pyroxene and 10% Fe-Ti oxides and brown glass.

TAN1213 10-2

Basalt. 30-40% groundmass, 10% phenocrysts, 60-65% vesicles. Phenocrysts consist of 60% plagioclase (0.8-1 mm) 80% acicular with simple twining, 20% euhedral and tabular with zoning and sieve-like textures, 35% olivine (0.2-1 mm) <5% pyroxenes (0.1-0.7 mm) and are non-foliated. Few glomecrysts consisting of predominantly plagioclase, olivine and pyroxenes. Vesicles range in size from 0.5-2 mm in size are singular and sub-rounded to rounded. Groundmass consists of

80% acicular plagioclase, 10% dark brown glass and Fe-Ti oxides, 5% olivine and pyroxene.

TAN1213 11-1

Basalt. 55-60% groundmass, 15-20% phenocrysts, 45% vesicles. Phenocrysts consists of 30-35% acicular plagioclase (0.2-1 mm), 60% olivine (0.5-1 mm), <5% pyroxene (0.6-1 mm) all appear to be interlocking and non-foliated. Vesicles range in size from 0.5-1 mm and are singular and sub- rounded. Groundmass consists of 25% dark brown glass and Fe-Ti oxides and 60% acicular plagioclase, 15% olivine and pyroxene.

TAN1213 47-1

Basalt. 40% groundmass, 5-10% phenocrysts, 35-45% vesicles. Phenocrysts consist of 30-35% plagioclase (0.1-0.8 mm), 90% acicular, 10% tabular and euhedral weakly zoned, 60% olivine (0.4-0.9 mm) few with opaque inclusions, <5% pyroxene (0.3-0.6 mm). Few glomecrysts (0.2-0.5 mm) consisting of plagioclase, olivine and pyroxene. Vesicles range in size from 0.3-1 mm, are generally singular and sub-angular to sub-rounded. Groundmass consists of 80% acicular plagioclase, 10% olivine and pyroxene, 10% brown glass and Fe-Ti oxides.

TAN1213 47-2

Basalt. 60% groundmass, 10% phenocrysts, 30% vesicles. Phenocrysts consists of 45% acicular and tabular plagioclase (0.3-0.7 mm) weakly zoned, 20% olivine (0.3-1 mm) <10% pyroxene (0.3-0.6 mm) both contain opaque inclusions. Few glomecrysts (0.3-0.8 mm) consisting of plagioclase, olivine and pyroxene. Vesicles range in size from 0.4-1.5 mm, are generally singular and sub-rounded few are coalesced. Groundmass consists of 80% acicular plagioclase, 15% olivine and pyroxene, <5% light brown glass and Fe-Ti oxides.

TAN1213 50-3

Basaltic Andesite. 60% groundmass, 15% phenocrysts, 25% vesicles. Phenocrysts consist of 50% plagioclase (0.4-0.8 mm), 90% acicular, 10% tabular with twining. 40% olivine (0.2-0.5 mm), 10% pyroxenes (0.1-0.5 mm). Few

glomecrysts present (0.3-0.8 mm) consisting of plagioclase, olivine and pyroxene. Tabular and euhedral plagioclase contain opaque inclusions (10-50μm). Vesicles range in size from 0.5-1 mm and are singular and sub-rounded. Groundmass consists of 70% acicular plagioclase, 20% brown glass and Fe-Ti oxide, 5% olivine and 5% pyroxene.

TAN1213 51-4

Basalt. 30-40% groundmass, 10-20% phenocryst, 40-50% vesicles. Phenocrysts consist of 50% plagioclase (0.3-0.8 mm) 70% acicular, 25% tabular 5% euhedral and weakly zoned. 45% olivine (0.3-1 mm) with opaque inclusions, 10-20% pyroxene (0.4-0.6 mm). Few glomecrysts (0.5-1 mm) consisting predominantly of plagioclase, few olivine and pyroxene. Vesicles range in size from 0.2-0.8 mm and are singular, sub-rounded to rounded. Groundmass consists of 75% acicular plagioclase, 15% olivine, 10% brown glass and Fe-Ti oxides.

TAN1213 55-2

Basalt. 30% groundmass, 10-20% phenocrysts, 60% vesicles. Phenocrysts consists of 40% plagioclase (0.4-1.5 mm) acicular, tabular with sieve-like textures and euhedral with weak to moderate zoning. 55% olivine (0.3-0.7 mm) with opaque inclusions, <5% pyroxene (0.3-0.7 mm). Few glomecrysts consisted of acicular plagioclase, olivine and pyroxene. Vesicles range in size from 0.2-1 mm and are sub-angular to sub-rounded generally singular, few coalesced. Groundmass consists of 25% acicular plagioclase, <5% olivine, 70% brown glass and Fe-Ti oxides.

TAN1213 56-1

Basalt. 45% groundmass, 5-10% phenocrysts, 40-45% vesicles. Phenocrysts consist of 30-40% acicular plagioclase (0.2-0.8 mm) few euhedral, 40% olivine (0.4-0.8 mm) with opaque inclusions. 10% pyroxene (0.3-0.6 mm). Few glomecrysts consisted of acicular plagioclase, olivine and pyroxene. Vesicles range in size from (0.2-1.5 mm) are both singular and coalesced and are typically sub-angular to rounded. Groundmass consists of 80% acicular plagioclase 10% olivine and pyroxenes, 10% brown glass and Fe-Ti oxides.

TAN1213 56-3

Basalt. 50% groundmass, 5-10% phenocrysts, 40-45% vesicles. Phenocrysts consist of 30-40% plagioclase (0.3-0.8 mm) acicular, tabular and euhedral. 40-50% olivine (0.4-0.7 mm) few with small opaque inclusions. 20% pyroxene (0.4-0.6 mm). Few glomecrysts consisted of acicular plagioclase, olivine and pyroxene. Vesicles range in size from 0.3-1.5 mm and are angular-sub-rounded and are generally singular. Groundmass consists of 65% acicular plagioclase, 5% olivine 30% brown glass and Fe-Ti oxides.

TAN1512 DR 10-2

Basalt. 55% groundmass, 15% phenocrysts, 30% vesicles. Phenocrysts consist of 40% plagioclase (0.4-0.9 mm) acicular, tabular and euhedral with zoning. 50% olivine (0.4-0.8 mm), 10% pyroxene (0.3-0.6 mm). Few glomecrysts consisting of predominantly plagioclase, few olivine and pyroxene (0.5-1 mm), Vesicles range in size from 0.1-1 mm, are sub-angular to rounded and are generally singular with few coalesced vesicles. Groundmass consists of 60% acicular plagioclase, 5% olivine, 35% brown glass and Fe-Ti oxides.

Appendix C: Whole rock major element data

Table C.0-1: Major element concentrations for whole rock samples from basins A-B analysed by XRF. Oxide abundances given in wt. %, LOI is weight loss on ignition at 1000°C for 1 hour

Basin	A	A	A	A	B	B	B
Sample number	3 2	3 5	006-1	006-3	55-2	56-3	56 Archive
Latitude	-36.619	-36.619	-36.5965	-36.5965	-35.828	-35.859	-35.859
Longitude	177.16	177.1598	177.1598	177.1598	178.281	178.3	178.2998
Major element oxides							
SiO_2	52.43	52.36	51.35	51.81	50.65	51.88	51.63
TiO_2	1.04	1.08	0.98	1.00	0.89	0.92	0.91
Al_2O_3	17.26	17.05	16.68	17.21	15.74	16.21	16.13
Fe_2O_3	7.69	7.91	9.37	9.11	11.38	9.27	9.33
MnO	0.14	0.14	0.16	0.16	0.15	0.16	0.16
MgO	6.47	6.36	7.78	6.83	9.59	7.68	7.87
CaO	10.97	10.76	9.85	10.08	10.81	10.24	10.20
Na_2O	3.29	3.59	2.92	2.83	2.52	3.00	3.11
K_2O	0.47	0.50	0.63	0.68	0.36	0.46	0.48
P_2O_5	0.24	0.24	0.28	0.28	0.19	0.18	0.18
LOI	0.588	0.552	1.783	1.062	0.3	0.263	0.132
Total	100.58	99.4	98.13	101.05	99.61	99.65	99.82

Table C.0-2: Major element concentrations for whole rock samples from basins C-E analysed by XRF.

Basin	C	C	D	D	D	E	E
Sample number	50-3	50-4	51-4	51-6	51-7	10 2	10 9
Latitude	-35.4318	-35.4318	-35.3933	-35.3933	-35.3933	-35.2052	-35.2052
Longitude	178.404	178.404	178.2277	178.2277	178.2277	178.587	178.587
Major element oxides							
SiO_2	52.81	52.5	51.3	51.1	51.21	51.10	51.95
TiO_2	1.12	1.10	0.94	0.95	0.91	0.93	0.75
Al_2O_3	16.20	16.11	16.18	16.13	16.21	15.96	17.26
Fe_2O_3	11.18	11.4	8.4	9.05	8.94	9.24	10.80
MnO	0.18	0.19	0.13	0.15	0.15	0.15	0.12
MgO	4.59	4.72	7.80	8.31	8.35	8.51	5.41
CaO	9.85	9.83	11.08	11.05	11.09	10.89	10.47
Na_2O	3.23	3.3	3.7	2.71	2.57	2.65	2.43
K_2O	0.63	0.6	0.3	0.36	0.39	0.38	0.63
P_2O_5	0.19	0.19	0.17	0.18	0.19	0.18	0.17
LOI	0.603	0.72	0.014	0.774	0	0.737	3.832
Total	98.95	99.11	100.19	99.12	100.57	99.26	99.15

Table C.0-3: Major element concentrations for whole rock samples from basins E-I analysed by XRF .

Basin	E	E	G	G	H	I	I
Sample number	10 13	11 1	47-1	47-2	TAN1313 DR15-1	TAN1513-040	TAN1513-040 Archive
Latitude	-35.2052	-35.1985	-34.7692	-34.7692	-35.9985	-35.3166	-35.3166
Longitude	178.587	178.6723	179.0802	179.0802	177.2583	177.7389	177.7389
Major element oxides							
SiO_2	51.45	51.96	51.4	51.6	50.19	49.03	48.58
TiO_2	0.97	0.98	1	1	0.88	0.75	0.74
Al_2O_3	16.75	15.95	16.32	16.31	16.25	13.80	14.19
Fe_2O_3	12.34	8.92	8.38	8.55	10.17	9.49	9.49
MnO	0.17	0.15	0.15	0.15	0.22	0.21	0.18
MgO	4.27	7.65	8.21	8.02	6.67	10.40	10.64
CaO	10.14	10.99	11.20	11.25	11.91	13.77	13.79
Na_2O	3.15	2.86	2.79	2.79	2.4	1.93	1.85
K_2O	0.58	0.35	0.47	0.46	0.43	0.44	0.38
P_2O_5	0.17	0.18	0.15	0.15	0.13	0.17	0.17
LOI	0.48	0.13	0.54	0.81	0.94	1.70	1.135
Total	99.51	99.86	99.6	99.2	100.2	100	100

Table C.0-4: Major element concentrations for whole rock samples from basins I-K analysed by XRF

Basin	I	I	I	J	K	K
Sample number	TAN1513-041	TAN1513-042	TAN1513-042 Archive	TAN1512 DR25-1	TAN1512 DR10-1	TAN1512 DR10-2
Latitude	-35.3269	-35.416	-35.416	-34.7235	-33.7077	-33.7077
Longitude	177.7823	177.9552	177.9552	178.0853	178.0853	178.0853
Major element oxides						
SiO_2	48.45	47.77	50.10	48.39	47.15	47.65
TiO_2	0.80	0.91	0.99	0.55	0.82	0.89
Al_2O_3	15.09	16.81	16.26	14.88	17.83	17.63
Fe_2O_3	9.59	11.22	9.12	9.46	11.04	11.60
MnO	0.21	0.21	0.20	0.17	0.18	0.18
MgO	10.14	8.43	9.19	9.74	5.91	5.85
CaO	12.98	11.89	11.49	13.51	12.57	12.50
Na_2O	1.90	2.34	2.21	1.45	2.54	2.98
K_2O	0.65	0.25	0.30	0.49	0.28	0.37
P_2O_5	0.19	0.16	0.13	0.23	0.27	0.45
LOI	2.19	4.01	1.98	1.51	1.8	1.7
Total	100	100	100	100.3	100.1	100.3

Note: samples from basin I were analysed previously and samples from basin J and K were analysed at Ontario Geosciences Lab.

Table C.0-5: Major element concentrations for whole rock samples from basins K analysed by XRF.

Basin	**K**	**K**
Sample number	TAN1512 DR10-3	TAN1512 DR10-4
Latitude	-33.7077	-33.7077
Longitude	178.0853	178.0853
Major element oxides		
SiO_2	47.45	49.04
TiO_2	0.90	0.94
Al_2O_3	17.47	17.12
Fe_2O_3	11.69	9.36
MnO	0.20	0.23
MgO	5.59	6.27
CaO	12.94	12.87
Na_2O	2.94	2.82
K_2O	0.37	0.39
P_2O_5	0.45	0.19
LOI	1.88	1.37
Total	100	100

Appendix D: Whole rock trace element data

Table D.0-1: Trace element concentrations for basin A (All trace element data is in ppm unless otherwise stated).

Location	Basin A			
Sample number	**3 2**	**3 5**	**006-1**	**006-3**
Structure	Ridge	Ridge	Floor	Floor
MgO (wt%)	6.36	6.13	7.64	6.59
Al2O3	16.93	16.31	16.33	16.67
CaO	10.59	10.38	9.48	9.54
MnO	0.14	0.14	0.16	0.16
Li (ppm)	3.87	4.10	6.13	5.70
Sc	33.1	33.8	30.7	31.0
V	210	210	216	218
Cr	135	124	217	180
Co	28.4	28.1	31.8	29.6
Ni	62.6	56.4	132	98
Cu	56.8	60.1	40.3	40.2
Zn	57	59	71	73
Ga	15.2	15.0	16.2	16.2
Rb	6.58	7.33	8.14	9.21
Sr	245	240	291	294
Y	22.3	22.7	24.1	24.2
Zr	97.2	100.0	129	130
Nb	4.12	4.26	5.56	5.51
Cs	0.14	0.15	0.23	0.24
Ba	110	112	178	178
La	6.92	7.10	11.3	11.3
Ce	17.6	18.1	27.6	27.7
Pr	2.57	2.60	3.73	3.75
Nd	12.0	12.3	16.1	16.0
Sm	3.17	3.15	3.75	3.73
Eu	1.15	1.21	1.18	1.22
Gd	3.65	3.81	4.11	4.13
Tb	0.60	0.62	0.65	0.65
Dy	4.03	4.19	4.14	4.18
Ho	0.82	0.85	0.88	0.89
Er	2.30	2.37	2.48	2.47
Tm	0.34	0.35	0.37	0.39
Yb	2.25	2.27	2.35	2.35
Lu	0.32	0.32	0.36	0.37
Hf	2.42	2.44	3.04	3.03
Ta	0.26	0.26	0.32	0.33
Pb	1.90	1.89	2.91	3.04
Th	0.58	0.63	0.85	0.84
U	0.24	0.19	0.27	0.27

Table D.0-2: Trace element concentrations for basin B

Location	Basin B				
Sample number	**055-1**	**055-2**	**055-2 dup**	**56 3**	**56 Archive**
Structure	Floor	Floor	Floor	Floor	Floor
MgO (wt%)	7.10	9.22	9.39	7.43	7.24
Al2O3	15.65	15.42	15.51	15.77	15.54
CaO	10.01	10.71	10.89	10.00	9.85
MnO	0.15	0.15	0.15	0.16	0.15
Li (ppm)	3.55	3.01	3.16	3.42	3.14
Sc	31.9	33.6	34.4	32.5	31.8
V	262	259	259	258	253
Cr	267	339	352	248	246
Co	33.5	38.4	40.3	35.9	34.8
Ni	105	174	177	110.7	108.7
Cu	59.8	62.3	63.8	58.8	56.8
Zn	60	69	55	59	62
Ga	15.6	14.5	14.4	15.2	14.6
Rb	7.83	5.02	5.08	7.19	6.96
Sr	251	241	240	250	239
Y	20.0	17.3	17.2	20.5	19.5
Zr	67	57	56	66.3	63.8
Nb	2.55	2.63	2.56	2.64	2.66
Cs	0.16	0.11	0.11	0.19	0.18
Ba	150	113	112	152	147
La	5.4	4.8	4.8	5.48	5.17
Ce	12.6	11.2	11.4	13.0	12.3
Pr	1.88	1.63	1.67	1.94	1.82
Nd	8.8	7.8	7.9	9.1	8.4
Sm	2.48	2.31	2.22	2.49	2.37
Eu	0.93	0.84	0.85	0.94	0.88
Gd	2.82	2.58	2.62	3.03	2.72
Tb	0.52	0.46	0.44	0.52	0.49
Dy	3.33	3.00	2.94	3.40	3.24
Ho	0.73	0.63	0.63	0.75	0.70
Er	2.01	1.73	1.77	2.07	1.99
Tm	0.31	0.28	0.28	0.32	0.31
Yb	2.04	1.72	1.78	2.03	2.02
Lu	0.30	0.25	0.25	0.30	0.28
Hf	1.76	1.57	1.48	1.75	1.68
Ta	0.20	0.22	0.20	0.18	0.19
Pb	1.14	0.92	0.89	1.21	1.20
Th	0.72	0.59	0.59	0.73	0.67
U	0.22	0.18	0.18	0.22	0.21

Table D.0-3: Trace element concentrations for basins C, D and E

Location	Basin C			Basin D			Basin E	
Sample number	**50 3**	**50 4**	**50 4 dup**	**51 4**	**51 6**	**51 7**	**010-2**	**10 9**
Structure	Ridge	Ridge	Ridge	Ridge	Ridge	Ridge	Ridge	Ridge
MgO (wt%)	4.57	4.56	4.40	7.08	7.84	7.94	8.58	5.07
Al2O3	15.39	15.12	14.69	15.31	14.99	14.87	16.07	15.96
CaO	9.63	9.17	8.71	10.23	10.11	10.50	11.02	9.74
MnO	0.19	0.18	0.17	0.12	0.14	0.14	0.15	0.12
Li (ppm)	3.45	3.98	3.77	2.45	3.03	2.88	2.86	4.84
Sc	37.0	34.8	33.9	33.6	33.9	34.2	35.0	34.9
V	334	311	298	250	257	255	285	303
Cr	7	12	11	256	260	270	305	26
Co	34.7	33.5	31.5	34.2	34.9	35.3	37.8	33.8
Ni	13.9	13.6	11.9	120.0	124.3	133.2	140	21.3
Cu	117.4	109.5	104.6	57.2	66.0	64.3	70.7	136.7
Zn	77	74	76	57	63	60	59	177
Ga	16.3	16.2	15.3	13.9	14.4	14.0	15.4	15.0
Rb	8.48	7.96	7.73	3.55	5.01	5.78	5.50	8.72
Sr	253	246	237	263	235	239	255	274
Y	23.8	23.2	22.6	17.4	17.3	17.4	18.6	15.9
Zr	74.2	70.8	68.0	54.9	56.7	55.2	60	41.3
Nb	2.51	2.43	2.31	2.63	2.66	2.68	2.70	0.75
Cs	0.16	0.19	0.20	0.10	0.12	0.13	0.12	0.11
Ba	185	178	172	108	115	117	127	301
La	5.83	5.51	5.38	4.75	4.85	4.95	5.1	4.26
Ce	14.4	13.7	13.1	11.0	11.4	11.7	12.1	9.3
Pr	2.19	2.03	1.97	1.66	1.72	1.72	1.79	1.40
Nd	11.0	10.2	9.8	7.8	7.7	8.0	8.4	6.8
Sm	3.11	2.96	2.89	2.15	2.19	2.16	2.36	2.04
Eu	1.15	1.07	1.02	0.79	0.82	0.83	0.90	0.76
Gd	3.68	3.42	3.32	2.50	2.63	2.63	2.76	2.37
Tb	0.63	0.62	0.61	0.46	0.47	0.47	0.47	0.42
Dy	4.40	4.02	3.82	2.91	2.96	2.90	3.13	2.85
Ho	0.90	0.85	0.84	0.65	0.64	0.63	0.68	0.58
Er	2.63	2.39	2.38	1.86	1.77	1.81	1.85	1.65
Tm	0.37	0.37	0.37	0.27	0.28	0.27	0.29	0.25
Yb	2.51	2.34	2.32	1.76	1.81	1.75	1.83	1.71
Lu	0.37	0.34	0.34	0.25	0.25	0.25	0.28	0.24
Hf	2.01	1.92	1.85	1.49	1.49	1.46	1.63	1.27
Ta	0.16	0.17	0.15	0.17	0.18	0.17	0.25	0.05
Pb	1.52	1.50	1.45	0.67	0.97	0.98	0.94	3.67
Th	0.68	0.66	0.63	0.56	0.58	0.59	0.62	0.55
U	0.28	0.22	0.22	0.24	0.19	0.18	0.19	0.24

Table D.0-4: Trace element concentrations for basin E, G and H.

Location	Basin E		Basin G		Basin H
Sample number	**10 13**	**11 1**	**47-1**	**47-2**	**14-1**
Structure	Ridge	Ridge	Floor	Floor	Ridge
MgO (wt%)	4.38	7.08			
Al2O3	16.93	15.23			
CaO	9.98	10.51			
MnO	0.17	0.15			
Li (ppm)	10.47	3.83	10	10	4.4
Sc	41.3	36.2	32.0	35.0	36.3
V	406	262	254	271	272
Cr	8.56	238	450	510	52
Co	38.9	33.5	38	38	40.1
Ni	11.6	97.1	129	130	64.4
Cu	137.0	78.1	77	78	117.9
Zn	86	60	58	60	71
Ga	17.0	14.2	15.1	16.1	15.2
Rb	17.41	6.48	7	7	6.98
Sr	311	218	260	274	276
Y	20.7	19.6	19.4	20.4	19.8
Zr	52.8	66.8	75	81	58
Nb	0.88	2.30	2.4	2.2	1.65
Cs	1.19	0.22	0.19	0.21	0.20
Ba	348	120	134	135	185
La	3.84	4.62	5.90	5.60	5.84
Ce	9.7	11.3	14.5	14.1	12.8
Pr	1.56	1.76			
Nd	8.1	8.4	10.3	10.2	10.0
Sm	2.47	2.47	2.93	2.91	2.70
Eu	0.98	0.93	1.06	1.05	0.96
Gd	3.01	3.02	3.41	3.28	3.26
Tb	0.55	0.50	0.56	0.59	0.53
Dy	3.74	3.56	3.48	3.69	3.44
Ho	0.78	0.75	0.76	0.82	0.74
Er	2.28	1.65	1.97	2.32	2.12
Tm	0.33	0.30	0.34	0.34	0.30
Yb	2.22	1.95	1.93	2.23	2.02
Lu	0.31	0.28	0.29	0.33	0.35
Hf	1.64	1.75	2.00	2.10	1.61
Ta	0.06	0.17	0.10	0.20	0.10
Pb	1.46	1.05	2.16	1.34	2.60
Th	0.53	0.53	0.86	0.71	1.00
U	0.26	0.16	0.46	0.27	0.30

Table D.0-5: Trace element concentrations for basin J and K.

Location	Basin J	Basin K			
Sample number	**DR25-1**	**DR10-1**	**DR10-2**	**DR10-3**	**DR10-4**
Structure	Ridge	Cone	Cone	Cone	Cone
MgO (wt%)				5.78	5.63
Al2O3				17.03	17.33
CaO				12.10	12.93
MnO				0.18	0.21
Li (ppm)	4.60			9.31	7.89
Sc	44.6	48.2	47.6	43.2	45.6
V	255	358	357	342	369
Cr	424	45	45	39	42
Co	47.1	39.3	39.2	37.3	39.0
Ni	153	46.2	49.2	45	44
Cu	60.6	97.5	145	127	98.3
Zn	69	92	86	86	91
Ga	11.6	15.8	15.5	15.3	15.8
Rb	5.48	2.70	2.96	4.20	3.49
Sr	347	331	330	320	338
Y	21.7	22.8	21.4	20.0	22.4
Zr	37	40	39	41	41
Nb	0.83	1.04	0.97	0.97	1.02
Cs	0.03	0.03	0.02	0.06	0.02
Ba	204	133	136	137	133
La	10.44	4.32	4.10	4.0	4.2
Ce	17.7	8.2	8.0	8.2	8.4
Pr				1.38	1.44
Nd	12.7	7.2	7.0	6.9	7.1
Sm	3.15	2.15	2.14	2.04	2.10
Eu	1.03	0.85	0.85	0.84	0.86
Gd	3.41	2.84	2.79	2.48	2.51
Tb	0.50	0.48	0.48	0.45	0.47
Dy	3.17	3.17	3.10	3.01	3.15
Ho	0.66	0.72	0.67	0.66	0.70
Er	1.92	2.18	2.15	1.87	1.98
Tm	0.27	0.32	0.31	0.29	0.31
Yb	1.67	2.06	1.95	1.87	2.01
Lu	0.25	0.31	0.31	0.27	0.31
Hf	1.06	1.18	1.17	1.23	1.26
Ta	0.04	0.06	0.06	0.12	0.12
Pb	3.20	1.90	1.70	1.41	1.49
Th	1.40	0.38	0.36	0.36	0.37
U	0.81	1.62	1.80	1.87	1.68

Appendix E: Mineral major element data

Table E.1: Major element composition for olivine from basin A. All major element data is in wt. % unless otherwise stated.

TAN1213-3-5							
Basin A							
Olivine	3-5-01-core	3-5-01-rim	3-5-02-core	3-5-02-rim	3-5-03-core	3-5-03-rim	3-5-04-core
Oxides							
SiO_2	39.44	39.28	39.42	39.42	39.65	39.59	39.44
TiO_2	0.00	0.00	0.01	0.00	0.00	0.00	0.00
Al_2O_3	0.01	0.03	0.03	0.01	0.02	0.00	0.05
FeOt	15.49	16.01	14.99	15.90	15.89	15.58	16.24
MnO	0.25	0.31	0.25	0.28	0.27	0.26	0.24
MgO	44.86	44.85	44.85	44.59	44.61	44.12	44.75
CaO	0.21	0.24	0.22	0.25	0.24	0.23	0.25
NiO	0.10	0.11	0.11	0.11	0.14	0.14	0.13
Cr_2O_3	0.04	0.01	0.02	0.00	0.00	0.01	0.02
Total	100.38	100.83	99.88	100.57	100.82	99.95	101.12

TAN1213-3-5							
Basin A							
Olivine	3-5-04-rim	3-5-05-core	3-5-05-rim	3-5-06-core	3-5-06-rim	3-5-07-core	3-5-07-rim
Oxides							
SiO_2	39.25	39.40	38.93	39.32	39.45	39.79	39.54
TiO_2	0.00	0.01	0.00	0.00	0.00	0.00	0.00
Al_2O_3	0.00	0.03	0.03	0.01	0.02	0.01	0.03
FeOt	15.76	15.74	16.11	15.28	16.05	15.64	15.85
MnO	0.27	0.27	0.25	0.27	0.27	0.26	0.28
MgO	44.34	43.98	43.81	44.40	44.43	44.67	44.15
CaO	0.28	0.23	0.25	0.25	0.27	0.26	0.25
NiO	0.11	0.08	0.12	0.10	0.13	0.09	0.11
Cr_2O_3	0.01	0.02	0.01	0.01	0.00	0.02	0.01
Total	100.02	99.76	99.51	99.64	100.62	100.73	100.21

TAN1213-3-5				
Basin A				
Olivine	3-5-08-core	3-5-08-rim	3-5-09-core	3-5-09-rim
Oxides				
SiO2	39.60	39.50	39.60	39.53
TiO2	0.01	0.00	0.00	0.00
Al2O3	0.03	0.01	0.01	0.01
FeOt	15.74	15.68	16.04	15.60
MnO	0.28	0.23	0.26	0.30
MgO	44.95	44.35	44.57	44.25
CaO	0.23	0.28	0.23	0.25
NiO	0.14	0.13	0.06	0.14
Cr2O3	0.00	0.01	0.01	0.04
Total	100.99	100.19	100.79	100.12

Table E.2: Major element composition of olivine for basin A.

TAN1213							
006-3 Basin A							
Olivine	006-3-01-core	006-3-01-rim	006-3-02-core	006-3-02-rim	006-3-03-core	006-3-03-rim	006-3-04-core
Oxides							
SiO_2	39.49	39.22	39.66	36.99	39.81	39.81	39.90
TiO_2	0.01	0.00	0.02	0.11	0.00	0.00	0.01
Al_2O_3	0.03	0.01	0.03	0.16	0.03	0.03	0.04
FeOt	16.24	16.75	15.59	28.42	15.29	14.83	14.50
MnO	0.25	0.25	0.21	0.58	0.27	0.26	0.23
MgO	44.91	43.85	44.31	31.84	45.75	45.15	45.51
CaO	0.21	0.23	0.26	0.46	0.17	0.19	0.19
NiO	0.19	0.15	0.21	0.03	0.20	0.20	0.28
Cr_2O_3	0.03	0.05	0.03	0.05	0.01	0.00	0.02
Total	101.36	100.50	100.32	98.65	101.53	100.48	100.67

TAN1213							
006-3 Basin A							
Olivine	006-3-04-rim	006-3-05-core	006-3-05-rim	006-3-06-core	006-3-06-rim	006-3-07-core	006-3-7-rim
Oxides							
SiO_2	39.82	40.11	40.20	39.98	40.69	40.17	40.08
TiO_2	0.00	0.00	0.00	0.00	0.01	0.00	0.00
Al_2O_3	0.02	0.02	0.02	0.01	0.02	0.02	0.00
FeOt	14.86	15.09	14.95	14.76	14.35	13.07	14.78
MnO	0.24	0.24	0.25	0.26	0.26	0.22	0.22
MgO	45.37	45.55	45.32	45.78	47.15	46.58	46.02
CaO	0.20	0.18	0.19	0.19	0.18	0.16	0.18
NiO	0.20	0.23	0.23	0.26	0.30	0.37	0.26
Cr_2O_3	0.01	0.06	0.05	0.03	0.00	0.04	0.01
Total	100.71	101.48	101.21	101.27	102.95	100.64	101.56

TAN1213							
006-3 Basin A							
Olivine	006-3-08-core	006-3-08-rim	006-3-09-core	006-3-09-rim	006-3-010-ore	006-3-010-rim	006-3-011-cor
Oxides							
SiO_2	39.98	39.86	39.85	38.35	39.76	39.30	40.40
TiO_2	0.00	0.01	0.01	0.03	0.00	0.01	0.00
Al_2O_3	0.03	0.03	0.03	0.01	0.03	0.02	0.01
FeOt	14.93	15.43	14.01	20.99	14.80	15.38	14.02
MnO	0.27	0.26	0.24	0.36	0.23	0.26	0.22
MgO	45.45	45.26	45.60	39.06	45.88	44.88	46.54
CaO	0.18	0.20	0.19	0.26	0.17	0.22	0.18
NiO	0.20	0.25	0.26	0.02	0.27	0.14	0.26
Cr_2O_3	0.01	0.02	0.03	0.05	0.03	0.05	0.04
Total	101.04	101.32	100.22	99.12	101.17	100.25	101.66

TAN1213					
006-3 Basin A					
Olivine	006-3-11-rim	006-3-012-core	006-3-012-rim	006-3-013-core	006-3-013-rim
Oxides					
SiO_2	39.51	40.16	40.17	40.00	40.05
TiO_2	0.00	0.00	0.02	0.00	0.00
Al_2O_3	0.02	0.04	0.02	0.02	0.00
FeOt	15.73	14.71	14.82	14.52	14.74
MnO	0.25	0.24	0.26	0.20	0.27
MgO	44.90	46.40	45.68	46.20	45.54
CaO	0.22	0.15	0.18	0.17	0.18
NiO	0.15	0.28	0.22	0.36	0.20
Cr_2O_3	0.03	0.03	0.01	0.05	0.00
Total	100.80	102.01	101.37	101.53	100.98

Table E.3: Major element compositions for olivine from Basin B.

TAN1213							
55-2 Basin B							
Olivine							
Oxides	55-2-01-Core	55-2-01-Rim	55-2-02-Core	55-2-02-Rim	55-203-Core	55-2-03-Rim	55-20-04-Core
SiO_2	40.36	39.87	40.40	40.17	40.30	40.43	40.25
TiO_2	0.00	0.00	0.01	0.01	0.01	0.00	0.00
Al_2O_3	0.01	0.00	0.04	0.01	0.02	0.02	0.04
FeOt	11.72	14.24	11.00	13.42	12.52	12.86	13.72
MnO	0.19	0.24	0.17	0.22	0.20	0.19	0.21
MgO	47.56	45.56	48.62	46.84	46.80	46.53	47.00
CaO	0.19	0.21	0.24	0.20	0.20	0.19	0.20
NiO	0.31	0.18	0.28	0.26	0.28	0.26	0.31
Cr_2O_3	0.06	0.02	0.02	0.03	0.01	0.02	0.00
Total	100.40	100.32	100.77	101.15	100.35	100.48	101.74

TAN1213								
55-2 Basin B								
Olivine								
Oxides	55-2-04-Rim	55-2-04-Core	55-2-06-Core	55-2-06-Rim	55-2-03-Core	55-2-07-Core	55-2 07_Rim	55-2-07-Core
SiO_2	37.94	40.28	40.01	40.04	39.91	39.89	39.85	40.49
TiO_2	0.01	0.01	0.00	0.00	0.00	0.00	0.01	0.00
Al_2O_3	0.24	0.04	0.03	0.01	0.03	0.00	0.01	0.02
FeOt	14.71	14.20	13.00	12.75	13.49	14.17	14.50	12.81
MnO	0.27	0.23	0.21	0.19	0.19	0.23	0.23	0.20
MgO	41.91	45.60	46.46	46.87	45.97	45.56	44.64	46.94
CaO	0.28	0.19	0.19	0.19	0.20	0.20	0.23	0.19
NiO	0.16	0.23	0.25	0.32	0.28	0.20	0.18	0.23
Cr_2O_3	0.03	0.30	0.03	0.03	0.28	0.05	0.00	0.07
Total	95.53	101.08	100.18	100.40	100.35	100.30	99.65	100.96

TAN1213			
55-2 Basin B			
Olivine			
Oxides	55-2-07-Core	55-2-08-Core	55-2-08-Rim
SiO_2	37.82	39.89	39.26
TiO_2	0.07	0.00	0.00
Al_2O_3	1.96	0.00	0.01
FeOt	14.04	13.84	14.33
MnO	0.22	0.21	0.24
MgO	43.52	46.36	44.98
CaO	0.19	0.21	0.25
NiO	0.21	0.23	0.15
Cr_2O_3	2.60	0.01	0.03
Total	100.62	100.74	99.25

Table E.4: Major element composition for olivine from Basin B

TAN1213							
56-3 Basin B							
Olivine	56-3-01-core	56-3-01-Rim	56-3-02-core	56-3-02-Rim	56-3-03-core	56-3-03-Rim	56-3-04-Core
Oxides							
SiO_2	39.27	38.92	39.97	39.87	40.18	39.47	39.61
TiO_2	0.015	0	0	0.007	0	0	0
Al_2O_3	0.004	0.024	0	0.028	0	0.027	0.001
FeOt	15.32	16.46	13.06	13.92	12.88	15.50	14.30
MnO	0.30	0.27	0.23	0.25	0.25	0.27	0.24
MgO	44.73	43.20	46.26	45.66	47.13	45.06	45.19
CaO	0.22	0.27	0.17	0.15	0.17	0.21	0.20
NiO	0.18	0.06	0.29	0.21	0.44	0.15	0.22
Cr_2O_3	0.02	0.03	0.03	0.03	0.04	0.00	0.03
Total	926.89	919.28	926.42	927.53	936.14	932.76	924.46

TAN1213								
56-3 Basin B								
Olivine	56-3-04-Rim	56-3-05-Core	56-3-05-Rim	56-3-06-Core	56-3-06-Rim	56-3-08-Core	56-3-08-Rim	56-3-09-Core
Oxides								
SiO_2	39.38	39.99	39.65	39.67	39.22	39.78	39.57	39.75
TiO_2	0.01	0.00	0.01	0.00	0.01	0.00	0.00	0.01
Al_2O_3	0.03	0.03	0.04	0.03	0.01	0.01	0.00	0.03
FeOt	14.13	13.47	14.89	14.85	15.74	14.28	15.55	14.88
MnO	0.26	0.24	0.30	0.27	0.26	0.25	0.29	0.26
MgO	45.34	46.02	45.97	45.32	44.57	45.79	44.69	45.56
CaO	0.23	0.20	0.24	0.23	0.26	0.20	0.21	0.23
NiO	0.16	0.24	0.09	0.18	0.16	0.20	0.20	0.20
Cr_2O_3	0.03	0.02	0.04	0.01	0.02	0.03	0.00	0.02
Total	922.42	928.41	937.67	931.55	928.84	931.32	931.07	935.00

TAN1213			
56-3 Basin B			
Olivine	56-3-09-Rim	56-3-010-Core	56-3-011-Core
Oxides			
SiO_2	39.67	39.60	39.33
TiO_2	0.02	0.01	0.00
Al_2O_3	0.01	0.02	0.04
FeOt	15.26	15.41	14.24
MnO	0.29	0.30	0.25
MgO	45.16	44.94	45.34
CaO	0.26	0.21	0.19
NiO	0.15	0.12	0.14
Cr_2O_3	0.02	0.03	0.37
Total	934.13	932.31	925.41

Table E.5: Major element composition for olivine from Basin C.

TAN1213								
50-3 Basin C								
Oxides	50-3-01-Rim	50-3-02-Core	50-3-02-Rim	50-3-03-core	50-3-03-Rim	50-3-04-Core	50-3-04-Rim	50-3-05-Core
SiO_2	37.46	37.78	41.84	41.77	40.23	36.50	38.42	39.12
TiO_2	0.03	0.00	0.04	0.02	0.03	0.001	0.000	0.01
Al_2O_3	0.03	0.03	0.03	0.19	0.00	0.00	0.01	0.02
FeOt	25.11	27.47	24.27	27.79	25.90	26.92	21.60	23.41
MnO	0.44	0.44	0.40	0.47	0.50	0.46	0.39	0.42
MgO	36.01	34.74	41.02	36.77	33.93	35.94	39.15	38.30
CaO	0.20	0.18	0.30	0.40	0.22	0.24	0.21	0.18
NiO	0.02	0.03	0.02	0.01	0.03	0.00	0.00	0.00
Cr_2O_3	0.00	0.02	0.00	0.01	0.01	0.00	0.01	0.00
Total	99.30	100.68	107.93	107.43	100.86	100.05	99.79	101.47

TAN1213			
50-3 Basin C	50-3-05-Rim	50-3-07-Core	50-3-07-Rim
Oxides			
SiO_2	37.77	38.36	38.41
TiO_2	0.005	0	0.003
Al_2O_3	0.019	0.01	0.002
FeOt	23.74	22.30	22.37
MnO	0.39	0.36	0.42
MgO	38.03	38.77	38.70
CaO	0.195	0.189	0.219
NiO	0.10	0.05	0.08
Cr_2O_3	0	0	0.02
Total	100.24	100.04	100.21

Table E.6: Major element composition for olivine from Basin D.

TAN1213							
51-4 Basin D							
Oxides	51-4-01-Core	51-4-01-Rim	51-4-02-Core	51-4-02-Rim	51-4-03-Core	51-4-03-Rim	51-4-04-Core
SiO_2	39.46	38.55	39.86	39.56	39.84	39.85	40.06
TiO_2	0.008	0.022	0	0	0.016	0	0.003
Al_2O_3	0.013	0.012	0.018	0.019	0.016	0.033	0
FeOt	13.77	19.73	12.84	14.81	11.87	13.71	12.43
MnO	0.23	0.30	0.15	0.20	0.16	0.21	0.23
MgO	45.21	40.65	46.46	44.93	47.08	45.93	46.66
CaO	0.197	0.232	0.201	0.243	0.195	0.203	0.205
NiO	0.20	0.10	0.33	0.16	0.35	0.27	0.29
Cr_2O_3	0.029	0	0.057	0.003	0.032	0.033	0.028
Total	99.13	99.59	99.91	99.92	99.58	100.24	99.91

TAN1213							
51-4 Basin D							
Oxides	51-4-04-Rim	51-4-05-Core	51-4-05-Core	51-4-06-Core	51-4-06-Rim	51-4-07-Core	51-4-07-Rim
SiO_2	39.76	39.75	39.69	39.68	39.63	39.48	39.83
TiO_2	0.00	0.00	0.03	0.00	0.00	0.00	0.00
Al_2O_3	0.04	0.04	0.02	0.02	0.01	0.00	0.00
FeOt	14.29	14.43	14.37	13.77	14.37	15.30	14.11
MnO	0.23	0.25	0.22	0.20	0.20	0.19	0.25
MgO	45.01	45.34	45.21	45.91	45.42	44.98	45.47
CaO	0.21	0.21	0.22	0.21	0.19	0.13	0.23
NiO	0.16	0.30	0.17	0.25	0.21	0.11	0.16
Cr_2O_3	0.04	0.02	0.02	0.06	0.04	0.02	0.05
Total	99.74	100.33	99.95	100.10	100.07	100.20	100.11

TAN1213							
51-4 Basin D							
Oxides	51-4-08-Core	51-4-08-Rim	51-4-09-Core	51-4-09-Rim	51-4-09-Core	51-4-09-Rim	51-4-010-Core
SiO2	39.80	39.55	39.90	39.80	39.73	39.77	40.16
TiO2	0	0.02	0	0.005	0.001	0	0.007
Al2O3	0.011	0.032	0.026	0.014	0.026	0.017	0.014
FeOt	13.93	13.29	12.62	14.50	12.70	13.98	12.59
MnO	0.21	0.24	0.18	0.26	0.25	0.22	0.18
MgO	45.99	45.71	46.56	45.11	47.23	45.64	46.83
CaO	0.201	0.211	0.179	0.222	0.203	0.215	0.182
NiO	0.21	0.22	0.26	0.19	0.26	0.18	0.26
Cr2O3	0.02	0.039	0.091	0.034	0.02	0.031	0.244
Total	100.37	99.32	99.82	100.13	100.42	100.05	100.45

Table E.7: Major element composition for olivine from Basin E

TAN1213							
11_1 Basin E							
Oxides	11-1-01-Core	11-1-01-Rim	11-1-02-Core	11-1-02-Rim	11-1-03-Core	11-1-03-Rim	11-1-04-Core
SiO_2	40.22	40.03	40.39	39.76	40.18	40.09	38.79
TiO_2	0.00	0.00	0.00	0.00	0.00	0.01	0.02
Al_2O_3	0.01	0.02	0.00	0.01	0.01	0.01	1.02
FeOt	12.15	13.55	12.48	13.37	12.77	14.16	12.94
MnO	0.21	0.24	0.19	0.20	0.23	0.22	0.19
MgO	48.00	46.41	47.99	46.86	47.52	46.66	45.77
CaO	0.21	0.19	0.20	0.20	0.19	0.26	0.22
NiO	0.22	0.18	0.25	0.22	0.17	0.08	0.24
Cr_2O_3	0.04	0.02	0.07	0.05	0.04	0.03	1.06
Total	101.06	100.64	101.58	100.66	101.11	101.51	100.26

TAN1213							
11_1 Basin E							
Oxides	11-1-04-Rim	11-1-05-Core	11-1-05-Rim	11-1-06-Core	11-1-06-Rim	11-1-07-Core	11-1-07-Rim
SiO_2	39.11	40.74	39.61	40.70	40.14	40.43	40.07
TiO_2	0.08	0.00	0.02	0.01	0.00	0.00	0.00
Al_2O_3	1.06	0.02	0.03	0.02	0.00	0.02	0.02
FeOt	26.57	10.78	16.95	11.49	13.53	11.81	14.22
MnO	0.44	0.18	0.30	0.19	0.24	0.16	0.22
MgO	30.66	48.87	43.70	49.06	46.87	48.38	46.54
CaO	1.44	0.19	0.22	0.19	0.21	0.18	0.22
NiO	0.11	0.32	0.08	0.32	0.26	0.36	0.17
Cr_2O_3	0.00	0.07	0.04	0.06	0.02	0.05	0.04
Total	99.48	101.17	100.93	102.02	101.26	101.38	101.50

TAN1213							
11_1 Basin E							
Oxides	11-1 -08-Core	11-1 -08-Rim	11-1 -09-Core	11-1 -09-Rim	11-1 -010-Core	11-1 -010-Rim	11-1-011-Core
SiO_2	40.32	39.60	40.34	40.34	40.55	40.45	39.60
TiO_2	0.01	0.02	0.00	0.00	0.00	0.00	0.02
Al_2O_3	0.03	0.01	0.00	0.02	0.03	0.02	0.01
FeOt	11.16	15.12	11.93	12.07	11.52	12.76	15.12
MnO	0.19	0.25	0.21	0.23	0.18	0.21	0.25
MgO	48.03	45.22	48.54	47.62	48.59	48.01	45.22
CaO	0.20	0.21	0.18	0.20	0.18	0.20	0.21
NiO	0.29	0.09	0.24	0.28	0.32	0.27	0.09
Cr_2O_3	0.01	0.02	0.06	0.06	0.01	0.04	0.02
Total	100.24	100.54	101.49	100.82	101.38	101.95	100.54

Table E.8: Major element composition for olivine from Basin G.

TAN1213-47-1							
Basin G							
Oxides	47-1-01-Core	47-1 -02-Rim	47-1-01-Core	47-1-02-Core	47-1-02-Rim	47-1-03-Core	47-1-03-Rim
SiO_2	39.88	39.88	40.10	39.89	40.02	40.20	40.15
TiO_2	0.00	0.00	0.00	0.01	0.00	0.00	0.00
Al_2O_3	0.01	0.01	0.15	0.02	0.02	0.04	0.03
FeOt	12.71	13.21	12.76	12.13	12.47	12.05	12.96
MnO	0.18	0.22	0.18	0.19	0.23	0.20	0.23
MgO	47.08	46.12	46.93	47.01	46.74	47.64	46.78
CaO	0.21	0.26	0.24	0.22	0.23	0.20	0.23
NiO	0.23	0.21	0.27	0.24	0.16	0.30	0.18
Cr_2O_3	0.04	0.01	0.25	0.03	0.01	0.03	0.02
Total	100.34	99.94	100.86	99.75	99.87	100.66	100.57

TAN1213-47-1							
Basin G							
Oxides	47-1-07-Core	47-1-07-Rim	47-1-07-Core	47-1-07-Core	47-1-08-Core	47-1-08-Rim	47-1-08-Rim
SiO_2	39.97	40.37	40.30	29.85	39.85	39.09	40.02
TiO_2	0.00	0.00	0.00	0.58	0.00	0.00	0.00
Al_2O_3	0.04	0.00	0.00	4.39	0.01	0.01	0.00
FeOt	13.14	13.11	12.84	15.79	13.79	13.41	13.44
MnO	0.22	0.23	0.19	0.24	0.24	0.22	0.21
MgO	46.77	46.62	46.55	40.21	45.70	40.75	46.23
CaO	0.24	0.27	0.21	0.18	0.26	0.23	0.25
NiO	0.20	0.21	0.25	0.21	0.15	0.16	0.16
Cr_2O_3	0.04	0.06	0.04	7.41	0.03	0.00	0.02
Total	100.62	100.86	100.38	98.85	100.03	93.87	100.34

TAN1213							
47-2 Basin G							
Oxides	47-2-01-Core	47-2-01-Rim	47-2-02-Core	47-2-02-Rim	47-2-02-Core	47-2-03-Core	47-2-03-Rim
SiO_2	40.14	39.96	40.04	40.11	40.13	40.48	40.48
TiO_2	0.00	0.00	0.00	0.00	0.00	0.00	0.00
Al_2O_3	0.01	0.01	0.01	0.02	0.03	0.02	0.04
FeOt	12.43	13.27	12.23	13.24	12.42	10.33	12.56
MnO	0.17	0.23	0.21	0.22	0.21	0.15	0.20
MgO	47.09	46.32	46.41	46.41	46.92	48.88	47.24
CaO	0.21	0.23	0.22	0.25	0.23	0.20	0.21
NiO	0.23	0.17	0.20	0.13	0.15	0.35	0.30
Cr_2O_3	0.04	0.01	0.02	0.03	0.18	0.03	0.01
Total	100.33	100.19	99.35	100.42	100.26	100.45	101.03

TAN1213							
47-2 Basin G							
Oxides	47-2 Olivine-03-Core	47-2-04-Core	47-2-04-Rim	47-2-05-Core	47-2-05-Rim	47-2-06-Core	47-2-06-Rim
SiO_2	39.91	40.24	40.42	40.47	41.66	40.02	40.16
TiO_2	0.09	0.00	0.00	0.00	0.00	0.02	0.00
Al_2O_3	2.10	0.03	0.00	0.02	0.03	0.03	0.01
FeOt	10.02	12.49	12.72	12.61	12.74	12.87	12.77
MnO	0.14	0.19	0.19	0.21	0.22	0.20	0.21
MgO	45.32	47.38	46.72	47.73	47.03	46.92	46.43
CaO	0.61	0.20	0.22	0.24	0.24	0.22	0.26
NiO	0.29	0.26	0.20	0.24	0.23	0.23	0.24
Cr_2O_3	1.27	0.04	0.01	0.03	0.03	0.03	0.03
Total	99.74	100.84	100.48	101.54	102.19	100.53	100.10

Table E.9: Major element composition for olivine from Basin G continued.

TAN1213				
47-2 Basin G				
Oxides	47-07-Core	47-1-07-Rim	47-1-08-Core	47-1-08-Rim
SiO_2	40.30	40.37	39.85	40.02
TiO_2	0.00	0.00	0.00	0.00
Al_2O_3	0.00	0.00	0.01	0.00
FeOt	12.84	13.11	13.79	13.44
MnO	0.19	0.23	0.24	0.21
MgO	46.55	46.62	45.70	46.23
CaO	0.21	0.27	0.26	0.25
NiO	0.25	0.21	0.15	0.16
Cr_2O_3	0.04	0.06	0.03	0.02
Total	100.38	100.86	100.03	100.34

Table E.10: Major element composition for olivine from Basin I.

TAN1512							
040-02 Basin I							
Oxides	040-02-01-Core	040-02-01-Rim	040-02-02-Core	040-02-02-Rim	040-02-02-Core	040-02-03-Core	040-02-03-Rim
SiO_2	40.68	40.38	40.93	40.44	40.81	40.36	40.28
TiO_2	0.00	0.00	0.00	0.00	0.01	0.00	0.00
Al_2O_3	0.00	0.01	0.02	0.00	0.08	0.03	0.02
FeOt	11.33	11.82	10.86	11.64	11.34	11.95	12.43
MnO	0.21	0.19	0.19	0.18	0.18	0.16	0.18
MgO	48.82	48.05	48.80	47.79	48.45	47.96	47.65
CaO	0.29	0.32	0.29	0.33	0.29	0.31	0.30
NiO	0.16	0.22	0.30	0.11	0.18	0.16	0.15
Cr_2O_3	0.05	0.02	0.02	0.02	0.59	0.04	0.02
Total	101.55	101.01	101.42	100.51	101.93	100.97	101.01

TAN1512							
040-02 Basin I							
Oxides	040-02-04-Core	040-02-04-Rim	040-02-05-Core	040-02-05-Rim	040-02-06-Core	040-02-06-Rim	040-02-07-Core
SiO_2	40.13	40.45	40.63	40.51	40.44	40.39	40.63
TiO_2	0.01	0.00	0.00	0.00	0.00	0.00	0.00
Al_2O_3	0.02	0.02	0.04	0.01	0.02	0.03	0.02
FeOt	11.57	12.38	10.87	12.02	11.19	12.22	11.01
MnO	0.19	0.21	0.19	0.17	0.17	0.23	0.20
MgO	48.04	47.59	48.42	47.90	48.77	47.78	48.62
CaO	0.32	0.36	0.29	0.32	0.34	0.31	0.30
NiO	0.12	0.17	0.22	0.20	0.25	0.16	0.20
Cr_2O_3	0.04	0.02	0.02	0.00	0.07	0.02	0.03
Total	100.45	101.20	100.69	101.14	101.25	101.13	101.00

Table E.11: Major element composition for olivine from Basin I.

TAN1512							
041-03 Basin I							
Oxides	042-2-01-Core	042-2-01-Rim	042-2-03-Core	042-2-03-Rim	042-2-04-Core	042-2-04-Rim	042-2-06-Core
SiO_2	39.93	40.27	39.30	39.32	39.60	40.26	39.45
TiO_2	0.00	0.00	0.00	0.00	0.00	0.00	0.01
Al_2O_3	0.03	0.03	0.00	0.02	0.00	0.02	0.02
FeOt	13.28	12.22	16.47	16.78	16.98	16.89	16.38
MnO	0.20	0.17	0.28	0.32	0.27	0.28	0.29
MgO	46.13	46.68	42.96	42.47	43.61	45.34	44.44
CaO	0.27	0.27	0.26	0.27	0.26	0.29	0.25
NiO	0.15	0.14	0.00	0.08	0.10	0.07	0.14
Cr_2O_3	0.02	0.02	0.00	0.00	0.03	0.00	0.01
Total	100.02	99.79	99.29	99.25	100.85	103.15	101.00

TAN1512				
041-03 Basin I				
Oxides	042-2-06-Rim	042-2-07-Rim	042-2-08-Core	042-2-08-Rim
SiO_2	39.33	39.60	39.64	39.36
TiO_2	0.00	0.00	0.00	0.00
Al_2O_3	0.01	0.02	0.01	0.02
FeOt	16.94	16.98	16.46	16.72
MnO	0.27	0.28	0.28	0.32
MgO	43.42	44.17	44.15	43.45
CaO	0.25	0.22	0.23	0.24
NiO	0.08	0.08	0.04	0.04
Cr_2O_3	0.01	0.00	0.00	0.00
Total	100.31	101.36	100.80	100.14

TAN1512			
040-02 Basin I			
Oxides	040-02-07-Rim	040-02-08-Core	040-02-08-Rim
SiO_2	40.35	40.73	40.65
TiO_2	0.00	0.01	0.00
Al_2O_3	0.02	0.02	0.01
FeOt	10.83	11.11	12.05
MnO	0.17	0.17	0.18
MgO	47.40	48.95	48.10
CaO	0.31	0.29	0.31
NiO	0.21	0.13	0.16
Cr_2O_3	0.05	0.02	0.04
Total	99.33	101.45	101.51

Table E.12: Major element composition for olivine from Basin K.

TAN1512							
DR 10-2 Basin K							
Oxides	10-2-01-Core	DR10-2-02-Rim	DR10-2-02-Core	DR10-2-02-Rim	DR10-2-03-Core	DR10-2-03-Rim	DR10-2-04-Core
SiO_2	39.95	39.97	39.77	39.43	39.61	39.57	39.75
TiO_2	0.01	0.00	0.01	0.00	0.01	0.00	0.00
Al_2O_3	0.02	0.02	0.00	0.02	0.03	0.04	0.02
FeOt	15.94	16.70	16.82	16.75	16.74	17.33	16.82
MnO	0.27	0.26	0.27	0.26	0.27	0.26	0.26
MgO	44.33	44.64	44.31	44.48	43.91	44.24	44.17
CaO	0.26	0.29	0.28	0.30	0.28	0.27	0.27
NiO	0.06	0.12	0.04	0.05	0.01	0.05	0.08
Cr_2O_3	0.00	0.01	0.00	0.04	0.00	0.01	0.00
Total	100.85	102.01	101.50	101.32	100.83	101.77	101.37

TAN1512							
DR 10-2 Basin K							
Oxides	DR10-2-04-Rim	DR10-2-04-Core	DR10-2-05-Core	DR10-2-05-Rim	DR10-2-06-Core	DR10-2-06-Rim	DR10-2-07-Core
SiO_2	39.41	38.24	39.59	39.64	39.66	39.21	39.68
TiO_2	0.01	0.00	0.00	0.00	0.00	0.00	0.00
Al_2O_3	0.03	0.03	0.02	0.03	0.04	0.04	0.01
FeOt	16.72	16.62	16.98	16.48	16.76	16.25	17.15
MnO	0.25	0.29	0.28	0.33	0.27	0.30	0.29
MgO	44.04	43.86	44.36	44.16	44.25	43.74	44.32
CaO	0.27	0.27	0.28	0.30	0.28	0.29	0.27
NiO	0.14	0.07	0.09	0.07	0.11	0.10	0.03
Cr_2O_3	0.00	0.00	0.02	0.00	0.00	0.00	0.00
Total	100.87	99.38	101.62	101.01	101.37	99.92	101.75

TAN1512							
DR 10-2 Basin K							
Oxides	DR10-2-07-Rim	DR10-2-08-Core	DR10-2-08-Rim	DR10-2-09-Core	DR10-2-09-Rim	DR10-2-010-Rim	DR10-2-011-Core
SiO_2	39.25	39.36	39.23	39.58	39.34	39.62	39.53
TiO_2	0.00	0.00	0.02	0.00	0.00	0.00	0.00
Al_2O_3	0.02	0.03	0.04	0.02	0.03	0.04	0.01
FeOt	16.43	17.20	17.28	16.63	16.61	15.77	15.67
MnO	0.26	0.30	0.31	0.29	0.29	0.25	0.30
MgO	44.09	43.65	43.28	44.01	43.99	43.73	44.42
CaO	0.26	0.28	0.29	0.27	0.28	0.30	0.27
NiO	0.09	0.09	0.12	0.04	0.00	0.11	0.14
Cr_2O_3	0.00	0.02	0.01	0.00	0.02	0.00	0.00
Total	100.40	100.93	100.57	100.85	100.56	99.81	100.34

Table E.13: Major element composition for spinel from Basin A.

TAN1213-006-3							
Basin A							
Oxides	006-3-Ol-04	006-3-Ol-05	006-3-Ol-05	006-3-Ol-06	006-3-Ol-06	006-3-Ol-08	006-3-Ol-010
SiO_2	0.06	0.04	0.05	0.04	0.05	0.08	0.07
TiO_2	0.92	0.99	0.98	1.02	1.06	1.05	1.09
Al_2O_3	23.07	22.74	22.97	24.51	24.52	24.52	24.02
FeOt	28.55	28.96	28.72	28.34	28.78	29.04	29.41
MnO	0.28	0.31	0.30	0.29	0.29	0.34	0.29
MgO	11.85	11.32	11.61	12.21	12.12	11.64	11.56
CaO	0.03	0.04	0.06	0.04	0.02	0.03	0.01
NiO	0.19	0.14	0.13	0.13	0.12	0.14	0.11
Cr_2O_3	32.67	34.00	33.51	30.83	30.36	30.89	30.83
Total	97.63	98.53	98.32	97.40	97.34	97.73	97.41

TAN1213-006-3									
Basin A									
Oxides	006-3-Ol-010	006-3-Ol-011	006-3-Ol-011	006-3-Ol-012	006-3-Ol-012	006-3-Ol-012	006-3-Ol-013	006-3-Ol-013	006-3-Ol-013
SiO_2	0.06	0.42	0.03	0.02	0.05	0.06	0.02	0.04	0.03
TiO_2	1.13	0.81	0.87	0.82	0.78	1.01	0.92	1.04	0.93
Al_2O_3	24.23	24.53	21.57	22.63	22.79	21.68	21.51	22.10	23.01
FeOt	30.15	26.55	27.44	26.47	26.94	27.60	27.64	28.36	27.51
MnO	0.28	0.31	0.31	0.30	0.25	0.30	0.27	0.30	0.31
MgO	11.52	13.10	11.21	11.80	11.83	11.30	11.57	11.57	11.73
CaO	0.00	0.02	0.04	0.00	0.00	0.06	0.00	0.00	0.01
NiO	0.09	0.15	0.17	0.27	0.15	0.21	0.18	0.15	0.11
Cr_2O_3	30.99	36.15	36.87	36.82	36.69	35.42	36.48	34.73	34.56
Total	98.45	102.05	98.51	99.16	99.50	97.69	98.61	98.27	98.21

Table 5.14: Major element composition for spinel from Basin B

TAN1213-55-2							
Basin B							
Oxides	55-2-Ol-01	55-2-Ol-01	55-2-Ol-01	55-2-Ol-02	55-2-Ol-02	55-2-Ol-02	55-2-Ol-03
SiO_2	0.26	0.30	0.23	0.26	0.24	0.23	0.32
TiO_2	0.59	0.58	0.75	0.52	0.53	0.53	0.83
Al_2O_3	12.85	12.89	14.39	13.58	13.70	13.58	12.19
FeOt	0.00	0.01	0.67	0.01	0.01	0.00	0.01
MnO	0.15	0.22	0.13	0.18	0.17	0.23	0.08
MgO	21.24	21.56	22.57	22.61	23.09	22.45	22.60
CaO	0.04	0.04	5.61	0.08	0.05	0.04	0.06
NiO	0.00	0.02	0.13	0.00	0.01	0.01	0.01
Cr_2O_3	39.87	38.67	34.25	41.47	40.35	40.06	36.28
Total	98.43	97.93	102.18	99.62	98.60	97.75	99.26

Table E.15: Major element composition for spinel from Basin B.

TAN1213-55-2					
Basin B					
Oxides	55-2-Ol-03	55-2-Ol-04	55-2-Ol-04	55-2-Ol-06	55-2-Ol-06
SiO_2	0.26	0.28	0.30	0.28	0.26
TiO_2	0.81	0.84	0.82	0.62	0.71
Al_2O_3	11.49	12.39	11.37	10.95	12.10
FeOt	0.01	0.01	0.00	0.02	0.00
MnO	0.17	0.12	0.14	0.14	0.12
MgO	21.78	21.46	20.58	19.29	21.75
CaO	0.08	0.08	0.07	0.05	0.04
NiO	0.00	0.00	0.01	0.00	0.00
Cr_2O_3	35.98	35.51	35.64	38.66	35.79
Total	96.72	98.87	95.14	97.48	96.44

TAN1213-56-3							
Basin B							
Oxides	56-3-Ol-02	56-3-Ol-011	56-3-Ol-08	56-3-Ol-08	56-3-Ol-05	56-3-Ol-05	56-3-Ol-04
SiO_2	0.03	0.06	0.08	0.26	0.62	0.09	0.10
TiO_2	0.99	0.86	0.66	0.92	1.04	1.11	1.10
Al_2O_3	18.35	18.61	19.96	19.87	20.17	20.33	20.40
FeOt	27.58	29.72	27.85	29.87	29.44	30.56	30.70
MnO	0.32	0.35	0.32	0.30	0.31	0.34	0.32
MgO	11.11	10.59	10.89	11.23	12.08	11.14	11.06
CaO	0.01	0.03	0.05	0.01	0.05	0.04	0.01
NiO	0.15	0.02	0.19	0.10	0.18	0.15	0.13
Cr_2O_3	38.81	37.86	37.65	34.93	34.15	33.39	33.18
Total	97.37	98.11	97.64	97.49	98.05	97.18	97.03

TAN1213-56-3			
Basin B			
Oxides	56-3-Ol-04	56-3-Ol-03	56-3-Ol-07
SiO_2	0.09	16.61	15.26
TiO_2	1.09	0.57	0.79
Al_2O_3	20.44	12.34	13.04
FeOt	30.89	21.69	27.17
MnO	0.34	0.29	0.31
MgO	11.28	24.71	24.23
CaO	0.03	0.08	0.14
NiO	0.17	0.20	0.14
Cr_2O_3	33.17	23.13	21.78
Total	97.50	99.63	102.85

Table E.16: Major element composition for spinel from Basin D.

TAN1213-51-4						
Basin D						
Oxides	51-4-Ol-02	51-4-Ol-02	51-4-Ol-02	51-4-Ol-06	51-4-Ol-07	51-4-Ol-010
SiO_2	0.04	0.05	0.53	0.03	1.35	0.08
TiO_2	0.55	0.61	0.78	1.00	0.81	0.75
Al_2O_3	19.62	18.89	20.56	18.01	22.66	20.80
FeOt	25.23	26.71	27.11	31.82	28.32	25.59
MnO	0.25	0.32	0.30	0.35	0.27	0.26
MgO	11.40	11.07	12.43	9.66	13.02	12.33
CaO	0.00	0.00	0.00	0.01	0.02	0.01
NiO	0.08	0.17	0.22	0.08	0.15	0.17
Cr_2O_3	40.11	40.10	35.79	36.60	31.98	37.24
Total	97.27	97.92	97.71	97.55	98.59	97.22

Table E.16: Major element composition for spinel from Basin E.

TAN1213-11-1							
Basin E							
Oxides	11-1-Ol-01	11-1-Ol-01	11-1-Ol-02	11-1-Ol-03	11-1-Ol-04	11-1-Ol-05	11-1-Ol-06
SiO_2	0.05	0.10	4.06	0.29	0.09	1.45	0.05
TiO_2	0.60	0.62	0.68	0.87	0.68	0.92	0.66
Al_2O_3	19.02	19.07	21.45	19.54	19.12	18.18	18.91
FeOt	24.22	24.22	24.43	25.92	24.83	28.63	23.22
MnO	0.23	0.30	0.28	0.30	0.28	0.40	0.26
MgO	11.97	12.03	12.93	11.86	11.85	9.56	12.42
CaO	0.01	0.01	0.17	0.00	0.04	0.29	0.01
NiO	0.19	0.15	0.16	0.14	0.14	0.07	0.18
Cr_2O_3	41.60	40.94	36.01	39.63	40.18	38.30	41.69
Total	97.89	97.44	100.29	98.56	97.21	97.84	97.42

TAN1213-11-1								
Basin E								
Oxides	11-1-Ol-06	11-1-Ol-06	11-1-Ol-07	11-1-Ol-09	11-1-Ol-09	11-1-Ol-09	11-1-Ol-010	11-1-Ol-010
SiO_2	0.05	0.25	0.15	0.71	0.08	0.20	0.12	0.11
TiO_2	0.62	0.73	0.71	0.74	0.64	0.70	0.57	0.60
Al_2O_3	18.42	18.96	20.08	19.50	17.92	18.90	17.98	18.03
FeOt	23.16	23.40	22.84	25.29	24.21	24.92	21.87	22.05
MnO	0.30	0.26	0.29	0.30	0.32	0.30	0.28	0.29
MgO	12.84	12.70	12.35	12.99	11.83	11.55	12.34	12.71
CaO	0.00	0.01	0.00	0.00	0.00	0.01	0.00	0.00
NiO	0.09	0.11	0.19	0.18	0.15	0.17	0.17	0.16
Cr_2O_3	43.49	41.24	40.48	40.35	42.77	41.38	44.21	44.54
Total	98.97	97.69	97.09	100.05	97.91	98.12	97.56	98.49

Table E.17: Major element composition for spinel from Basin G.

TAN1213-47-1							
Basin G							
Oxides	47-1 -Ol-01	47-1-Ol- 01	47-1-Ol-02	47-1-Ol-02	47-1-Ol-02	47-1-Ol-02	47-1-Ol-03
SiO_2	0.25	0.30	0.35	0.32	0.27	0.32	0.27
TiO_2	0.86	0.74	0.52	0.52	0.87	0.86	0.62
Al_2O_3	12.96	13.35	11.67	11.63	12.92	13.00	12.74
FeOt	0.01	0.01	0.00	0.00	0.01	0.01	0.04
MnO	0.16	0.14	0.18	0.07	0.17	0.18	0.18
MgO	21.96	21.22	14.97	14.95	22.32	22.66	20.57
CaO	0.08	1.04	0.05	0.05	0.16	0.28	0.16
NiO	0.02	0.00	0.01	0.00	0.01	0.02	0.00
Cr_2O_3	37.53	36.57	48.77	48.53	36.34	36.63	40.25
Total	97.40	97.70	99.15	98.55	97.16	97.53	97.61

TAN1213-47-1								
Basin G								
Oxides	47-2-Ol-04	47-1-Ol-05	47-1 Olivine_05_S	47-1-Ol-06-05	47-1-Ol-06	47-1-Ol-06	47-1-Ol-08	47-1-Ol-08
SiO_2	0.26	0.29	0.30	0.27	0.29	0.28	0.23	0.25
TiO_2	0.94	0.70	0.82	0.93	0.84	0.77	0.92	0.92
Al_2O_3	12.18	11.15	11.79	12.24	12.52	12.68	12.14	12.27
FeOt	0.05	0.02	0.06	0.01	0.01	0.00	0.00	0.01
MnO	0.10	0.08	0.14	0.12	0.13	0.08	0.12	0.11
MgO	21.26	15.07	18.11	21.20	21.68	22.23	21.56	21.86
CaO	0.02	0.05	0.27	0.08	0.07	0.09	0.04	0.07
NiO	0.02	0.00	0.01	0.00	0.01	0.00	0.01	0.02
Cr_2O_3	36.62	46.26	42.13	36.70	37.34	37.10	36.46	36.26
Total	97.14	98.19	98.23	97.35	97.92	97.80	97.22	98.21

TAN1213-47-2							
Basin G							
Oxides	47-2-Ol-01	47-2-Ol-03	47-2-Ol-04	47-2 -Ol-04	47-2-Ol-05	47-2-Ol-05	47-2-Ol-05
SiO_2	40.14	40.48	40.24	40.42	40.47	41.66	40.02
TiO_2	0.00	0.00	0.00	0.00	0.00	0.00	0.02
Al_2O_3	12.78	12.59	3.79	11.89	13.47	12.38	12.60
FeOt	0.84	0.79	0.68	0.84	0.88	0.89	0.85
MnO	0.28	0.26	0.18	0.34	0.25	0.31	0.26
MgO	0.01	0.05	2.41	0.00	0.00	0.01	0.00
CaO	0.21	0.19	0.01	0.14	0.08	0.16	0.19
NiO	0.07	0.17	29.42	0.05	0.06	0.07	0.06
Cr_2O_3	22.15	21.44	19.73	19.50	25.78	22.34	22.31
Total	100.30	99.35	100.84	100.48	101.54	1002.19	100.53

Table E.18: Major element composition for spinel from Basin I.

TAN1513-040-02							
Basin I							
Oxides	040-Ol-02	040-Ol-02	040-Ol-04	040-Ol-05	040-Ol-05	040-Ol-07	040-Ol-08
SiO_2	0.05	0.05	0.11	0.03	0.05	0.06	0.02
TiO_2	0.47	0.42	0.50	0.48	0.53	0.57	0.38
Al_2O_3	15.68	15.52	15.92	14.39	14.37	16.32	11.91
FeOt	22.28	22.39	24.03	24.37	24.21	23.45	22.89
MnO	0.30	0.32	0.36	0.33	0.31	0.30	0.33
MgO	12.30	12.10	12.07	11.48	11.52	11.86	11.53
CaO	0.00	0.00	0.00	0.04	0.02	0.00	0.02
NiO	0.07	0.10	0.09	0.06	0.12	0.08	0.02
Cr_2O_3	46.34	46.58	45.10	47.02	46.36	44.45	51.26
Total	97.52	97.49	98.19	98.20	97.48	97.10	98.36

TAN1513-040-02	
Basin I	
Oxides	040-Ol-08
SiO_2	0.09
TiO_2	0.42
Al_2O_3	11.96
FeOt	23.05
MnO	0.30
MgO	11.53
CaO	0.01
NiO	0.10
Cr_2O_3	50.75
Total	98.21

Table E.19: Major element composition for clinopyroxene from Basin B.

TAN1213-55-2			
Basin B			
Oxides	55-2-01-Core	55-203-Rim	55-2-03-Core
SiO_2	53.28	51.33	40.93
TiO_2	0.29	0.46	0.89
Al_2O_3	1.91	3.97	11.34
FeOt	3.24	3.15	8.71
MnO	0.11	0.13	0.18
MgO	18.41	16.75	13.74
CaO	20.33	21.36	16.34
NiO	0.00	0.00	0.00
Cr_2O_3	0.00	0.00	0.00
Total	100.57	100.90	99.72
Wo	41.95	45.34	38.67
En	52.83	49.44	45.23
Fs	5.21	5.22	16.09
Fo	91.02	90.46	73.76
Mg#	91.02	90.45	73.76

TAN1213-56-3					
Basin B					
Oxides	56-3-02-Core	56-3-02-Rim	56-3-03-Core	56-3-03-Rim	56-3-04-Core
SiO_2	51.72	45.79	50.52	53.39	53.82
TiO_2	0.38	1.41	0.57	0.39	0.28
Al_2O_3	3.11	6.32	4.38	2.14	1.78
FeOt	3.25	4.58	3.74	4.72	3.49
MnO	0.14	0.20	0.22	0.25	0.19
MgO	17.04	13.65	17.15	20.44	18.69
CaO	21.61	20.44	19.35	15.94	19.73
NiO	0.00	0.00	0.00	0.00	0.00
Cr_2O_3	0.00	0.00	0.00	0.00	0.00
Total	100.73	96.53	100.07	100.76	101.14
Wo	45.16	47.53	41.95	33.18	40.72
En	49.53	44.15	51.71	59.15	53.65
Fs	5.30	8.32	6.33	7.66	5.63
Fo	90.33	84.15	89.09	88.54	90.51
Fe	0.05	0.06	0.05	0.07	0.05
Mg	0.42	0.34	0.43	0.51	0.46
Mg#	90.33	84.15	89.09	88.54	90.51

Table E.20: Major element composition for clinopyroxene from Basin D.

TAN1213-51-4									
Basin D									
Oxides	51-4-01-Core	51-4-01-Rim	51-4-02-Core	51-4-02-Rim	51-4-03-Core	51-4-03-Rim	51-4-05-Core	51-4-05-Rim	51-4-06-Core
SiO_2	53.42	49.51	52.46	49.58	50.41	48.66	54.22	51.62	50.98
TiO_2	0.31	0.96	0.46	1.07	0.76	1.22	0.57	0.53	0.75
Al_2O_3	1.47	3.63	2.58	3.94	3.45	4.08	5.67	3.49	4.20
FeOt	3.92	5.10	3.62	5.48	5.24	5.72	3.40	3.37	3.43
MnO	0.20	0.14	0.18	0.20	0.24	0.18	0.17	0.13	0.09
MgO	19.02	14.15	17.73	14.91	15.75	14.10	14.08	16.70	15.36
CaO	18.35	20.64	19.96	19.50	19.00	19.77	18.10	20.84	21.30
NiO	0.00	0.00	0.00	0.00	0.00	0.00	0.00	0.00	0.00
Cr_2O_3	0.00	0.00	0.00	0.00	0.00	0.00	0.00	0.00	0.00
Total	99.82	98.67	100.29	99.39	99.19	98.79	100.17	99.90	100.78
Wo	38.33	46.60	42.07	43.81	42.23	45.09	44.88	44.63	46.99
En	55.26	44.41	51.97	46.58	48.68	44.72	48.54	49.73	47.10
Fs	6.40	8.98	5.95	9.61	9.09	10.18	6.57	5.63	5.90
Fo	89.62	83.18	89.73	82.91	84.27	81.45	88.08	89.83	88.87
Mg#	62.36	62.36	62.36	62.36	62.36	62.36	62.36	62.36	62.36

Table E.21: Major element composition for clinopyroxene from Basin E.

TAN1213-10-2							
Basin E							
Oxides	10-2-01-Core	10-2-01-Rim	10-2-010-Core	10-2-02-Core	10-2-03-Rim	10-2-04-Core	10-2-04-Rim
SiO_2	50.59	51.42	44.76	50.77	52.27	49.28	46.16
TiO_2	0.46	0.55	1.63	0.55	0.28	0.80	1.57
Al_2O_3	3.25	3.32	6.66	3.06	1.76	4.02	7.00
FeOt	5.99	7.49	10.04	6.50	6.02	7.05	12.19
MnO	0.23	0.31	0.29	0.26	0.29	0.26	0.58
MgO	15.63	15.07	10.82	15.56	17.07	14.81	10.12
CaO	18.43	16.04	16.60	17.99	17.69	18.10	13.51
NiO	0.00	0.00	0.00	0.00	0.00	0.00	0.00
Cr_2O_3	0.00	0.00	0.00	0.00	0.00	0.00	0.00
Total	99.20	99.99	98.87	99.64	99.80	99.88	100.81
Wo	41.09	37.44	42.04	40.25	38.35	40.96	36.42
En	48.47	48.90	38.11	48.40	51.45	46.59	37.93
Fs	10.43	13.65	19.84	11.35	10.19	12.45	25.64
Fo	82.30	78.18	65.76	81.01	83.48	78.92	59.67
Mg#	82.29	78.18	65.76	81.01	83.47	78.92	59.66

TAN1213-10-2									
Basin E									
Oxides	10-2-05-Core	10-2-05-Rim	10-2-06-Co	10-2-07-Core	10-2-07-Rir	10-2-08-Co	10-2-08-Rim	10-2-09-Core	10-2-09-Rim
SiO_2	50.89	47.67	50.15	48.95	45.69	45.60	48.65	49.79	49.03
TiO_2	0.44	1.06	0.80	1.00	1.39	1.36	0.74	0.69	0.94
Al_2O_3	2.93	5.33	3.89	4.64	7.71	7.63	4.75	3.32	4.26
FeOt	5.74	7.66	7.83	7.40	8.72	8.08	7.04	6.70	7.39
MnO	0.19	0.27	0.27	0.25	0.26	0.28	0.23	0.22	0.22
MgO	15.80	14.21	16.56	15.00	11.84	11.73	14.24	14.82	14.48
CaO	19.51	17.12	14.95	16.72	17.08	17.04	18.24	18.55	18.30
NiO	0.00	0.00	0.00	0.00	0.00	0.00	0.00	0.00	0.00
Cr_2O_3	0.00	0.00	0.00	0.00	0.00	0.00	0.00	0.00	0.00
Total	99.93	99.42	100.42	99.77	99.95	98.46	99.49	99.22	100.48
Wo	42.45	39.94	33.91	38.56	42.32	42.97	41.90	41.78	41.39
En	47.79	46.10	52.22	48.11	40.81	41.13	45.47	46.43	45.54
Fs	9.75	13.95	13.86	13.32	16.86	15.90	12.62	11.78	13.06
Fo	83.06	76.77	79.03	78.32	70.76	72.12	78.28	79.76	77.72
Mg#	83.06	76.77	79.03	78.32	70.76	72.12	78.27	79.76	77.72

Table E.22: Major element composition for clinopyroxene from Basin E.

TAN1213-11-1							
Basin E							
Oxides	11-1-01-Core	11-1-01-Rim	11-1-02-Rim	11-1-03-Core	11-1-04-Core	11-1-04-Core	11-1-05-Core
SiO_2	51.44	54.10	54.23	52.49	52.11	52.08	54.17
TiO_2	0.77	0.26	0.28	0.43	0.42	0.44	0.30
Al_2O_3	3.95	1.73	2.01	3.50	3.49	3.64	1.95
FeOt	3.82	3.25	2.73	2.99	2.83	2.91	2.60
MnO	0.15	0.17	0.14	0.12	0.13	0.12	0.13
MgO	16.87	19.05	18.37	17.45	17.09	16.80	18.28
CaO	20.48	20.06	21.38	20.88	21.47	21.93	21.52
NiO	0.00	0.00	0.00	0.00	0.00	0.00	0.00
Cr_2O_3	0.00	0.00	0.00	0.00	0.00	0.00	0.00
Total	100.84	101.51	102.02	101.56	101.14	101.60	101.74
Wo	43.65	40.86	43.58	43.97	45.25	46.11	43.94
En	49.99	53.96	52.07	51.10	50.08	49.11	51.91
Fs	6.35	5.17	4.34	4.91	4.66	4.77	4.14
Fo	88.73	91.26	92.32	91.23	91.49	91.15	92.62
Mg#	88.73	91.25	92.31	91.23	91.49	91.15	92.62

TAN1213-11-1				
Basin E				
Oxides	11-1-05-Core	11-1-05-Core	11-1-05-Rim	11-1 clino_05_rim
SiO_2	51.51	53.69	51.97	51.45
TiO_2	0.59	0.24	0.59	0.92
Al_2O_3	4.14	1.99	3.24	3.95
FeOt	3.53	2.71	4.36	4.31
MnO	0.13	0.14	0.18	0.15
MgO	17.30	18.56	17.09	16.03
CaO	20.17	20.84	19.90	20.59
NiO	0.00	0.00	0.00	0.00
Cr_2O_3	0.00	0.00	0.00	0.00
Total	101.03	100.98	100.86	101.10
Wo	42.92	42.73	42.27	44.52
En	51.20	52.92	50.48	48.19
Fs	5.87	4.34	7.23	7.27
Fo	89.72	92.42	87.47	86.89
Mg#	89.72	92.42	87.47	86.89

Table E.23: Major element composition for clinopyroxene from Basin G.

TAN1213-47-1					
Basin G					
Oxides	47-1-01-Core	47-1-02-Core	47-1-02-Rim	47-1-03-Core	47-1-04-Core
SiO_2	51.35	48.82	52.13	52.14	48.65
TiO_2	4.42	6.45	3.52	3.51	6.63
Al_2O_3	4.59	5.96	3.72	8.00	6.48
FeOt	0.08	0.11	0.06	0.16	0.09
MnO	13.60	12.30	14.03	12.01	12.01
MgO	21.38	20.62	21.88	15.49	21.01
CaO	21.41	20.65	21.91	15.51	21.04
NiO	0.00	0.00	0.00	0.00	0.00
Cr_2O_3	0.00	0.00	0.00	0.00	0.00
Total	116.84	114.92	117.25	106.83	115.92
Wo	41.81	41.79	41.82	41.72	41.80
En	58.05	58.03	58.08	57.93	58.04
Fs	0.13	0.17	0.09	0.34	0.14
Fo	99.79	99.71	99.85	99.41	99.75
Mg#	99.79	99.71	99.85	99.41	99.75

TAN1213-47-2		
Basin G		
Oxides	47-2-01-Core	47-2-01-Rim
SiO_2	51.91	52.10
TiO_2	0.40	0.39
Al_2O_3	3.87	3.67
FeOt	2.61	2.53
MnO	0.07	0.07
MgO	16.81	17.03
CaO	21.24	21.58
NiO	0.08	0.03
Cr2O3	1.09	1.09
Total	100.44	100.80
Wo	45.54	45.68
En	50.10	50.13
Fs	4.36	4.18
Fo	92.00	92.31
Mg#	91.99	92.31

Table E.24: Major element composition for clinopyroxene from Basin I.

TAN1513-040-02							
Basin I							
Oxides	040-02-01-Core	040-02-02-Core	040-02-02-Rim	040-0-02-Core	040-02-03-Core	040-02-03-Rim	040-02-03-Rim
SiO_2	52.09	52.28	52.64	53.62	52.65	54.97	54.23
TiO_2	0.29	0.27	0.24	0.21	0.41	0.23	0.23
Al_2O_3	3.48	3.39	3.05	2.15	2.24	2.17	2.12
FeOt	2.37	2.31	2.17	2.29	4.08	2.37	2.54
MnO	0.10	0.12	0.07	0.09	0.18	0.09	0.14
MgO	16.85	16.92	17.23	18.04	16.20	18.41	18.61
CaO	22.43	22.54	22.57	22.23	21.50	22.02	21.59
NiO	0.00	0.00	0.00	0.00	0.00	0.00	0.00
Cr_2O_3	0.00	0.00	0.00	0.00	0.00	0.00	0.00
Total	100.99	100.96	101.02	101.11	100.36	102.87	102.13
Wo	47.00	47.09	46.80	45.26	45.53	44.51	43.66
En	49.11	49.14	49.68	51.09	47.72	51.74	52.33
Fs	3.88	3.76	3.51	3.64	6.74	3.74	4.00
Fo	92.67	92.90	93.40	93.34	87.63	93.25	92.89
Mg#	92.67	92.89	93.40	93.34	87.62	93.25	92.89

TAN1513-040-02				
Basin I				
Oxides	040-02-04-Core	040-02-04-Rim	040-02-05-Core	040-02-05-Rim
SiO_2	50.01	53.81	49.31	53.14
TiO_2	0.91	0.21	0.84	0.20
Al_2O_3	6.57	2.15	7.14	2.83
FeOt	3.67	2.53	3.49	2.21
MnO	0.10	0.13	0.13	0.07
MgO	15.04	18.37	14.83	17.32
CaO	21.95	21.09	21.52	22.86
NiO	0.00	0.00	0.00	0.00
Cr_2O_3	0.00	0.00	0.00	0.00
Total	101.76	100.95	100.60	101.51
Wo	48.00	43.38	47.97	46.96
En	45.73	52.54	45.96	49.49
Fs	6.27	4.07	6.07	3.54
Fo	87.95	92.82	88.34	93.32
Mg#	87.95	92.82	88.34	93.32

Appendix F: EMPA Analytical Standards

Table F.1: List of preferred values for major element abundances EMPA standard San Carlos. Reference values were obtained from Jarosweich et al. (1980).

Standard	n=49		
San Carlos olivine	**Mean concentration**	**SD**	**Ref**
Oxide			
SiO_2	40.91455102	0.15105737	40.81
TiO_2	0.002634615	0.00374694	
Al_2O_3	0.033365385	0.01285575	
FeOt	9.431346154	0.17305189	9.55
MnO	0.142326923	0.01606923	0.14
MgO	49.59159615	0.36519927	49.42
CaO	0.143769231	0.02688767	<0.05
NiO	0.345846154	0.04061659	0.37
Cr_2O_3	0.012096154	0.01222113	
Total	98.26173077	9.55383908	100.29

Table F.2: List of preferred values for major element abundances EMPA standard Kakanui Augite. Reference values were obtained from Jarosweich et al. (1980).

Standard	n=32		
Kakanui Augite	**Mean concentration**	**SD**	**Ref**
Oxide			
SiO_2	50.4715625	0.228374	50.73
TiO_2	0.818	0.021234	8.73
Al_2O_3	8.65934375	0.093518	0.74
FeOt	6.18584375	0.152416	6.34
MnO	0.14028125	0.016583	0.13
MgO	16.410625	0.14903	16.65
CaO	15.76896875	0.1041	
NiO	0.03734375	0.024152	
Cr_2O_3	0.1541875	0.018333	0.15
Total	99.91578125	0.396153	100.56